

THE UNIVERSITY OF CALGARY

Towards More Realistic Molecular Modeling of Catalysis with Density Functional
Theory: Combined QM/MM and *ab initio* Molecular Dynamics Methods.

by

Tommy Kwong Woo

A THESIS SUBMITTED TO THE FACULTY OF GRADUATE STUDIES IN
PARTIAL FULFILLMENT OF THE REQUIREMENTS FOR THE DEGREE OF
DOCTOR OF PHILOSOPHY

DEPARTMENT OF CHEMISTRY

CALGARY, ALBERTA

AUGUST, 1998

© Tommy Kwong Woo 1998



National Library
of Canada

Acquisitions and
Bibliographic Services

395 Wellington Street
Ottawa ON K1A 0N4
Canada

Bibliothèque nationale
du Canada

Acquisitions et
services bibliographiques

395, rue Wellington
Ottawa ON K1A 0N4
Canada

Your file Votre référence

Our file Notre référence

The author has granted a non-exclusive licence allowing the National Library of Canada to reproduce, loan, distribute or sell copies of this thesis in microform, paper or electronic formats.

The author retains ownership of the copyright in this thesis. Neither the thesis nor substantial extracts from it may be printed or otherwise reproduced without the author's permission.

L'auteur a accordé une licence non exclusive permettant à la Bibliothèque nationale du Canada de reproduire, prêter, distribuer ou vendre des copies de cette thèse sous la forme de microfiche/film, de reproduction sur papier ou sur format électronique.

L'auteur conserve la propriété du droit d'auteur qui protège cette thèse. Ni la thèse ni des extraits substantiels de celle-ci ne doivent être imprimés ou autrement reproduits sans son autorisation.

0-612-34712-5

Canada

Abstract

In recent years, Kohn-Sham density functional theory (DFT) has emerged as the premier method to perform practical 'first principles' quantum mechanical calculations due to the method's favourable balance of efficiency and accuracy in dealing with chemical systems. Despite the efficiency of the method, DFT calculations often neglect large ligand effects, solvent effects and finite (non-zero) temperature effects because of the high computational expense of including them. In some cases, these neglected effects are not trivial, but critical to the chemistry of the molecular systems. This thesis involves the development and application of more realistic computational models that account for these often neglected effects, using the *ab initio* molecular dynamics method and the combined quantum mechanics and molecular mechanics (QM/MM) approach. For this purpose, the combined QM/MM methodology of Singh and Kollman has been implemented into both a conventional density functional electronic structure package (ADF) and a Car-Parrinello *ab initio* molecular dynamics package (PAW). The IMOMM coupling scheme of Maseras and Morokuma has been adapted as to allow for energy conserving dynamics and harmonic normal-mode frequency calculations to be performed thereby allowing free energy surfaces to be mapped out with the method. Additionally, a multiple time-step QM/MM molecular dynamics technique has been developed which allows the MM region to be sampled at a faster rate than the QM region. This provides faster equilibration and better ensemble averaging during the calculation of the free energy barriers, without increasing the expense of QM calculation. These implemented methodologies have been applied to examine recently developed transition metal based homogenous catalysts for olefin polymerization. Most notably we have examined the Ni-diimine catalyst of Brookhart in which the extended ligand structure plays a critical role in controlling the polymerization chemistry. We have also evaluated the applicability of using *ab initio* molecular dynamics as a practical tool in studying transition metal based catalysis. Finally, features have been implemented into the Car-Parrinello QM/MM method to allow for solvent simulations in the near future. The impact of this thesis has been to extend the envelope of high level mechanistic computational modeling to include large ligand effects, finite temperature effects and eventually reactions in condensed phases.

Acknowledgments

This thesis would never have been completed without the help and generosity of others. First, I wish to thank my supervisor, Professor Tom Ziegler, for his continuous support, skillful guidance and encouragement throughout this work. I am also thankful for his kindness, friendship and thoughtful advice.

I would like to thank the members of my supervisory committee, Professors Arvi Rauk (who introduced me to the subject of computational chemistry), Michael Boorman for their advice and support. I also wish extend thanks to Professors Ron Kydd, Warren Piers and Brian Keay for their advice.

I am grateful for the financial support of NSERC, the Alberta Heritage Scholarship Fund, the Izaak Walton Killam Memorial Foundation, the University of Calgary and the Department of Chemistry. In this category I also thank Union Carbide.

I enjoyed many fruitful collaborations with others, particularly, Dr. Liqun Deng, Dr. Peter Margl, Dr. Luigi Cavallo, Dr. John Lohrenz, Dr. Peter Blöchl and Dr. Liangyou Fan. I cannot express the value of your contributions. I want to include a special thanks to Liqun for making the office a pleasant place to be and for memories of his great cooking. I also have to thank the folks at Novacore Research and Technology of Calgary, most of all Daryll for his support and encouragement.

I am indebted to other members of the Z-team for the valuable discussions and for sharing their experiences with me, namely, Drs. Attila, Heiko, Steve, Rochus, Cory, Ross, George, and Elizabeth.

I wish to thank all of my friends, Todd, Michelle, Andreas, Fred, Carl, Jennifer and particularly Mark for sharing all those coffees with me and for discussing things outside of chemistry.

I have to thank Mom and Dad, for showing me the value of hard work. Also, for watching the kids and for cooking all those meals for us without notice. Thanks to Gary and Perla for letting me set up an 'office' in their kitchens.

I also thank my girls, Jade and Kiata for helping keep things in perspective and for being the joys of my life.

Most of all, I need to thank my dearest friend and wife, Bonnie, for her endless support and love. I am forever indebted to you for the sacrifices you have made.

FOR MY FAMILY

Table of Contents

Approval Page	ii
Abstract	iii
Acknowledgments	iv
Table of Contents	vi
List of Figures	ix
List of Tables	xiii
Abbreviations	xv
Chapter 1. Introduction	1
1.1 General Introduction	1
1.2 Combined QM/MM	2
1.3 <i>ab initio</i> Molecular Dynamics.....	3
1.4 Objectives.....	4
1.5 Summary of Chapters.....	5
Appendix 1.A Introduction to 'QM' and 'MM' Methods	5
Chapter 2. The QM/MM Methodology and Its Implementation into the ADF Quantum Chemistry Package	10
2.1 Introduction	10
2.2 QM/MM Coupling Schemes	10
2.3 Adaptation of the QM/MM Coupling Scheme of Maseras and Morokuma	14
2.4 QM/MM Implementation into the ADF Density Functional Package.....	16
2.5 IMOMM Frequencies and Thermodynamic Properties	18
2.6 Conclusions	25
Chapter 3. A Combined QM/MM Study of Brookhart's Ni(II) Diimine Olefin Polymerization Catalyst	26
3.1 Introduction	26
3.2 Computational Details.....	29
3.3 Results and Discussion.....	30
3.4 Conclusions	52

3.5	Towards <i>a priori</i> Catalyst Design with the Combined QM/MM Method.	53
Chapter 4.	<i>ab initio</i> Molecular Dynamics Simulations as a Practical Tool For Studying Catalysis.....	58
4.1	Introduction	58
4.2	What is Molecular Dynamics?	58
4.3	Car-Parrinello <i>ab initio</i> Molecular Dynamics.....	60
4.4	Projector Augmented Wave (PAW) Car-Parrinello AIMD	62
4.5	Reaction Free Energy Barriers with AIMD	63
4.6	Thermostating and Mass Rescaling	66
4.7	Mass Rescaling	67
4.8	<i>ab initio</i> Molecular Dynamics Study of Olefin Polymerization Chemistry.	68
4.9	Studying Fluxionality and Time Scales with AIMD.	70
4.10	Using AIMD to Chart Reaction Paths on Flat Potential Surfaces.	71
4.11	New Reaction Pathways with AIMD.....	73
4.12	Reaction Free Energy Barriers with the Slow Growth AIMD Simulations.....	75
Chapter 5.	A Combined Car-Parrinello QM/MM Implementation For <i>Ab Initio</i> Molecular Dynamics Simulations of Extended Systems.....	81
5.1	Introduction	81
5.2	Combined QM/MM Car-Parrinello <i>ab initio</i> Molecular Dynamics	81
5.3	Energy Conservation of IMOMM Molecular Dynamics	83
5.4	Combined QM/MM AIMD Simulation of Chain Termination in Brookhart's Ni-Diimine Olefin Polymerization Catalyst.	85
5.5	QM/MM Multiple Time Step Dynamics	91
5.6	Test Results of the Multiple Time-step QM/MM Approach	95
5.7	Conclusions	108
Chapter 6.	Monomer Capture in Brookhart's Ni(II) Diimine Olefin Polymerization Catalyst: A Static and Dynamic QM/MM Study.....	110
6.1	Summary	110
6.2	Chain Branching Control in Brookhart's Ni-diimine Olefin Polymerization Catalyst System	111
6.2.1	Introduction	111
6.2.2	Computational Details.....	114

6.2.3	Results and Discussion.....	115
6.2.4	Conclusions	124
6.3	Olefin Capture Barrier in Brookhart's Catalyst - A Static and Dynamics Study	125
6.3.1	Introduction	125
6.3.2	Computational Details.....	127
6.3.3	Results and Discussion.....	129
6.3.4	Conclusions	145
Chapter 7.	Towards Solvation Simulations with the PAW QM/MM Method	147
7.1	Introduction	147
7.2	Periodic Boundary Conditions	148
7.3	The QM/MM Solute-Solvent Intermolecular Potential	152
7.4	QM/MM Electrostatic Coupling in PAW	157
7.5	Testing of the PAW QM/MM Coupling: Molecular Dynamics	161
7.6	Testing of the PAW QM/MM Coupling: Li-Water Interaction Potential	163
7.7	Fitting of Bimolecular Hydrogen Bond Interactions	171
7.7	Conclusions	180
Chapter 8.	Conclusions and Outlook.....	182
References	186

List of Figures

Figure 1.1	An example of a chemical system (a) and various computational models of it (b-d).....	2
Figure 2.1	Treatment of the link bond in various QM/MM coupling schemes.....	11
Figure 2.2	Schematic representation of the ADF QM/MM implementation.	17
Figure 2.3	List of structures 2 - 14 showing the partitioning of QM and MM regions.	19
Figure 3.1	Proposed reaction mechanisms of (a) insertion, (b) chain termination and (c) chain branching mechanisms for the Brookhart Ni-diimine olefin polymerization catalyst.	26
Figure 3.2	Axial(Ax) and equatorial(Eq) coordination sites of the metal center and their potential steric interactions with the bulky substituents.	28
Figure 3.3	The QM/MM partitioning of the Ni-diimine catalyst, (ArN=C(CH ₃)-C(CH ₃)=NAr)Ni-R ⁺ used in this study.	29
Figure 3.4	Optimized QM/MM metal alkyl cation and metal alkyl π -ethylene resting state structures.	31
Figure 3.5	Definition of the "ring-plane" angle, θ	32
Figure 3.6	Energy profile for the chain propagation process.	36
Figure 3.7	Optimized geometries of the intermediate π -complexes of the in-plane insertion channel.....	37
Figure 3.8	Transition state and kinetic product for the in-plane insertion channel.	39
Figure 3.9	Transition state and kinetic product for the out-of-plane insertion channel.	41
Figure 3.10	Optimized structure of the thermodynamic β -agostic insertion product.	42
Figure 3.11	Transition state and product of the isomerization or chain branching process.....	44
Figure 3.12	Energy profile for the chain termination process.	46
Figure 3.13	Transition state and product of the chain termination process.....	48
Figure 3.14	McConville's living olefin polymerization catalyst.	54
Figure 3.15	Modification of McConville's Zr diamide catalyst.	55
Figure 4.1	Schematic representation of the hysteresis in a slow growth free energy plot.....	65
Figure 4.2	Constrained Geometry Catalyst (CGC).	68
Figure 4.3	Cossée-Arlman mechanism for chain propagation in the Constrained Geometry single-site olefin polymerization catalyst.	68

Figure 4.4	Selected structural quantities as a function of the simulation time for the AIMD simulation of the Ti-propyl model of the resting state.	71
Figure 4.5	Selected snapshot structures from the AIMD slow growth simulation of the olefin insertion in the constrained geometry catalyst.	72
Figure 4.6	Unimolecular chain termination initiated from the β -agostic alkyl complex was expected to give rise to a olefin-hydride complex.	73
Figure 4.7	Selected structural and electronic quantities as a function of the reaction coordinate for the slow growth simulation of the unimolecular chain termination process.....	74
Figure 4.8	Four chain termination processes studied with the slow growth AIMD method in order to estimate reaction free energy barriers.	76
Figure 4.9	Definition of the midplane reaction coordinate.	77
Figure 4.10	The integrated force on the reaction coordinate traced as a function of the mid plane reaction coordinate for the AIMD simulation the alkyl s-bond metathesis chain termination reaction.	79
Figure 4.11	Comparison of the static and dynamic transition state structures for the alkyl σ -bond metathesis chain termination reaction.	80
Figure 5.1	QM/MM partitioning of 3-methylhexane.	83
Figure 5.2	Plot of the a) kinetic energy of the nuclei (QM and MM) and b,c) the total conserved energy during a combined QM/MM molecular dynamics simulation of 3-methylhexane, 32	84
Figure 5.3	The relative free energy as a function of the mid-plane reaction coordinate for the chain termination process.	88
Figure 5.4	Selected structural and energetic quantities as a function of the reaction coordinate from the combined QM/MM simulation.	89
Figure 5.5	Snapshot structure from the transition state region of the combined QM/MM molecular dynamics simulation.	90
Figure 5.6	Representation of a simple multiple time step scheme within the Car-Parrinello framework.	92
Figure 5.7	Schematic representation of a Tuckerman's reversible multiple time step procedure implemented within the PAW QM/MM method.....	93
Figure 5.8	a) Kinetic energy of the QM and MM nuclei for a multiple time step QM/MM dynamics simulation of 4-ethylnonane.....	97
Figure 5.9	Deviation in the distance terminal carbons (C1-C9) in 4-ethylnonane between the standard Verlet trajectory and multiple time step trajectories.	98
Figure 5.10	a) Potential energy of the QM model system for the standard Verlet and the multiple time step Verlet 20:1 and 10:1 over-sampled.	99
Figure 5.11	Comparison of the energy conservation during simulations of 4-ethylnonane.	100
Figure 5.12	Mass rescaling schemes used for the QM/MM dynamics simulations of 4-ethylnonane.	101

Figure 5.13	Comparison of the energy conservation of the multiple time step simulations of 4-ethylnonane.	102
Figure 5.14	QM/MM partitioning, mass rescaling scheme and constraint definition for the molecular dynamics simulations of n-undecane.	103
Figure 5.15	Temperatures of the QM and MM subsystems of the dynamics simulation undecane with a) standard masses and b) rescaled masses.	105
Figure 5.16	Temperature evolution of the QM and MM subsystems of the dynamics simulation undecane with standard masses and the standard Verlet propagator.	106
Figure 5.17	Evolution of the average constraint force during the standard(solid lines) and multiple time step(dashed lines) dynamics of undecane.	108
Figure 6.1	Proposed chain branching mechanism in Brookhart's Ni(II) diimine olefin polymerization catalyst system.	111
Figure 6.2	Possible indirect steric effect of the R' diimine substituents on the monomer capture process.	114
Figure 6.3	Optimized metal alkyl and π -complex structures of the model systems 1b and 3b	119
Figure 6.4	Full chain termination process including the loss of the olefin terminated polymer chain.	126
Figure 6.5	'Static' linear transit energy profiles of the capture process.	130
Figure 6.6	Slow growth free energy profiles of the capture process at 300 K for models 4 , 5 and 6	132
Figure 6.7	a) Deviation of the plane angle from perpendicular orientation of the aryl rings relative to the diimine ring extracted from the slow growth simulation of the capture process for models 5 and 6 . b) definition of the angle φ	137
Figure 6.8	Slow growth free energy profile of the olefin ejection process for model catalyst system 6	138
Figure 6.9	Optimized structure for the double olefin π -complex of model 6	142
Figure 6.10	Static energy profile for the formation of the double olefin π -complex in catalyst 6	143
Figure 7.1	a) Continuum solvation model. b) explicit solvation model.	147
Figure 7.2	Two dimensional representation of periodic boundary conditions.	149
Figure 7.3	Example of the minimum image convention.	150
Figure 7.4	Truncated octahedron.	152
Figure 7.5	Example of a van der Waals non-bonded potential between atoms.	154
Figure 7.6	Schematic representation of the PAW QM/MM electrostatic coupling.	158
Figure 7.7	Various energetic quantities traced during the PAW QM/MM simulation of ethane in ethane.	162

Figure 7.8	Partitioning of the Li ⁺ - water system.	164
Figure 7.9	Li ⁺ -water interaction profile for the pure QM reference potential and the hybrid PAW/AMBER potential.	166
Figure 7.10	Comparison of the Li-water interaction potentials for various hybrid PAW QM/MM potentials.....	170
Figure 7.11	Bimolecular complexes used in the parameterization of the PAW QM/MM potential.	172

List of Tables

Table 2.1	Summary of features in the ADF QM/MM implementation.	18
Table 2.2	Summary of features in the core molecular mechanics code.	18
Table 2.3	Comparison of IMOMM and Pure QM Frequencies and Zero Point Energies.....	21
Table 2.4	Comparison of IMOMM and Pure QM Relative Thermochemical Data at 298 K.	24
Table 3.1	Energy decomposition for insertion, termination and isomerization processes.	34
Table 3.2	Comparison of calculated barriers to experimental relative barriers.	49
Table 3.3	Comparison of the catalytic capability of the new catalysts with the mcconville and brookhart catalysts for polymerization of ethylene.	57
Table 4.1	Comparison of the "static" and "dynamic" reaction free energy barriers.	78
Table 6.1	Experimental chain branching data.	113
Table 6.2	Capture energies without steric effects.	116
Table 6.3	The effect of R' substitutions on the charge density on ni and the back-bonding in the π -complex.....	117
Table 6.4	Capture Energies without electronic influence of the R' substituents.....	118
Table 6.5	Change in geometry and energy components during olefin complexation.	121
Table 6.6	Capture Energies with both steric and electronic effects incorporated.	122
Table 6.7	Free energy barriers including hysteresis from slow growth simulations of the capture process.	133
Table 6.8	Thermodynamic data at 298 K for the olefin complexation for model catalyst 4 relative to the free species.....	134
Table 6.9	Thermodynamic data at 298.12 K for the olefin complexation for model catalyst 6 based on a QM/MM frequency calculation.	139
Table 7.1	Typical van der Waals parameters from the AMBER-95 molecular mechanics force field.	155
Table 7.2	Water-Li+ interaction energies and fitted charge of the water molecule.	165
Table 7.3	Comparison of the fitted charges from the PAW QM/MM calculation and a pure QM PAW calculation.....	167
Table 7.4	Li+ van der Waals parameters used in the various hybrid potentials.	168
Table 7.5	Comparison of the optimized PAW/MM potentials with the pure QM Water-lithium ion potential.	169
Table 7.6	Optimized Lennard-Jones Parameters for the Combined Hartree-Fock 3-21G and TIP3P potential of Freindorf and Gao.....	174

Table 7.7	Computed interaction energies for the monomer-water fit set with various potentials.	175
Table 7.8	Optimized Lennard-Jones Parameters for the PAW QM/MM potential using an effective electrostatic scaling factor of 0.95	176
Table 7.9	PAW QM/MM interaction energies using an electrostatic scaling factor of 0.95	178
Table 7.10	Computed interaction distances for the Monomer-water Fit Set	179

List of Abbreviations

ADF	Amsterdam Density Functional package
AIMD	<i>ab initio</i> molecular dynamics
AMBER95	molecular mechanics force field of Kollman and coworkers. ⁷⁷
amu	atomic mass units
ANAP	acenaphthalene
BP86	Becke's exchange ¹⁰³ with Perdew's 1986 correlation ^{104,118} functional
BSSE	basis set superposition error
CGC	constrained geometry catalyst
CP	Car-Parrinello
Cp	cyclopentadienyl
DFT	density functional theory
HF	Hartree-Fock
IMOMM	integrated molecular orbital and molecular mechanics
MC	Monte Carlo
MD	molecular dynamics
MM	molecular mechanics
QM	quantum mechanics
QM/MM	quantum mechanics and molecular mechanics
PAW	projector augmented wave
OPLS-AA	all-atom molecular mechanics force field for simulation of liquids by Jorgensen and coworkers. ¹⁵⁹
RC	reaction coordinate
RMS	root mean square
ZPE	zero point energy
STO	Slater-type orbital
SCF	self consistent field
TIP3P	molecular mechanics force field for liquid water simulations by Jorgensen and coworkers. ³²
TS	transition state
UFF	Universal Force Field of Rappé and coworkers. ⁸¹
vdW	van der Waals

Chapter 1

Introduction

1.1 General Introduction

Computational chemistry, also referred to as molecular modeling, involves simulating chemical reactions and processes at the atomic level within the virtual space of a computer. This type of modeling is establishing itself as a valuable tool for chemists of all disciplines and this will only become more evident as computer technology continues to advance. In the pharmaceutical industry, for example, computational chemistry is considered an integral part of the drug design process and not just a novel academic endeavour. Despite the proven success of modeling, the application of it to studying transition metal based catalytic systems still presents a challenge for established methods.

The computational modeling of catalytic reactions necessitates a high level quantum mechanical treatment because lower level methods cannot accurately treat the bond breaking and forming that occurs during these processes. However, a high level quantum mechanical study often involves a stripped down model system that only vaguely resembles the true system. An example of this is depicted in Figure 1.1 where the 'real' catalyst system that is being modeled is shown in (a), while a likely model of it used for a quantum mechanical calculation is shown in (b). Thus, if large ligands are involved, they are most often neglected in high level calculations with the hope that they do not substantially influence the nature of the reaction mechanisms. Unfortunately, the surrounding ligand system, protein matrix, or solvent can often play a critical mechanistic role. One dramatic example in organometallic catalysis is that of the recently developed Ni(II) Brookhart polymerization catalyst, **1** (Figure 1.1).^{1,2} Without an extended ligand system the catalyst acts only as a dimerization catalyst. However, by attaching an extended and sterically demanding ligand system, Brookhart and co-workers were able to transform the poor polymerization catalyst into a commercially viable one.³ Therefore, quantum mechanical models which do not treat the extended ligand structure or solvent environment may yield results which are inconclusive, suspect or possibly erroneous. Even with the rapid development of computer technology and modern linear scaling methods,⁴⁻⁶ the full quantum mechanical treatment of these extended systems is not expected to be practical in the near future.

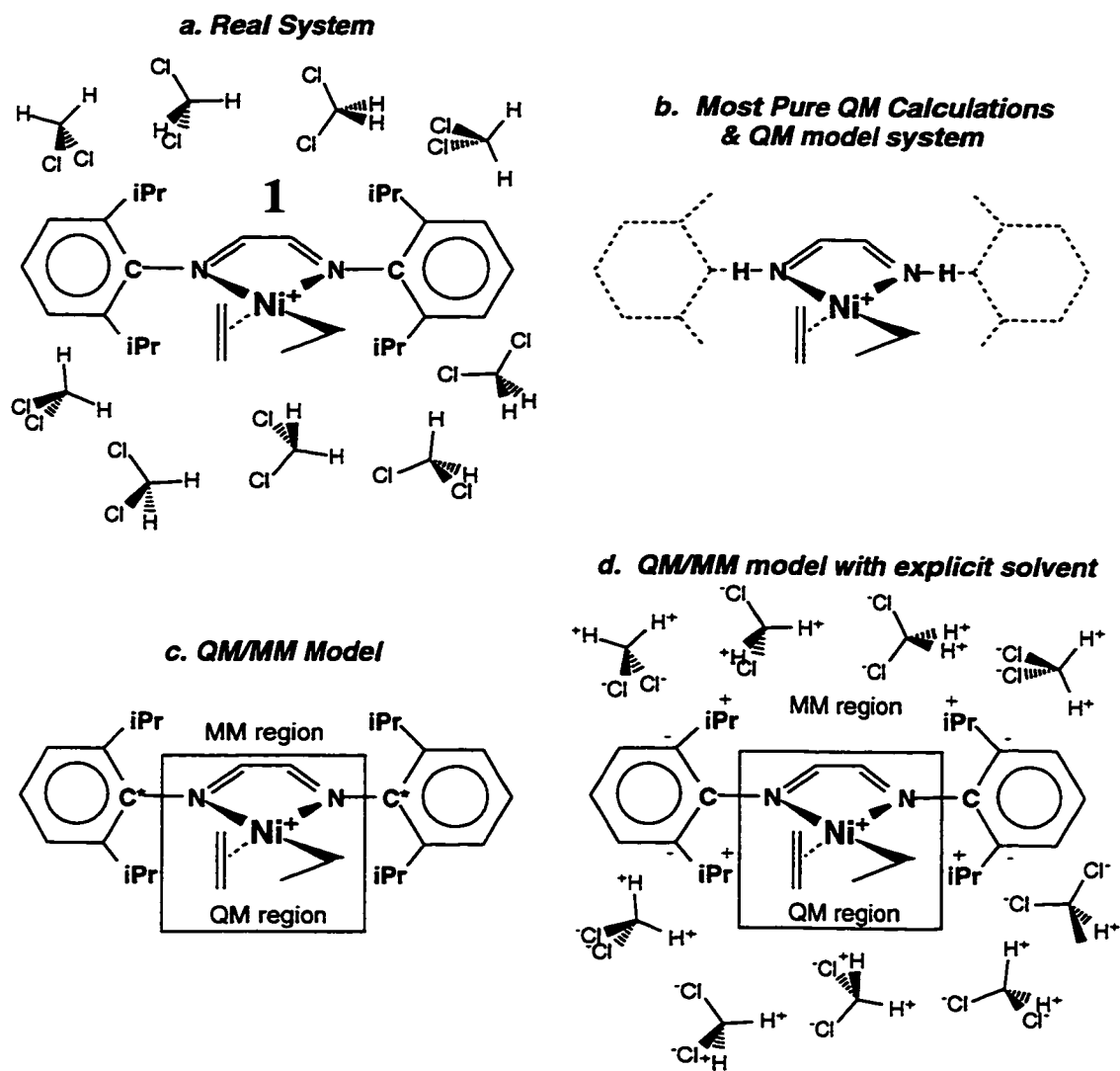


Figure 1.1. An example of a chemical system (a) and various computational models of it (b-d).

1.2 Combined QM/MM

One reasonable approach to escape this problem is the combined quantum mechanics and molecular mechanics (QM/MM) method.⁷⁻⁹ In this hybrid method part of the molecular potential, such as the active site region, is determined by a quantum mechanical calculation while the remainder of the molecular potential is determined using a much faster molecular mechanics force field calculation. Such a partitioning is illustrated in Figure 1.1c. The promise of the QM/MM method is that it allows for simulations of bond breakage and formation at the active site, while still allowing for the role of the extended system to be modeled in an efficient and computationally tractable

manner. The key feature of the QM/MM method is that the QM calculation is performed on a truncated "QM model"(Figure 1.1b) of the active site, where the large ligands have been removed and replaced with capping atoms. Then, a molecular mechanics calculation is performed on the remainder of the system and the effects of the attached ligands are incorporated to form the potential surface of the whole system where the QM and MM regions interact with one another via steric and electrostatic potentials.

The combined QM/MM methodology dates back to work by Warshel and Levitt⁷ in 1976, but it was not until 1986 that a practical QM/MM prescription was developed by Singh and Kollman.⁸ Despite its history, QM/MM methods have only recently¹⁰ received serious attention as a practical modeling tool to examine extended systems too large for pure QM methods.^{8,9,11-19} Most applications have been concentrated in the areas of treating solvation^{10,18} and the simulations of proteins and nucleic acids.^{12,20-24} In the arena of solvent simulations the combined QM/MM method has been shown to correctly model the charge reorganization of an active site due to the solvent and to provide accurate free energy barriers in the condensed phase.^{10,14,25-27} The QM/MM modeling of proteins has also been successful despite the impressive challenges that these complicated macromolecules impose. An area which has only begun to be explored with hybrid QM/MM potentials is transition metal containing catalytic systems, such as metalloenzymes¹² and organometallic²⁸⁻³⁰ complexes.

1.3 *Ab initio* Molecular Dynamics

Conventional electronic structure calculations can be classified as "static" simulations. In these calculations, reaction mechanisms are generally examined by optimizing stationary points (minima and transition states) on the potential surface at the zero temperature limit. There is no doubt that these studies are valuable since these stationary points play a central role in determining the kinetics and thermodynamics of a catalytic system. However, it is really the finite temperature free energy profile of a system that can be directly related to rate constants and thermodynamic properties derived from experiment.

Relative free energies of a chemical system can be mapped out at the molecular level using classical statistical thermodynamics. Here it is necessary to generate a series of configurations which sample a chosen statistical ensemble. The resulting ensemble averages provide the basis of the calculated thermodynamic properties. Computer simulations can be used to sample ensembles probabilistically using Monte Carlo (MC) sampling methods or deterministically by integrating Newton's equations of motion, via

molecular dynamics(MD). MC and MD methods have a long and diverse history of studying chemical systems. They include simulations of liquid water,^{31,32} proteins and nucleic acids.^{33,34} Because of the enormous cost of properly sampling an ensemble, high level quantum mechanical methods have not traditionally been used. Instead, empirical molecular mechanics force fields have been utilized for these simulations because of their computational efficiency. As previously mentioned, the major drawback of molecular mechanics methods is that chemical reactions cannot be properly simulated and transition metal complexes are problematic. For these problem cases (and others), finite temperature free energy profiles have traditionally been calculated from conventional 'static' electronic structure calculations. The approach involves constructing an approximate partition function at each stationary point based on a harmonic frequency calculation. The 'static' approach to examining the finite temperature free energy surface is most efficient when reaction barriers are high and the potential surface has a high curvature.³⁴ However, when the potential surface is flat and the molecular system has a high degree of configurational variability, the static approach becomes inefficient and tedious to apply.

The potential energy surfaces of transition metal based catalyst systems, particularly those adept at mediating chemical transformations, can be flat and complicated. This often means that entropy and other finite temperature effects play an important role in determining the reactivity of the systems. Recently, the rapid advances in computational power have allowed molecular dynamics (and MC) techniques to be applied at the QM level. With this approach, which has been termed *ab initio* molecular dynamics, the potential surface is generated from a full electronic structure calculation as opposed to a molecular mechanics force field. This has allowed traditional, well-established molecular dynamics techniques to be applied to study chemical reactions and transition metal based systems.

1.4 Objectives

The goal of this work is to apply and further develop the combined QM/MM and *ab initio* molecular dynamics methods so as to build more realistic computational models of catalytic reactions that take into account extended ligand effects, finite temperature effects and eventually solvation effects. Figure 1.1 nicely illustrates this objective starting from a 'real' chemical system, moving to more and more sophisticated computational models of it. The thesis contains both implementation and application components to it. In terms of implementation, the thesis describes the development and

incorporation of the QM/MM method into both a conventional 'static' density functional package and into the framework of a Car-Parrinello *ab initio* molecular dynamics package. On the application side, we have examined the chemistry of several newly developed single-site olefin polymerization catalysts. (These transition metal based catalysts are expected to revolutionize the multi-billion dollar polyolefin industry.³⁵) In most cases, the studies in this thesis represent the first time these novel techniques have been applied to study transition metal based catalyst systems of this type. For this reason, we also hope to evaluate how these new methods can be effectively used to study the systems of interest. The ultimate goal of both the applications and implementation work is to help us gain a deeper understanding of the chemistry of single-site olefin polymerization systems and possibly contribute to the design of new catalyst systems.

1.5 Summary of Chapters

Appended to this chapter, is a brief overview of the so called 'QM' and 'MM' methods for readers not familiar with the computational techniques. In Chapter Two we begin to discuss the QM/MM methodology in more detail. We also describe how we have adapted an existing QM/MM approach as to allow for both frequency calculations and molecular dynamics simulations with it. Details of the combined QM/MM implementation into the ADF density functional quantum chemistry package³⁶⁻³⁹ are also presented in this chapter. Chapter Three details how the ADF QM/MM implementation has been applied to study the recently developed olefin polymerization catalyst systems of Brookhart¹ and McConville.⁴⁰ Chapter Four summarizes our experience with utilizing *ab initio* molecular dynamics as a practical tool to study homogeneous catalysis. Next, in Chapter Five we present our implementation of the QM/MM method into the Car-Parrinello PAW⁴¹ *ab initio* molecular dynamics package. Here we also introduce and validate the multiple-time step QM/MM molecular dynamics methodology that we have developed. In Chapter Six we have applied both the ADF and PAW QM/MM programs to study the monomer capture process in olefin polymerization systems. Chapter Seven details the QM/MM PAW implementation to allow for eventual solvation simulations at the *ab initio* molecular dynamics level. The thesis is concluded in Chapter Eight with a summary of the work and an outlook.

Appendix 1.A Introduction to 'QM' and 'MM' Methods

Computational techniques have been used to predict anything from NMR spectra to the average shape of a solvated protein at 298 K. To study catalytic processes at the

molecular level, it is necessary to model reaction energetics, dynamics and geometries. Here the molecular potential energy surface plays a fundamental role. There are a great variety of different methods available to calculate a system's potential energy surface. However, they can be roughly divided into two categories: quantum mechanical methods and molecular mechanics methods. Provided in this section is an elementary introduction to the methods.

Quantum Mechanical Methods. Perhaps the most direct way of determining the energetics and structure of a molecular system is to solve the quantum mechanical Schrödinger equation. This is a computationally demanding process and consequently only small molecular systems can be treated. The results, however, can be very accurate with experimental accuracy being attained in some cases. Other properties, such as transition state structures, reaction barriers and reaction profiles cannot be easily determined experimentally and are best calculated by computational means. Quantum mechanical methods can also provide a detailed picture of the electronic structure of a molecular system, which can yield invaluable insights into the nature of the system. Elementary reaction steps in homogenous catalysis have been investigated with increasing success by quantum mechanical methods over the past decade.⁴²

First Principles QM Methods. The Schrödinger equation can be solved to varying degrees of accuracy by a variety of different methods. Quantum mechanical methods can be further grouped into 'first principles' (or 'ab initio' methods) and semi-empirical approaches. The "first principles" techniques are so-called because they are derived from the basic postulates of quantum mechanics and require little or no parameterization. The most widely used 'first principles' scheme is the *ab initio* Hartree-Fock method.^{43,44} Another quantum mechanical method known as density functional theory⁴⁵⁻⁴⁷ or DFT is quickly emerging as the preferred methodology to deal with transition metal complexes and large sized systems. The reason for this is that it has been shown to be faster and generally more accurate than Hartree-Fock based methods for these types of systems.⁴⁸ To date, DFT is the method of choice for theoretically studying single-site catalyst systems and many such systems have been examined by DFT.⁴⁹⁻⁶³

The theoretical rigor of quantum mechanical based methods affords several advantages. In terms of studying catalysis, the most significant feature of QM based methods is that chemical reactions can be modeled at the molecular level. Thus, reaction intermediates, transition states and barriers can be determined and detailed reaction profiles can be elicited. From this, important kinetic and thermodynamic information of

the catalytic processes can be determined. At the density functional level, reaction barriers can be estimated to within 3.5 kcal/mol.^{60,61,64,65}

The primary disadvantage of 'first principles' QM based methods is that their theoretical rigor also demands extensive computational resources. At the present time, detailed and expedient studies of molecular systems are limited to systems of under one hundred atoms. For this reason, calculations are generally performed on truncated model systems which can be a severe approximation to the real system. For example, in modeling single-site catalyst systems, the solvent and counter-ion are generally ignored.

Semi-empirical QM Methods. When the labour of an *ab initio* type calculation becomes too great, semi-empirical⁶⁶⁻⁶⁸ methods are often employed. These methods have interesting acronyms such as CNDO,⁶⁹ INDO,⁷⁰ MINDO,⁷¹ MNDO,⁷² AM1,⁷³ and PM3.⁷⁴ With semi-empirical methods many approximations are made in solving the Schrödinger equation that are designed to speed up the calculations. To make up for these approximations, many empirical parameters are introduced that have been fitted to experimental or *ab initio* results. The fitted parameters that are introduced give these methods the name "semi-empirical".

Semi-empirical methods have gained wide acceptance by organic chemists and have developed into a useful tool for experimentalists. For modeling transition metal complexes, parameterization of semi-empirical methods^{75,76} have been less successful. To date there is no method available that contains a single parameter set that provides both good geometries and energetics for these types of complexes. As a result, semi-empirical studies of transition metal complexes need to be augmented with higher level 'first principles' calculations in order to obtain meaningful results. As yet, for studying single site catalysts, semi-empirical methods are largely untested and therefore unreliable for mapping out potential energy surfaces.

Molecular Mechanical Methods Molecular mechanics is fundamentally different from 'first principles' and semi-empirical QM based methods, in that there is no attempt to solve the Schrödinger equation. There are no wave functions or molecular orbitals in molecular mechanics. In fact the electronic system is not treated explicitly (its effects of course are felt). Instead of blanketing the nuclei with a complicated electron density, in order to determine how much a geometric deformation increases or decreases the potential energy of a molecular system, the potential energy surface is determined from a set of very simple mathematical functions that are fit to reproduce experimental results. In this case, simplicity is a virtue because molecular mechanics methods can

effectively treat large macromolecules such as proteins, involving tens of thousands of atoms.

One way of describing molecular mechanics is that it treats molecules as a set of balls connected together by springs. Each type of bond (e.g. C-C or C-H bond) is represented with a different kind of spring with a specific stiffness and equilibrium distance. If a bond is stretched, Hooke's law is assumed which results in a restoring force and a rise in energy of the system. In this way, each type of bond possesses a unique potential surface that is characteristic of the bond's natural length and strength. This is at the heart of molecular mechanics, the idea that a particular structural feature such as a C-H bond distance is essentially the same whether it is in butane or in DNA. In general, this is also true for bond angles, bond torsions, strain energies and so on. Thus, the structure and energy of large molecules can be formulated in terms of empirical parameters derived from the elementary features of smaller, well known molecules. Together, the sum of all the energy terms for the bond stretches (E_b), angles (E_θ), dihedrals (E_ϕ), and non-bonded interactions (E_{nb}) of a molecule forms the potential energy surface.

$$E_T = \sum E_b + \sum E_\theta + \sum E_\phi + \sum E_{nb}$$

The functional forms of the various energy terms, and the parameters contained within them, make up what is called a force field. A force field is highly parameterized in order to provide reasonable agreement with experiment. Furthermore, the parameters are often fit to a specific group or type of molecular system and therefore force fields are generally designed to treat specific classes of molecules. For example, the AMBER⁷⁷ and CHARMM⁷⁸ force fields are designed to treat proteins and nucleic acids while the MMx⁷⁹ group of force fields are designed to treat small organic and main group inorganic molecules.

For studying transition metal based catalytic processes, molecular mechanics methods possess two serious limitations. First, bond breaking and formation of covalent bonds can not be treated and therefore chemical reactions cannot be simulated accurately. Secondly, force fields that can effectively deal with the complicated and varied bonding schemes of transition metals are only currently being developed.⁸⁰⁻⁸² These limitations confine molecular mechanics studies of transition metal catalysts to the qualitative regime. Studies of metallocene catalysts by molecular mechanics was pioneered by Corridini and co-workers.⁸³⁻⁸⁶ These studies have contributed significantly to our understanding of the control of stereospecific α -olefin polymerization by metallocene

catalysts. Attempts to apply molecular mechanics to obtain quantitative or semi-quantitative results have been met with limited success.^{58,87-91}

Chapter 2

The QM/MM Methodology and Its Implementation into the ADF Quantum Chemistry Package

2.1 Introduction

The combined QM/MM approach involves partitioning the system into QM and MM regions whereby the molecular potential is determined partially by a quantum mechanical electronic structure calculation and partially by a molecular mechanics force field calculation. There have been many different approaches proposed to couple the two types of calculation in order to generate a single hybrid potential energy surface. In this chapter, a brief introduction to a few of the common QM/MM coupling schemes is given (At least those implemented in our ADF QM/MM program). We also introduce an adaptation of Morokuma's popular IMOMM¹⁵(Integrated Molecular Orbital and Molecular Mechanics) QM/MM coupling scheme in order to allow for practical normal-mode frequency calculations and molecular dynamics simulations to be performed with the method. Although the modification is simple, it allows for free energy surfaces to be investigated with the IMOMM method(via frequency and MD calculations). Following this, a summary of the QM/MM implementation into the ADF density functional package is given. Finally, we explore the applicability of utilizing the combined QM/MM method for performing frequency calculations and deriving thermochemical data.⁹⁸ This aspect of the QM/MM hybrid potentials has only been previously explored to a limited extent.⁹²

2.2 QM/MM Coupling Schemes

Although the combined QM/MM method is conceptually simple, there are some substantial practical issues to contend with. This is particularly true, if the QM/MM partition occurs within the same molecule as illustrated in Figure 1.1c. Here, the difficulty lies in the fact that at least one covalent bond will involve an atom from the QM region and one from the MM region, and therefore the electronic system of the QM region must in some way be truncated as the QM/MM boundary is crossed along these bonds. A simple solution to this truncation problem first proposed by Singh and Kollman,⁸ involves capping the electronic system of the QM region with "capping" atoms. In this way, the electronic structure calculation is performed on a what is referred to as the QM model system, as shown in Figure 1.1b. We shall in the following refer to the 'real system' (Figure 1.1a) as the system consisting of all QM and MM atoms, except

for the capping atoms. Compared to other truncation approaches,^{7,93,94} the primary advantage of the capping atom approach is that no special treatment of the electronic system is necessary, thereby allowing the QM/MM methodology to be easily implemented within existing electronic structure codes. For this reason, we have opted to use Singh and Kollman's capping atom approach (and variations of it) in our QM/MM implementations.

Within the capping atom framework, the covalent bonds that cross the QM/MM boundary involve three atoms that we will label the QM-link atom, the capping atom, and the MM-link atom as shown in Figure 2.1a. The QM and MM-link atoms make up the covalent bond in the real system that links the QM and MM regions. The capping atom is introduced to satisfy the valences of the QM system and is not part of the 'real' system. The relationship between the coordinates of the two link atoms and the capping atom, is different amongst different QM/MM approaches.^{8,15,95}

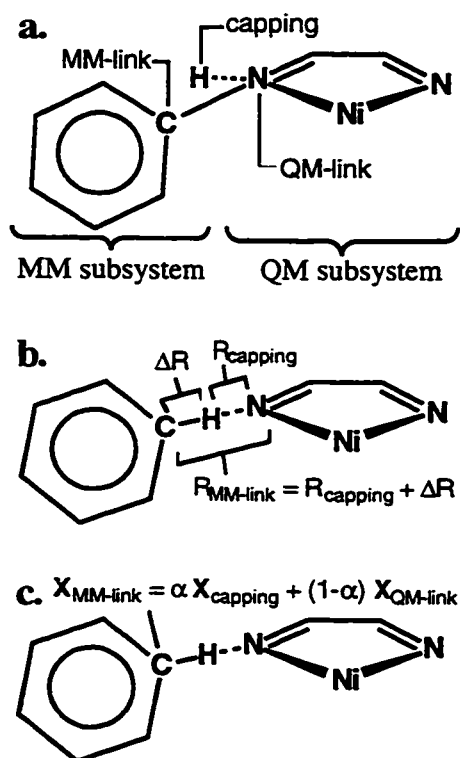


Figure 2.1. Treatment of the link bond in various QM/MM coupling schemes. a) The coupling scheme of Singh and Kollman.⁸ b) The original coupling scheme of Maseras and Morokuma.¹⁵ c) Our adaptation of the coupling scheme of Maseras and Morokuma.

In the popular capping atom prescription of Singh and Kollman, all three atoms in the link bond exist as independent variables. The combined QM/MM total energy in this framework can be defined as in equation 2-1,[†] where E_{QM} is simply the energy of the QM model system with the capping atom included, and E_{MM} is the sum of all of the molecular mechanics energy terms of the real system that contain at least one MM atom (For example, the bond stretching potential between the QM-link atom and the MM-link atom is handled by the appropriate molecular mechanics stretching potential).

$$E_{QM/MM} = E_{QM} + E_{MM} \quad (2-1)$$

In this approach the total energy of equation 2-1 is optimized with respect to all the degrees of freedom of the real system as well as the three degrees of freedom of each capping atom. In most cases this approach is appropriate and method has been applied successfully to numerous systems.^{9,12,21,23} However, in cases where a geometry optimization of $E_{QM/MM}$ leads to a structure where the three atoms (QM-link, MM-link and capping) deviate from a collinear arrangement, the approach becomes somewhat dissatisfying, because some geometric distortions involving the link bond will not be manifested in the electronic structure of the QM model system. This situation is exaggerated in Figure 2.1a. Another undesirable feature of the method is that compared to the real system, the QM/MM system possesses extra degrees of freedom due to the capping atoms. In certain situations, such as frequency calculations, this can be problematic.

More recently, Maseras and Morokuma¹⁵ have developed a new QM/MM coupling scheme that they have termed the IMOMM method which is based on Singh and Kollman's capping atom method. In the IMOMM method the position of the MM-link atom is no longer an independent variable and a strict relationship between the coordinates of the link atoms and the capping atom is enforced. Specifically, the MM-link atom is positioned along the QM-link atom - capping atom bond vector at a distance $R_{MM-link}$ from the QM-link atom as shown in Figure 2.1b. Thus, the bond distance, bond angle and dihedral angle ($R_{MM-link}$, $\theta_{MM-link}$, and $\phi_{MM-link}$, respectively) used to define the position of the MM-link atom are related to the analogous quantities used to define the position of the capping atom ($R_{capping}$, $\theta_{capping}$, $\phi_{capping}$). The specific relationships are defined in equations 2-2 through 2-4 where ΔR is a constant.

[†]Many authors define the total combined QM/MM energy expression with a component that expresses the interaction energy between the QM and MM regions. In equation 1, E_{QM} and E_{MM} include these interaction energies.

$$R_{MM-link} = R_{capping} + \Delta R \quad (2-2)$$

$$\theta_{MM-link} = \theta_{capping} \quad (2-3)$$

$$\phi_{MM-link} = \phi_{capping} \quad (2-4)$$

As a result of the relations enforced in Equations 2-2 to 2-4, geometric distortions involving the link bond are exhibited in the electronic structure of the QM model system (Figure 2.1b). Again the total energy $E_{QM/MM}$ is given by an expression similar to that of equation 2-1. However, the MM terms included in the total energy expression (Equation 2-1) are different from those of the Kollman scheme.⁸ In the IMOMM approach, MM potentials are only included if they depend on atoms which do not have a corresponding atom in the QM model system. For example, the MM bond stretching potential comprising of the QM-link and the MM-link atom is not included since this potential is assumed to be adequately handled by the corresponding bond in the QM model system involving the capping atom and the QM-link atom (see reference 15 for more details and exceptions).

Since the relationship defining the position of the MM-link atom is expressed in internal coordinates, the original IMOMM implementation⁹ requires that the QM and MM gradients first be transformed into internal coordinates before being added.¹⁵ The combined QM/MM gradients in internal coordinates are simply:

$$\frac{\partial E_{QM/MM}}{\partial R_i} = \frac{\partial E_{QM}}{\partial R_i} + \frac{\partial E_{MM}}{\partial R_i} \quad (2-5)$$

$$\frac{\partial E_{QM/MM}}{\partial \theta_i} = \frac{\partial E_{QM}}{\partial \theta_i} + \frac{\partial E_{MM}}{\partial \theta_i} \quad (2-6)$$

$$\frac{\partial E_{QM/MM}}{\partial \phi_i} = \frac{\partial E_{QM}}{\partial \phi_i} + \frac{\partial E_{MM}}{\partial \phi_i} \quad (2-7).$$

where i runs over all degrees of freedom of the real system, except that the degrees of freedom of the MM-link atoms are replaced by the degrees of freedom of the capping atom through equations 2-2 to 2-4. Thus, the gradient that characterize the capping atom are defined (with the help of equations 2-2 to 2-4) as:

⁹It should be noted that the IMOMM approach can be generalized to any coordinate system but the implementation described is restricted to an internal coordinate system.

$$\frac{\partial E_{QM/MM}}{\partial R_{capping}} = \frac{\partial E_{QM}}{\partial R_{capping}} + \frac{\partial E_{MM}}{\partial R_{MM-link}} \frac{\partial R_{MM-link}}{\partial R_{capping}} = \frac{\partial E_{QM}}{\partial R_{capping}} + \frac{\partial E_{MM}}{\partial R_{MM-link}} \quad (2-8)$$

$$\frac{\partial E_{QM/MM}}{\partial \theta_{capping}} = \frac{\partial E_{QM}}{\partial \theta_{capping}} + \frac{\partial E_{MM}}{\partial \theta_{MM-link}} \quad (2-9)$$

$$\frac{\partial E_{QM/MM}}{\partial \phi_{capping}} = \frac{\partial E_{QM}}{\partial \phi_{capping}} + \frac{\partial E_{MM}}{\partial \phi_{MM-link}} \quad (2-10).$$

Equations 2-8 to 2-10 reveal that, although the position of the MM-link atoms are not free variables, the forces acting on these atoms are passed onto other atoms via the chain rule.

For some types of applications, the transformation of the MM gradients between coordinate systems or even the definition of the internal coordinates can present practical problems. Macromolecular systems such as enzymes which typically contain 10^3 - 10^4 atoms, the coordinate transformation can be cumbersome since it involves the inversion of a $3N \times 3N$ matrix where N is the number of atoms in the 'real' system. Moreover, when explicit solvent molecules are considered, the transformation is likely to become ill-defined during the course of an optimization or molecular dynamics simulation (unless of course efforts are made to redefine the internal coordinates as to prevent the evolution of linear or near linear angles). Since the original IMOMM implementation requires a coordinate transformation that can be impractical in some situations, we have modified the method to circumvent these problems.

2.3 Adaptation of the QM/MM Coupling Scheme of Maseras and Morokuma

In this section we describe a modification of the IMOMM methodology of Maseras and Morokuma where no coordinate transformation is required, thereby avoiding the potential difficulties associated with utilizing internal coordinates. The modification allows for practical IMOMM simulations of macroscopic systems, explicitly solvated systems, and it allows for energy conserving molecular dynamics simulations and frequency calculations to be performed. The combined QM/MM coupling scheme described here is based on the original IMOMM scheme of Maseras and Morokuma.¹⁵ All of the rules for determining which MM potentials to accept and discard are the same as in the original IMOMM scheme. We will deal exclusively with defining the relationship between the atoms associated with a QM/MM link bond and how the QM and MM based gradients are combined.

We start by defining the relationship between the link atoms and the capping atoms that are involved in a covalent bond that crosses the QM/MM boundary. In the IMOMM scheme, the position of the MM-link atom is not an independent variable. Instead, the MM-link atom is always placed along the bond vector of the QM-link atom and the capping atom bond. Expressed in Cartesian coordinates, this relationship can be defined by equation 2-11 (and rearranged in equation 2-12).

$$\mathbf{X}_{MM-link} = \mathbf{X}_{QM-link} + \alpha(\mathbf{X}_{capping} - \mathbf{X}_{QM-link}) \quad (2-11)$$

$$\mathbf{X}_{MM-link} = (1 - \alpha)\mathbf{X}_{QM-link} + \alpha\mathbf{X}_{capping} \quad (2-12)$$

If α is defined in the following way,

$$\alpha = \frac{\|\mathbf{X}_{capping} - \mathbf{X}_{QM-link}\| + \Delta R}{\|\mathbf{X}_{capping} - \mathbf{X}_{QM-link}\|} = \frac{R_{capping} + \Delta R}{R_{capping}} \quad (2-13)$$

then the original implementation of Maseras and Morokuma is recovered in Cartesian coordinates where equation 2-2 is satisfied. In our implementation we define α as a constant parameter. In this way the bond distance, R_{MM} , between the QM and MM-link atoms is defined as a constant factor of the QM-link - capping atom bond distance, $R_{capping}$, such that equation 2-14 is satisfied.

$$R_{MM-link} = \alpha R_{capping} \quad (2-14)$$

The relationship defined in equation 2-14 is analogous to equation 2-2 of the original scheme, and the α 's for each link bond are chosen in a similar fashion as ΔR as described by Maseras and Morokuma.¹⁵ Comparison of the relationships (Eqns 2-2 and 2-14) reveals that they are similar in that both allow changes in $R_{capping}$ to be reflected in the bond distance $R_{MM-link}$. There is no clear advantage in using either relationship in terms of the physical model of the QM/MM link bond. However, by defining α as a constant, combining the MM and QM forces in Cartesian coordinates is simplified.

By applying the relationship defined in equation 2-12 where α is a constant and applying the chain rule, the combined QM/MM gradients on the QM-link atom and the capping atom are expressed by equations 2-15 and 2-16, respectively.

$$\frac{\partial E_{QM/MM}}{\partial \mathbf{X}_{QM-link}} = \frac{\partial E_{QM}}{\partial \mathbf{X}_{QM-link}} + \frac{\partial E_{MM}}{\partial \mathbf{X}_{QM-link}} + (1 - \alpha) \frac{\partial E_{MM}}{\partial \mathbf{X}_{MM-link}} \quad (2-15)$$

$$\frac{\partial E_{QM/MM}}{\partial \mathbf{X}_{capping}} = \frac{\partial E_{QM}}{\partial \mathbf{X}_{capping}} + \alpha \frac{\partial E_{MM}}{\partial \mathbf{X}_{MM-link}} \quad (2-16)$$

Equations 2-15 and 2-16 are valid in the Cartesian coordinate system and there is no need to add the QM and MM forces in an internal coordinate system.[◊]

2.4 QM/MM Implementation into the ADF Density Functional Package.

The combined QM/MM method has been implemented within the Amsterdam Density Functional (ADF) quantum chemistry package version 2.3, developed by Baerendset *al.*^{36,37,39,96,97} The source code of the original ADF package was modified only slightly whereas the molecular mechanics engine was written from scratch. The three QM/MM coupling schemes described in Sections 2.2 and 2.3 have been implemented, namely i) the original capping atom QM/MM coupling scheme of Singh and Kollman,⁸ ii) the IMOMM method of Maseras and Morokuma¹⁵ and iii) our adaptation of the IMOMM scheme.⁹⁸

Illustrated in Figure 2.2 is an outline of the QM/MM implementation within ADF. The basic philosophy in this QM/MM implementation is that the QM atoms (model system) are controlled by ADF as they would in a normal pure QM run. The MM environment acts as a perturbation to the QM subsystem such that the MM atoms are fully optimized at each geometry step. In other words, a QM/MM run can be thought of as a normal ADF run where the QM system is under the influence of the MM environment where the MM atoms are fully relaxed (optimized) at each geometry step. Thus, almost all features of ADF(both in geometry optimization and electronic structure) can be applied during a QM/MM run. For example, optimization can be performed in internal or Cartesian coordinates, constraints can be applied, transition states and linear transit runs are applicable. The most notable ADF feature not available is that symmetry constraints cannot be applied during the optimization. Features available and notable limitations in the ADF QM/MM implementation are summarized in Table 2.1.

[◊]Equations equivalent to 2-15 and 2-16 can also be easily derived with α defined by equation 2-13. This would recover the original implementation of Maseras and Morokuma where the constraints in equations 2-4 are satisfied.

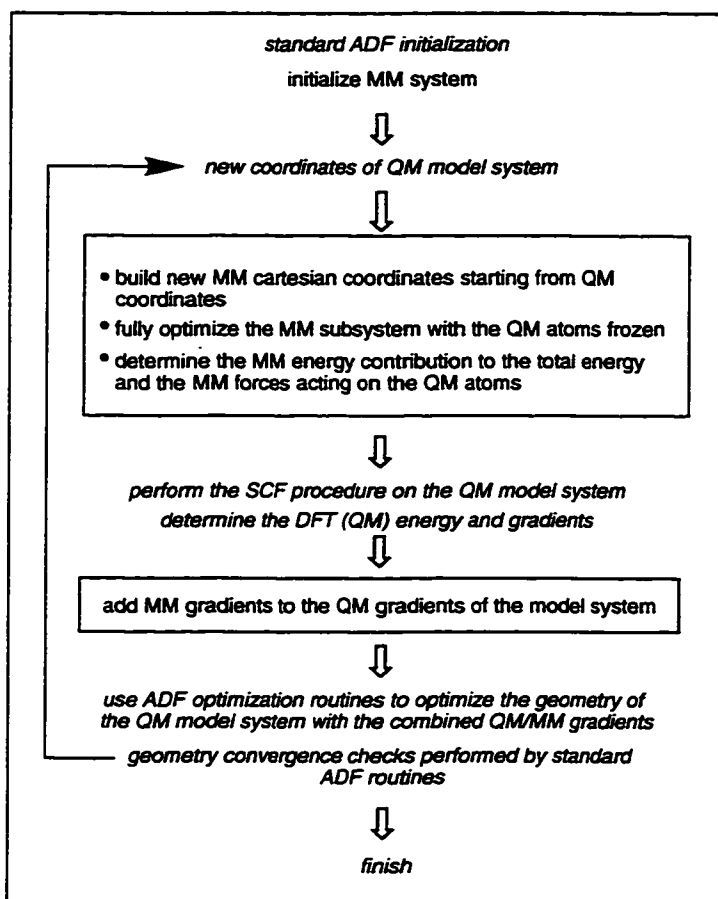


Figure 2.2. Schematic representation of the ADF QM/MM implementation. Portions that are italicized represent the original functions of the ADF package.

As part of the QM/MM implementation into ADF, a molecular mechanics code was written from scratch in the Fortran 90 programming language. This "core" molecular mechanics code was also used for the Car-Parrinello PAW QM/MM implementation described in Chapter 5. Details of the molecular mechanics code including input descriptions can be found in the ADF and PAW QM/MM users manual.¹⁰⁰ Here, only a summary of features is provided as shown in Table 2.2.

Table 2.1 Summary of features in the ADF QM/MM implementation.

The ADF QM/MM program currently supports the following features:

- geometry optimization
- linear transit calculations
- transition state optimization
- frequency calculations (of the whole QM/MM system)
- most recently, polarizable electrostatic coupling with energy gradients.⁹⁹

Notable limitations include:

- symmetry constraints cannot be applied in a QM/MM run
 - geometry constraints involving MM atoms are not possible
-

Table 2.2 Summary of features in the core molecular mechanics code.

- AMBER95^{77,101} and UFF⁸¹ force field function types.
 - Periodic boundary conditions.³¹
 - BFGS Hessian based quasi-Newton geometry optimization algorithm.^a
 - Steepest descent geometry optimization algorithm.^a
 - Molecular dynamics based, simulated annealing-like global geometry optimization algorithm.^a
 - A grid search algorithm for locating global minima.^a
This method searches for global minima by systematically rotating specified covalent bonds in the MM subsystem.
 - free form and modifiable force field parameter file
 - All code written in standard FORTRAN90.
-

^aoptimization algorithms only apply to the optimization of the MM subsystem.

2.5 IMOMM Frequencies and Thermodynamic Properties

The quality of properties such as geometries, relative conformational energies, solvation free energies, obtained by hybrid potential energy surfaces of a variety of flavours has been evaluated by a number of researchers over the years. The results of these studies have in general been promising and in some cases exceptional. The IMOMM methodology in particular has been studied extensively by Morokuma and

coworkers.^{15,28,102} However, the testing of the IMOMM hybrid potential energy surface has focused primarily on geometries and relative conformational energies. One area in which the IMOMM method that (and other QM/MM methods for that matter⁹²) has not been extensively tested is in providing normal-mode vibrational frequencies and corresponding thermodynamic properties. In this section, we evaluated the IMOMM methodology for calculating these properties.⁹⁸ The primary purpose of this implementation is to allow us to examine free energies on the hybrid QM/MM potential surface through frequency calculations.

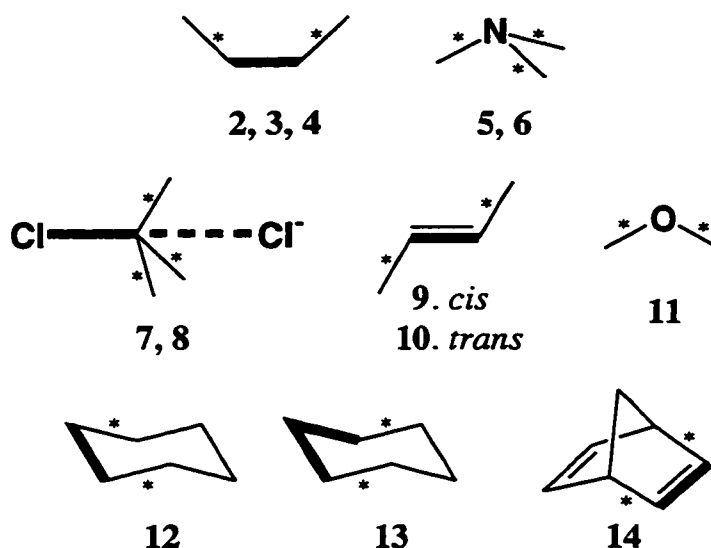


Figure 2.3. List of structures 2 - 14 showing the partitioning of QM and MM regions. Thick bonds represent the QM region, while thin bonds represent the MM region. Covalent bonds labeled with asterisks denote the QM/MM link bonds. All of the link bonds have been capped with hydrogen atoms in the QM model system.

Using the adapted IMOMM framework outlined in Section 2.3 and 2.4, we have calculated normal-mode vibrational frequencies and thermodynamic properties for a number of minimum and transition state structures, 2 - 14, which are shown in Figure 2.3. The combined QM/MM frequencies and properties have been compared to results generated from both pure quantum mechanical and pure molecular mechanics potential surfaces.

Computational Details. For both the pure QM and IMOMM results reported were performed with the local exchange-correlation potential of Vosko *et al.* for the gradients, while the energies reported were obtained with Becke's exchange¹⁰³ and Perdew's correlation^{104,105} corrections to the LDA energies as a perturbation of the LDA

charge density. Double- ζ STO basis sets for hydrogen (1s), carbon, nitrogen and oxygen and chlorine, augmented with a single 3d (2p for H) polarization function was used. The inner shells on the carbon, nitrogen, oxygen and chlorine, were treated within the frozen core approximation. For the molecular mechanics potential, the AMBER-95⁷⁷ force field was utilized. Van der Waals parameters for chlorine were taken from Rappé's UFF.⁸¹ The pure QM, pure MM and QM/MM vibrational frequencies were evaluated from a Hessian constructed from the numerical differentiation of analytical energy gradients at the corresponding optimized geometry. Thermodynamic properties were evaluated according to standard textbook procedures.^{43,106} All the reported analyses were performed at 298 K. Masses of the capping hydrogen atoms in structures 2-14 were rescaled to that of the corresponding MM-link atom.

Table 2.3 compares the frequencies and zero point energy corrections derived from the IMOMM and pure QM potential surfaces. The RMS difference between the IMOMM frequencies and the pure QM frequencies is shown for frequencies less than 1000 cm^{-1} and for all normal-mode frequencies. The RMS difference, averaged over all structures is 55 cm^{-1} for frequencies less than 1000 cm^{-1} and 117 cm^{-1} for all frequencies. For the three transition states considered, that is the eclipsed conformation of *n*-butane(4), the planar trimethylamine inversion transition state(6) and chloride $\text{S}_{\text{N}}2$ transition state(8), the value of the imaginary frequency corresponding to the transition vector compare reasonably. The IMOMM values for these vibrations are 189i, 261i, 199i cm^{-1} for structures 4, 6 and 8 respectively, whereas they are 226i, 308i, 322i cm^{-1} , respectively, for pure QM calculations.

Since our test suite contains complexes with larger MM regions than QM regions, we have examined the same frequencies calculated from a pure MM force field calculation. Vibrational frequencies based on the pure MM (AMBER) potential surface were calculated for the same set of structures with the exception of structures 7 and 8 for which the MM force field is inappropriate. The RMS difference between the pure MM and pure QM vibrational frequencies averaged over all of the structures was determined to be 60 cm^{-1} for frequencies less than 1000 cm^{-1} and 73 cm^{-1} for all frequencies. Thus, for the low frequency vibrations the IMOMM and the pure MM frequencies deviate approximately the same amount from the pure QM frequencies. In the high frequency range, the IMOMM frequencies deviate significantly more than the pure MM

frequencies. Inspection of the frequencies reveals that the IMOMM frequencies are systematically higher than the pure QM frequencies.[◊]

Table 2.3 Comparison of IMOMM and Pure QM Frequencies and Zero Point Energies.

no ^a	species ^b	R.M.S. deviation in frequencies (cm ⁻¹)		zero point energy (kcal/mol)	
		<1000 cm ⁻¹	all	IMOMM	pure QM % diff
2	<i>n</i> -butane C-C-C-C = 180°	25	85	82.6	80.0 +3.1
3	<i>n</i> -butane C-C-C-C = 60°	36	85	82.6	80.1 +3.1
4	<i>n</i> -butane C-C-C-C = 0° [TS]	49	85	82.5	80.2 +2.8
5	N(CH ₃) ₃	45	130	77.0	73.1 +5.4
6	N(CH ₃) ₃ inversion [TS]	60	152	76.1	72.0 +5.6
7	ClCMe ₃ + Cl ⁻ complex	56	128	78.9	74.4 +6.1
8	Cl--CM ₃ --Cl ⁻ [TS]	108	152	78.4	73.4 +6.9
9	<i>cis</i> -2-butene	80	99	68.0	65.6 +3.8
10	<i>trans</i> -2-butene	51	88	67.8	65.4 +3.6
11	dimethyl ether	36	113	50.6	48.6 +4.0
12	cyclohexane	34	116	107.8	103.3 +4.4
13	cyclohexane	36	117	107.4	103.3 +4.0
14	norbornadiene	100	167	81.9	78.5 +4.4
average:		55	117		+4.4

^aQM/MM partitioning illustrated in Figure 2.3. ^bSpecies marked with the [TS] label represent transition states.

[◊]This is also evidenced by the systematic over estimation of the zero-point energies shown in Table 2.3.

The source of this systematic deviation is a result the nature of the link bond in the IMOMM scheme and the relationship defined between the link atoms and the capping atoms in Equation 2-14. In other combined QM/MM schemes, such as the ONIOM/IMOMO scheme of Morokuma and coworkers^{95,107} or the scheme of Kollman,⁸ the strength (force constant) of the link bond is primarily determined by the appropriate molecular mechanics force constant. In contrast, the strength of the link bond in the IMOMM scheme is primarily determined by the strength of the corresponding capping atom bond in the QM model system. Thus, if the real link bond is a C-C bond and the corresponding bond in the model QM system is a C-H bond, then the bond stretching frequency of this C-C bond will correspond to that of a much higher C-H bond stretching frequency.[§] One can minimize this effect, as we have, by rescaling the mass of the capping atom to that of the corresponding MM-link atom. In this way, the difference in the bond stretching frequency is not due to the light mass of the proton, but due to the difference in the bond stretching force constants. For the above example, a C(sp³)-H bond stretching force constant is only about 10% larger than the corresponding C(sp³)-C(sp³) force constant,^{77,108} and, therefore, the bond stretching frequency of the C-C link bond in the IMOMM scheme will be about 4% higher than a typical C-C bond.[¶]

The results presented in Table 2.3 reveal that the IMOMM method may not be appropriate for determining absolute frequencies. Although this may not seriously limit the applications of the IMOMM method, it may present a problem when determining those properties derived from the frequencies such as finite temperature, zero-point energy, and entropic corrections. This aspect of utilizing the IMOMM method will be examined next.

IMOMM ZPEs and Finite Temperature Corrections. Table 2.3 compares the pure QM and IMOMM zero-point energy corrections for structures 2-14. The IMOMM zero point energies are higher for all structures compared to the pure QM zero point energies. The percent difference between the QM and IMOMM zero point energies averaged over all structures is only +4.4%. Since the differences are all in the positive direction, this again reveals that the frequencies generated from the IMOMM potential surface are systematically higher than the pure QM frequencies. Moreover, within each of the conformational groups (2-4, 5-6, 7-8, and 9-10), the percent differences in the zero-

[§] The same effect also exists for bond angles and torsions that are approximated by the QM model system in the IMOMM scheme.

[¶] 'Off-diagonal' elements are also effected, such that normal mode vibrations other than those that can be assigned to the stretching vibrations of the link bonds are also shifted.

point energy corrections are approximately constant. For example, for the conformations of *n*-butane, 2-4, the percent differences are all roughly 3.0% and for the trimethyl amine complex, 5, and inversion transition state, 6, the percent differences are both about 5.5%.

Table 2.4 compares the relative free energies, ΔG , and selected components determined from the IMOMM and pure QM potential surfaces. More specifically, a decomposition of the relative free energy for various conformations and/or transition states of *n*-butane (2-4), 2-butene (9,10), trimethylamine inversion (5,6) and for a chloride S_N2 reaction(7,8), are reported. Table 2.4 reveals that for components of ΔG that depend on the normal-mode vibrational analysis (ΔH_{vib} and $T\Delta S$), the IMOMM results compare exceptionally well to the pure QM values. The differences in ΔH_{vib} and $T\Delta S$ are of the order of 0.5 kcal/mol. The large deviations in the relative free energy, ΔG , between the two methods can be attributed to large differences in the pure QM and the combined IMOMM potential energies, ΔE .^o However, the QM/MM partitioning in these systems is severe and the electronic structure of QM model systems is a poor representation of that in the real systems. In practice, the partitioning of the QM and MM regions is generally chosen much more judiciously as to minimize the problem of charge transfer effects across the link bond. It is not our intent to highlight this aspect of the QM/MM approach since it has been thoroughly studied elsewhere.^{9,13,15,17,28,102}

The approximations in treating the QM/MM link bonds inherent to the IMOMM scheme precludes the precise calculation of vibrational frequencies with the scheme without additional modification to the potential energy expression. However, the results presented in Table 2.4 indicate that without further modification or parameterizations, the IMOMM scheme is capable of evaluating the *relative* thermodynamic properties, ΔH_{vib} , ΔE_{ZPE} and ΔS_{vib} , adequately. We have found that this is true even for systems where the partitioning of QM and MM regions is so severe that the relative potential energies are not well represented by the QM/MM method. In other words, the fashion in which the link bonds are treated in the IMOMM scheme does not adversely effect the calculation of these properties which are based on the vibrational frequencies.

^oThe reason for the unusually large disparity in the pure QM and QM/MM reaction barriers for the S_N2 reaction is due to the fact that electrostatic interactions between the QM and MM regions were neglected for the results presented in Tables 2.3 and 2.4.

Table 2.4. Comparison of IMOMM and Pure QM Relative Thermochemical Data at 298 K.

no ^a	species	$\Delta E^{b,c}$		$\Delta H_{vib}^{b,d}$		$T\Delta S^{b,e}$		ΔG^b	
		IMOMM	QM	IMOMM	QM	IMOMM	QM	IMOMM	QM
2	<i>n</i> -butane C-C-C-C = 180°	0.00	0.00	0.00	0.00	0.00	0.00	0.00	0.00
3	<i>n</i> -butane C-C-C-C = 60°	0.53	0.90	-0.03	0.04	-0.12	-0.09	0.62	1.03
4	<i>n</i> -butane C-C-C-C = 0° [TS]	4.53	5.75	-0.18	0.06	-0.26	-0.27	4.51	6.08
5	N(CH ₃) ₃	0.00	0.00	0.00	0.00	0.00	0.00	0.00	0.00
6	N(CH ₃) ₃ inversion [TS]	4.93	7.97	-2.04	-2.06	-1.71	-1.54	4.60	7.45
7	ClCMe ₃ + Cl ⁻ complex	0.00	0.00	0.00	0.00	0.00	0.00	0.00	0.00
8	Cl--CMe ₃ --Cl ⁻ [TS]	9.90	22.30	-1.64	-1.90	-2.02	-1.41	10.28	21.81
9	<i>cis</i> -2-butene	0.00	0.00	0.00	0.00	0.00	0.00	0.00	0.00
10	<i>trans</i> -2-butene	-0.49	0.82	-0.09	-0.01	0.18	0.18	-0.40	0.99

^aQM/MM partitioning illustrated in Figure 2.3. ^bkcal/mol. ^cInternal potential energy. ^dIncludes zero point energy correction. ^eIncludes ΔS_{rot} , ΔS_{vib} and ΔS_{trans} .

2.6 Conclusions

The QM/MM method has been incorporated with the ADF density functional package, in a way that allows the QM and MM regions to simultaneously reside within the same molecule. For this purpose the general capping atom approach first developed by Singh and Kollman has been utilized.⁸ The differences between the original QM/MM coupling scheme of Singh⁸ and the newer IMOMM coupling scheme developed by Maseras and Morokuma is outlined.¹⁵ We have also introduced a modification to the IMOMM scheme as to allow both frequency calculations and molecular dynamics simulations to be performed. We have evaluated the adapted IMOMM QM/MM coupling scheme to calculate normal-mode vibration frequencies and thermochemical data on a number of minimum and transition state structures. Although the absolute value of the frequencies generated by the IMOMM scheme can deviate significantly from those determined from the corresponding pure QM potential surface, the deviations are systematic in nature and of a known origin. This is an essential feature since the cancellation of errors allows for the reliable IMOMM calculations of relative thermochemical properties, namely, ΔH_{vib} , ΔE_{ZPE} and $T\Delta S$. The application of the adapted IMOMM scheme presented here to molecular dynamics simulations will be explored in Chapter 5.

Chapter 3

A Combined QM/MM Study of Brookhart's Ni(II) Diimine Olefin Polymerization Catalyst

3.1. Introduction

Brookhart and coworkers^{1,2,109} have recently developed Ni(II) and Pd(II) diimine based catalysts of the type $(\text{ArN}=\text{C}(\text{R})-\text{C}(\text{R})=\text{NAr})\text{M}-\text{CH}_3^+$ which have emerged as promising alternatives to both Ziegler-Natta systems and metallocene catalysts for olefin polymerization. Traditionally, such late metal catalysts are found to produce dimers or extremely low molecular weight oligomers due to the favorability of the β -elimination chain termination process.¹¹⁰ With the Brookhart systems very high molecular weight polymers can be produced. They also exhibit high activities which are competitive with commercial metallocene catalysts.³ Not only can these catalysts convert ethylene into high molecular weight polyethylene, but the polymers also exhibit a controlled level of short chain branching. NMR studies which indicate the presence of multiple methine, methylene and methyl signals suggests branches of variable length with methyl branches predominating.¹ The extent of the branching is a function of temperature, monomer concentration and catalyst structure. Thus, by simply varying these parameters, polymers which are highly branched or virtually linear can be tailored.

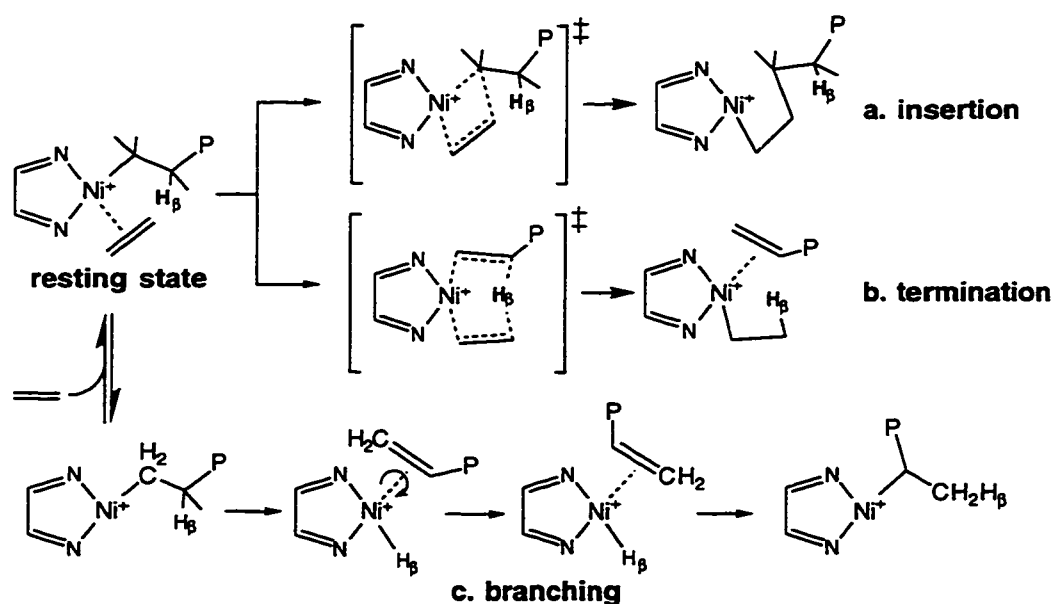


Figure 3.1. Proposed reaction mechanisms of (a) insertion, (b) chain termination and (c) chain branching mechanisms for the Brookhart Ni-diimine olefin polymerization catalyst. The large bulky substituents have been removed for clarity.

Brookhart's group has studied the mechanistic details of the polymerization including the role of the bulky substituents on the diimine ligands.^{1,2} Three main processes are thought to dominate the polymerization chemistry of these catalyst systems, namely propagation, chain branching and chain termination. Following cocatalyst activation of the precatalyst, a diimine methyl cation is formed. First insertion of ethylene yields a diimine alkyl cation which upon uptake of another ethylene molecule produces a metal alkyl olefin π -complex. This π -complex has been established by NMR studies¹ to be the catalytic resting state of the system. The chain propagation cycle is depicted in Figure 3.1a. The first step involves the insertion of the coordinated olefin moiety to form a metal alkyl cationic species. Rapid uptake of monomer returns the system to the initial resting state π -complex. The unique short chain branching observed with these catalysts is proposed to occur via an alkyl chain isomerization process as sketched in Figure 3.1c. In this proposed process, β -hydride elimination first yields a putative hydride olefin π -complex. Rotation of the π -coordinated olefin moiety about its coordination axis, followed by reinsertion produces a secondary carbon unit and therefore a branching point. Consecutive repetition of this process allows the metal center to migrate down the polymer chain, thus producing longer chain branches. Chain termination occurs via monomer assisted β -hydrogen elimination, either in a fully concerted fashion as illustrated in Figure 3.1b or in a multistep associative mechanism as implicated by Johnson *et al.*¹

Similar Ni and Pd catalysts developed by Keim¹¹¹ and others^{112,113} which do not possess the bulky ligand systems have been used to produce dimers or extremely low molecular weight oligomers.[◇] Brookhart has suggested¹ that the bulky aryl ligands act to preferentially block the axial sites of the metal center as illustrated by Figure 3.2. This feature in the catalyst system must in some way act to retard the chain termination process relative to the propagation process, thereby allowing these catalysts to produce high molecular weight polymers.

[◇] These systems have been calculated theoretically by Fan and Ziegler.^{55,57}

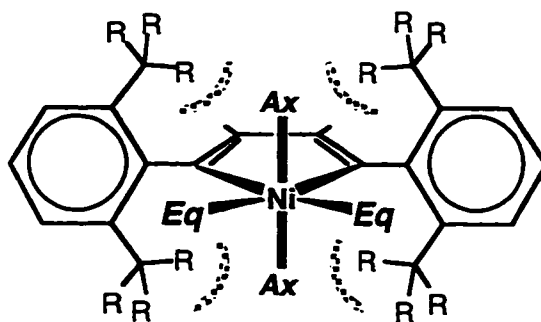


Figure 3.2. Axial(Ax) and equatorial(Eq) coordination sites of the metal center and their potential steric interactions with the bulky substituents.

In an earlier pure quantum mechanical study Deng and Ziegler⁵⁹ neglected the role of the bulky diimine substituents by modeling the catalyst system with a Ni(II) coordinated to an unsubstituted diimine ligand ($\text{HN}=\text{CH}-\text{CH}=\text{NH}$). With this unsubstituted model system, the chain termination process was found to be more favorable than the propagation and therefore the catalyst would not produce the high molecular weight polymers as demonstrated by Brookhart's catalyst. Rather, the model system would only be useful as a dimerization catalyst. The barriers for propagation, chain isomerization (branching) and chain termination were calculated to be $\Delta H^\ddagger = 16.8$, 12.8 and 9.7 kcal/mol, respectively. Although the truncated model system did not reproduce the established order of the barrier heights, the structure of the optimized transition states did offer insights into the role of the bulky ligands. As suspected by Johnson *et al.*, the transition state for chain termination occupies both axial positions of the metal whereas the insertion transition states only occupies the equatorial coordination sites. Thus, the bulky aryl substituents likely destabilize the transition state of the termination process more so than the insertion transition state.

In this study we intend to examine, in a detailed manner, the role of the bulky diimine substituents in the Brookhart catalyst system with the combined quantum mechanics/molecular mechanics (QM/MM) approach^{8,9,15} of Morokuma and Maseras.¹⁵ We will examine the $(\text{ArN}=\text{C}(\text{R})-\text{C}(\text{R})=\text{NAr})$ Ni(II) based catalyst system where $\text{R}=\text{methyl}$ and $\text{Ar}=2,6\text{-C}_6\text{H}_3(i\text{-Pr})_2$. The bulky R and Ar groups will be treated by a molecular mechanics potential while the remainder of the system will be described by a density functional potential.

3.2. Computational Details

All stationary points presented here have been optimized with the ADF-QM/MM program using the original IMOMM coupling scheme of Maseras and Morokuma.¹⁵ Figure 3.3a depicts the QM/MM partitioning of the full Ni-diimine catalyst, $(\text{ArN}=\text{C}(\text{R})-\text{C}(\text{R})=\text{NAr})\text{Ni}-\text{X}^+$ where $\text{R}=\text{CH}_3$ and $\text{Ar}=\text{Ar}=2,6\text{-C}_6\text{H}_3(i\text{-Pr})_2$. Carbon atoms in Figure 3.3a labelled with asterisks represent the MM-link atoms at the QM/MM boundary. The difference, ΔR (as defined in Equation 2-2), between the QM-link atom bond distance with the capping atom and the MM-link atom was fixed to $\Delta R=0.41 \text{ \AA}$ for the R substituents giving a C-C bond of roughly 1.51 \AA and fixed to $\Delta R=0.35 \text{ \AA}$ for the Ar substituents providing a N-C(aryl) distance of roughly 1.38 .

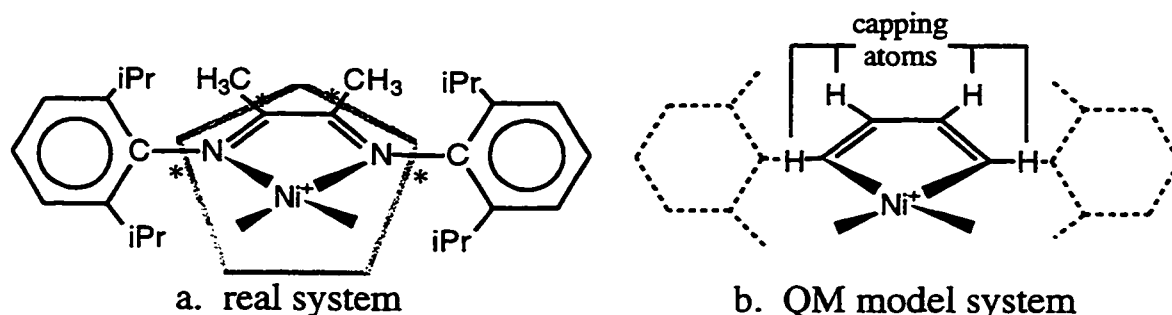


Figure 3.3. The QM/MM partitioning of the Ni-diimine catalyst, $(\text{ArN}=\text{C}(\text{CH}_3)-\text{C}(\text{CH}_3)=\text{NAr})\text{Ni}-\text{R}^+$ used in this study. a) The so called 'real system' where the link bonds are labeled with asterisks. b) The QM model system.

For the model QM system electronic configurations of the molecular systems were described by a triple- ζ basis set on nickel^{114,115} for 3s, 3p, 3d, 4s, and 4p. Double- ζ STO basis sets were used for carbon (2s, 2p), hydrogen (1s) and nitrogen (2s,2p), augmented with a single 3d polarization function except for hydrogen where a 2p function was used. The $1s^2 2s^2 2p^6$ configuration on nickel and the $1s^2$ shell on carbon and nitrogen were assigned to the core and treated within the frozen core approximation. A set of auxiliary¹¹⁶ s, p, d, f, and g STO functions, centered on all nuclei, was used in order to fit the molecular density and present Coulomb and exchange potentials accurately in each SCF cycle. Energy differences were calculated by augmenting the local exchange-correlation potential by Vosko¹¹⁷ *et al.* with Becke's¹⁰³ nonlocal exchange corrections and Perdew's^{104,118} nonlocal correlation correction. Geometries were optimized including nonlocal corrections. First-order scalar relativistic corrections^{119,120} were added to the total energy, since a perturbative relativistic approach is sufficient for 3d metals. In view of the fact that all systems investigated in this work

show a large HOMO-LUMO gap, a spin restricted formalism was used for all calculations.

An augmented AMBER95 force field⁷⁷ was utilized to describe the molecular mechanics potential. Employing the AMBER atom type labels as described in reference 77, the diimine carbon was assigned with atom type "CM" parameters, the diimine N with "N2", aryl ring carbon atoms with "CA", aryl ring hydrogen atoms with "HA" and the remaining carbon and hydrogen atoms of the MM region with "CT" and "HC", respectively. For the propagation and termination processes, the reacting ethene monomer was assigned with sp^2 "C" van der Waals parameters through to the transition state structure and changed to sp^3 "CT" parameters in the product. A similar procedure was followed for the isomerization process. Alkyl carbon and hydrogen atoms of the active site were assigned "CT" and "HC" van der Waals parameters, respectively. Ni was assigned the "Ni4+2" van der Waals parameters of Rappé's UFF.⁸¹ Electrostatic interactions were not included in the molecular mechanics potential.

All structures shown correspond to minimum points on the potential surface, except those prefixed by **TS**, which represent transition states. Transition states were obtained by full transition state optimization. No symmetry constraints were used. All reported linear transit calculations involve full geometry optimization along a reaction coordinate which is constrained in each step. Normal mode frequency calculations were not performed on the stationary points.

3.3 Results and Discussion

a. Propagation

Ni-alkyl complex and the Resting State: Displayed in Figure 3.4 are the optimized geometries of the most stable Ni-propyl cation, **15a**, and Ni-propyl π -ethylene, **16a**, conformations found. The pure MM atoms are ghosted for clarity, while the capping hydrogen atoms are omitted. Parenthetic values refer to the same geometric parameter found in the corresponding pure QM geometry as described in reference 59.

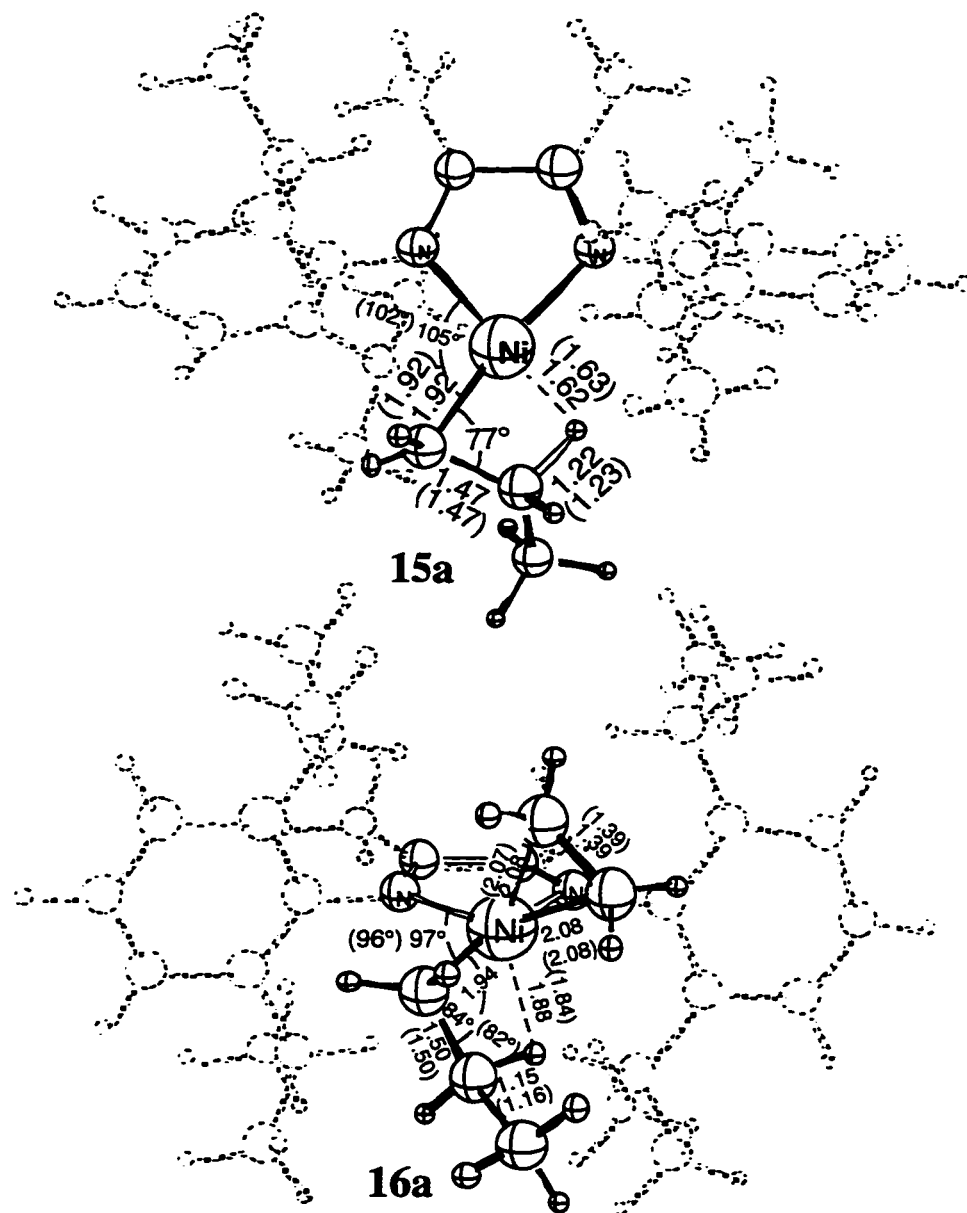


Figure 3.4. Optimized QM/MM metal alkyl cation and metal alkyl π -ethylene resting state structures. MM atoms (set 3 and set 4 atoms as defined in reference 15) are ghosted for clarity, while the dummy hydrogen atoms (set 2) are omitted. Parenthetical values refer to the same geometric parameter found in the corresponding pure QM geometry as described in reference 59. Distances and angles shown are in Angstroms and degrees, respectively.

The QM domain of the β -agostic Ni-alkyl complex, **15a**, remains essentially unchanged when compared to the pure QM model system. This is expected since the α -carbon and the β -agostic hydrogen atoms occupy the unencumbered square planar coordination sites of the Ni center as opposed to the sterically hindered axial sites (Figure 3.2). The most notable change upon introduction of the bulky diimine substituents is that

the N-Ni-C $_{\alpha}$ angle is increased slightly from 102° in the pure QM model to 105° in the QM/MM model. We will see that this is a common effect of the bulky ligands as they tend to compress the groups within the active site together. The aryl rings are twisted away from a perpendicular orientation with respect to the Ni-diimine ring. This not only minimizes steric interactions with the alkyl chain, but there is also an electronic preference for this. There exists a stabilizing interaction between the π -systems of the Ni-diimine ring and the aryl rings that is enhanced when the rings are twisted away from the perpendicular orientation. In our model, this orientational preference of the rings is described by a molecular mechanics N-C(aryl) bond torsion potential. We note that a fully coplanar orientation of the rings cannot be achieved because of severe steric interactions incurred between the aryl rings, the diimine ring, and both their substituents. Since the alkyl moiety of **15a** occupies the equatorial coordination plane, this allows the ortho substituted aryl rings to twist away from the perpendicular alignment with the diimine plane. We quantify this twist with the angle, θ , between the aryl ring plane and the Ni-diimine ring plane as illustrated in Figure 3.5.[◇] When θ is 90°, the rings are roughly perpendicular and when θ is 0°, the rings are coplanar. In **15a** the θ angles are 64 and 68°.

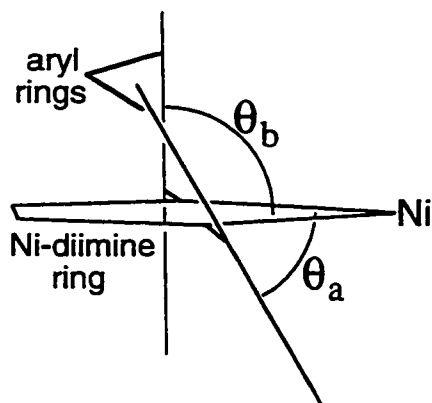


Figure 3.5. Definition of the "ring-plane" angle, θ . The angle θ is defined as the angle between the normal vectors of the two planes defined by the Ni, N, C(diimine) atoms and C1, C2, C6 atoms of the aryl rings.

Uptake of an ethylene unit by **15a** yields a Ni alkyl π -olefin complex which has been shown by Johnson *et al.*¹ to be the resting state of the catalytic system. The most

[◇] The reported values are the angle between the normal vectors of the two planes defined by the Ni, N, C atoms of the Ni-diimine ring and C1, C2, C6 atoms of the aryl ring.

stable confirmation, **16a**, is sketched in Figure 3.4. Linear transit calculations[§] reveal that the resting state forms without a noticeable steric or electronic barrier when free ethylene is complexed to **15a**. This contrasts the conjecture of Brookhart and coworkers,^{1,2} that the extreme bulk of the substituents hinder the complexation of the monomer. Here we suggest that the complexation barrier is entropic in nature, and that increases in the steric bulk of the substituents will act to increase the entropic barrier. This is supported by our linear transit calculations which show for the pure QM model system both axial and lateral attacks of the monomer are possible whereas for the QM/MM model only the lateral attack is possible. This will be discussed in more detail in Chapter 6.

Although the parameters displayed in Figure 3.4 do not show it to the full extent, the structure of the resting state, **16a**, is perturbed by the bulky ligands more so than the Ni-alkyl complex, **15a**. This is expected since the active site groups in the resting state occupy the axial positions, which are more sterically hindered than the equatorial sites. The steric demands of the aryl substituents act to bring the ethylene unit and the alkyl moiety closer together compared to the pure QM model. This is evidenced by a decrease in the C α -C(olefin) distances which are reduced to 2.88 and 2.90 Å in the QM/MM model from 2.92 and 2.95 Å in the pure QM model. The same is observed for the olefin midpoint-Ni-H β angle which is decreased to 108° from 116°. Expansion of the Ni-C α -C β angle and elongation of the Ni-H β distance are also observed as a consequence of the compression of the active site units. This results in the weakening of the β -agostic bond as indicated in the shortening of the C β -H β distance by 0.01 Å when the bulky ligands are introduced.

A related resting state structure, **16b**, (not shown) which was located lies 1.4 kcal/mol above **16a**. The β -agostic resting states **16a** and **16b** differ by the orientation of the methyl group of the alkyl chain through a rotation about the C α -C β bond by approximately 60 degrees. The rotational barrier linking **16a** and **16b** is expected to be very low since there is no steric hindrance to the process and since a stabilizing β -agostic interaction can be maintained throughout the rotation. For related polymerization catalysts, similar rotational barriers have been calculated and found to be less than 3 kcal/mol.^{53,59,121} The bulky aryl ligands have a similar effect on **16b** as described for **16a**.

[§] Two linear transit calculations were performed in which one of the Ni-C(ethylene) distances was used as the reaction coordinate. The reverse process, from the resting state to the free Ni alkyl cation and free ethylene unit, was also examined. This process will be examined in more detail in Chapter 6.

Table 3.1. Energy decomposition for insertion, termination and isomerization processes.

species	ΔE_{TOT}^a	ΔE_{MM}^a	ΔE_{QM}^a	$\Delta E^{a,b}$ (pure QM)	ring plane angle, θ^c		$\Delta E_{\text{torsion}}$ (N-CI) ^{a,d}		$\Delta E_{\text{vdw}}^{a,e}$ aryl substituents with...		
					a	b	a	b	ethene	propyl	methyl
insertion ^f											
16a	0.0	0.00	0.00	0.0	78	83	0.00	0.00	0.00	0.00	0.00
16b	1.4	0.44	0.96	-0.5	81	86	0.25	0.05	0.30	-0.29	0.11
15a + ethene	14.7	-4.87	19.57	-18.9	64	68	-3.54	-2.85	-	-1.20	-0.09
TS[16b-19]	13.2	-5.89	19.09	17.0	69	67	-2.48	-4.60	-0.21	0.02	0.35
TS[16a-19]	14.3	-5.32	19.62	-	70	68	-2.06	-4.37	-0.13	0.09	0.32
TS[17-20]	17.3	1.57	15.73	16.3	79	86	0.05	0.32	0.89	0.93	-0.07
termination ^f											
TS[16a-23b]	18.6	4.80	13.80	9.2	89	89	0.90	0.36	1.56	1.25	1.54
TS[16b-23a]	20.5	5.14	15.36	9.2	74	86	-0.64	0.31	1.14	0.25	1.56
isomerization ^g											
TS[15a-2]	15.3	4.01	11.29	12.8	64	88	0.42	3.19	-	1.12	-0.17
22	-0.8	0.06	-0.86	-1.8	69	71	0.53	0.43	-	-0.06	-0.23

^aEnergies are reported kcal/mol. ^bRelative energies of the analogous pure QM structures from reference 60. ^cThe angle between the aryl rings and the Ni-dimine ring. Specifically, the angle θ is defined as the angle between the normal vectors of the two planes defined by atoms Ni, N, C(diimine) and C1, C2, C6, respectively. "a" and "b" refer to the each of the two aryl rings. ^dRelative molecular mechanics N-C1 bond torsion energies. "a" and "b" refer to each of the two aryl rings. ^eRelative molecular mechanics van der Waals interaction energy of the aryl fragments with the i) ethene and ii) propyl fragments of the active site and iii) methyl fragment of the diimine ligand. ^fEnergy components are relative to the resting state structure **16a**. ^gEnergy components are relative to the Ni-propyl cation **15a**.

The bulky diimine substituents drastically reduce the calculated ethylene uptake energy. The ethylene complexation energy in **16a** is 14.7 kcal/mol whereas the most favorable uptake energy in the pure QM model was determined⁵⁹ to be 19.4 kcal/mol. Thus, the bulky ligands as modeled by the MM force field reduce the ethylene uptake energy by 4.9 kcal/mol. Over 95% of the change in uptake energy is accounted for by a destabilization exhibited in the MM contribution. In other words, changes in the QM electronic structure due to the perturbation of the geometry account for only 5% of the lowered uptake energy. A decomposition of the molecular mechanics energy which is summarized in Table 3.1 reveals that the destabilization can primarily be accounted for by two factors. First, as intuitively expected, there is an increased steric interaction between the active site fragments and the aryl rings. This occurs because both axial coordination sites of the metal are occupied in the resting state and therefore steric interactions involving the aryl rings and the active site fragments cannot be significantly reduced by rotation of the aryl rings. In particular, rotation of the rings which may alleviate the steric hindrance between one of the ortho substituents with 'top' axial coordination site will only enhance the interaction between the other ortho substituent with the bottom axial coordination site, and *vice versa*. To quantify the increase in steric interaction, we have analyzed the MM van der Waals interaction energy involving the aryl rings (including the *o*-isopropyl groups) and the propyl fragment of the active site. We find that there is a 1.2 kcal/mol increase in this interaction energy in going from **15a** to **16a**. The second dominant source of destabilization occurs because the aryl rings in the resting state are forced to adopt a less favorable perpendicular orientation with respect to the Ni-diimine ring. For example, the angles, θ_a and θ_b , between aryl ring planes and the Ni-diimine ring plane (see Figure 3.5) are 78 and 83° in the resting state, **16a**, whereas they are 64 and 68° in the Ni-alkyl cation, **15a**. As described earlier, the molecular mechanics N-C(aryl) bond torsion potential has a maximum at the perpendicular orientation and a minimum at a parallel orientation of the rings. This physically corresponds to the stabilizing interaction between the π -systems of the two rings which is maximized at a parallel orientation. This rotation of the aryl rings with respect to the Ni-diimine ring destabilizes the MM torsion energy by 3.5 and 2.9 kcal/mol for the two rings, respectively.

The possibility that the resting state complex really possesses two coordinated monomer units (as opposed to one) which occupy each of the axial coordination sites of the metal center has been examined. We have found that the addition of a second olefin unit provides virtually no stabilization with $\Delta E = -0.5$ kcal/mol. Consequently, this

auxiliary coordination is easily overcome by entropic factors and we conclude that the single olefin π -complex is indeed the resting state.

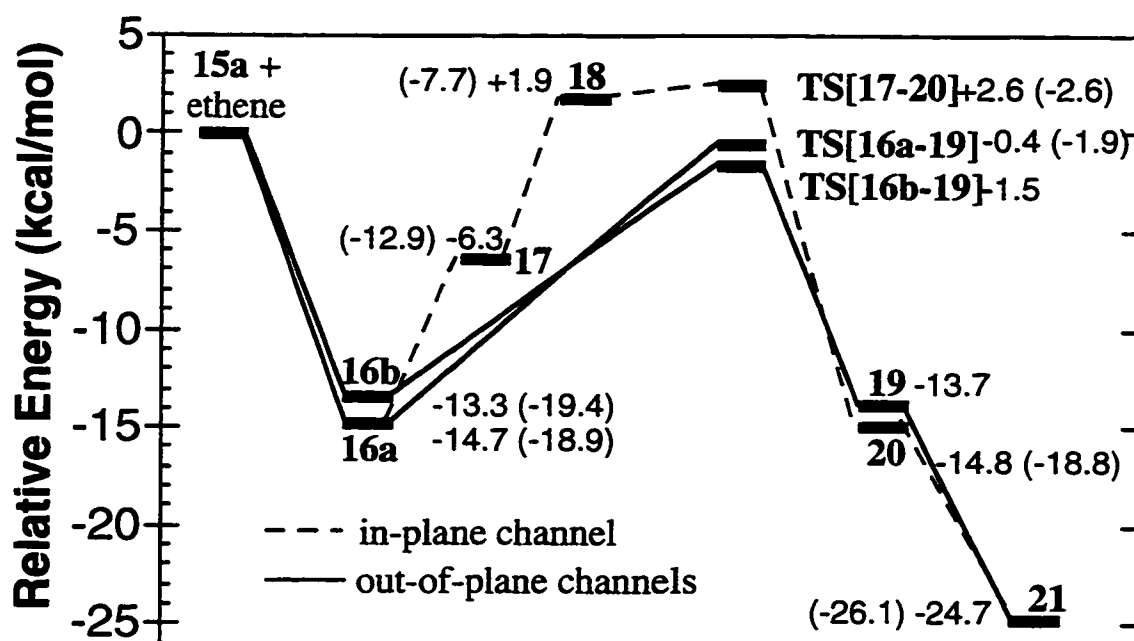


Figure 3.6. Energy profile for the chain propagation process. Parenthetical values refer to the analogous relative energies of the equivalent pure quantum mechanical structures.⁵⁹ All energies in kcal/mol.

Insertion:[◇] In both the pure QM and the hybrid QM/MM models, we find two distinct insertion channels which we have labeled the "in-plane" and "out-of-plane" insertion channels. Displayed in Figure 3.6 are the energy profiles of the out-of-plane insertion channels (solid) and the in-plane insertion channel (dotted). For the out-of-plane insertion we have explored two pathways, one initiated from the resting state structure **16a** and the other initiated from its rotamer **16b**.

[◇] We have also examined the first insertion or chain initialization process with our pure QM/MM model. The first insertion of ethylene into the Ni-methyl bond is calculated to proceed through a barrier of 5.7 kcal/mol. This is significantly diminished from the pure QM model which gives a first insertion barrier of 11.1 kcal/mol.

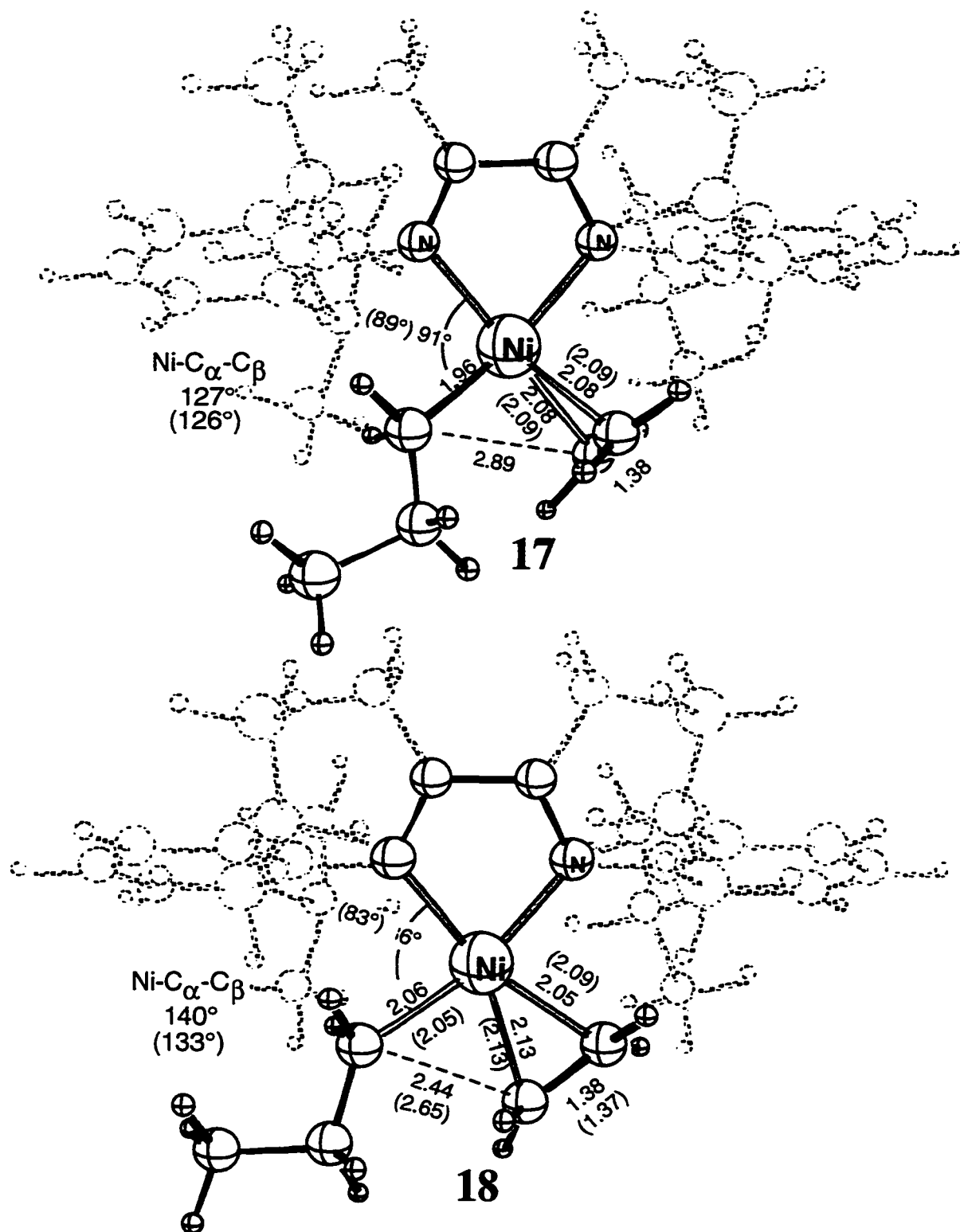
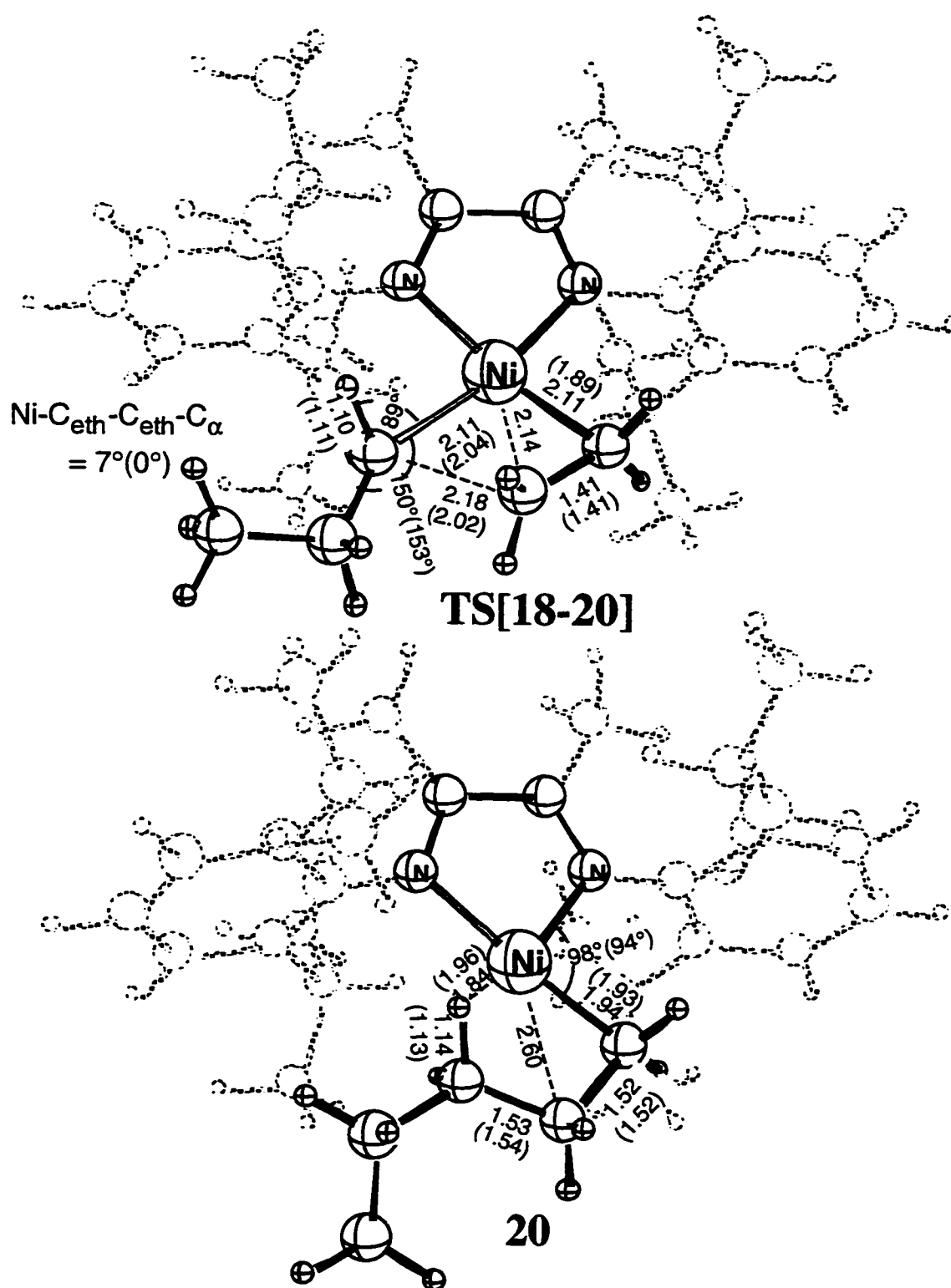


Figure 3.7. Optimized geometries of the intermediate π -complexes of the in-plane insertion channel. Conventions as in Figure 3.4.

The in-plane channel occurs in a stepwise fashion whereby two intermediate π -complexes are involved in addition to the incipient resting state π -complex, **16a**. The first intermediate observed, **17**, can be characterized as a π -complex in which the ethylene moiety is oriented perpendicular to the plane of the Ni-diimine ring. Rotation of the coordinated ethylene group in **17**, such that both carbon atoms lie in the diimine ring plane, yields the second intermediate **18**. Here, the alkyl group, the Ni-diimine fragment and the ethene moiety are all coplanar. The optimized QM/MM structures of both these intermediates, **17** and **18**,[◇] are shown in Figure 3.7. The bulky substituents act to destabilize the in-plane π -complexes, **17** and **18**, compared to their pure QM counterparts. Structures **17** and **18**, respectively, lie 8.4 and 16.6 kcal/mol higher in energy than the resting state structure **16a**, whereas the equivalent pure QM complexes lie 6.0 and 11.2 kcal/mol higher than the pure QM resting state. The most noticeable geometric consequence of the bulky ligands occurs in **18** where the C $_{\alpha}$ -C(olefin) distance decreases from 2.65 Å in the pure QM complex to 2.44 Å in the QM/MM structure. Furthermore, the Ni-C $_{\alpha}$ -C $_{\beta}$ angle increases from 133° to 140° as a result of the bulky aryl ligands. The transition state for the in-plane insertion, TS[**18-20**], which is shown in Figure 3.8 lies 17.3 kcal/mol higher in energy than the resting state structure **16a**. This is only slightly higher than the 16.3 kcal/mol barrier observed with the pure QM system. Interestingly, the C(olefin)-C $_{\alpha}$ distance in TS[**18-20**] is actually 0.16 Å larger than in its pure QM counterpart. We suggest that an earlier transition state is formed due to the bulky groups. Since the in-plane insertion channel is less favorable than the out-of-plane channel when the bulky ligands are included, the transition states linking the π -complex **16a** to **17** and **17** to **18** were not located. We, however, do not expect these transformation barriers to be large based on our pure QM study⁵⁹ where these barriers were found to be less than 2 kcal/mol. The kinetic product of the in-plane insertion is a γ -agostic Ni-pentyl cation, **20**, which lies 1.0 kcal/mol above the resting state complex, **16a**. Species **20** which is pictured in Figure 3.8 has two γ -agostic hydrogens as evidenced by the short 1.84 and 1.99 Å Ni-H $_{\gamma}$ distances.

[◇] The QM/MM structures **17** and **18** of this work correspond to the pure QM structures **7a** and **8a** of reference 59.



The insertion process in the second pathway, the "out-of-plane" channel, proceeds directly from the resting state structures and does not involve additional intermediary π -complexes. Here, the direct insertion initiated from both resting state conformations **16a** and **16b** have been explored. Although **16a** is the more stable of the resting states, the insertion transition state commencing directly from it lies slightly above the transition state derived from **16b**. As shown in Figure 3.6, TS[**16b-19**], which lies 11.8 kcal/mol above the resting state **16b**, is 1.1 kcal/mol more stable than TS[**16a-19**], which lies 14.3 kcal/mol above **16a**. Figure 3.9 displays the optimized QM/MM transition state structure TS[**16b-19**]. Since the interconversion of the two rotamers **16a** and **16b** is expected to be facile, it can be argued that the out-of-plane insertion commencing from the more stable resting state, **16a**, will likely lead to the more stable transition state, TS[**16b-19**]. Therefore, the most appropriate estimate of the out-of-plane insertion transition state is $\Delta E^\ddagger = 13.2$ kcal/mol. This value compares well with the experimental free energy barrier of propagation which is estimated to be $\Delta G^\ddagger = 10 - 11$ kcal/mol.¹²²

The analogous out-of-plane insertion process in the pure QM model system has a barrier of 17.5 kcal/mol.⁵⁹ Thus, the bulky substituents in the hybrid QM/MM model act to lower the out-of-plane insertion barrier by 4.3 kcal/mol. This is primarily due to the destabilization of the QM/MM resting state by the steric bulk of the aryl groups. More specifically, a more favorable orientation of the aryl rings with respect to the Ni-diimine ring in TS[**16b-19**] can be adopted compared to that in the resting state **16a**. As compiled in Table 3.1, these ultimately lead to a 5.9 kcal/mol decrease in molecular mechanics energy for TS[**16b-19**]. It is notable that for the pure QM model system, the in-plane insertion is calculated to be more favorable than the out-of-plane insertion - the opposite of what is presented here for the QM/MM system.

The initial kinetic product of the out-of-plane insertion channel is a γ -agostic Ni-pentyl cation, **19**, which is displayed in Figure 3.9. Although **19** lies 1 kcal/mol above the resting state **16a**, it is likely to rearrange rapidly to form the thermodynamic β -agostic product **21** which lies 11 kcal/mol below **19** and is sketched in Figure 3.10. We have not determined the transition state linking **19** to **21**. However, since the process is not sterically hindered by the bulky ligands, we expect the barrier to be very modest. For the pure QM model⁵⁹ and other related systems,¹²¹ this rearrangement process from a γ -agostic metal-alkyl complex to a β -agostic complex is found to have a barrier of less than 3 kcal/mol. Structure **21** completes the propagation cycle, since we have calculated the monomer coordination and insertion process from β -agostic (**15a**) to β -agostic (**21**) Ni-alkyl complexes. The overall exothermicity of the insertion process (from **15a** + ethene

to **21**) is $\Delta E = -24.7$ kcal/mol which approaches the equivalent value of 26.1 kcal/mol in the pure QM model system.

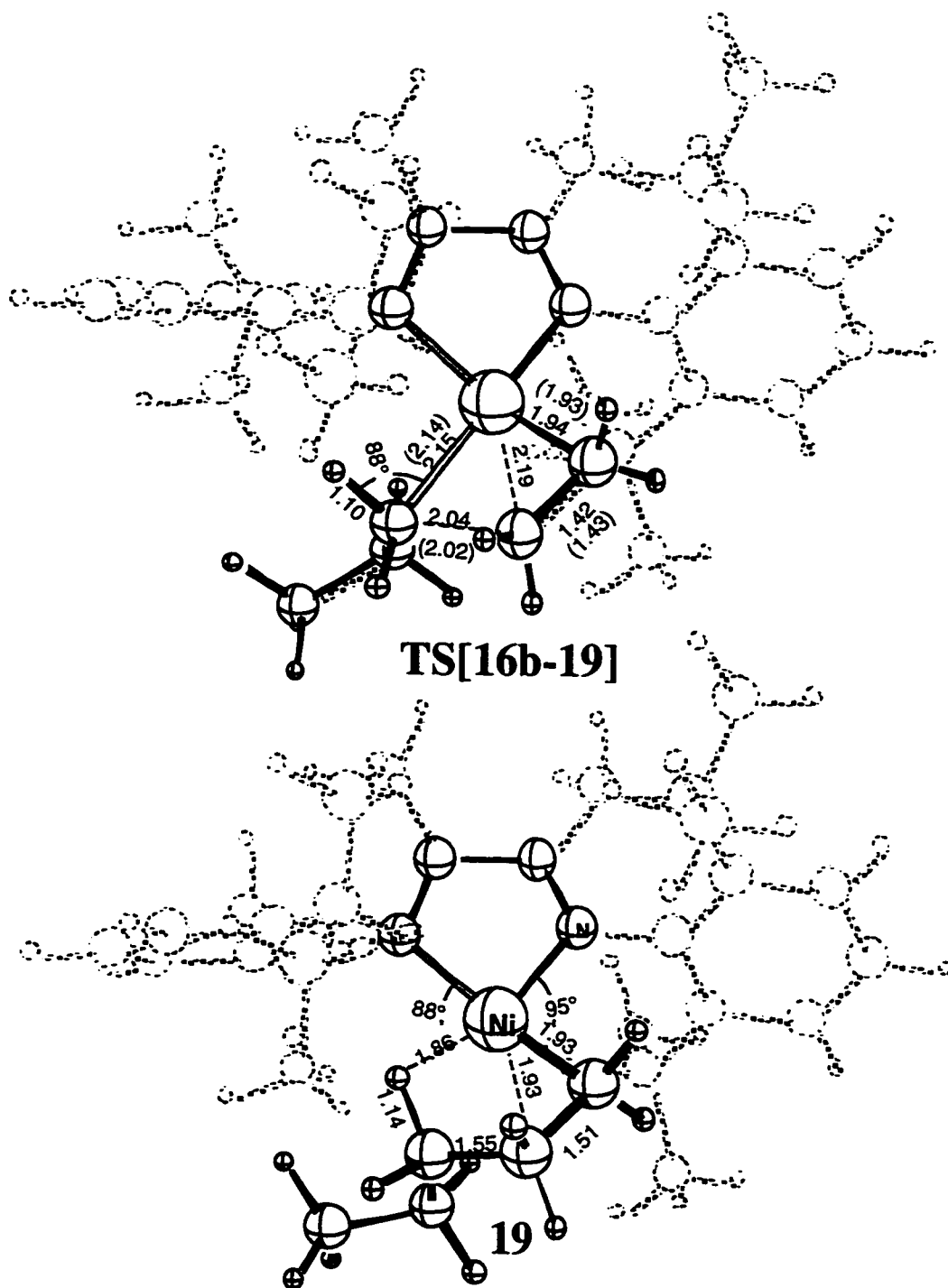


Figure 3.9. Transition state and kinetic product for the out-of-plane insertion channel. Conventions as in Figure 3.4.

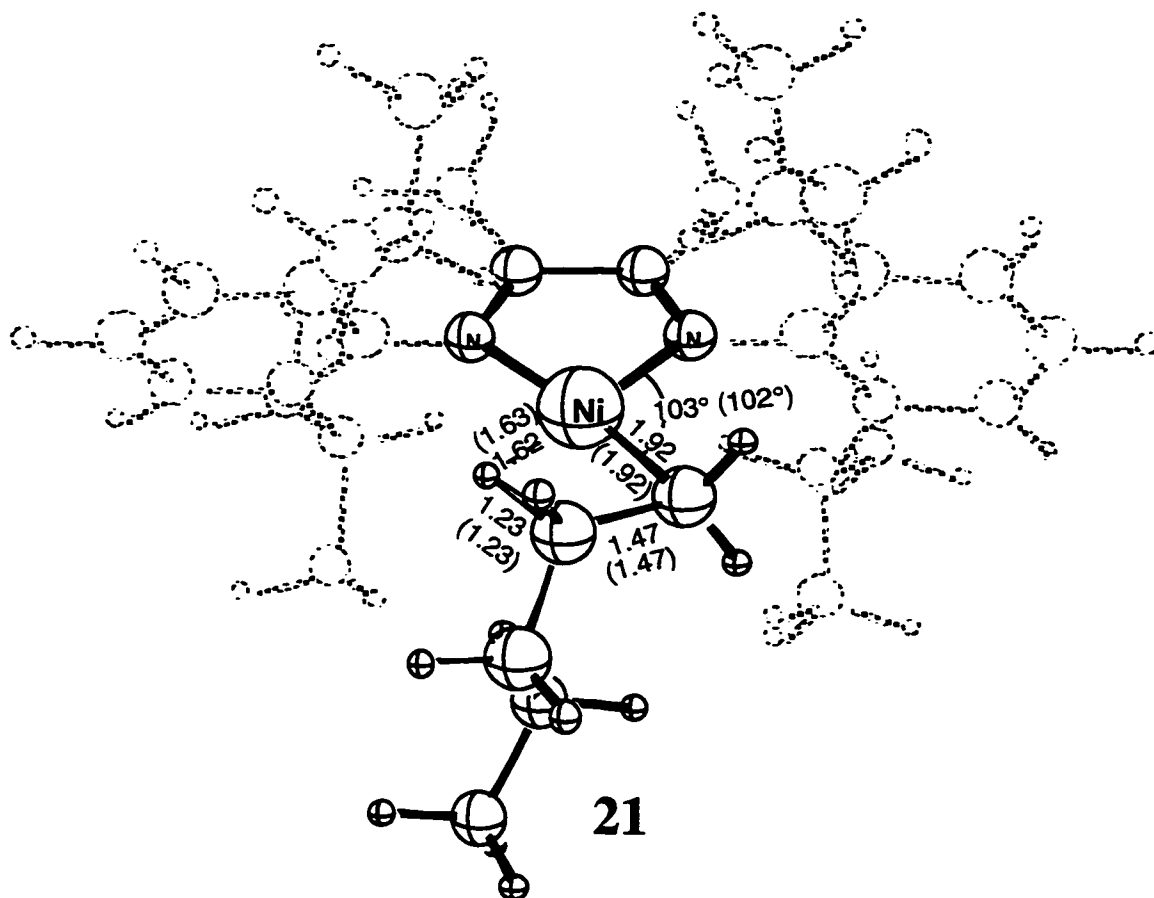


Figure 3.10. Optimized structure of the thermodynamic β -agostic insertion product. Conventions as in Figure 3.4.

From the hybrid QM/MM model, we conclude that the insertion barrier is 13.2 kcal/mol and proceeds directly from the resting state π -complex through the out-of-plane insertion channel. This is significantly diminished from the insertion barrier of the pure QM model system which was determined to be 16.8 kcal/mol and proceeded through the stepwise in-plane channel. The primary effect of the bulky aryl ligands in the insertion process is to reduce the stability of the resting state complex, which results in a lowered insertion barrier. This is supported by the fact that relative to the reactant Ni-alkyl complex and free ethene molecule, the resting state is destabilized by 4.2 kcal/mol in the QM/MM model compared to the pure QM model, whereas both the insertion transition state and the thermodynamic product maintain their positions relative to the initial reactants in both the pure QM and QM/MM models. In other words, for both models the insertion transition states lie roughly 1-2 kcal/mol below the reactants and the thermodynamic products lie 25-26 kcal/mol below the reactants. This contrasts the

resting state which lies 14.7 kcal/mol below the reactants for the QM/MM model but 18.9 kcal/mol below the reactants for the pure QM system.

b. Chain Branching (Isomerization)

Sketched in Figure 3.1c is the proposed mechanism¹ which gives rise to the unique short chain branching observed with the Brookhart catalyst systems. With this proposed mechanism, the branching occurs by a chain isomerization process whereby the β -hydrogen of the alkyl chain is eliminated, yielding a hydride olefin complex. Rotation of the π -coordinated olefin about the Ni-olefin bond, followed by reattachment of the hydride produces a secondary carbon and, consequently, a branching point. Commencing from the monomerless Ni-alkyl cation, the pure QM calculations show that there is no stable hydride-olefin complex, thereby implicating a concerted isomerization pathway. A 12.8 kcal/mol isomerization barrier was determined for the pure QM model system. These calculations were repeated with the hybrid QM/MM model system which was initiated from the β -agostic Ni-propyl cation, **15a**.

Concordant with the pure QM calculations, no stable hydride-olefin complex could be located. The optimized isomerization transition state, **TS[15a-22]**, lies 15.3 kcal/mol above **15a**. The bulky ligands, therefore, increased the isomerization barrier by 2.5 kcal/mol compared to the pure QM model system. Figure 3.11 shows that the isomerization transition state, **TS[15a-22]**, is somewhat compacted by the bulky aryl groups. This is illustrated by the slight compression of the C_{β} -H_{hydride} and Ni- C_{β} distances and slight dilation of the N-Ni- C_{α} angle as a result of the introduction of the aryl ligands by the QM/MM method. The destabilization of the transition state due to the bulky ligands is not manifested in the electronic QM energy, but rather emerges in the MM energy. Again, there is a van der Waals component and a torsion component as detailed in Table 3.1. The torsional component arises because as the propene-like moiety rotates it forces one of the aryl rings to adopt an unfavorable perpendicular orientation such that the θ angle is 88° in **TS[15a-22]**.

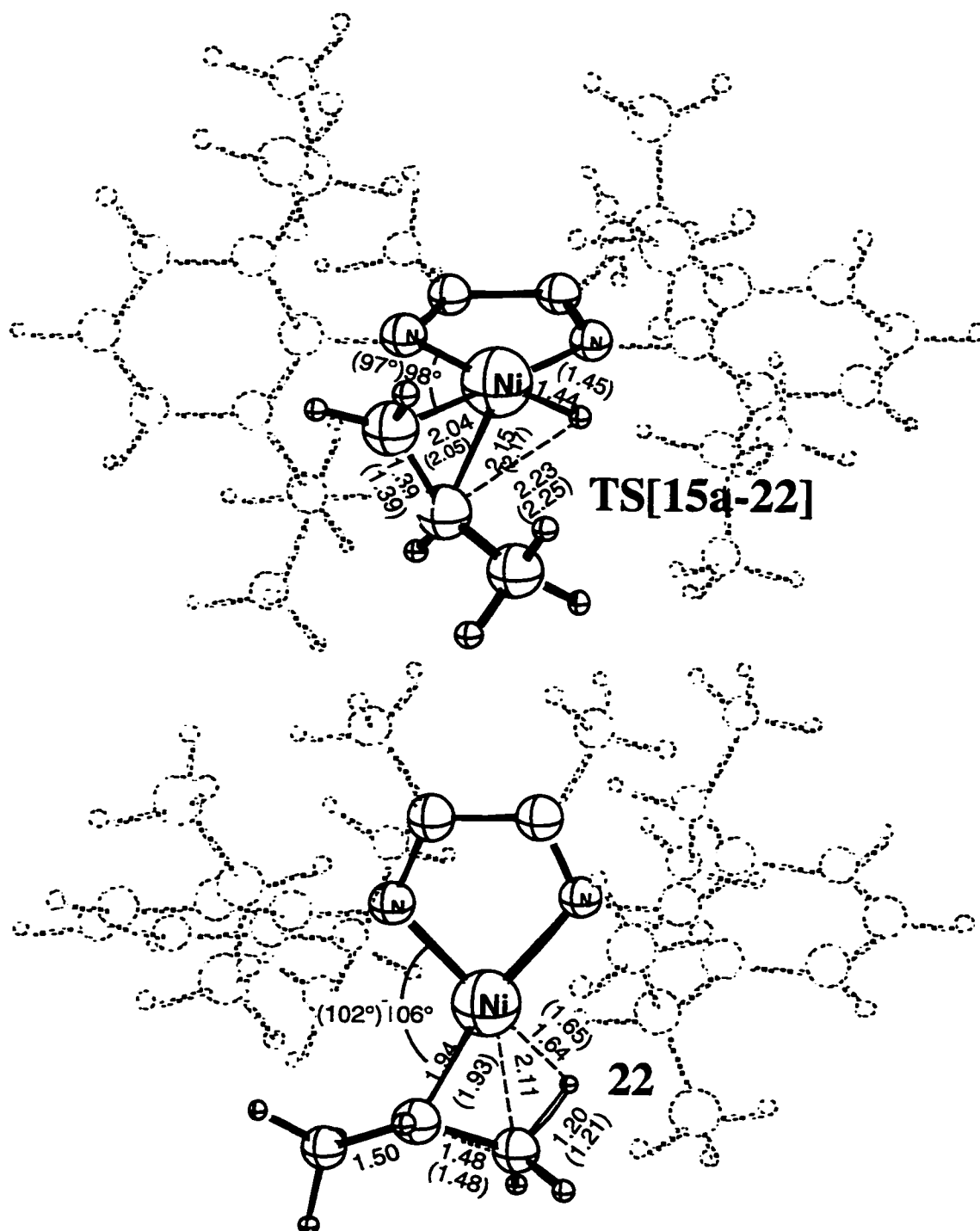


Figure 3.11. Transition state and product of the isomerization or chain branching process. Conventions as in Figure 3.4.

The overall QM/MM isomerization process is only exothermic by $\Delta E = -0.8$ kcal/mol which is virtually unchanged from the pure QM system where the isomerization process is only 1 kcal/mol more exothermic with $\Delta E = -1.8$ kcal/mol. As summarized in

Table 3.1, there is essentially no change in the MM energy between **15a** and the isomerization product, **22**. The 1 kcal/mol destabilization of the QM/MM isomerization product appears in the QM electronic energy. Figure 3.11 which depicts the optimized geometry of the isomerization product reveals that the N-Ni-C α angle is increased from 102° in the pure QM model to 106° in the hybrid model. Since there are no other significant changes in the geometry of the isomerization product, it is most likely this small perturbation in the active site that gives rise to the modest 1 kcal/mol decrease in the exothermicity of the isomerization process.

It is possible that chain isomerization could commence from the resting state, such that the isomerization occurs in the presence of the π -coordinated monomer. With our pure QM model system, we have located such a transition state which lies 3 kcal/mol higher than termination transition state. Since this transition state and the termination transition state are very similar in nature, the inclusion of the bulky aryl groups would make this process even more unfavorable. Therefore, our calculations show that the chain isomerization does not likely commence from the resting state.

c. Chain Termination:

The chain termination is proposed to occur by an olefin assisted β -hydrogen elimination process. Brookhart and coworkers^{1,2} have suggested that the termination is initiated by β -hydrogen transfer to the metal, to form an olefin hydride complex. In this picture, the termination is then completed by the association of monomer followed by insertion of the monomer into the metal-hydrogen bond. Since, we could find no stable olefin hydride complex, we suggest that the termination is more concerted in nature such that the process is best described as a β -hydrogen transfer to the monomer. This subtle variant is detailed in Figure 3.1b. Our earlier pure QM study of the termination reveals that the hydrogen transfer to the monomer involves a weak double π -olefin hydride complex whereby the transferred hydrogen is shared equally between the two olefin moieties which occupy the axial coordination sites. Neglecting the bulky ligands, the termination barrier was calculated to be 9.7 kcal/mol, significantly less than the pure QM propagation barrier of 16.8 kcal/mol. This is consistent with the fact that similar Ni and Pd systems which contain no bulky ligands are used as dimerization and oligomerization catalysts.¹¹¹⁻¹¹³

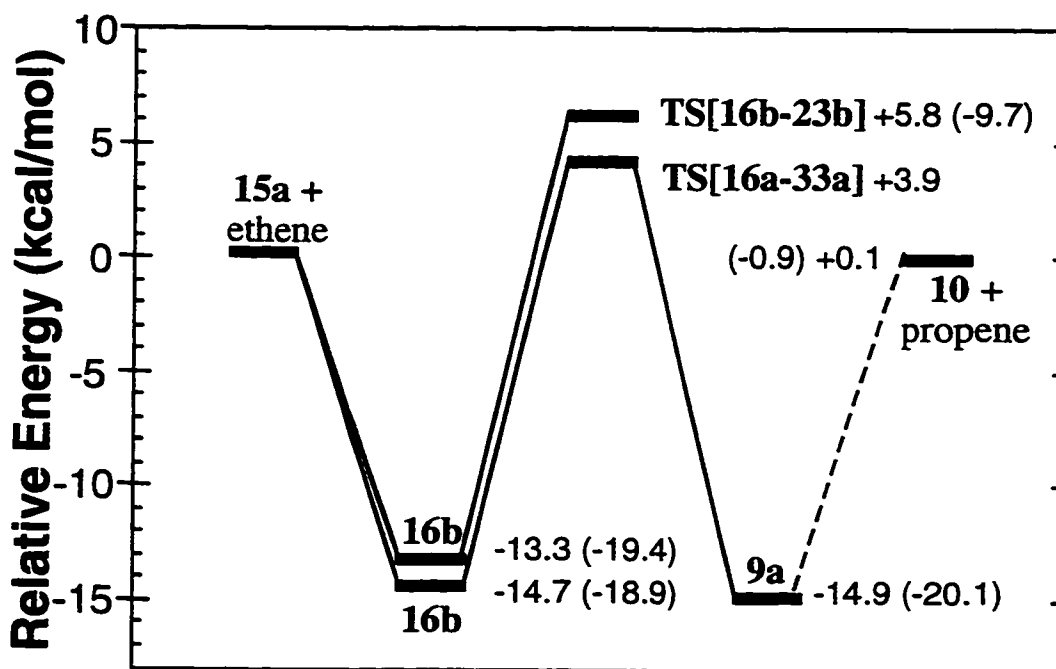


Figure 3.12. Energy profile for the chain termination process. Parenthetical values refer to the analogous relative energies of the equivalent pure quantum mechanical structures.⁵⁹ All energies in kcal/mol.

In this study we have examined the termination process commencing from both resting states, **16a** and **16b**. The calculated QM/MM energy profiles are displayed in Figure 3.12. Unlike the termination process in the pure QM model, no discernible intermediate hydride complex could be located. Thus, in the QM/MM system the β -hydrogen is transferred directly from the alkyl chain to the monomer (compare Figure 3.12 with Figure 5 of reference 59). The termination pathway initiated from resting state structure **16a** leads to a 18.6 kcal/mol barrier, of which the optimized transition state, TS[16a-23a], is displayed in Figure 3.13. The transition state, TS[16b-23b] (not shown), for the pathway initiated from **16b** lies 1.9 kcal/mol above TS[16a-23a] giving rise to a 19.1 kcal/mol barrier. These QM/MM termination barriers roughly double those of their pure QM counter parts. Table 3.1 reveals that there is a mutual destabilization exhibited in the QM electronic system and the MM system which gives rise to the increased termination barrier in the QM/MM system. For example, the pure QM termination barrier is 9.7 kcal/mol which compares to the change in the QM contribution of the total QM/MM energy of 13.8 kcal/mol for TS[16a-23a]. Thus, compared to the pure QM transition state, the electronic system of the QM/MM model is additionally destabilized by 4.1 kcal/mol. This perturbation of the electronic system by the bulky MM substituents is also evident in the geometric distortion of the transition state structure. Most notably,

there is a contraction of the C β -H_{hydride} bond of 0.12 Å. The destabilization of the transition state due to the MM potential accounts for 4.8 kcal/mol, roughly half of the overall destabilization. The last three columns of Table 3.1 show that most of the MM destabilization is a result of an increased steric interaction between the aryl rings and the active site fragments (ethene and propyl). In addition to these steric interactions, there is an ~1.5 kcal/mol increase in the steric interaction between the aryl rings and the auxiliary methyl fragments bound to the diimine ligand. Thus, the substituents on the diimine ligand play an important role in destabilizing the termination transition state. It has been observed experimentally that if the diimine methyl groups are replaced by hydrogen atoms, the molecular weights decrease substantially from 8.1×10^5 to 2.8×10^5 g•mol⁻¹.¹

d. Comparison of Theoretical and Experimental Results:

The reaction barriers calculated from our combined QM/MM model are in excellent agreement with the experimentally determined free energy barriers, both in absolute and relative terms. This contrasts the results of the pure QM study where the bulky ligands were not modeled and the order of the barriers was not reproduced. The role of the bulky ligands can be examined in detail since we have two model systems, one in which the bulky aryl rings are modeled by a molecular mechanics potential and one where there are no bulky aryl rings.

Propagation: The calculated QM/MM propagation barrier of $\Delta E^\ddagger = 13.2$ kcal/mol agrees well with the experimental free energy barrier¹²² of $\Delta G^\ddagger = 10-11$ kcal/mol. This compares with the calculated pure QM propagation barrier of 16.8 kcal/mol. As previously discussed, the bulky ligands act primarily to reduce the stability of the resting state while the energies of the thermodynamic product and the transition state remain unchanged relative to the Ni-alkyl cation. Thus, the polymerization activities should actually increase with increasing steric bulk. This peculiar effect has been observed experimentally.¹ For example, when the *o*-isopropyl groups are replaced by less bulky *o*-methyl groups, the catalyst activities are found to decrease from 7680 to 1800 kg per mol of Ni per hour.

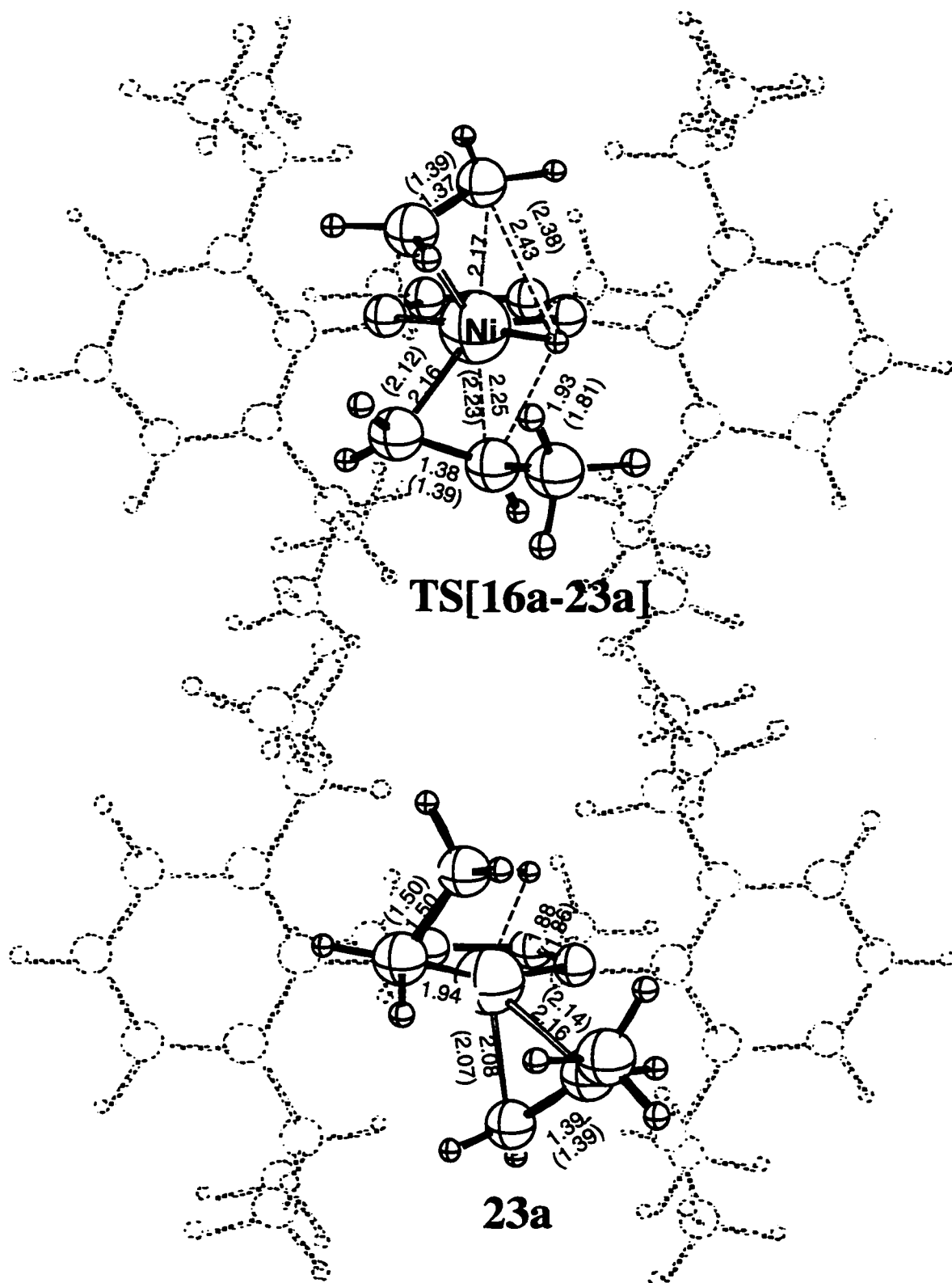


Figure 3.13. Transition state and product of the chain termination process. Conventions as in Figure 3.4.

Table 3.2. Comparison of Calculated Barriers to Experimental Relative Barriers.

	reaction barriers (kcal/mol)		
	insertion	branching	termination
<i>absolute:</i>			
Pure QM ^a (ΔE^\ddagger)	16.8	12.8	9.7
QM/MM (ΔE^\ddagger)	13.2	15.3	18.6
Experimental ^b (ΔG^\ddagger)	10 - 11	-	-
<i>relative to insertion:</i>			
Pure QM ^a ($\Delta\Delta E^\ddagger$)	0.0	-4.0	-7.1
QM/MM ($\Delta\Delta E^\ddagger$)	0.0	2.1	5.4
Experimental ^c ($\Delta\Delta G^\ddagger$)	0.0	1.3 ^d	5.6 ^e

^aReference 59. ^bReference 122. ^cReference 1. Polymerization of 1.6×10^{-6} mole of $(ArN=C(R)C(R)=NAr)Ni(CH_3)(OEt_2)]^+[B(3,5-C_6H_3(CF_3)_2)_4]^-$ where $Ar = 2,6-C_6H_3(i-Pr)_2$ and $R = Me$ in 100 mL of toluene at 0°C for 15 min. ^dNMR studies provide a ratio of 48 isomerization events per 500 insertions, assuming that all branches are methyl branches (methyl branches are experimentally observed to predominate). Applying Boltzmann statistics to this ratio at 273.15 K yields a $\Delta\Delta G$ of 1.3 kcal/mol. ^eThe weight-average molecular weight, M_w , of 8.1×10^5 g/mol provides an estimate for the ratio of termination events to insertion events of 1:28900. Using Boltzmann statistics, this ratio gives a $\Delta\Delta G$ of 5.6 kcal/mol.

Chain Branching (Isomerization): Table 3.2 summarizes the reaction barriers for the pure QM model system, the present QM/MM model system and experimental results in both relative and absolute terms. Based on the frequency of secondary carbon atoms in the polymer chain as determined from NMR experiments, and assuming that the fraction of branching can be equated with the rate of isomerization, the isomerization barrier is estimated to be 1.3 kcal/mol greater than the insertion barrier. This is in reasonable agreement with our calculated QM/MM isomerization barrier of 15.3 kcal/mol which lies 2.1 kcal/mol above the calculated insertion barrier. We note that monomer concentration effects are not taken into account in our model and therefore the above comparison is dubious since the extent of branching may be highly dependent on the rate of monomer trapping. It has been demonstrated experimentally¹ that increasing the steric bulk of the ortho substituents increases the branching frequency. This is somewhat at odds with our theoretical result which shows that there is a modest increase in the isomerization barrier of 2.5 kcal/mol in moving from the bare QM system which has no steric bulk to the hybrid QM/MM model. We therefore conclude that the dominant role of the bulky groups (pertaining to the branching process) is to impede the formation of

the resting state thereby promoting the branching process to occur.[◇] We will address this issue in more detail in Chapter 6.

Chain Termination: Our model systems show that of all the processes studied, the bulky ligands have the most dramatic effect on the termination, virtually doubling the termination barriers in going from the pure QM system to the QM/MM system (Table 3.2). This is in agreement with the fact that without the bulky ligands these Ni diimine systems are mere dimerization catalysts, but with the bulky ligands these systems are commercially viable polymerization catalysts. Our theoretical results are also in agreement with the related finding that as the steric bulk of the diimine ligands is increased, there is a correspondent increase in the molecular weights. As previously discussed, our analysis of the destabilizing interactions in the termination transition state reveals that the methyl groups bound to the diimine ligands interact strongly with the bulky aryl substituents. Again this is consistent with the experiments which show that the polymer molecular weights drop when the methyl groups are replaced by hydrogens.

From the weight-average molecular weight, M_w , we can estimate the ratio of termination events to insertion events, which can in turn be used to determine the difference between the termination and insertion free energy barriers, $\Delta\Delta G^\ddagger$. As shown in Table 3.2, there is a remarkable agreement between the experimental ($\Delta\Delta G^\ddagger = 5.6$ kcal/mol) and QM/MM ($\Delta\Delta E^\ddagger = 5.4$ kcal/mol) termination barrier relative to the insertion.

In calculating $\Delta\Delta G^\ddagger$ we have assumed that every hydrogen transfer event leads to the loss of the chain and, consequently, chain termination. However, the vinyl terminated chain in **9a** can reinsert. If the reinsertion is competitive with chain loss then the above assumption is invalid. Other polymerization systems, namely early transition metal metallocenes, generally exhibit the behavior that the higher the α -olefin, the higher the barrier to insertion.¹²³ This would pin point the reinsertion barrier to be at least as high as the normal monomer insertion barrier. In the worst case, this would imply that our assumption is incorrect. Here, we argue that our chain loss barrier is a gas phase barrier and that the loss of olefin is in actuality assisted by the solvent or ethylene, resulting in a barrier substantially lower than that in the gas phase. This further implies that the barrier to olefin loss is significantly lower than the barrier to reinsertion and, consequently, indicates that our approximation is justifiable.

[◇] This is further corroborated by the experimental observation that increased ethylene pressures decrease the branching, while not dramatically affecting the polymer yields or molecular weights.

e. General Discussion.

For the Brookhart catalyst system the combined QM/MM method is clearly an improvement over the truncated pure QM model because of the critical importance of the bulky aryl substituents which are neglected in the pure QM model. Our calculations further show that the QM/MM model is a clear improvement over a stepwise QM followed by MM method.^{88,91,124-126} In the stepwise QM/MM method, QM calculations are first performed using a truncated model system in which the bulky substituents are neglected. Then a MM calculation is performed on the whole system using active site geometries extracted from the pure QM calculation. The most important difference between the stepwise QM/MM method and the present combined QM/MM method is that during geometry optimization in the stepwise method, the pure QM geometry is fixed.[◊] Therefore, there is no relaxation of the active site structure in order to accommodate the bulky substituents. For sake of comparison, we have performed such a stepwise QM/MM calculation whereby the pure QM geometry of reference 59 were frozen in an MM calculation using the same force field as described above. The results of the stepwise QM/MM calculations are poor. For example, the barriers for insertion, branching and termination are $\Delta E^\ddagger = 18.5, 14.0$ and 25.7 kcal/mol, respectively. This compares to $\Delta E^\ddagger = 13.2, 15.8$ and 18.6 kcal/mol, respectively, for the combined QM/MM method. Another noteworthy result of the stepwise QM/MM method is that it overestimates the energy difference between the two resting state rotamers **16a** and **16b**. The stepwise method predicts that **16a** is 5.3 kcal/mol more stable than **16b** whereas the combined QM/MM results provide a difference of 1.0 kcal/mol. We conclude that for this system full optimization of both the QM and MM regions, as is done in the combined QM/MM method, is necessary to provide even qualitatively correct results.

The primary goal of this study was to examine, in detail, the role that the bulky substituents play in the polymerization chemistry of the Brookhart Ni-diimine catalysts. By simple examination of the catalyst structure one can ascertain that the bulky substituents block the axial coordination sites. Our previous pure QM study, which revealed the nature of the generic intermediates and transition states involved, suggested that the bulky ligands would have the most dramatic effect on the termination process which utilizes both axial coordination positions. This combined QM/MM study reaffirms this picture. Analysis of the molecular mechanics energy contributions as previously discussed suggest that there is a second important feature of the aryl ligands apart from

[◊] Comparison of the combined QM/MM and the stepwise QM then MM methodologies can be found in reference 28.

the positioning of the steric bulk. We observe that preferential orientation of the aryl rings away from a perpendicular alignment to the Ni-diimine ring provides stabilization in both the Ni-alkyl complexes and the insertion transition states. This factor contributes to the reduction of the propagation barrier as compared to the pure QM model system. It is difficult to ascertain the relative importance of this secondary effect since strong steric effects can often manifest themselves in other molecular mechanics energy terms, such as bond bending and torsion energies terms. Despite this, we suggest that increasing the preference for a more parallel alignment of the aryl rings by increasing the π -orbital interactions between the aryl rings and the diimine ring will have an effect of increasing the activity of the catalyst and increasing the molecular weights. This can be achieved (other ramifications not considered) by an appropriate functionalization of the aryl rings. Another possibility is to functionalize the diimine R group such that it interacts with the ortho *i*-propyl group so as to pull the aryl rings into a more co-planar orientation. Unfortunately, our model suggests that this would also lead to diminished branching since the isomerization TS has a destabilizing torsional component.

In the current QM/MM model, the electrostatic coupling between the QM and MM atoms has been neglected. In some systems this approximation may be severe. However, in the present case we feel that this approximation is justified since the dominant non-bonded interactions between the QM (ethene and propyl moieties) and MM (isopropyl and methyl groups) regions do not involve any highly polarized groups. The good agreement between the calculated and experimental results further suggests that this approximation is reasonable in this case.

3.4 Conclusions

We have successfully applied the combined QM/MM methodology to study Brookhart's Ni(II) diimine ethylene polymerization catalysts of the type $(\text{ArN}=\text{C}(\text{R})-\text{C}(\text{R})=\text{NAr})\text{Ni}(\text{II})-\text{R}'^+$ where $\text{R}=\text{Me}$ and $\text{Ar}=2,6\text{-C}_6\text{H}_3(i\text{-Pr})_2$. In the combined QM/MM model, the bulky Ar and R groups were treated by a molecular mechanics potential while the remainder of the system was treated by density functional theory (Becke88-Perdew86). Chain propagation, chain branching and chain termination were studied and calculated to have barriers of $\Delta E^\ddagger = 13.2, 15.3$ and 18.6 kcal/mol, respectively. These calculated enthalpic barriers are in good agreement with experiment in both absolute and relative terms (where available). This contrasts an earlier pure QM study which neglects the bulky ligands. There the propagation, branching and termination barriers were calculated to be $\Delta E^\ddagger = 16.8, 12.8$ and 9.7 kcal/mol, respectively, which is the reverse

order of barriers as that determined experimentally. In the present QM/MM study, we find that the bulky ligands act to destabilize the resting state complex. This has the effect of *lowering* the insertion barrier since the relative energy of the insertion transition state is not significantly perturbed by the bulky substituents. With respect to the chain branching and chain termination processes, the bulky ligands destabilized the transition states. This is particularly true of the termination process in which there is a two fold increase in the barrier.

The results of our pure QM⁵⁹ and the present QM/MM study concurs with the experimental observation that the generic Ni(II) diimine systems are intrinsically dimerization catalysts, but can be converted into polymerization catalysts with the addition of suitable substituents. Our study suggests that two criteria need to be met by the bulky substituents for this to be successful. First and foremost, the substituents must disproportionately block the axial coordination sites of the Ni center over the equatorial coordination sites, as was first suggested by Johnson *et al.*¹ Secondly, our calculations suggest that the substituents must also have a conformational preference to vacate the axial sites. In the particular case of the aryl ring substituents, it is more favorable for the rings to orient themselves (more) parallel to the Ni-diimine plane than to remain perpendicular to it.

We conclude that the combined QM/MM method can be effectively applied to a study of transition metal based catalytic processes in an detailed and efficient manner. Moreover, we have demonstrated that the unique features of the QM/MM method have allowed for deeper insights into the substituent effects to be achieved compared to either the truncated pure QM model or the stepwise QM then MM model.

3.5 Towards *A Priori* Catalyst Design with the Combined QM/MM Method.

To date, computational modeling of metallocene catalysts (published in the open literature) has been confined to examining polymerization catalysts that have already been synthesized in the lab and shown to be promising. Although understanding how these existing catalysts function is valuable, the ultimate and more difficult challenge of molecular modeling is to design effective catalysts on the computer before significant time (and money) is spent on their synthesis in the lab. In this section we summarize our most recent¹²⁷ efforts towards this goal with the combined ADF QM/MM method.

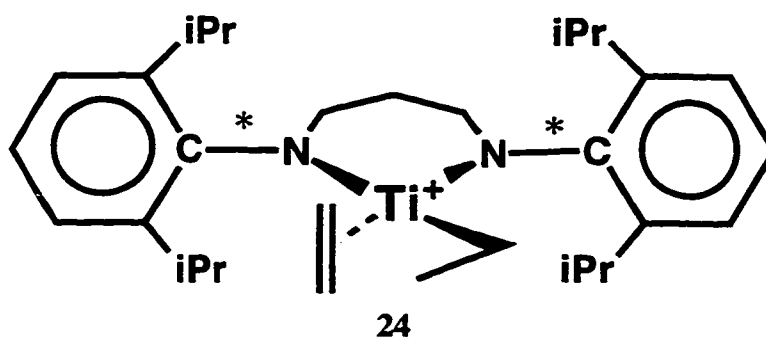


Figure 3.14 McConville's living olefin polymerization catalyst.

An important development in the search for a new single-site systems has been the discovery of the first living Ziegler-Natta type olefin polymerization catalyst by McConville and coworkers.⁴⁰ (In this context, "living" refers to a catalyst system that appears to polymerize indefinitely such that there is little observable chain termination.) Similar in structure to Brookhart's system, the catalyst is a Ti(IV) diamine system of the type $[\text{ArNCH}_2\text{CH}_2\text{CH}_2\text{NAr}]\text{TiR}^+$ where $\text{Ar} = 2,6\text{-iPr}_2\text{C}_6\text{H}_3$ as shown in Figure 3.14. One intriguing characteristic of the catalyst system is that while the titanium system is a living polymerization catalyst, its zirconium analog lies on the opposite end of the polymerization spectrum - it produces only very low molecular weight oligomers with $n=2-7$.¹²⁸ The combined QM/MM approach has been applied not only to understand the drastically different behavior of the Ti and Zr systems, but also to design a new ligand structure for the zirconium diamine system as to boost its performance in terms of its activity and molecular weight profiles.

The computational methodology is the same as that of our examination of the Brookhart catalyst presented earlier in this chapter. Again the full catalyst system is too large to be wholly treated at the DFT level, and consequently the QM/MM methodology was applied. Figure 3.14 shows the full catalyst system where the QM/MM link bonds are labeled with the asterisks. Hydrogen atoms were used to cap the QM model system. Full computational details are provided elsewhere.¹²⁷

In terms of the length of the polymer chains produced, dimerization catalysts and living olefin polymerization catalysts can be considered opposites. The polymer length which is measured experimentally by the polymer molecular weight (M_w) can be related to the difference in the rate of chain growth and chain termination. With a dimerization catalyst, chain termination is more favorable than chain growth. As a result, once a monomer is added, the chain is immediately terminated as to produce a dimer. On the other hand, with a living polymerization system the rate of chain termination compared to

chain propagation is so insignificant that termination is not observed and the polymer appears to grow indefinitely. It is interesting that by simply changing the Ti to Zr, the McConville catalyst system is flipped from one end of the molecular weight scale to the other. Although the catalytic behaviour of Zr and Ti analogs often exhibit differences, this is an extreme case.

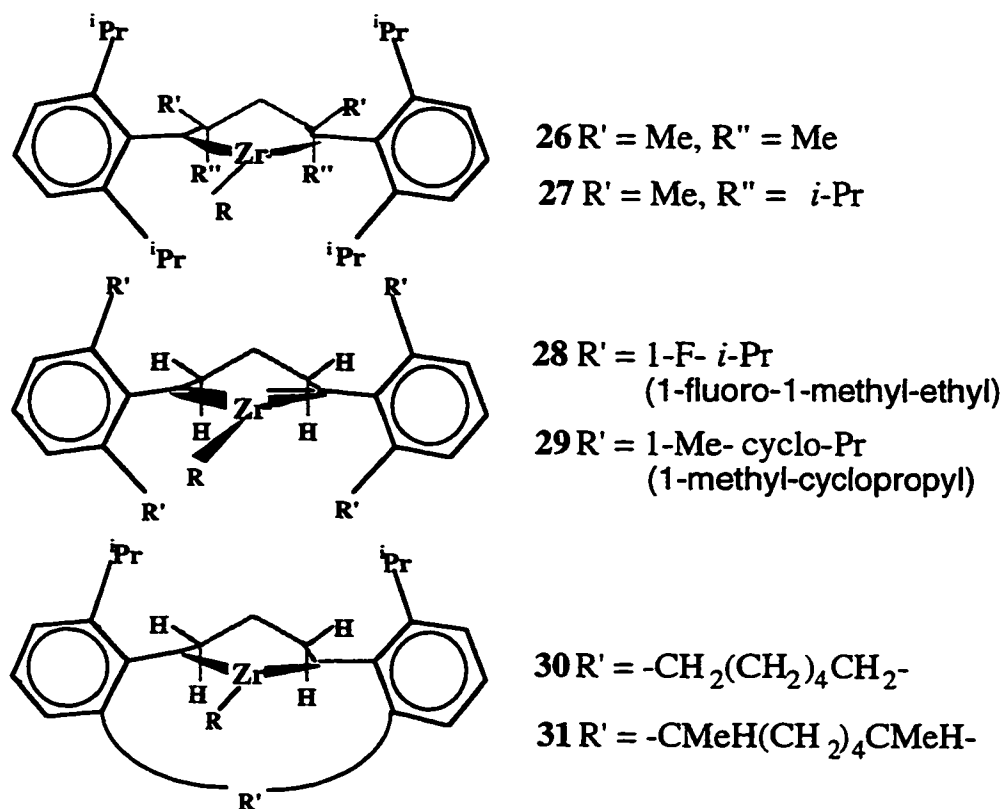


Figure 3.15 Modification of McConville's Zr diamide catalyst.

When the combined QM/MM method was applied to the original McConville catalyst $[\text{ArN}(\text{CH}_2)_3\text{NAr}]\text{TiR}^+$ ($\text{Ar} = 2,6\text{-}i\text{Pr}_2\text{-C}_6\text{H}_3$) the barrier of termination was calculated to be 9.8 kcal/mol higher than the barrier of propagation. On the other hand, when the method was applied to the zirconium analog, the difference was found to be a mere 0.1 kcal/mol. These computational results are in line with the findings by McConville that the titanium complex is a living olefin polymerization catalyst whereas the homologous zirconium complex is able only to oligomerize olefins. (It is notable that the computed results for the zirconium system were predicted before the experimental results were available.¹²⁸) An analysis of the results showed that the iso-propyl substituted aryl rings in the titanium system are forced to stay perpendicular to the N-M-N plane in order to avoid the steric bulk of the diamide bridge. In this orientation the

axial sites above and below the N-Ti-N plane are blocked and the termination transition state destabilized. This same steric interaction between the diamide bridge and the aryl rings in the zirconium analogue is significantly reduced due to the longer Zr-N bonds compared to Ti-N bonds. As a result, the aryl rings in the Zr system can move out of the perpendicular ring plane position and the *iso*-propyl groups are less effective in retarding the chain termination by blocking the axial sites.

The lack of sufficient steric bulk in the zirconium diamide complex to retard the chain termination has lead us to suggest a number of modified complexes based on this general principle. The modifications, which are shown in Figure 3.15, involve: i) increasing the steric bulk on the diamide bridge as in **26** and **27**; ii) increasing the steric bulk on the aryl rings as in **28** and **29**; and iii) blocking one axial position by a hydrocarbon bridge as in **30** and **31**. Results from the combined QM/MM calculations indicate that the ligand modifications, particularly those expressed in **29** and **31**, might generate zirconium based living olefin polymerization catalysts with much higher activities than the original titanium diamide catalyst of McConville. Gathered in Table 3.3 are the activities and molecular weights for the modified system as predicted by the combined QM/MM model. The results are also compared with the original McConville and Brookhart systems with experimental values where available.

Work by Piers *et al.*¹²⁹ is now in progress to synthesize a living zirconium-based diamide olefin polymerization catalysts similar to those suggested here. If the actual polymerization capabilities the new Zr based catalysts that we have suggested match those predicted theoretically by our QM/MM model, this would be the first example of a computer designed polymerization catalyst and a significant landmark in the area of molecular modeling in this area.

Table 3.3 Comparison of the Catalytic Capability of the New Catalysts with the McConville and Brookhart Catalysts for Polymerization of Ethylene.

Catalyst System	barriers ^a (kcal/mol)		$\Delta(\Delta E^\ddagger)^b$	Predicted ^a
	insertion	termination		M_w^c
<i>Original McConville Catalyst:</i>				
$[\text{ArN}(\text{CH}_2)_3\text{NAr}]\text{MR}^+{}^d$				
M = Ti, Ar = 2,6- <i>i</i> Pr ₂ C ₆ H ₃ (24)	9.4	19.3	9.9	5.6 x 10 ⁸ (living)
M = Zr, Ar = 2,6- <i>i</i> Pr ₂ C ₆ H ₃ (25)	11.8	11.7	-0.1	dimer (n=2 - 7)
<i>Modified McConville Catalyst:</i>				
$[\text{ArNCR}'\text{R}'\text{CH}_2\text{CR}'\text{R}''\text{NAr}]\text{ZrR}^+$				
R' = R'' = CH ₃ (26)	9.2	12.0	2.8	3.3 x 10 ³
R' = CH ₃ , R'' = <i>i</i> Pr (27)	2.9	6.7	3.8	1.8 x 10 ⁴
$[\text{ArN}(\text{CH}_2)_3\text{NAr}]\text{ZrR}^+$				
Ar=2,6-(CMe ₂ F) ₂ -C ₆ H ₃ (28)	2.1	9.2	7.1	4.9 x 10 ⁶
Ar=2,6-(1-Me-cyclo-Pr) ₂ -C ₆ H ₃ (29)	-1.7	7.2	8.9	1.0 x 10 ⁸
<div style="text-align: center;">--- R' --- $[\text{ArN}(\text{CH}_2)_3\text{NAr}]\text{ZrR}^+$ (Ar = 1-<i>i</i>Pr, 6-R'-C₆H₃)</div>				
R' = -CH ₂ (CH ₂) ₄ CH ₂ - (30)				
R' = -CHMe(CH ₂) ₄ CHMe- (31)	8.2	10.0	1.8	6.0 x 10 ²
<i>Brookhart Catalyst:</i>	3.3	11.9	8.6	6.2 x 10 ⁷
$[\text{ArNCH}_2\text{CH}_2\text{NAr}]\text{NiR}^+$				
Ar = 2,6-(<i>i</i> Pr) ₂ C ₆ H ₃				
	13.2 (10-11)	18.6	5.4 (5.6)	5.8 x 10 ⁴ (8.1 x 10 ⁴)

^aValues in parenthesis are experimentally determined. ^b $\Delta(\Delta E^\ddagger)$: the difference in activation energy between insertion (chain propagation) and termination. Experimental values in parenthesis. ^cWeight-average molecular weight, M_w , estimated from the $\Delta(\Delta E^\ddagger)$ values using Boltzmann statistics at 296.15 K for the diamide systems, and at 298.15 K for the Brookhart system. In the parentheses are the experimental results. ^dThe McConville catalysts, references 40 and 128. Monomer used in the experiments are 1-hexene.

Chapter 4

Ab Initio Molecular Dynamics Simulations as a Practical Tool For Studying Catalysis

4.1 Introduction

The recent development of the Projector Augmented Wave (PAW)⁴¹ Car-Parrinello¹³⁰ method has allowed for practical *ab initio* molecular dynamics simulations of transition metal complexes to be performed.^{131,132} We have recently applied the method to study olefin polymerization catalysis.^{121,133-135} In this chapter, a summary how we^{121,133,135} have found the *ab initio* molecular dynamics method to be a practical computational tool for studying homogenous catalysis will be provided. Since the *ab initio* molecular dynamics is not widely utilized by quantum chemists, a succinct review of the method⁰ will first be presented with a particular focus on the aspects and methodologies that we have applied to study transition metal based catalysis.

4.2 What is Molecular Dynamics?

Conventional electronic structure calculations can be classified as static simulations. In these calculations the nuclear positions are optimized to locate local minima and transition states on the potential surface at the zero temperature limit. This involves, for each nuclear geometry, converging the electronic structure in order to determine the energy and forces on the nuclei. Using special algorithms, this information is then used to move the nuclei to a more optimal geometry. In classical molecular dynamics the nuclei are allowed to move on the potential surface according to Newton's classical laws of motion (Eqn. 4-1) as to simulate nuclear motion at finite (non-zero) temperatures.

$$m_i \ddot{\vec{x}}_i = \vec{F}_i(t) = -\frac{\partial E_{TOT}}{\partial \vec{x}_i} \quad i=1, 2..N_{nuc} \quad (4-1)$$

The nuclear motion generated in a molecular dynamics simulation can be utilized for a variety of purposes. Stationary points can be optimized by simply applying friction to the nuclear motion, thereby causing the system to settle into a local minimum. The motion can also be used to sample configuration space as to construct a partition function from which properties can be derived rigorously from statistical mechanics. There are

⁰Other reviews of the *ab initio* molecular dynamics method can be found in references 136, 137.

also global minimization schemes which utilize molecular dynamics, such as simulated annealing.

Integration Schemes. In a molecular dynamics simulation, the motion of the nuclei is determined by integrating Newton's equations (Eqn 4-1), a second order differential equation. Generally there is no analytical solution to the problem for molecular systems and numerical methods have to be utilized. In other words, given the velocities and positions at a time t , one determines the same quantities with reasonable accuracy at a later time $t+\Delta t$ using the calculated forces on the nuclei. Consider the motion of an atom along a coordinate x . Knowing the position $x(t)$ at time t , the position at time $t+\Delta t$ is given by a standard Taylor expansion as shown in equation 4-2.

$$x_i(t + \Delta t) = x_i(t) + \dot{x}_i(t)\Delta t + \ddot{x}_i(t)\frac{\Delta t^2}{2} + O(\Delta t^3) + \dots \quad (4-2)$$

There are a variety of integration schemes for solving the above problem. The most common methods truncate after the quadratic term and therefore are of 3rd-order of accuracy in the time step Δt . One such method is the Verlet^{138,139} integration scheme that is commonly used in *ab initio* molecular dynamics. In Verlet dynamics, the position of system at a time $t+\Delta t$ is given by a function of the position at the current time step, $x_i(t)$, previous time step, $x_i(t - \Delta t)$, and the forces, $F_i(t)$, at the current time step as related in equation 4-3.

$$x_i(t + \Delta t) = 2x_i(t) - x_i(t - \Delta t) + \frac{F_i(t)}{m_i}\Delta t^2 \quad (4-3)$$

With each new time step, a new geometry is generated and therefore the forces on the nuclei have to be recalculated. In order to simulate molecular vibrations, the time step Δt must be at least a third smaller than the period of the fastest vibration. Thus in order to simulate C-H bond stretching which has a period of 0.01 psec, the Δt must be less than 0.003 psec. Even a relatively short 10 ps simulation requires over 3300 time steps and therefore 3300 gradient calculations. (To put this in perspective, even the fastest enzyme catalyzed reactions have turnover periods of greater than 1000 picoseconds.[◊]) For this reason, most MD simulations are performed with a molecular mechanics force field. Their computational simplicity allows for extremely large simulations to be performed. An impressive example of this is the molecular dynamics simulations of protein folding processes, which often involve 10^4 atoms and require

[◊] The fastest olefin polymerization catalysts have turnover periods significantly greater than this.¹

simulation times of over 10^{-3} seconds. However, the empirical nature of molecular mechanics force fields has its limitations. For example, transition metal complexes are problematic because there is currently no force field general enough to handle all of the complicated bonding schemes available to these complexes. Moreover, chemical reactions cannot be simulated accurately (if at all) with a molecular mechanics force field. To overcome these problems *ab initio* or QM potentials can be used in conventional classical molecular dynamics. With the *ab initio* molecular dynamics (AIMD) method the forces are not determined from a molecular mechanics force field, but rather they are derived from a full electronic structure calculation at each time step. Although this is computationally demanding, it allows for bond breaking and forming processes to be simulated and it allows for molecular dynamics to be performed on systems where a molecular mechanics force field is not readily applicable.

4.3 Car-Parrinello *Ab Initio* Molecular Dynamics

Conventional AIMD involves moving the nuclei with the forces calculated from an electronic structure calculation. The electronic structure is normally described by a set of orthonormal molecular orbitals, ϕ_i , which are expanded in terms of a basis set, χ_k such that $\phi_i = \sum_k c_{ik} \chi_k$. The optimal coefficients are solved variationally with the constraint that the molecular orbitals remain orthogonal. Generally this is done in a self consistent manner by the diagonalization of the Hamiltonian matrix or equivalent.⁴³ An alternative method for determining the optimal coefficients draws analogy to nuclear dynamics which can be used to optimize nuclear geometries. By assigning fictitious masses to the coefficients, fictitious dynamics can be performed on the coefficients which then move through electronic configuration space with forces given by the negative gradient of the electronic energy. The equivalent equations of motion are:

$$\mu \ddot{c}_{i,k} = -\frac{\partial E^{el}}{\partial c_{i,k}} - \sum_j \lambda_{i,j} c_{i,k} \langle \phi_i | \phi_j \rangle \quad (4-4)$$

where μ is a fictitious mass, $\ddot{c}_{i,k}$ is the coefficient acceleration, and the last term corresponds to the constraint force imposed to maintain orthogonality of the molecular orbitals. The coefficients move through electronic configuration space with a fictitious kinetic energy and by applying friction the coefficients can be steadily brought to settle into an optimal configuration.

In 1985 Car and Parrinello¹³⁰ developed a scheme by which to perform the nuclear dynamics and the electronic coefficient dynamics in parallel as to improve the

efficiency of the AIMD approach. In this way the electronic MD and nuclear MD equations are coupled:

$$\mu \ddot{c}_{i,k} = -\frac{\partial E^{el}}{\partial c_{i,k}} - \sum_j \lambda_{i,j} c_{i,k} \langle \phi_i | \phi_j \rangle \quad m_I \ddot{x}_I = -\nabla E(x_I, c_{i,k})$$

Formally, the nuclear and electronic degrees of freedom are cast into a single, combined Lagrangian:

$$\mathcal{L} = \frac{1}{2} \sum_i \mu_i \langle \dot{\phi}_i | \dot{\phi}_i \rangle + \frac{1}{2} \sum_I M_I \dot{R}_I^2 - E_{DFT}(|\phi\rangle, R) + \sum_{i,j} \Lambda_{ij} \langle \phi_i | \phi_j \rangle \quad (4-5)$$

where the first two terms represent the kinetic energy of the wave function and nuclei, respectively, the third term is the potential energy and the last term accounts for the orthogonality constraint of the orbitals. If the fictitious masses are such that the fictitious kinetic energy of the wave function is very small compared to the physically relevant kinetic energy of the nuclei, then the Car-Parrinello method propagates the electronic configuration very near to the proper Born-Oppenheimer surface.[§] The generated electronic structure oscillates around the Born-Oppenheimer surface, which over time gives rise to stable molecular dynamics. The coupled Car-Parrinello dynamics, therefore, results in a speed up over conventional AIMD since the electronic wave function does not have to be converged at every time step, instead it only has to be propagated. The primary disadvantage of the Car-Parrinello MD scheme is that the electronic configuration oscillates about the Born-Oppenheimer wavefunction at a high frequency. Therefore, in order to generate stable molecular dynamics a very small time step must be used, usually an order of magnitude smaller than in conventional *ab initio* molecular dynamics.

Although other "first-principles" methods can be used,[¶] the Car-Parrinello coupled dynamics approach has mostly been implemented within the density functional framework with plane wave basis sets (as opposed to atom centered basis sets). Therefore, Car-Parrinello *ab initio* molecular dynamics generally refers only to this type

[§]If the fictitious kinetic energy of the electronic wave function is too large, then thermal equilibration between the system occurs where the electrons tend to heat up and leave the Born-Oppenheimer surface, accompanied by a cooling of the nuclear system.

[¶]Carter and coworkers^{140,141} have implemented the Car-Parrinello combined Lagrangian in various non-DFT wave-function methods allowing for *ab initio* molecular dynamics to be performed on excited state surfaces. Additionally, these implementations use atom centered basis functions instead of plane wave basis sets.

of implementation. Applications of the Car-Parrinello AIMD method are concentrated in the area of condensed phase molecular physics.

The use of plane waves has its advantages in that the computational effort for the required integrations becomes minute on a per function basis. On the other hand, an enormous number of plane waves is required (even when pseudo potentials are utilized) to approximate the rapid oscillations of the wave function in the core region. To accurately treat transition metals and first row elements, the number of plane waves required becomes inhibitive large. This is clearly a problem in our research on homogenous catalysis since such systems almost always contain transition metals and the substrates are often made up of first row elements. Plane wave basis sets also introduce another problem since periodic images are created automatically such that the simulation actually describes a periodic crystal where interaction between the periodic images exists. If non-periodic systems are to be simulated, the interaction between periodic images is undesirable. This interaction can be divided into two components, the wave function overlap and the electrostatic interaction. The former can be made negligible by making the cell size of the periodic systems sufficiently large that the wave functions of the images no longer overlap.(supercell approximation) For this criteria to be met, a vacuum region of approximately 5 Å between images is required. The second contribution, is long range in nature and the supercell approximation can not always be applied since the computational effort of the methodology increases with the cell size. For simulations of neutral non-polar systems, the supercell approximation is probably acceptable. However, if charged systems or systems with large dipole moments are simulated, the long range electrostatic interactions between periodic images will be substantial and will result in artificial effects.¹⁴² Again, this is problematic in our research since many transition metal catalysts are charged species.

4.4 Projector Augmented Wave (PAW) Car-Parrinello AIMD

The Projector Augmented Wave (PAW) Car-Parrinello AIMD program developed by Peter Blöchl overcomes the aforementioned problems such that AIMD simulations of transition metal complexes has become practical. PAW utilizes a full all-electron wavefunction with the frozen core approximation which allows both accurate and efficient treatment of all elements including first row and transition metal elements. In the PAW method, the plane waves are augmented with atomic based functions near the nuclei such that the rapidly oscillating nodal structure of the valence orbitals near the nuclei are properly represented. One can think of it as smoothly stitching in an atomic-

like function into the plane waves such that the plane waves describe regions where the orbitals are smooth, allowing for rapid convergence of the plane waves. The plane wave expressions of PAW and those of the pseudopotential method are similar enough that the numerical techniques for the most computationally demanding operations are related and equally efficient. Therefore, PAW combines the computational advantages of using plane waves with the accuracy of all-electron schemes. The details of the implementation are elaborately described in the papers of Blöchl.^{41,142,143} To deal with charged systems, PAW has a charge isolation scheme to eliminate the spurious electrostatic interactions between periodic images. The charge isolation scheme involves fitting atomic point charges such that the electrostatic potential outside the molecule is reproduced (ESP fit). The ESP charges are then used to determine the electrostatic interaction between periodic images via Ewald sums. The spurious interactions between images is then subtracted. These features of the PAW AIMD package make it ideal to study transition metal catalysts at the *ab initio* molecular dynamics level.

4.5 Reaction Free Energy Barriers with AIMD

Reaction free energy barriers are routinely calculated from conventional static electronic structure calculations. Here, the excess free energy of the reactants and transition state can be determined by constructing a partition function from a frequency calculation and using a harmonic (normal mode) approximation. In most cases where the interactions are strong, the approximation is good. However, for processes where weak intermolecular forces dominate, the harmonic or quasi-harmonic approximation breaks down.³⁴ Alternatively, *ab initio* molecular dynamics simulations can be utilized to determine reaction free energy barriers. An MD simulation samples the available configuration space of the system as to produce a Boltzmann ensemble from which a partition function can be constructed and used to determine the free energy. However, finite MD simulations can only sample a restricted part of the total configuration space, namely the low energy region. Since estimates of the absolute free energy of a system requires a global sampling of the configuration space, only relative free energies can be calculated.

A number of special methodologies have been developed to calculate relative free energies. Since we are interested in reaction free energy barriers, the method we use in our research is derived from the method of thermodynamic integration.^{144,145} Assuming we are sampling a canonical NVT ensemble the free energy difference, ΔA , between an initial state with $\lambda=0$ and a final state with $\lambda=1$, is given by Equation 4-6.

$$\Delta A_{(0 \rightarrow 1)} = \int_0^1 \frac{\partial A(\lambda)}{\partial \lambda} d\lambda \quad (4-6)$$

Here the continuous parameter λ is such that the potential $E(\lambda)$ passes smoothly from initial to final states as λ is varied from 0 to 1. Since the free energy function can be expanded in terms of the partition function:

$$A(\lambda) = -kT \ln \left[\int \cdots \int e^{-\frac{E(X^N, \lambda)}{kT}} dX^N \right] \quad (4-7)$$

the relative free energy ΔA can be rewritten as:

$$\Delta A_{(0 \rightarrow 1)} = \int_0^1 \left(\int \cdots \int \frac{\partial E(X^N, \lambda)}{\partial \lambda} dX^N \right)_{\lambda} d\lambda \quad (4-8)$$

or

$$\Delta A_{(0 \rightarrow 1)} = \int_0^1 \left\langle \frac{\partial E(X^N, \lambda)}{\partial \lambda} \right\rangle_{\lambda} d\lambda \quad (4-9)$$

where the subscript λ represents an ensemble average at fixed λ . Since the free energy is a state function λ can represent any pathway, even non-physical pathways. However, if we choose λ to be a reaction coordinate as to represent a physical reaction path, this provides us with a means of determining an upper bound for a reaction free energy barrier by means of thermodynamic integration. The choice in reaction coordinate is important since a poorly chosen reaction coordinate will result in larger sampling errors and potentially significant over estimate of the barrier (with finite simulation times). The more the reaction coordinate resembles the intrinsic reaction coordinate (IRC) the potentially better the estimate. The reaction coordinate can be sampled with discrete values of λ on the interval from 0 to 1 or carried out in a continuous manner in what is termed a "slow growth" simulation¹⁴⁶ by

$$\Delta A = \sum_{i=1}^{N_{\text{steps}}} \langle F_{\lambda} \rangle_i \Delta \lambda_i \quad (4-10)$$

where F_{λ} is the force on the constraint and i indexes the step number. Here the free energy difference becomes the integrated force on the reaction coordinate and can be thought of as the work necessary to change the system from the initial to final state.¹⁴⁴

The discrete sampling resembles a linear transit calculation such that a series of simulations is set up corresponding to successive values of the reaction coordinate from the initial to final state. For each sample point, the dynamics must be run long enough to achieve an adequate ensemble average force on the fixed reaction coordinate. In a slow growth simulation¹⁴⁶ the reaction coordinate is continuously varied throughout the dynamics from the initial to the final state. Thus, in each time step the reaction coordinate is incrementally changed from that in the previous time step. Formally speaking the system is never properly equilibrated unless the change in the RC is infinitesimally small (reversible change). However, the smaller the rate of change the better the approximation. Since the RC is changed at each time step, the force on the reaction coordinate is biased depending on the direction in which the RC is varied. Therefore a forward and reverse scan of the RC is likely to give different results as depicted in Figure 4.1. This hysteresis as it is called is a direct consequence of the imperfect equilibration. Thus it is generally a good idea to perform both forward and reverse scans to reduce this error and to determine whether the rate of change of the reaction coordinate is appropriate. In other words, a slow growth simulation with virtually no hysteresis has its RC changed adequately slow, whereas a simulation with large hysteresis has its RC sampled too quickly. The advantage of the slow growth simulation is that the dynamics is not disrupted when the reaction coordinate is changed and hence the system only has to be thermally equilibrated once. On the other hand the method has the disadvantage that both the forward and reverse scans should be performed.

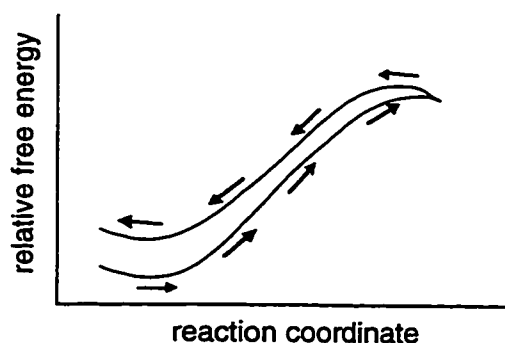


Figure 4.1. Schematic representation of the hysteresis in a slow growth free energy plot. The arrows designate the direction of the scan in terms of the reaction coordinate.

It should be noted that although the forces at each time step are determined from a full quantum mechanical electronic structure calculation, the dynamics itself is still classical. Therefore, quantum dynamical effects such as tunneling are not included in the

estimates of the reaction free energy barriers. Since the classical vibrational energy levels are continuous, $H_{\text{vib}} = \Sigma RT/2$ for all states, the zero point energy correction and ΔE_{vib} are also not included in the free energy barriers derived from the AIMD simulation.

4.6 Thermostating and Mass Rescaling

Thermostating. When the nuclei of a molecular simulation follow Newton's equations of motion, the total energy of the system is conserved. Furthermore, when the volume is held constant (cell size fixed) then the simulation will generate a microcanonical (NVE) ensemble. When studying chemical reactions, this type of dynamics may be undesirable because the excess heat that is dissipated or absorbed during a reaction could alter the temperature of the system to unwanted values. For this reason the temperature of a molecular dynamics simulation is often controlled, or thermostated, such that a canonical or NVT ensemble is generated. A common thermostating procedure is to coupling the molecular system to a heatbath through the method of Nosé¹⁴⁷. In this method,[†] an extra degree of freedom corresponding to the heatbath is added to the existing degrees of freedom of the molecular system. A kinetic energy and a potential energy term representing the heatbath are added to the Hamiltonian which allows energy to flow dynamically back and forth between the system and the heatbath. The Nosé thermostat effects the nuclear motion via a velocity dependent friction term in the equations of motion as expressed in equation 4-12.

$$m_i \ddot{x}_i = F_i - m_i \dot{x}_i \dot{\zeta} \quad (4-12)$$

The friction term is governed by the variable ζ which obeys its own equation of motion as given by equation 4-13.

$$Q \ddot{\zeta} = 2 \left[\sum_i \frac{1}{2} m_i \dot{x}_i^2 - \frac{1}{2} g k_B T \right] \quad (4-13)$$

In this way, the kinetic energy of the nuclei fluctuates about the mean value $\frac{1}{2} g k_B T$, where g is the number of degrees of freedom of the nuclear system, k_B is the Boltzmann constant and T is the desired physical temperature of the simulation. Q in equation 4-13 is an inertial parameter which controls the time scale of the thermal fluctuations. It should be noted that a simulation that is Nosé thermostated also conserves energy if the thermostat potential, $g k_B T \zeta$, and kinetic energy, $\frac{1}{2} Q \dot{\zeta}^2$, are added to the total energy.

[†] The method was subsequently reformulated by Hoover¹⁴⁸ and so this technique is often referred to as a Nosé-Hoover thermostat.

It has recently been shown by Blöchl and Parrinello¹⁴⁹ that the Nosé thermostating method for maintaining constant temperature molecular dynamics can be extended to the fictitious kinetic energy of the wave function in the Car-Parrinello methodology. In this context the thermostat acts to prevent the electronic wave function from slowly drifting away from the Born-Oppenheimer potential surface. The thermostating of the wave function in this way allows stable Car-Parrinello molecular dynamics to be performed for long periods of time without the need of periodically quenching the wave function to the Born-Oppenheimer potential surface.

Equilibration. In order to properly sample the canonical ensemble, the system must be thermally equilibrated. Thermal equilibration is often done by instantly exciting the system to the desired temperature with a random excitation vector. This is followed by thermostated dynamics for at least a few picoseconds thereby ensuring that all vibrational modes are excited to an equal extent. There are two problems with this approach in the Car-Parrinello scheme. First, an immediate pulse of kinetic energy in order to excite the nuclei to the desired temperature is likely to dislodge the wave function from the Born-Oppenheimer surface. Second, long periods of equilibration are expensive with *ab initio* molecular dynamics. For these reasons we take a modified approach to equilibration. First, the nuclei are excited by a series of slowly growing pulses. Each of the excitation vectors is chosen to be orthogonal to the already excited modes, thereby ensuring an evenly distributed thermal excitation. This is followed by a short period of thermostated dynamics. We have found this approach more efficiently achieves a thermally equilibrated system than the conventional method.

4.7 Mass Rescaling

Since the configurational averages in classical molecular dynamics do not depend on the masses of the nuclei,¹⁵⁰ a common technique to increase the sampling rate involves replacing the true masses with more convenient ones. Since nuclear velocities scale with $m^{-1/2}$, smaller masses move faster and therefore potentially sample configuration space faster. As a result, the masses of the heavy atoms can be scaled down in order to increase sampling. For example, we commonly rescale the masses of C, N and O in our simulations from 12, 14 and 16 amu, respectively, to 2 amu. There is a limit to the mass reduction, because at some point the nuclei move so fast that the simulation time step has to be reduced. At this point there is no gain in reducing the masses further because if the time step has to be shortened, we have to perform more time steps to

achieve the same amount of sampling. It is for this reason, we generally scale our hydrogen masses up from 1 amu to 1.5 amu or higher in order to use a larger time step.

4.8. *Ab Initio* Molecular Dynamics Study of Olefin Polymerization Chemistry.

Recently, we have applied PAW to examine the chemistry of a Ti(IV) metallocene olefin polymerization catalyst.^{121,133-135} In studying this system we have found that *ab initio* molecular dynamics can be used to (i) determine the time scales of processes, (ii) efficiently explore complicated free energy surfaces in a synergistic fashion with traditional static methods, (iii) find new reactions, and (iv) to provide a general way of determining finite temperature free energy barriers.

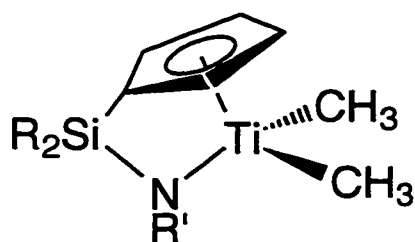


Figure 4.2. Constrained Geometry Catalyst (CGC).

Single-site catalyzed olefin polymerization technology is expected to revolutionize the immense polyolefin industry. Amongst the first single-site catalysts to have been commercialized¹⁵¹ are the mono Cp "constrained-geometry" catalysts of the form $(\text{CpSiR}'_2\text{NR})\text{Ti-X}_2$ where $\text{X}=\text{CH}_3, \text{Cl}$ (e.g. Figure 4.2). For most group 4 metallocenes,

the catalytic resting state is believed to be a cationic metal alkyl complex, e.g. $(\text{CpSiR}'_2\text{NR}')\text{Ti-R}^+$, where R represents the growing alkyl chain. Commencing from the resting state Ti-alkyl complex, Figure 4.3 depicts the assumed and well-established Cossée-Arlman mechanism for the chain growth. Addition of olefin to the resting state forms an olefin π -complex. From the π -complex a four centered transition state is formed whereby the olefin inserts into the Ti-C_α bond. The initial or kinetic product is a γ -agostic Ti-alkyl complex. In "static" studies⁵³ of similar bis-Cp zirconocene catalysts, the initial γ -agostic complex is believed to rapidly rearrange to the more favorable β -agostic resting state complex. Olefin uptake and insertion therefore likely commences from the β -agostic complex as opposed to the γ -agostic complex. Therefore, to study the insertion process, it is important to know the structure of the resting state.

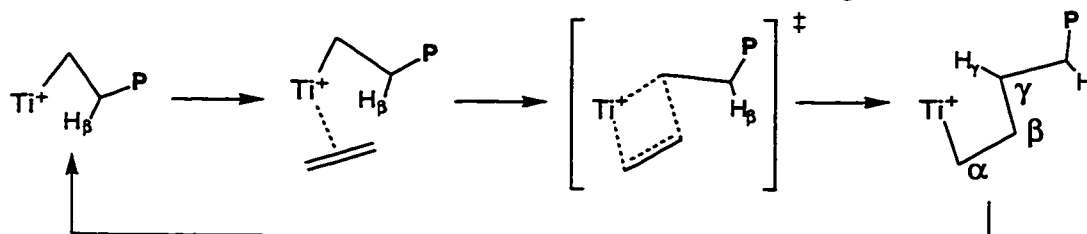


Figure 4.3. Cossée-Arlman^{152,153} mechanism for chain propagation in the Constrained Geometry single-site olefin polymerization catalyst.

Computational Details. The reported "static" density functional calculations were all carried out by the ADF program system version 1.1.3.^{36,39,96,97} For the description of the electronic configuration (3s, 3p, 3d, 4s, and 4p) of titanium we used an uncontracted triple- ζ STO basis set.^{114,115} For carbon (2s, 2p) and hydrogen (1s) a double- ζ STO basis, augmented with a single 3d or 2p polarization function respectively, was applied. No polarization functions were employed for carbon and hydrogen atoms on the Cp ring. The $1s^2 2s^2 2p^6 3s^2$ configuration on Ti, the $1s^2 2s^2 2p^2$ configuration on Si and the $1s^2$ shell on C and N were assigned to the core and treated with the frozen core approximation.³⁸ In order to fit the molecular density and to represent Coulomb and exchange potentials accurately a set of auxiliary s, p, d, f, and g STO functions,¹¹⁶ centered on all nuclei was used in every SCF cycle. Energy differences were calculated by including the local exchange-correlation potential by Vosko¹¹⁷ *et al.* with Becke's¹⁰³ nonlocal exchange corrections and Perdew's^{104,105} nonlocal correlation correction. The spin restricted formalism was used for all calculations. Geometries were optimized *without* including nonlocal corrections. In a previous publication, we have shown that in systems such as the one under investigation here the energetics derived by such a procedure deviate by less than 2.4 kcal/mol from energetics obtained by nonlocal geometry optimization.⁵³ All saddle point determinations were initialized by a linear transit search from reactant to product along an assumed reaction coordinate where all degrees of freedom were optimized except for the reaction coordinate which was frozen for each step. Transition states were then fully optimized and validated by a frequency calculation where the backbone (Cp, silane and amido groups) of the constrained geometry catalyst was frozen. This approach has been justified in reference 121.

The details of the Car-Parrinello PAW⁴¹ are as follows. The wave function was expanded in plane waves up to an energy cutoff of 30 Ry. We employed the frozen core approximation for the [Ar] core on Ti, the [Ne] core for Si, and the [He] core of the first row elements. Periodic boundary conditions were used, with a unit cell spanned by the lattice vectors ([0.0 8.5 8.5] [8.5 0.0 8.5] [8.5 8.5 0.0]) (\AA units). All simulations were performed using the local density approximation in the parametrization of Perdew and Zunger,¹¹⁸ with gradient corrections due to Becke¹⁰³ and Perdew.^{104,105} Electrostatic interactions between neighboring unit cells were minimized by the charge isolation scheme of Blöchl¹⁴² as discussed in Section 4.4. A temperature of 300 K was maintained for all simulations by a Nosé thermostat.^{147,148} The fictitious kinetic energy of the electrons was contained near the Born-Oppenheimer surface by a Nosé thermostat.¹⁴⁹ In order to span large portions of configuration space in a minimum of time, the true masses

of the nuclei were rescaled to 5.0 (Ti), 2.0 (Si, N and C) and 1.5 (H) atomic mass units. Together with an integration time step of 7 a.u. (≈ 0.17 fs), this choice ensures good energy conservation during the dynamics simulation without computational overhead due to heavy atomic nuclei. Since the nuclear velocities scale with $m^{-1/2}$ the sampling is sped up by a factor of 1.5-2. Therefore, all reported simulation times are effectively increased by a factor of 1.5-2, so that a 4 ps simulation yields a sampling accuracy corresponding to a 6 ps simulation. The "slow-growth" technique as outlined in section 4.5 was utilized to investigate high-lying transition states. The total scan time chosen was about 35000 time steps (≈ 6 ps real time) for the slow-growth simulations. The reaction coordinates used are described for each individual simulation.

4.9 Studying Fluxionality and Time Scales with AIMD.

With the intent of studying the nature and fluxionality of the resting state we have performed an AIMD simulation where R was modeled by a propyl chain.¹²¹ (Note that the resting state in the case of the constrained geometry catalyst is the metal alkyl complex and not the π -complex as with the Brookhart catalyst.) A propyl group was used as a model for the growing chain in order to investigate the possible rearrangement of the assumed γ -agostic kinetic product of the insertion. Initiated from a γ -agostic Ti-propyl complex, a 4 ps simulation at 300 K was performed. In order to enhance the sampling, the masses were rescaled to 5.0(Ti), 2.0 (Si, N and C), and 1.5 (H) atomic mass units. Therefore, the time scales are fictitious and the 4 ps simulation is approximately equivalent to a 7 ps simulation.

The MD simulation revealed that there was rapid inter conversion between β - and γ -agostic Ti-alkyl complexes. The right hand side of Figure 4.4 shows two snapshot structures from the simulation representative of the γ -agostic complex and the β -agostic complex. The two graphs in Figure 4.4 trace structural quantities during the dynamics important in characterizing the resting state. Graph (a) follows the Ti-H $_{\gamma}$ distance while (b) follows the Ti-H $_{\beta}$ distances, with the shaded regions indicating the formation of γ - and β - agostic bonds, respectively. The trajectory reveals that the propyl chain rapidly inter converts between the γ - and β -agostic alkyl complexes, spending roughly equal time in each of the conformations. Although the time scales in the AIMD simulation are fictitious because of the mass rescaling, the simulation demonstrates that the fluctuation of the resting state alkyl complex is extremely rapid. The graphs in Figure 4.4 also show that there is always an agostic interaction present. When the γ -agostic bond is lost, it is immediately replaced by another γ -agostic bond or a β -agostic bond. Thus, the strong

preference for the formation of agostic interactions demonstrates the stabilization accrued from these interactions. Another excellent demonstration of the PAW AIMD method to study fluxionality and time scales is that of Margl and coworkers¹³² who have examined the dynamics of beryllocene.

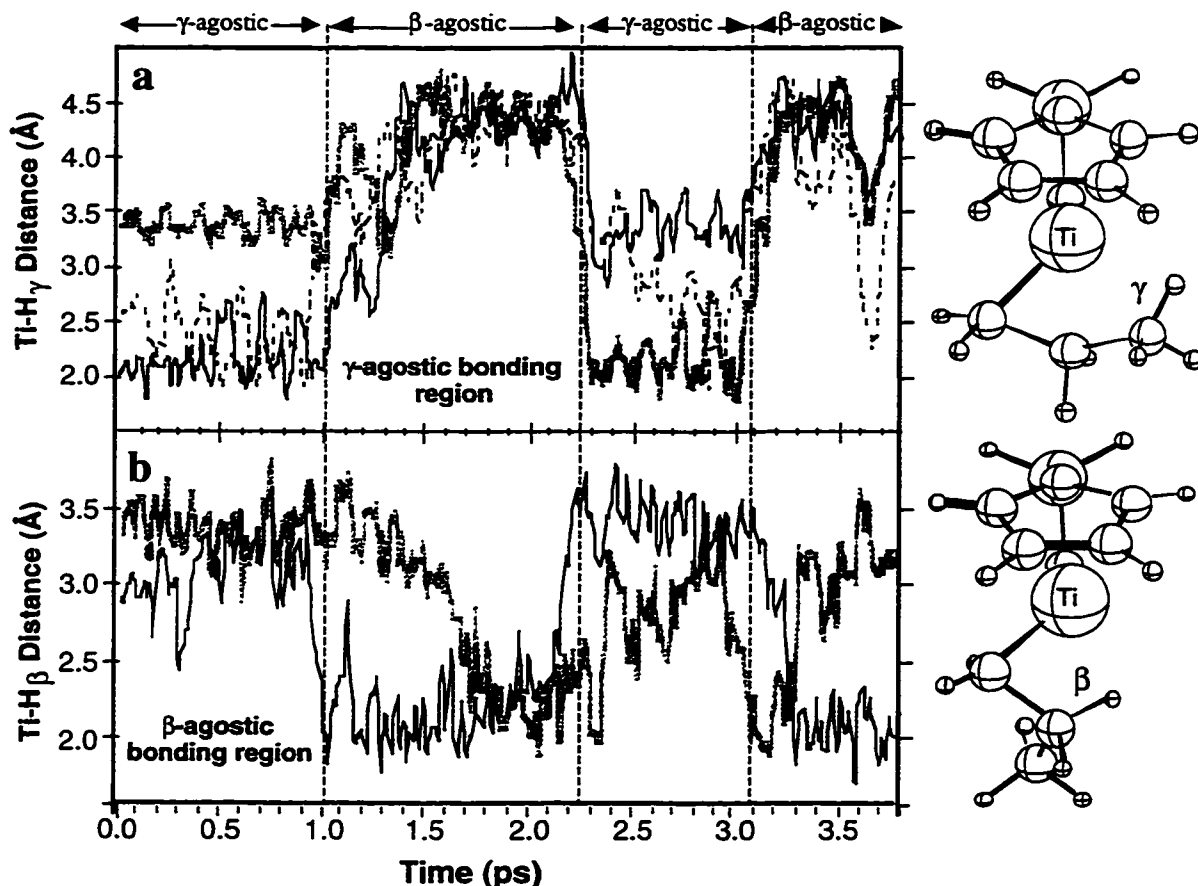


Figure 4.4. Selected structural quantities as a function of the simulation time for the AIMD simulation of the Ti-propyl model of the resting state. Shaded regions in graphs a and b indicate agostic bonding. Vertical lines separate where the Ti-propyl cation can be characterized as γ - and β -agostic complexes. Shown to the right of the graphs are two snap shot structures from the simulation characteristic of the γ - and β -agostic complexes.

4.10 Using AIMD to Chart Reaction Paths on Flat Potential Surfaces.

We have used AIMD to chart reaction pathways in systems with high configurational variability. Such "flat" potential energy surfaces are often difficult and tedious to explore with conventional static methods. By using the slow growth technique, AIMD can be utilized to initially scan the optimal reaction pathway. As demonstrated by the simulation of the resting state in Figure 4.4, the potential energy surface associated with the constrained geometry system exhibits these problematic traits. In studying the olefin insertion process in the constrained geometry catalyst, initial static calculations

revealed that there were at least four β -agostic π -complexes that were all within a small 2.4 kcal/mol range. Rather than explore the insertion process commencing from each of the four π -complexes, the insertion process was mapped out using the slow growth method whereby an ethene molecule was gradually inserted into the Ti-C bond of the Ti-propyl⁺ resting state. In this simulation the distance between the C _{α} and the midpoint of the C-C bond of the ethene was used as the slow growth reaction coordinate. A rapid 20000 time step simulation was performed where the RC was varied from 5.1 Å, a distance in which the incoming olefin is too far to form a strong π -bond, to a value of 1.9 Å. Again the simulation was thermostated at 300 K and the masses were rescaled as in the previous resting state simulation.

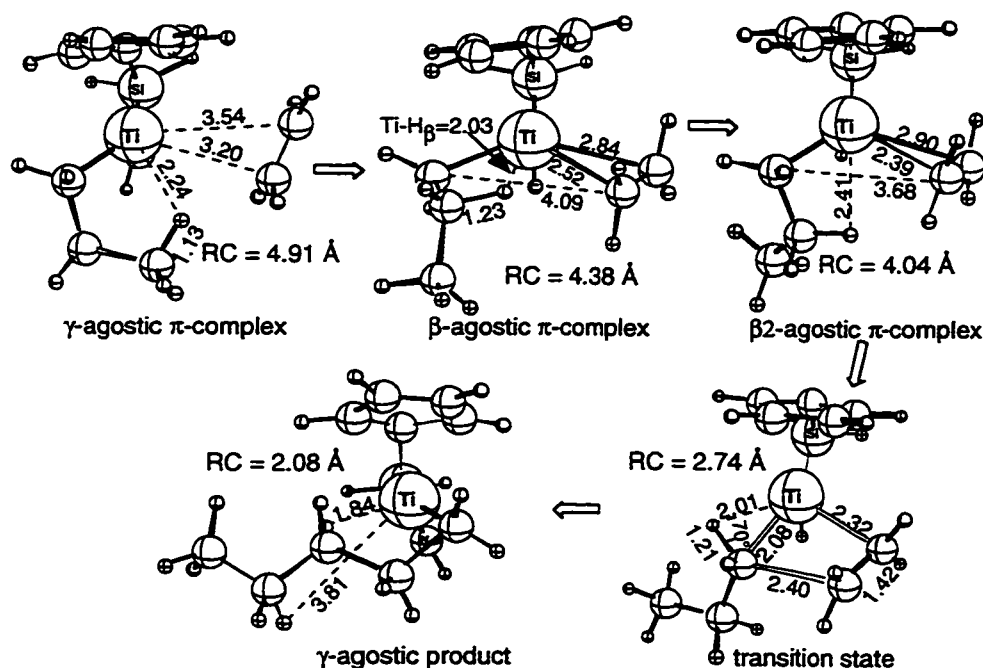


Figure 4.5. Selected snapshot structures from the AIMD slow growth simulation of the olefin insertion in the constrained geometry catalyst. The snapshots provide qualitative picture of the insertion mechanism. The reaction coordinate (RC) used in the simulation was the distance between the α carbon of the Ti-alkyl moiety and the midpoint of olefin double bond.

Figure 4.5 depicts several snapshots of the simulation which provides a qualitative picture of the insertion process. More detailed monitoring of the structural and energetic quantities can be found in reference 121 and are not shown here. Since the simulation was initiated from the γ -agostic alkyl complex, a weak γ -agostic π -olefin complex is formed in the early stages of the simulation. The first snap shot structure in Figure 4.5 taken at a reaction coordinate value of 4.91 Å is indicative of the early complexation. As

the olefin is drawn closer, the γ -agostic π -complex gives way to an "in-plane" β -agostic π -complex where the olefin carbon atoms and the β -hydrogen are coplanar. The second snapshot structure at $RC=4.38$ Å is representative of this "in-plane" β -agostic complex. As the RC is further contracted, β -methylene group rotates out of the coordination plane in order to allow for the α -carbon and the olefin carbon bond to form. Such a "out-of-plane" β -agostic π -complex is shown in Figure 4.5 with a $RC=4.04$ Å. From here, the transition state and the γ -agostic product are formed at approximately $RC=2.74$ Å and $RC=2.08$ Å, respectively.

Using the AIMD simulation as a guideline, stationary points along the potential surface were mapped with traditional static methods. (Eventually, the insertion process commencing from all four initial β -agostic π -complexes was examined.) The lowest energy insertion pathway was indeed found to follow essentially the same pathway as resolved from the MD simulation. Stationary points corresponding to each of the structures in Figure 4.5 along the insertion pathway were located which provided an accurate energetic picture of the potential surface. This application demonstrates that the AIMD method can be utilized effectively in a cooperative fashion with the traditional static methods.

4.11 New Reaction Pathways with AIMD.

In studying the β -hydride elimination process in the constrained geometry catalyst with a slow growth simulation, the PAW AIMD simulation generated an unexpected but more energetically favorable reaction which the static calculations did not detect.¹³⁵ Further calculations revealed that the unexpected product was indeed the most favourable unimolecular chain termination product.

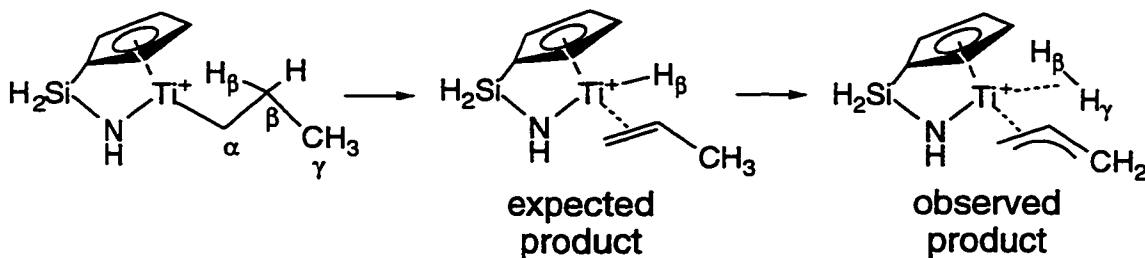


Figure 4.6. Unimolecular chain termination initiated from the β -agostic alkyl complex was expected to give rise to a olefin-hydride complex. Instead, as shown by the molecular dynamics simulation, the olefin-hydride complex was only briefly formed before giving rise to a more stable allyl dihydrogen complex.

The product turned out to be the most favorable unimolecular chain termination process which was later observed experimentally. Figure 4.6 shows the β -hydride elimination process that was to be examined and the allyl dihydrogen formation process that was actually observed.

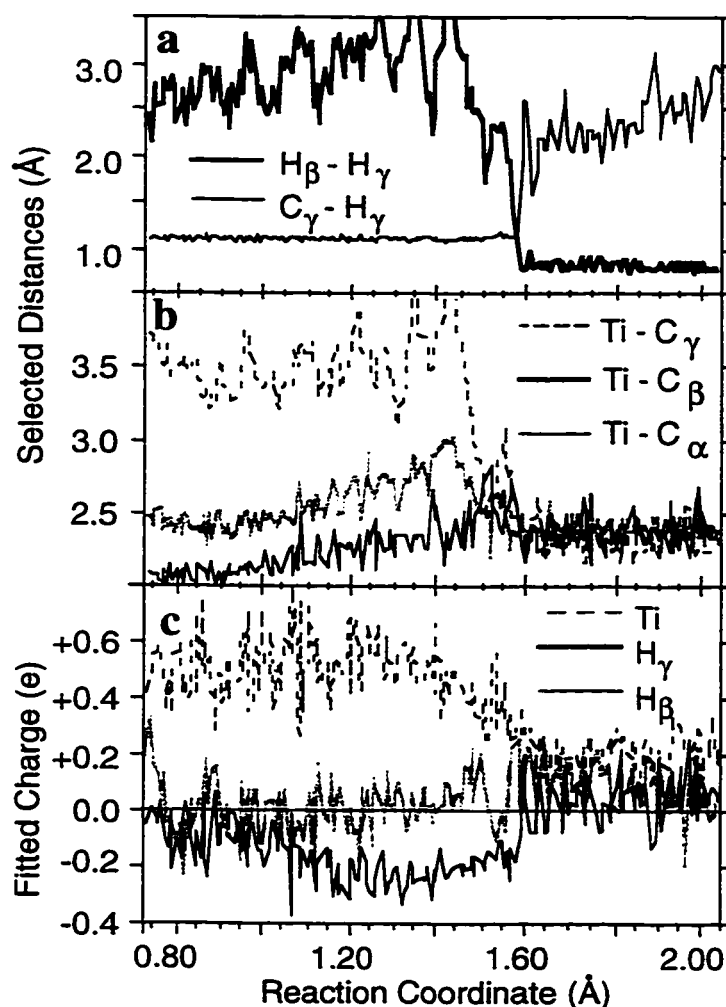


Figure 4.7. Selected structural and electronic quantities as a function of the reaction coordinate for the slow growth simulation of the uni-molecular chain termination process. The dramatic change in the plotted quantities at a RC value of 1.6 Å marks the formation of the unexpected allyl-dihydrogen complex.

A slow growth simulation designed to determine the reaction free energy at 300 K of the β -hydride elimination process to form a olefin-hydride complex was performed.¹³⁵ In this simulation the distance from C_{β} to the $H_{\beta}-H_{\beta}$ midpoint was used as the reaction coordinate. Commencing from the β -agostic alkyl complex the $C_{\beta}-H_{\beta}$ distance expanded

during the simulation. Plotted in Figure 4.7 are various structural and electronic quantities which best characterizes the reaction observed. Up to a reaction coordinate value of approximately 1.6 Å, the expected β -elimination process progresses as anticipated. However, at a reaction coordinate value of roughly 1.6 Å all of the quantities traced in Figure 4.7 change dramatically, marking the rapid formation of the allyl-dihydrogen complex from the transient olefin hydride complex. Graph (a) shows the rapid formation of the dihydrogen bond with the simultaneous breaking of the $C_\gamma-H_\gamma$ bond. The Ti-C distances in graph (b) illustrates the change in the bonding description between the propyl fragment and the Ti center. With two short and one long Ti-C distances a β -agostic alkyl interaction dominates the initial part of the simulation. When the allyl complex forms, all three Ti-C bond distances converge suggesting the η^3 bonding pattern of the allyl. Plot (c) follows the net ESP fitted charges on the Ti, H_β and H_γ atoms, again revealing an abrupt change at approximately $RC=1.6$ Å. The sudden deionization of the Ti center suggests that the formation of the allyl moiety stabilizes the complex through electron donation to the Ti center.

Static calculations on the olefin-hydride and the allyl-dihydrogen complex reveal that the allyl-dihydrogen complex is in fact 5.2 kcal/mol more stable than the olefin-hydride suggesting that the unimolecular β -elimination process does not form an olefin hydride, but in fact produces dihydrogen and an Ti-allyl complex. Spurious formation of hydrogen gas has been observed in slurry phase metallocene catalyzed olefin polymerization experiments¹⁵⁴ providing experimental evidence of the allyl formation. Based on our predictions, Resconi and co-workers have recently used the formation of an allyl intermediate to account for a number of side products seen in isotactic polypropylene polymerization systems catalyzed by metallocene catalysts.

It is important to state that the actual thermodynamic product of β -hydrogen elimination - namely the allyl dihydrogen complex - was first located by AIMD simulations and would not have been found otherwise by us. This shows the uniquely powerful predictive ability of the AIMD method, which searches configuration space more globally instead of locally and thus has a greater chance of hitting unexpected, but important, reaction paths and products.

4.12 Reaction Free Energy Barriers with the Slow Growth AIMD Simulations.

The previous examples nicely demonstrate that the slow growth technique can be used to chart "difficult" potential energy surfaces for static calculations. As previously outlined in Section 4.5, the slow growth method can also be used to estimate free energy

barriers by means of thermodynamic integration. We have applied the slow growth technique to estimate the free energy barriers at 300 K of four chain termination processes associated with the constrained geometry catalyst. Illustrated in Figure 4.8 are the four processes: a) hydrogen transfer to the monomer, b) β -hydrogen elimination, c) olefinic C-H activation and d) is an alkyl C-H activation. Since this method for the determination of reaction free energy barriers is somewhat novel, free energy barriers of the same four processes were then calculated using more established "static" methods and compared.

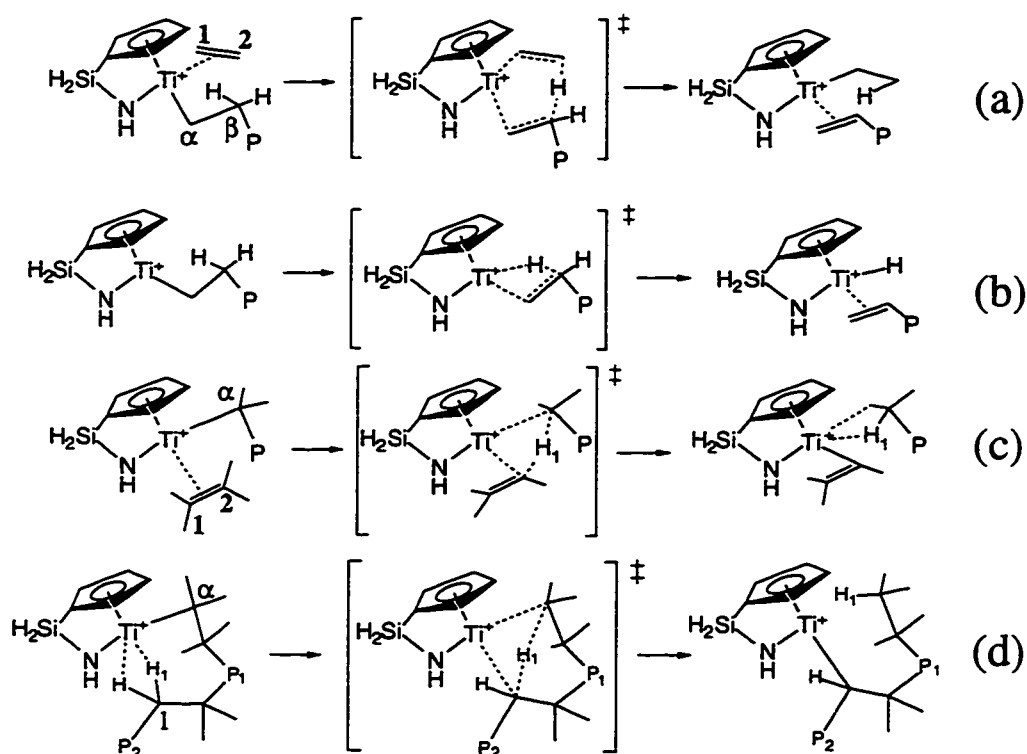


Figure 4.8. Four chain termination processes studied with the slow growth AIMD method in order to estimate reaction free energy barriers. a) hydrogen transfer to the monomer, b) β -hydrogen elimination, c) olefinic C-H activation and d) is a alkyl C-H activation.

For processes (a), (c) and (d) which involve the transfer of a hydrogen from one carbon to another a special mid-plane reaction coordinate was developed. The "mid-plane" reaction coordinate is depicted in Figure 4.9. If C_1 is the carbon that the hydrogen atom is initially bound to and C_2 is the carbon atom that the hydrogen is to be transferred to, then the midplane plane reaction coordinate is defined as the ratio r/R , where R is the length of the vector between C_1 and C_2 and r is the length of the projection of the C_1 -H vector onto R . The reaction coordinate constrains the H atom to lie on the plane

perpendicular to and passing through the endpoint of the vector \mathbf{r} . When the midplane RC is small, the hydrogen is still bound to C_1 while when it is equal to 0.5 the hydrogen lies halfway between the two carbons. The midplane constraint was used because it is presumed to be the most reversible reaction coordinate for the transfer process and therefore the least susceptible to large hysteresis. For process (b) the hydrogen transfer to the metal, the distance from C_β to the center of mass of the two H_β atoms was utilized as the slow growth reaction coordinate.

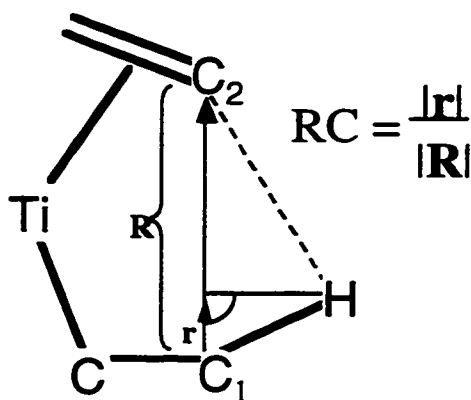


Figure 4.9. Definition of the midplane reaction coordinate.

In each of the simulations the system was thermostated at 300 K and the masses were rescaled as in previous simulations of the Ti constrained geometry catalyst. About 35000 time steps were performed for each simulation or approximately 6 ps of real time (9-12 ps when mass rescaling is considered). Both forward and reverse scans were performed from the reactant to the approximate transition state. In the static calculations, reactants and transition states were fully optimized without constraints. Frequency calculations were performed on each of the stationary points and the calculation of the free energies followed standard text book procedures.¹⁰⁶ Full details of the calculations can be found in reference 133.

Table 4.1. Comparison of the "static" and "dynamic" Reaction Free Energy Barriers.

Process	Free Energy Barrier ΔF^\ddagger (kcal/mol) at 300 K		
	Car-Parrinello simulation ^{a,b}	static ^c	static with quantum effects ^d
a) hydrogen transfer to monomer ^e	10.3 \pm 1.9	10.2	9.5
b) hydrogen transfer to metal ^f	13.6 \pm 0.7	15.6	12.8
c) olefin σ -bond metathesis ^e	20.7 \pm 1.2	22.3	21.8
d) alkyl σ -bond metathesis ^e	16.7 \pm 0.7	19.3	17.2

^aDoes not include any quantum dynamical corrections such as zero point energy correction. Additionally, since the classical vibrational energy levels are continuous, $H_{\text{vib}} = \Sigma RT/2$ and $\Delta H_{\text{vib}} = 0$ for the MD simulations. ^bReported values are the average of the forward and reverse scans. The reported error bars are half the difference between the forward and reverse scans. ^cDoes not include zero-point energy correction and ΔH_{vib} to more correctly compare with Car-Parrinello MD free energies ($\Delta F = \Delta E_{\text{el}} - T\Delta S_{\text{total}}$). ^dIncludes zero-point energy correction and ΔH_{vib} ($\Delta F = \Delta E_{\text{el}} + \Delta H_{\text{vib}} + \Delta ZPE - T\Delta S_{\text{total}}$). Does not include quantum tunneling. ^e An ethyl group is used to model growing chain in the static simulation whereas a propyl group is used to model the growing chain in the molecular dynamics simulation. ^fA propyl group is used to model the growing chain in both static and dynamic simulations.

Table 4.1 compares the free energy barriers of the static calculations to those obtained by the Car-Parrinello simulations. It is important to note that although the Car-Parrinello method involves a quantum mechanical calculation to determine the electronic structure, the actual dynamics is purely classical in nature. Therefore, quantum dynamical effects such as the zero-point energy correction are not accounted for. As a result, in Table 4.1 there are two columns referring to the static calculations, one with all of the quantum dynamical effects eliminated for a more proper comparison and one with the quantum effects included. Although there are several important differences in the two simulations, the static and dynamic free energy barriers are in remarkable agreement with one another. The mean absolute deviation between dynamically and "statically" (i.e. from the partition function of a harmonic oscillator) derived ΔF^\ddagger values is 0.8 kcal/mol (signed mean: -0.07 kcal/mol), and 2.1 kcal/mol (signed mean: -1.6 kcal/mol) if one corrects for the terms not present in the molecular dynamics simulations.

These results clearly demonstrate that the molecular dynamics simulations both complement and further corroborate the results of the static calculations well. The Car-Parrinello molecular dynamics method provides a general method of calculating accurate free energy barriers that are in excellent agreement with established static methods. We

reiterate here that the Car-Parrinello simulations do not include any quantum dynamical effects. However, it is apparent from Table 4.1 that the *relative* vibrational enthalpies and zero-point energies are a minor factor in the reactions studied. Finally we point out that both static and dynamic methods do not account for quantum tunneling effects.

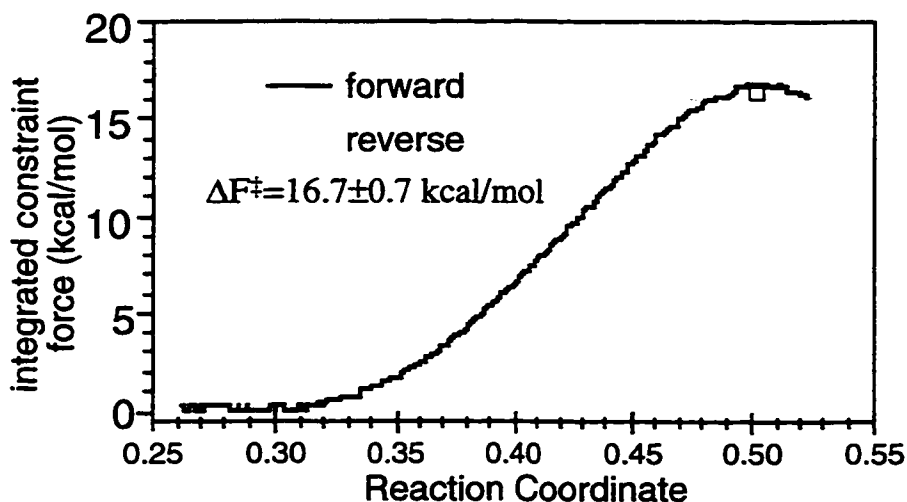


Figure 4.10. The integrated force on the reaction coordinate traced as a function of the mid plane reaction coordinate for the AIMD simulation the alkyl σ -bond metathesis chain termination reaction. The box on the forward scan marks the point in the simulation at which the snap shot structure shown in Figure 4.11 is taken from.

Plotted in Figure 4.10 is the free energy profile obtained from the forward and reverse slow growth simulation of the alkyl σ -bond metathesis chain termination reaction displayed in Figure 4.8d. For this process the hysteresis is small with the forward and reverse estimates of the reaction free energy barrier differing by only 1.4 kcal/mol. Furthermore, in both cases the transition state occurs at the reaction coordinate value of $RC=0.5$. The average slow growth value of 16.7 kcal/mol is in reasonable agreement with the static free energy barrier of 19.3 kcal/mol when all quantum effects, not taken into account in the AIMD simulation are factored out. When the quantum effects in the static estimate are included the free energy barrier of 17.1 kcal/mol is in better agreement with the slow growth result.

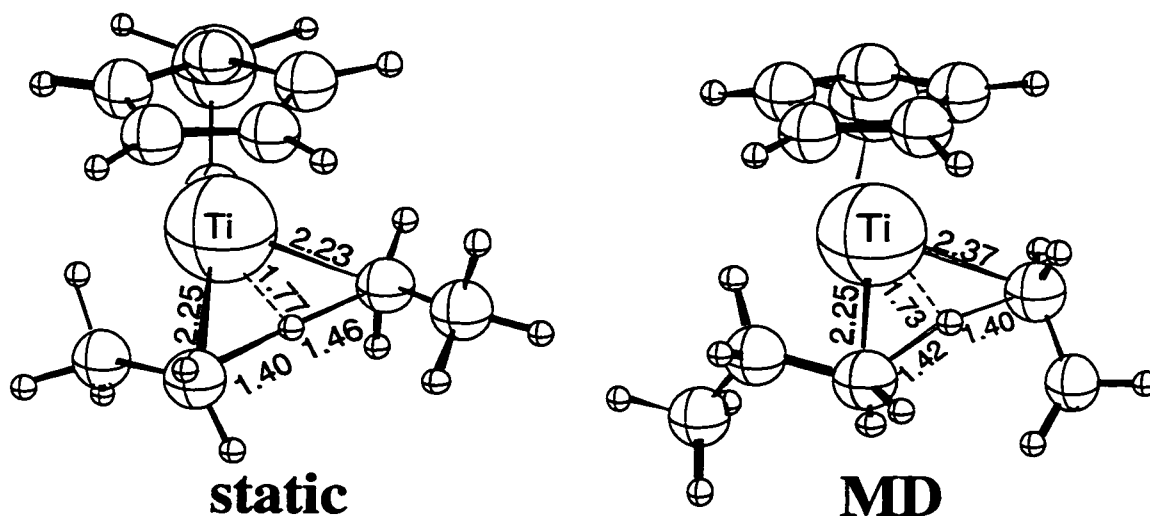


Figure 4.11. Comparison of the static and dynamic transition state structures for the alkyl σ -bond metathesis chain termination reaction. The static structure is a fully optimized transition state whereas the MD structure is simply a snap shot structure extracted from the forward scan of the slow growth simulation.

Shown in Figure 4.11 is the optimized transition state structure from the static calculation and a snapshot structure taken from the transition state region of the forward scan of the slow growth simulation. The similarity in the two structures is striking, further showing that the AIMD slow growth method for determining reaction barriers provides results in good agreement with more established static techniques.

4.13 Concluding Remarks

The *ab initio* molecular dynamics method shows great potential for becoming a standard computational chemistry tool particularly for exploring processes which have a high degree of configurational variability. Through a series of studies,^{121,133,135} we have applied the methodology to several transition metal based homogenous catalytic systems, clearly demonstrating the usefulness of the method.

Chapter 5

A Combined Car-Parrinello QM/MM Implementation For *Ab Initio* Molecular Dynamics Simulations of Extended Systems.

5.1 Introduction

There have been many approaches, such as linear scaling methods^{155,156} and sophisticated techniques for integrating the equations of motion,^{157,158} that have been introduced to increase the efficiency of Car-Parrinello¹³⁰ based *ab initio* molecular dynamics simulations to treat extended molecular systems. Taking a different route, we have implemented the combined quantum mechanics and molecular mechanics (QM/MM) method⁸ into the Car-Parrinello *ab initio* molecular dynamics framework. Our implementation includes a multiple-time step scheme¹⁵⁷ such that the molecular mechanics region can be sampled at a faster rate than the quantum mechanics region, thereby providing better ensemble averaging during the calculation of the free energy barriers. In this chapter the details of the implementation are provided with selected test applications to demonstrate the potential utility of the methods.

5.2 Combined QM/MM Car-Parrinello *Ab Initio* Molecular Dynamics

The combined QM/MM methodology has been implemented within the PAW *ab initio* molecular dynamics package of Blöchl⁴¹ by extending the Car-Parrinello Lagrangian first introduced in Eqn. 4-3 to include a molecular mechanics subsystem:

$$\begin{aligned} \mathcal{L} = & \frac{1}{2} \sum_i \mu_i \langle \dot{\phi}_i | \dot{\phi}_i \rangle + \frac{1}{2} \sum_I M_I \dot{R}_I^2 - E_{DFT}(|\phi\rangle, R) + \sum_{i,j} \Lambda_{ij} \langle \phi_i | \phi_j \rangle \\ & + \frac{1}{2} \sum_I^{MM\ atoms} M_{I,MM} \dot{R}_{I,MM}^2 - E_{MM}(R_{QM}, R_{MM}) \end{aligned} \quad (5-1)$$

The first three terms of equation 5-1 are equivalent to those in equation 4-3 whereas the last two terms in equation 5-1 refer to the kinetic energy of the MM nuclei and the potential energy derived from the MM force field. Equation 5-1 essentially describes the coupled equations of motion of three subsystems: the QM nuclei, the QM wave function and the MM nuclei. It was our intent to implement the combined QM/MM methodology within the Car-Parrinello PAW framework so as to allow for the QM/MM boundary to lie within the same molecular system. As with the ADF QM/MM implementation described in Chapter 2, we have adopted the general capping atom approach first introduced by Singh and Kollman to truncate the electronic system over covalent bonds that cross the QM/MM boundary. In this way, the first three terms of equation 5-1 refer to the kinetic

and potential energy of the "capped" QM model system. (The QM/MM coupling schemes introduced in Chapter 2 will be discussed in the next section.)

Thermostating. A separate Nosé thermostat for the molecular mechanics subsystem has been implemented. Since the MM and QM regions are strongly coupled, there will be energy flux between the two subsystems and their thermostats during a simulation. To prevent strong coupling between the thermostats themselves, the inertial parameters Q (Section 4.6) are chosen to maintain a large disparity in the time scales of the heatbath fluctuations in the QM and MM regions (approximately 5 times difference). A single Nosé thermostat for the whole QM/MM nuclear system was not implemented because of the complications that would arise with the QM/MM multiple time step methodology to be described later in this Chapter.

Equilibration. Again, the QM and MM regions are strongly coupled, the MM region cannot be instantly heated to a desired simulation temperature without abruptly dislocating the wave function of the QM region from the Born-Oppenheimer surface. For this reason, the slow warm-up procedure described in Section 4.6 has been implemented for the MM subsystem.

Periodicity. The periodicity of the plane basis sets method may be thought to inhibit the practical application of the QM/MM method within the Car-Parrinello framework. It is often assumed that the simulation cell of the Car-Parrinello simulation must be large enough to encapsulate the both the QM and MM regions. If this were true a larger MM region would then require a larger simulation cell and greater computational effort[◊] even though the QM model system may remain the same. However, this is not true and the size of the molecular mechanics region is inconsequential to the choice of QM cell size. Even when true electrostatic coupling between the QM and MM regions is evoked the size of the MM system does not affect the cell size of the QM model system (this will be demonstrated in Chapter 7). Furthermore, the molecular mechanics region can itself have periodic boundary conditions with a cell size and type that is independent of the cell size of the QM calculation. The addition of periodic boundary conditions in the MM region is necessary for QM/MM solvent simulations.

QM/MM Features. The molecular mechanics code has been completely written in FORTRAN90 and the core components of the code are shared with the QM/MM implementation within the ADF program(Chapter 2). Thus, all of the features of the ADF QM/MM implementation described in Table 2.2 are shared with the PAW QM/MM

[◊] Computational effort of the Car-Parrinello method with plane wave basis scales in part with the dimensions of the simulation cell.

implementation. Detailed explanation of the features and usage of the implementation are described in the PAW QM/MM user's manual.¹⁰⁰

5.3 Energy Conservation of IMOMM Molecular Dynamics

Consistent energies and gradients are required for performing proper energy conserving molecular dynamics simulations. Thus, of the three QM/MM coupling schemes introduced in Chapter 2, only the original method of Singh and Kollman⁸ and our adaptation of Morokuma's IMOMM scheme⁹⁸ are feasible for use within a molecular dynamics framework. Both of these coupling schemes have been implemented within the PAW-QM/MM program. To date, most if not all published combined QM/MM molecular dynamics simulations^{8,9,12,21,23} in which the QM/MM boundary crosses covalent bonds utilize the original QM/MM coupling scheme of Singh and Kollman. As a result, the suitability of the Singh and Kollman QM/MM coupling scheme for performing molecular dynamics has been amply demonstrated. In this section, we will verify that the adapted IMOMM coupling scheme described in Chapter 2 is also suitable for performing energy conserving combined QM/MM molecular dynamics.

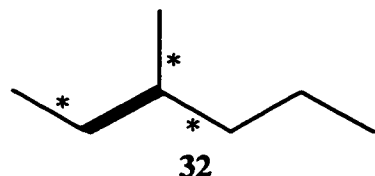


Figure 5.1 QM/MM partitioning of 3-methylhexane. Conventions as in Figure 2.3.

A 4000 time-step (~700 fs) combined QM/MM molecular dynamics simulation of solvated 3-methylhexane, **32**, has been performed with a time step of $\Delta t = 3.0$ au. Figure 5.1 illustrates the partitioning in **32** where the bold region represents the QM subsystem and the bonds labeled with asterisks denote the QM/MM link bonds which join the two regions. In this simulation the three link bonds are capped with hydrogen atoms such that the electronic structure calculation is performed on ethane. The system is solvated by 14 isobutane molecules in a 20 Å cubic cell for which periodic boundary conditions³¹ have been applied with a 10 Å non-bonded cutoff (Solvation and periodic boundary conditions will be described in more detail in Chapter 7). Jorgensen's OPLS-AA¹⁵⁹ molecular mechanics force field⁰ was used for both the solvent and the MM components of the solute. Non-bonded electrostatic interactions between the QM and MM regions were treated in the familiar molecular mechanics fashion. For each of the three link bonds, an α (as defined in equation 2-3) was assigned a value of 1.38. Masses of the capping atoms were rescaled to those of the corresponding MM-link atom. In other words, the capping hydrogen atoms were

⁰This molecular mechanics force field is based on Kollman's AMBER force field and the two force fields share the same functional forms.

assigned a mass of 12.0 amu. For the calculation of the QM model system, the wave function was expanded in plane waves up to an energy cutoff of 30 Ry within a periodic cell spanned by the lattice vectors [0.0 6.5 6.5], [6.5 0.0 6.5], [6.5 6.5 0.0] (in Å). The local density approximation according to the parameterization of Perdew and Zunger¹¹⁸ with gradient corrections due to Becke¹⁰³ and Perdew^{104,105} was utilized. The trajectory presented was pre-equilibrated and pre-thermostated¹⁴⁷ at 300 K for 2000 time-steps. Although the thermostat was turned off, an average temperature of 300 K was still retained over the course of the simulation presented.

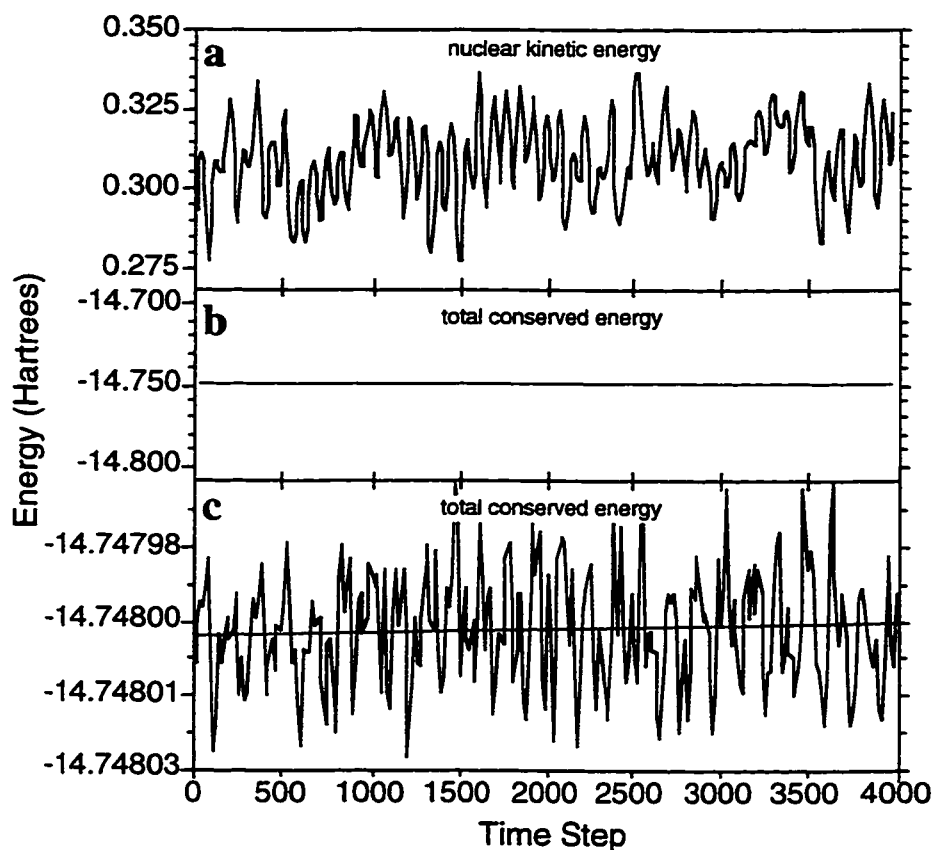


Figure 5.2. Plot of the a) kinetic energy of the nuclei (QM and MM) and b,c) the total conserved energy during a combined QM/MM molecular dynamics simulation of 3-methylhexane, **32**. The total energy in b) is plotted at the same scale as the kinetic energy whereas it is shown at a magnified scale in c). The best fit line in c) shows a linear drift in the total energy. During the simulation the average temperature of the system is 300 K.

One measure of the accuracy and validity of a molecular dynamics simulation is conservation of energy. Figure 5.2 illustrates the energy conservation of the QM/MM molecular dynamics simulation of **32**. In the upper portion of Figure 5.2, the kinetic energy of the nuclei is plotted in a). Since the MM-link atoms are not free dynamic

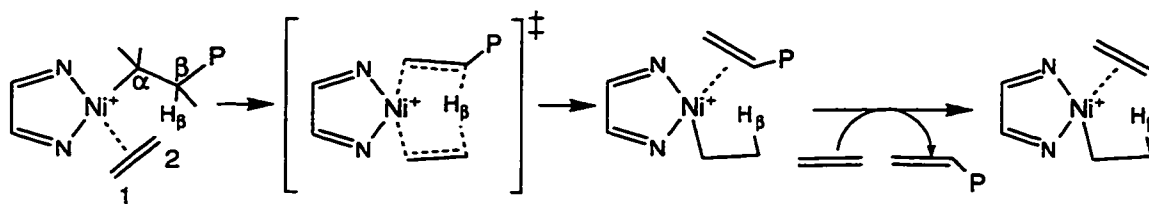
variables in the IMOMM scheme, they have no kinetic energy associated with their motion. Thus, the kinetic energy that is plotted is that of the $3N$ nuclear degrees of freedom where N is the number of atoms in the real system. Here, nine of the degrees of freedom correspond to those of the three capping atoms where the masses of the capping hydrogen atoms have been rescaled to 12.0 amu. The total conserved energy is plotted in Figure 5.2b at the same scale that the kinetic energy is plotted in Figure 5.2a. At this scale there is no observable drift. In Figure 5.2c the total energy is plotted with a magnified scale where the best fit line is also sketched. The drift in the total energy amounts to 6×10^{-6} Hartrees per picosecond. The exceptional energy conservation¹³⁷ demonstrates that the adapted IMOMM scheme can be utilized to perform QM/MM molecular dynamics (including systems with explicit solvent molecules).

Numerous molecular dynamics simulations with a hybrid QM/MM potential surface have been performed since the first.⁹ Most have been performed at the semi-empirical Hartree-Fock level^{11,12,23,160-163} but now simulations in which the QM subsystem is treated with density functional theory or *ab initio* Hartree-Fock level are now emerging.^{18,164,165} To the best of our knowledge, this is the first implementation the combined QM/MM methodology within the Car-Parrinello *ab initio* molecular dynamics framework.³⁰ In the next section we will demonstrate that the PAW QM/MM method can be used to perform *ab initio* level molecular dynamics involving transition metal systems of unprecedented size.

5.4 Combined QM/MM AIMD Simulation of Chain Termination in Brookhart's Ni-Diimine Olefin Polymerization Catalyst.

In Chapter 3, the "static" ADF-QM/MM approach was applied to study a Ni(II) diimine olefin polymerization catalyst of the type $(\text{ArN}=\text{C}(\text{R})-\text{C}(\text{R})=\text{NAr})\text{Ni}(\text{II})-\text{R}'^+$ ($\text{R}=\text{Me}$ and $\text{Ar}=2,6\text{-C}_6\text{H}_3(i\text{-Pr})_2$) which was discovered by Brookhart and coworkers.¹ It was found that the combined QM/MM approach provided detailed mechanistic insights not attained from either the experimental studies^{1,2} or the pure QM studies^{59,63} of the system. In this polymerization system the bulky aryl groups play a crucial role, since without the bulky substituents the catalyst acts only as a dimerization catalyst due to the favourability of the β -elimination chain termination process. From the structure of the catalyst, it is evident that the bulky aryl substituents partially block the axial coordination sites of the Ni center and it was proposed by Johnson *et al.*¹ that it is likely this steric feature which impedes the termination relative to the insertion process. Our "static" QM/MM calculations presented in Chapter 3 confirmed this notion. It was found that the termination transition state has both axial coordination sites occupied whereas the

insertion transition state has only the equatorial sites occupied. Furthermore, the enthalpic termination barrier was calculated to be $\Delta E^\ddagger = 18.6$ kcal/mol which is in satisfactory agreement with the experimental free energy barrier of $\Delta G^\ddagger \approx 15.5$ -16.5 kcal/mol.[◊] In this section we intend to demonstrate and validate our combined *ab initio* molecular dynamics Car-Parrinello QM/MM methodology by determining the free energy barrier of the chain termination process (Scheme 5.1 and Figure 3.1b) with Brookhart's Ni-diimine olefin polymerization catalyst.



Scheme 5.1

Computational Details. The QM/MM division of the catalyst is the same as it was with the static ADF-QM/MM study presented in Chapter 3. Thus, the bulky $R=Me$ and $Ar=2,6-C_6H_3(i-Pr)_2$, are treated by a molecular mechanics potential whereas the Ni-diimine core including the growing chain and monomer are treated by a density functional potential. The primary difference between the QM/MM simulations presented here and those in Chapter 3 are the QM/MM coupling scheme of Singh and Kollman⁸ is utilized here whereas the IMOMM coupling scheme¹⁵ was used previously.[§]

An augmented AMBER95 force field⁷⁷ was utilized to describe the molecular mechanics potential. Employing the AMBER atom type labels as described in reference 77, the diimine carbon was assigned with atom type "CM" parameters, the diimine N with "N2", aryl ring carbon atoms with "CA", aryl ring hydrogen atoms with "HA" and the remaining carbon and hydrogen atoms of the MM region with "CT" and "HC", respectively. The reacting ethene monomer was assigned with sp^2 "C" van der Waals parameters throughout the simulation. Alkyl carbon and hydrogen atoms of the active site were assigned "CT" and "HC" van der Waals parameters, respectively. Ni was

[◊]The free energy barrier of olefin insertion is experimentally estimated to be $\Delta G^\ddagger = 10$ -11 kcal/mol.¹²² The weight-average molecular weight, M_w , of 8.1×10^5 g/mol provides an estimate for the ratio of termination events to insertion events of 1:28900. Applying Boltzmann statistics to this ratio gives a $\Delta\Delta G^\ddagger$ of 5.6 kcal/mol and an estimate for the termination barrier of 15.5-16.5 kcal/mol. In calculating $\Delta\Delta G^\ddagger$ we have assumed that every hydrogen transfer event leads to the loss of the chain and, consequently, chain termination.

[§]At the time this study was performed, the adaptation of the IMOMM coupling scheme that allows for molecular dynamics simulations to be performed had not been introduced.

assigned the "Ni4+2" van der Waals parameters of Rappé's UFF.⁸¹ Non-bonded interactions between the QM and MM regions were treated with a molecular mechanics van der Waals potential. Electrostatic interactions were neglected. Torsional and angle parameters not available in the AMBER95 force field were replaced with similar parameters from the same force field.[§]

The quantum mechanical Car-Parrinello calculations were performed on the 26 atom Ni diimine molecule - [(HN=C(H)-C(H)=NH)Ni-propyl + ethene]⁺ for both the combined QM/MM simulation and the pure QM simulation. The details of the molecular dynamics simulation are essentially the same as those presented in Chapter 4^{121,133,166} with minor differences described below. Periodic boundary conditions were used with a unit cell spanned by the lattice vectors ([0.0 8.5 8.5][8.5 0.0 8.5][8.5 8.5 0.0]. All simulations were performed with the local density approximation in the parameterization of Perdew and Zunger¹¹⁸ with gradient corrections due to Becke¹⁰³ and Perdew.^{104,105} The frozen core approximation was utilized with an Ar core used for Ni and a He core used for the first row elements. A Nosé thermostat¹⁴⁷ was used to maintain an average temperature of 300 K. Separate thermostats were used for the QM and MM regions. Masses of the nuclei were rescaled to 50.0 amu for Ni, 2.0 amu for N and C, and 1.5 amu for H. The free energy barriers were calculated using the "slow growth" technique. The "midplane" slow growth reaction coordinate (c.f. Figure 4.9) was utilized. In the simulations that are presented here, the total scan time chosen was about 39000 time steps. All calculations were performed on an IBM RS/6000 3CT (375) workstation with 128 MB of memory. Each of the simulations required three weeks of dedicated CPU time.

Results and Discussion. We have performed a uni-directional scan of the chain termination process (Scheme 5.1) commencing from the resting state π -complex to the approximate transition state. The computational effort has been focused on simulating the first half of the hydrogen transfer process in order to estimate the free energy barrier for the process. Two simulations have been performed, one which models the bulky substituents with a combined QM/MM potential and one pure QM simulation which neglects the bulky substituents altogether. In these simulations the midplane reaction coordinate which is illustrated in Figure 4.9 was utilized. In the initial π -complex, the

[§] CM-N2-CA, Ni-N2-CA and N2-CM-CT angle parameters were replaced by CM-N*-CT, H-N2-CA and CM-CM-CT angle parameters of the AMBER95 force field, respectively. The X-N2-CM-X torsional parameters was replaced by the X-N2-CA-X parameter of the AMBER95 force field. The X-Ni-N2-X torsional parameter was assigned a barrier of zero.

value of the RC is initially small (approximately 0.18) indicating that the H atom to be transferred is still bound to the C β of the alkyl chain. As the reaction progresses the midplane value increases. When the value of the reaction coordinate is 0.5, this indicates that the transferred H β atom lies on a plane midway between the two atoms C β and C α .

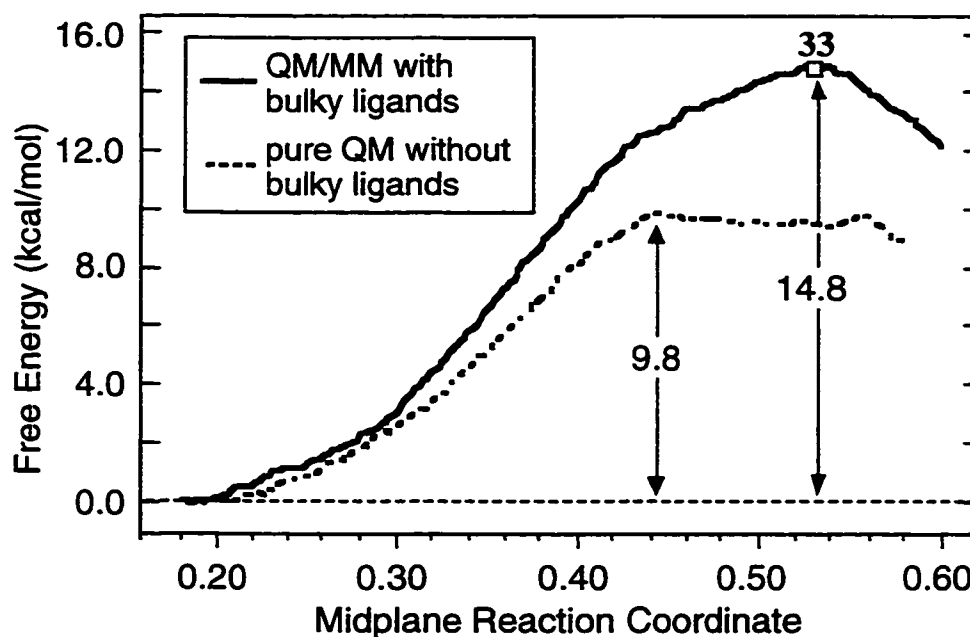


Figure 5.3. The relative free energy as a function of the mid-plane reaction coordinate for the chain termination process (Scheme 5.1). The solid profile refers to the combined QM/MM simulation whereby the bulky alkyl and aryl substituents are treated by a molecular mechanics force field. The dotted profile refers to the pure QM simulation on the model system without the bulky substituents. The position of the snapshot structure 33 is depicted.

Figure 5.3 displays the free energy as a function of the midplane reaction coordinate for both simulations. The plots reveal that the bulky ligands significantly increase the free energy barrier for chain termination. The pure QM simulation which does not account for the bulky ligands provides a free energy barrier of $\Delta F = 9.8$ kcal/mol whereas the combined QM/MM simulation provides a barrier of 14.8 kcal/mol. The combined QM/MM free energy barrier of 14.8 kcal/mol is in excellent agreement with the experimental free energy barrier of ≈ 16 kcal/mol. We note that this simulation does not include any quantum effects, namely the correction from the zero-point energy which we expect to be small.¹³³ These values are also in reasonable agreement with previously calculated energy barriers calculated from "static" simulations.^{29,59}

Figure 5.3 reveals that there is a plateau in the free energy profile for the simulation without the bulky substituents indicating the presence of a transient double olefin hydride complex where the RC ~ 0.5 . When the bulky ligands are added with the

molecular mechanics potential, the plateau vanishes leaving a single distinct termination transition state. This interesting feature of the energy profiles was also observed with static calculations first presented in Chapter 3 and reference 59.

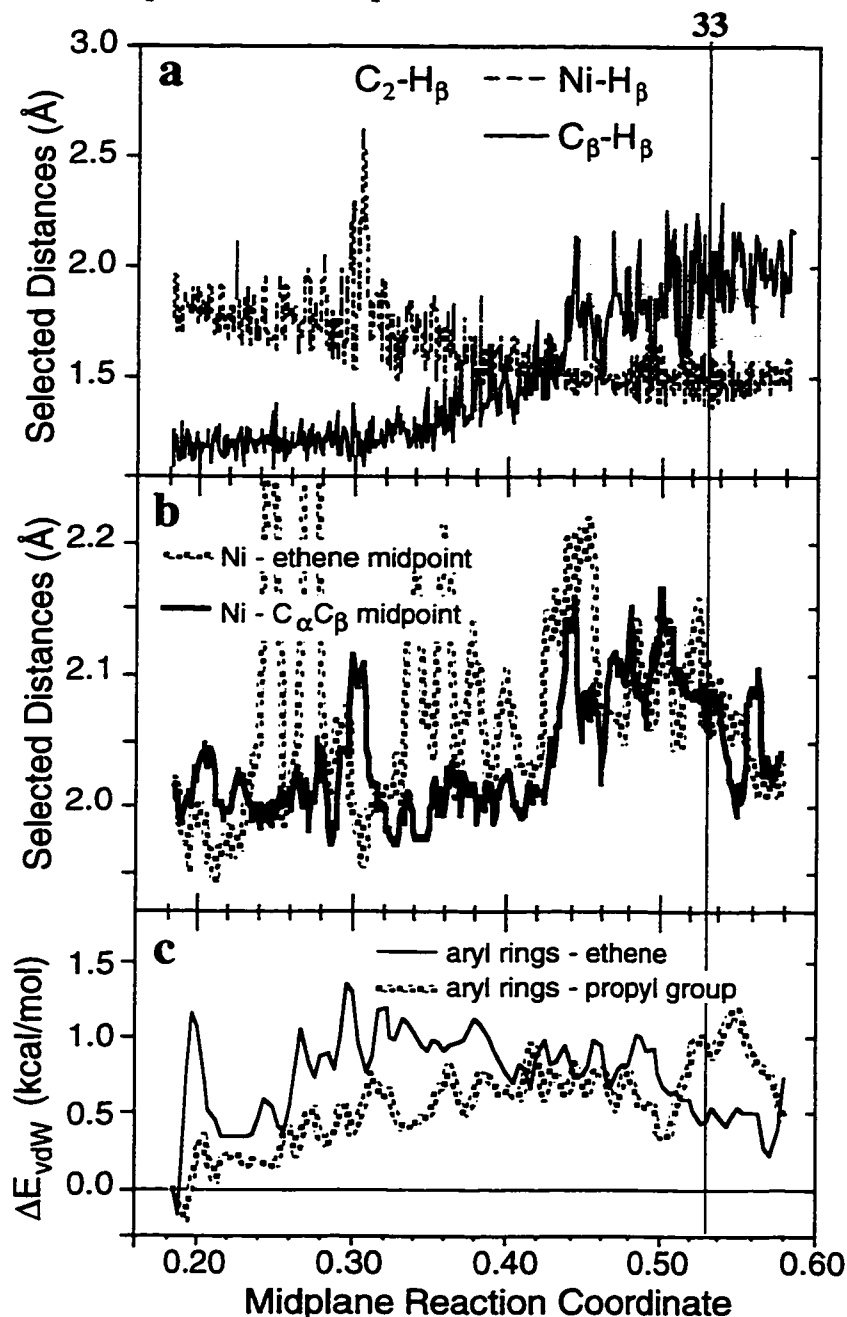


Figure 5.4. Selected structural and energetic quantities as a function of the reaction coordinate from the combined QM/MM simulation. (a) and (b): Selected distances. (c): The molecular mechanics van der Waals interaction energies between the two bulky aryl groups and the active site ethene and propyl groups relative to the resting state value. The energies plotted have been "smoothed" and are the running average over 500 time steps. The vertical line running through all three plots represents the position of the snapshot structure 33.

Selected geometric and energetic quantities are plotted in Figure 5.4 as a function of the slow growth reaction coordinate for the QM/MM simulation. A snapshot structure of the QM/MM simulation at the approximate transition state is illustrated in Figure 5.5. Figure 5.4a traces the $C_\beta-H_\beta$, C_2-H_β and $Ni-H_\beta$ bond distances to portray the transfer process (see Scheme 5.1 for labeling convention). As the reaction proceeds from the π -complex through to the transition state, the $C_\beta-H_\beta$ bond slowly increases as the C_2-H_β distance correspondingly decreases. The transition state occurs at a midplane value of approximately 0.52 where the hydrogen is roughly midway between the two carbon atoms. As the hydrogen is transferred, it is pulled into the Ni atom as demonstrated by the $Ni-H_\beta$ distance which varies from roughly 1.75 Å in the resting state to roughly 1.5 Å in the transition state region.

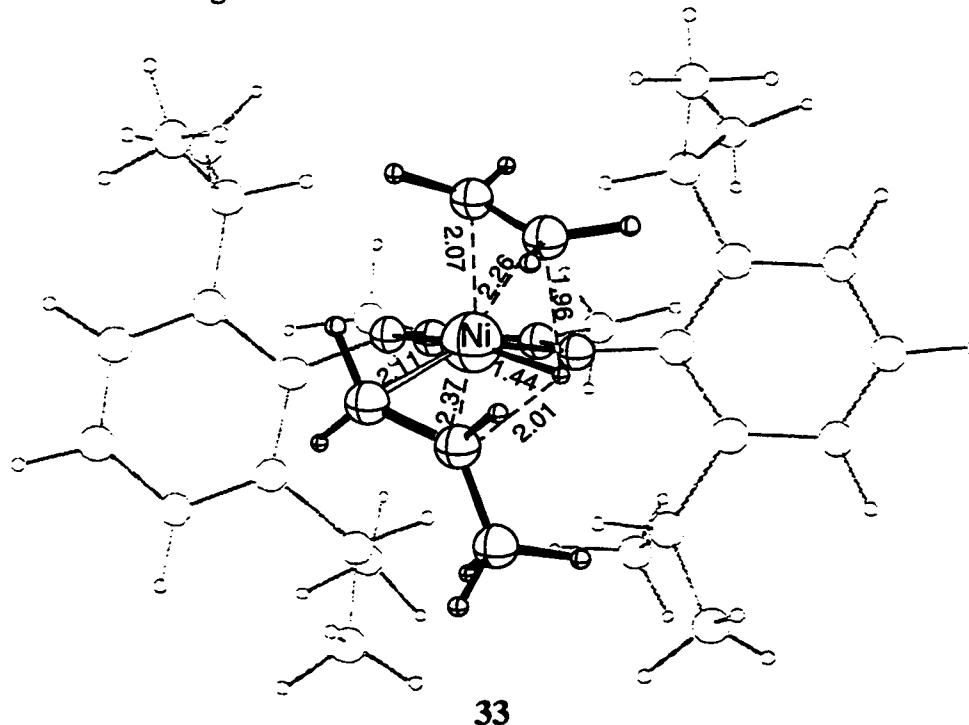


Figure 5.5. Snapshot structure from the transition state region of the combined QM/MM molecular dynamics simulation. The molecular mechanics atoms are ghosted for clarity, while the dummy hydrogen atoms are omitted. The value of the midplane reaction coordinate in **33** is $RC=0.526$. Bond distances reported are in Ångstroms.

The distances plotted in Figure 5.4b shows the expansion of the active site during the hydrogen transfer process which peaks at the transition state region. Since the ethene and propyl moieties of the active site occupied the axial positions as shown in Figure 5.5, the expansion results in an increased steric interaction with the iso-propyl substituents of

the aryl rings. In the present QM/MM model, the steric interaction between these groups is accounted for by the molecular mechanics van der Waals potential. Plotted in Figure 5.4c is the sum of all the van der Waals interaction energies between the aryl rings and the active site moieties as a function of the reaction coordinate (relative to the initial resting state value). Figure 5.4c, therefore, expresses the increase in the steric interactions between the aryl rings and the active site ethene and propyl fragments as the reaction progresses. The interaction involving the propyl group peaks at the transition state region and amounts to roughly 1 kcal/mol. On the other hand, the interaction involving the ethene molecule peaks somewhat prior to the transition state region at a reaction coordinate value of roughly 0.35 and at the transition state the steric interaction has diminished somewhat, amounting to only about $\Delta E_{\text{vdw}} = 0.5$ kcal/mol.

The applicability and efficiency of the combined QM/MM *ab initio* molecular dynamics approach to study transition metal catalysis has been demonstrated. The PAW QM/MM method will allow for *ab initio* level molecular dynamics simulations of extended systems to be performed. For our research in olefin polymerization catalysis, this will allow us to incorporate realistic ligand effects into our molecular dynamics simulations. We feel this will be an important advance in computational modeling of single-site catalysts since there is a trend towards larger more complex ligand systems, particularly in the area of stereospecific α -olefin polymerization.^{88,123,167}

5.5 QM/MM Multiple Time Step Dynamics

Interest in the linear scaling of electronic structure calculations has surged with the recent developments from the groups of Yang,^{6,168} Head-Gordon⁵ and Scuseria.⁴ Although these techniques allow the time of an electronic structure calculation to scale linearly with the size of the system, they do not address the problem of non-linear scaling of the geometry optimization or sampling of configuration space. In this section, we address the issue within the framework of the QM/MM *ab initio* molecular dynamics methodology. Our goal is to increase the configurational sampling of the MM region without significantly increasing the computational effort put into the QM region.

A QM/MM simulation will most often involve a small QM region embedded within a much larger MM domain, such as with the simulation of the active site chemistry within an enzyme. Associated with the larger size of the MM region is a potential energy surface that is more complex and one which is likely to possess a higher degree of configurational variability. This necessitates an increased degree of sampling in the MM region in order to obtain meaningful ensemble averages from a simulation. In principle,

increased sampling of the MM region can be achieved by the technique of mass rescaling. In classical molecular dynamics, configurational averages do not depend on the masses of the nuclei,[†] and therefore the true nuclear masses can be replaced with more convenient values.^{150,169} Rescaling of nuclear masses to smaller values, which allows the particles to move faster, increases the rate of configurational sampling which is proportional to the inverse square root of the mass, $m^{-1/2}$, of the particles. Therefore, by decreasing the masses of the MM nuclei relative to those in the QM region, one can differentially sample the configuration space of the two regions. However, if the same time step is used for both regions a limit to the practical over sampling is quickly reached. This is because as we rescale the masses and increase the speed of the MM nuclei, a smaller time step is required in order to accurately integrate the equations of motion of the fast moving system. Thus, when the QM and MM regions are propagated simultaneously, the "slow" QM region will be propagated with unnecessarily small time steps. This is undesirable because the QM derived forces will be changing slowly and much time will be wasted recalculating these forces at each of the small time steps.

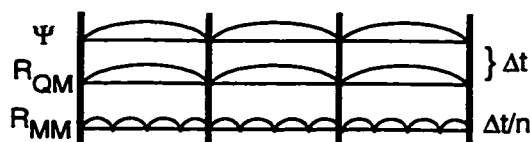


Figure 5.6. Representation of a simple multiple time step scheme within the Car-Parrinello framework. The wave function and the QM subsystems are propagated a time step Δt , while the MM subsystem is over sampled with a smaller time step $\Delta t/n$.

One way to overcome this problem is to propagate the two regions asynchronously with what has been termed multiple time-step molecular dynamics.¹⁷⁰ The multiple time-step method in the Car-Parrinello QM/MM framework is represented in Figure 5.6 where the wave function and the QM nuclei are propagated with a large time step, Δt , while the less computationally demanding MM region is n times over sampled with a time step of $\Delta t/n$. Thus, the multiple time step method in combination with mass rescaling can be applied to the QM/MM molecular dynamics methodology as

[†] The atomic masses do not appear in the configurational integral, e.g.

$$A = -kT \ln \left[\int \dots \int e^{-\frac{E(X^N)}{kT}} dX^N \right]$$

therefore equilibrium properties of a system are independent of the masses.

to differentially sample the QM and MM regions, thereby increasing the sampling of the MM domain without increasing the computational expenditure in the QM region.

The multiple time step techniques have been developed since 1978¹⁷⁰ to more efficiently treat systems with high and low-frequency motion and/or short and long-range forces. However, the simple algorithm often used (as depicted in Figure 5.6) has no rigorous basis in theory.¹⁷¹ Recently, Tuckerman and co-workers^{158,172,173} have pioneered the development of multiple time-step methods where there is a rigorous separation of time scales. We have adopted the reversible multiple time step algorithm of Tuckerman *et al.*¹⁵⁸ which allows for numerically stable, energy conserving multiple time step molecular dynamics to be performed. In our implementation the original formalism which was based on the velocity Verlet propagation algorithm has been modified to accommodate the standard Verlet algorithm used in the PAW program.

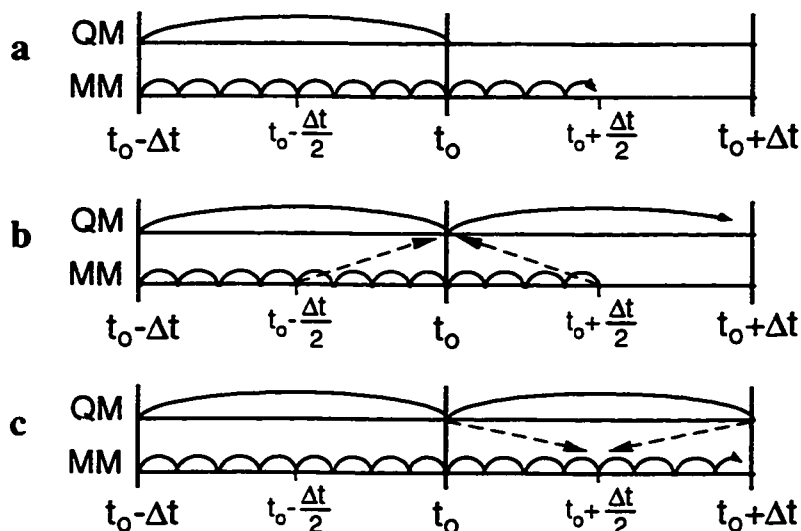


Figure 5.7. Schematic representation of a Tuckerman's reversible multiple time step procedure implemented within the PAW QM/MM method. a) depicts the propagation of the first half of the MM subsystem starting at $T=t_0$. b) the propagation the slow QM subsystem which occurs at $T=t_0+\Delta t/2$. c) the propagation of the second half of the MM subsystem. The dashed arrows in b) and c) illustrate what forces are used to propagate the systems in these intervals (see text for more details).

Sketched in Figure 5.7 is a schematic representation of the reversible multiple time step procedure. Consider the system at a time $T=t_0$ where we are propagating the slow QM subsystem with a long time-step Δt and the faster MM subsystem with a short time-step $\Delta t/n$. First the faster MM subsystem is propagated $n/2$ times for half of the long interval, $\Delta t/2$, as shown in Figure 5.7a. Now the slow QM degrees of freedom are propagated for a full long time step as shown in Figure 5.7b. It is crucial to point out that

the forces used to propagate the slow QM system are the average of the forces evaluated at the half-interval ($T=t_0-\Delta t/2$ and $t_0+\Delta t/2$) values of the MM degrees of freedom. Thus, the new positions of the QM degrees of freedom (both nuclear and electronic) are expressed in Equation 5-1:

$$x_{QM}(t_0 + \Delta t) = 2x_{QM}(t_0) - x_{QM}(t_0 - \Delta t) + \frac{\Delta t^2}{M_{QM}} F_{QM} \quad (5-1)$$

where the forces on the QM nuclei are defined in equation 5-2 where $c(t)$ denotes the expansion coefficients of the Kohn-Sham wave function.

$$F_{QM}(t_0) = \frac{1}{2} \left[F_{QM} \left\{ x_{QM}(t_0), c(t_0), x_{MM}(t_0 - \frac{\Delta t}{2}) \right\} + F_{QM} \left\{ x_{QM}(t_0), c(t_0), x_{MM}(t_0 + \frac{\Delta t}{2}) \right\} \right] \quad (5-2)$$

Following the propagation of the slow QM system with the large time step, the second half of the small time-steps involving the MM subsystem is executed. In this interval, the forces on the MM subsystem at time $T=t_0+\Delta t/2$ are evaluated using the updated values of the QM degrees of freedom at $t_0+\Delta t$ averaged with the same values at time t_0 . This is expressed in Equation 5-3.

$$F_{MM}(t_0 + \frac{\Delta t}{2}) = \frac{1}{2} \left[F_{MM} \left\{ x_{QM}(t_0), c(t_0), x_{MM}(t_0 + \frac{\Delta t}{2}) \right\} + F_{MM} \left\{ x_{QM}(t_0 + \Delta t), c(t_0 + \Delta t), x_{MM}(t) \right\} \right] \quad (5-3)$$

The forces on the MM subsystem for the remainder of the interval are given by equation 5-4.

$$F_{MM} = F_{MM} \{ x_{QM}(t_0 + \Delta t), c(t_0 + \Delta t), x_{MM}(t) \} \quad (5-4)$$

We reiterate that the slow QM degrees of freedom are propagated with forces derived from the MM degrees of freedom at $T=t_0+\Delta t/2$ and not $T=t_0$. Conversely, the faster MM degrees of freedom are half propagated with forces derived from the QM degrees of freedom at $T=t_0$ and the half with forces derived from the QM degrees of freedom at $T=t_0+\Delta t$. For both the QM degrees of freedom and the MM degrees of freedom, this gives a better or more "averaged" representation of the complementary degrees of freedom over the entire large time step.

Generally, when the 'trick' of mass rescaling is used in classical molecular dynamics simulations the masses of light atoms such as hydrogen are scaled up to make them heavier.¹⁶⁹ (We made use of this in our Car-Parrinello studies presented in Section 5.4 and Chapter 4.) This allows for larger time steps to be used during the integration of the equations of motion and therefore effectively increases the simulation times. Conversely, when masses are rescaled to smaller values, the particles move faster and are able to sample configuration space faster. When the masses of the MM atoms are scaled to smaller values, the multiple time-step procedure allows for the proper integration of the faster moving atoms without increasing the number of force evaluations from the electronic structure calculation of the QM model system. Thus, in the combined QM/MM molecular dynamics framework this unique combination of techniques allows for oversampling of the MM partition of the system, without increasing the computational expense of the QM subsystem. Since we are the first to develop the multiple time-step method in this way, the next section will be devoted to testing the validity of the combined QM/MM multiple time step dynamics approach.

5.6 Test Results of the Multiple Time-step QM/MM Approach

Test results of the multiple time step QM/MM methodology with mass rescaling will be presented in this section. The method will first be showcased in order to establish how the methodology is intended to be applied. This will be followed by a more systematic validation of the methodology.

A combined QM/MM multiple time step dynamics simulation of 4-ethylnonane (Figure 5.8) has been performed. The QM/MM partitioning of the system is shown in Figure 5.8b where the link bonds are denoted with asterisks. The calculation involved ethane as the model QM system for which the electronic structure was calculated at the gradient-corrected BP86 DFT level.^{103,104,118} A time step of 3.0 a.u. (~ 0.07 fs) was used for the QM system whereas the MM subsystem was over sampled by a ratio of 20:1 such that a small time step of $3.0/20=0.15$ a.u. was utilized for the MM region. The simulation involved 10000 QM time steps (720 fs) and 200000 MM time steps. The rescaling of the masses is depicted in Figure 5.8b. Masses of 12.0 amu and 1.5 amu were used for the C and H atoms, respectively, in the QM system whereas the masses in the MM region were rescaled 400 fold to enhance the sampling rate by a factor of approximately 20. The rescaling of the masses is detailed in Figure 5.8b.

Plotted at the top of Figure 5.8a is the kinetic energy of the MM and QM subsystems. The disparity in the frequency of QM and MM kinetic energies reveals how

differential sampling of the two regions is achieved with the method. In this simulation, an average temperature of 300 K is maintained throughout the simulation for both the QM and MM regions. However, as a result of the mass rescaling in the MM region, the MM kinetic energy oscillates much more rapidly than the QM kinetic energy. This is the goal of the methodology since the faster fluctuations in the MM kinetic energy implies a faster motion of the MM subsystem and ultimately a more rapid sampling of the configuration space. (This will be further illustrated later)

Figure 5.8a also displays total energy of the system plotted at the same energy scale as the QM and MM kinetic energies. This illustrates the stability of the multiple time step method which displays no significant drift in the total energy over the period of the whole simulation. There is also no drift in either the kinetic energies of the MM or QM nuclei shown in Figure 5.8a. This is notable because it points out that there is no significant energy flux between the nuclear kinetic energies and the fictitious kinetic energy of the QM wave function. It is conceivable that the rapidly fluctuating kinetic energy of the MM subsystem might couple with the fictitious kinetic energy of the QM wavefunction. This would lead to an eventual dislodging of the wavefunction from the Born-Oppenheimer surface and unphysical dynamics in the QM subsystem. The stability in the nuclear kinetic energies[§] during the course of this simulation reveals that this is not occurring. We note here that no thermostating was applied to any of the subsystems during the dynamics.

We now turn our attention to a systematic validation of the method and implementation. First we intend to demonstrate that starting from the exact same system (structure and masses), the multiple time step propagator generates the same trajectory as the standard Verlet propagator. For this we have performed three simulations of 4-ethylnonane, starting from the same structure with no initial velocities.[◊] Acting as our control is a simulation performed with the standard Verlet propagator with a time step of 3.0 a.u. for both the QM and MM subsystems. Two QM/MM multiple time step simulations were performed with oversampling ratios of 10:1 and 20:1 such that the time steps in the MM region are 0.3 au and 0.15 a.u., respectively. In all three simulations, the QM/MM partitioning is the same as that depicted in Figure 5.8b such that ethane

[§] Drift can also result from net energy flux between the kinetic energies of the QM and MM nuclei, a real physical effect in a non-equilibrium state. However, in this simulation the dynamics shown in Figure 5.7a was pre-equilibrated.

[◊] In these simulations the dynamics was initiated from a frozen structure and the resulting temperature of the system was approximately 100 K.

constitutes the QM model system. However, unlike the simulation depicted in Figure 5.8, the masses in these simulations were not rescaled.

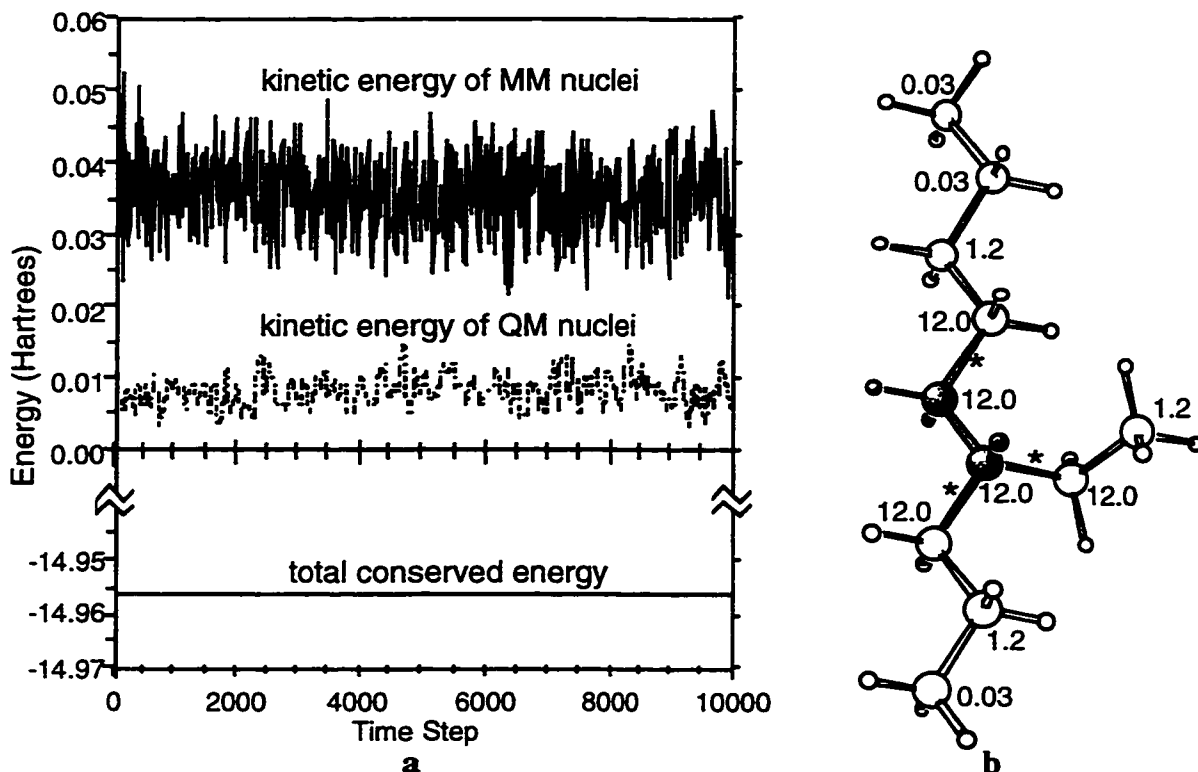


Figure 5.8. a) Kinetic energy of the QM and MM nuclei for a multiple time step QM/MM dynamics simulation of 4-ethylnonane with the rescaling of the masses depicted in b). To demonstrate energy conservation of the dynamics, the total energy of the system is shown at the same scale as the kinetic energies. b) The QM/MM partitioning of 4-ethylnonane where the shaded regions represent the QM region. Covalent bonds labeled with asterisks denote the QM/MM link bonds. All of the link bonds have been capped with hydrogen atoms such that the QM model system is ethane. The rescaling of the atomic masses of carbon are depicted in atomic mass units.

Small structural changes in the backbone of the 4-ethylnonane system are likely to be magnified at the extremities of the alkane. Thus, a geometric parameter that is likely to be sensitive to differences in the trajectories is the distance between the two terminal carbons (C1 and C9) of 4-ethylnonane system. Plotted in Figure 5.9 is the deviation in this distance between the standard Verlet trajectory and the two multiple time step trajectories. The difference in this parameter throughout the simulation remains exceptionally small (of the order of 10^{-4} Å).

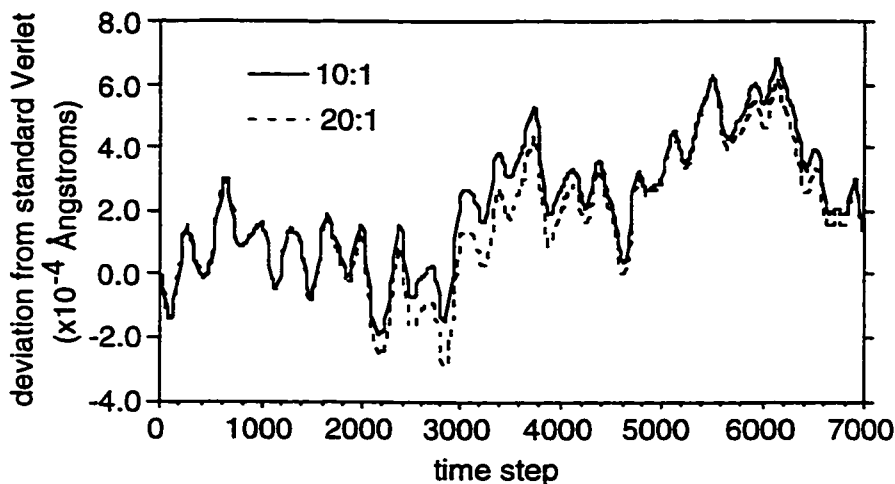


Figure 5.9 Deviation in the distance terminal carbons (C1-C9) in 4-ethylnonane between the standard Verlet trajectory and multiple time step trajectories.

Another property that is highly sensitive to geometric differences in the trajectory is the electronic energy of the QM model system. Figure 5.10a plots the total DFT energy of the QM model system for all three trajectories. At the scale of the oscillations in this energy, the three trajectories can not be distinguished over the course of the simulation (~500 fs). Shown in Figure 5.10b is the magnitude at which the electronic energy of the two trajectories generated from the multiple time step method (10:1 and 20:1) and the standard Verlet propagator deviate. The deviation in the DFT energy is of the order of 10^{-5} Hartrees with no progressive increase during the 500 fs simulation. We conclude that, well within chemical accuracy, the multiple time step propagator generates the same trajectory as the standard Verlet propagator.

We now turn our attention to the energy conservation of the multiple time step QM/MM molecular dynamics. In order to determine the limitations of the multiple time step QM/MM method, we will compare the energy conservation of a series of molecular dynamics simulations of 4-ethylnonane where various mass rescaling schemes and multiple time step over-sampling ratios have been adopted. Acting as our control is the standard Verlet simulation of the system where the masses have not been rescaled. Compared in Figure 5.11 is the energy conservation of a series of simulations where the masses in the MM region have been rescaled by a factor of 1/400 as to over-sample the MM region by a ratio of 20:1. The atomic masses of the alkane have been rescaled in an abrupt manner and a gradual manner. The abrupt rescaling of the masses is shown in Figure 5.12a and corresponds to what is labeled rescaling scheme a. In this rescaling scheme, the atomic masses are immediately rescaled by a factor of 1/400 as we move from the QM region to the MM region. In this way, a carbon atom which has a mass of

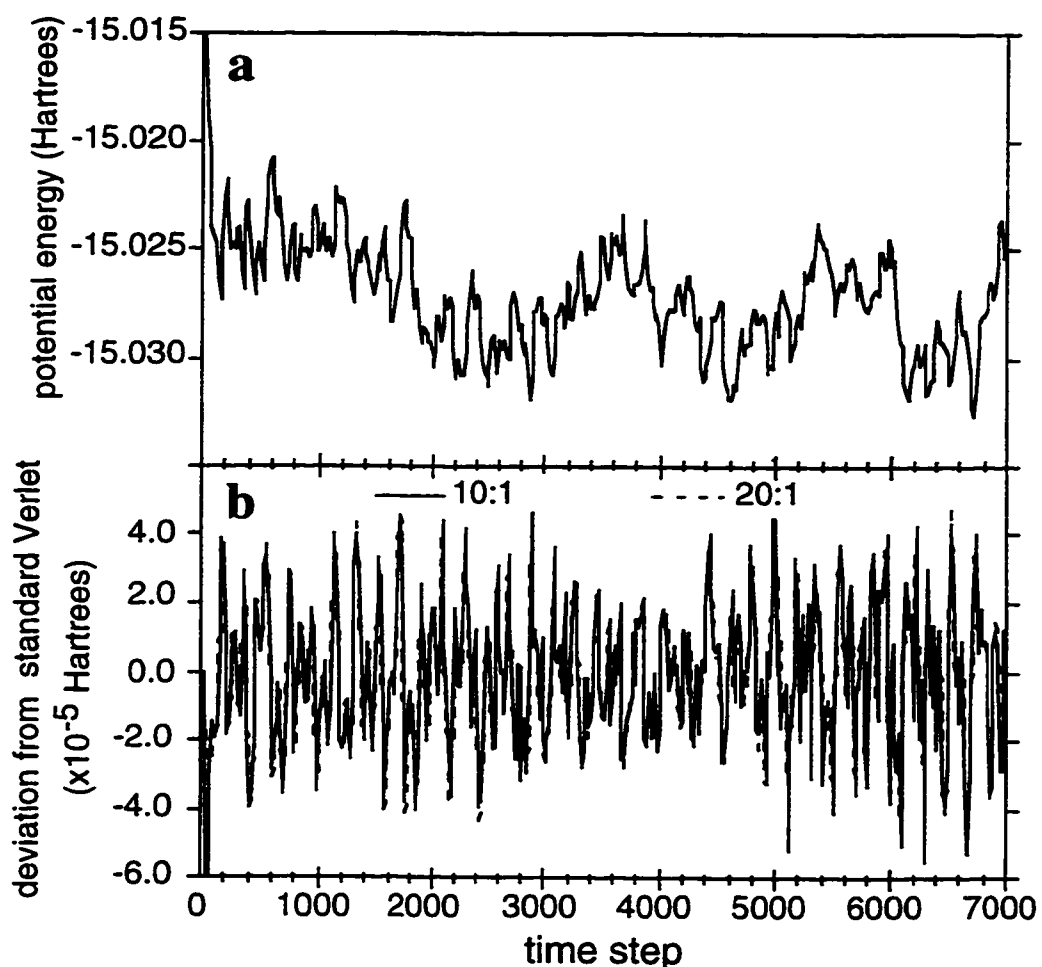


Figure 5.10. a) Potential energy of the QM model system for the standard Verlet and the multiple time step Verlet 20:1 and 10:1 over-sampled. In the scale shown, the potential energy of the various trajectories can not be differentiated. b) The deviation in the potential energy between the standard Verlet algorithm and the multiple time step Verlet algorithm 10:1 (solid) and 20:1 (dashed) over-sampled. The plots illustrate the similarity between the standard Verlet and multiple time step Verlet trajectories which were initiated from the same structure.

12.0 amu will be bonded to a carbon atom with a rescaled mass of 0.03 amu. A more gradual rescaling of the masses is adopted in scheme b as depicted in Figure 5.12b. Here the masses of atoms adjacent in connectivity to the MM link atoms[◊] are first rescaled by a factor of 1/10. All other MM atoms further away in connectivity are rescaled by a factor of 1/400. Thus, there is a gradual rescaling of the masses as we pass from the QM region to the MM region.

[◊]We have used the modified IMOMM coupling scheme. In this coupling scheme the MM link corresponds to the nuclear degree of freedom of the QM dummy atom. Since the QM dummy atom is propagated by the large time step, its mass is not rescaled.

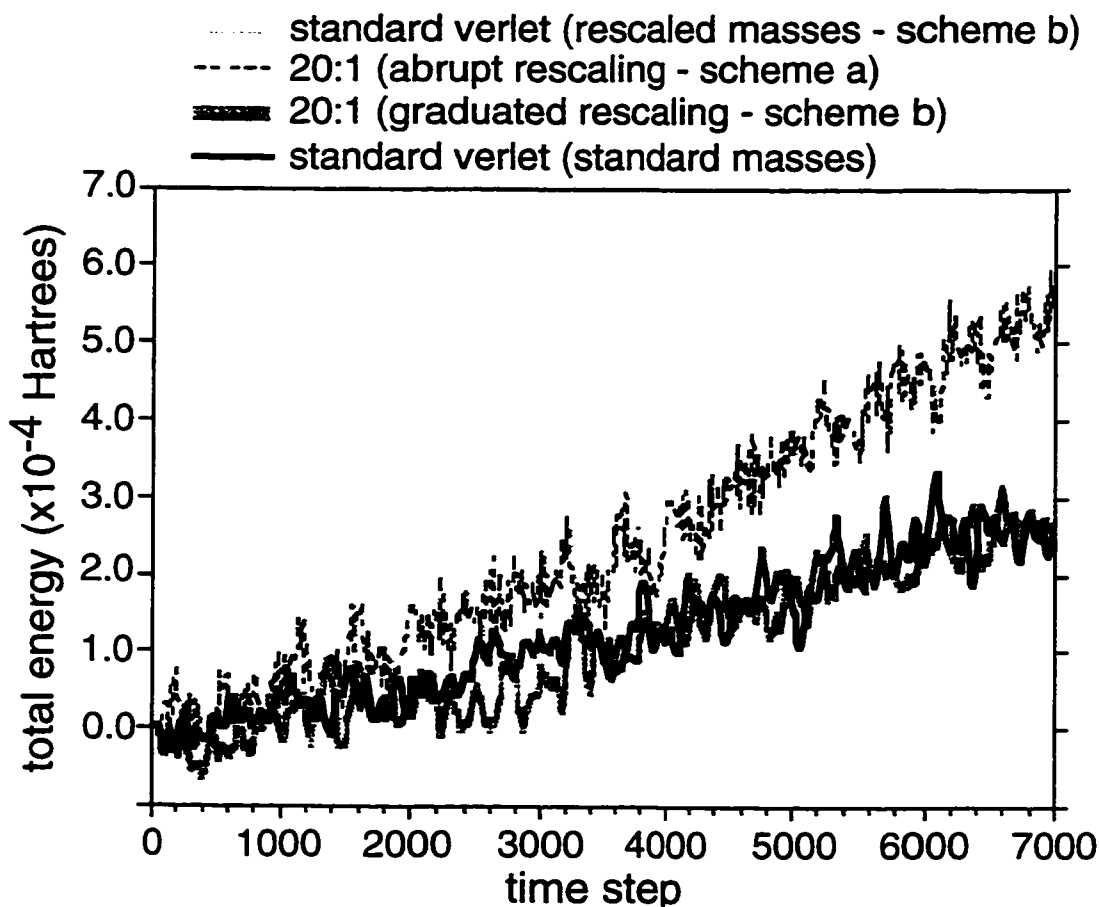


Figure 5.11 Comparison of the energy conservation during simulations of 4-ethylnonane. Plotted are the total (conserved) energies of the simulations relative to the initial value. The schemes referred to in the plot legend correspond to the mass rescaling schemes depicted in Figure 5.12. The temperature in these simulations was 300 K.

The total energy of the systems relative to the initial value is plotted in Figure 5.11. The control system (standard Verlet and no mass rescaling) exhibits a slow linear drift of approximately $+6 \times 10^{-7}$ Hartrees for each femtosecond of simulation time. The energy conservation of the simulation with the gradual mass rescaling scheme matches that of the control simulation. However, with the abrupt rescaling scheme the drift rate is double that of the control, indicating a loss of integration accuracy compared to the control. With an abrupt rescaling, the high frequency motions of the light MM atoms are propagated into the QM region. This degrades the energy conservation because the larger time step used for the QM subsystem is unable to properly integrate this high frequency motion. This effect is minimized when the masses are gradually rescaled since the high frequency motions of the MM subsystem are dampened by the progressively heavier

masses. We conclude that in order to apply the multiple time step QM/MM method, there must be a graduated rescaling of the masses.

Also shown in Figure 5.11 is the energy conservation when the masses are rescaled (scheme b of Figure 5.12b) but the multiple time step method is not used. In this simulation, the same large time step is used to integrate both the fast MM and slow QM subsystems. It is apparent from the large fluctuations and the rapid drift of the total energy during this simulation, that the large time step is unable to properly capture the fast motion of the light MM atoms. Thus, in order to effectively rescale the masses as to increase the sampling in the MM region, a multiple time step integrator is necessary.

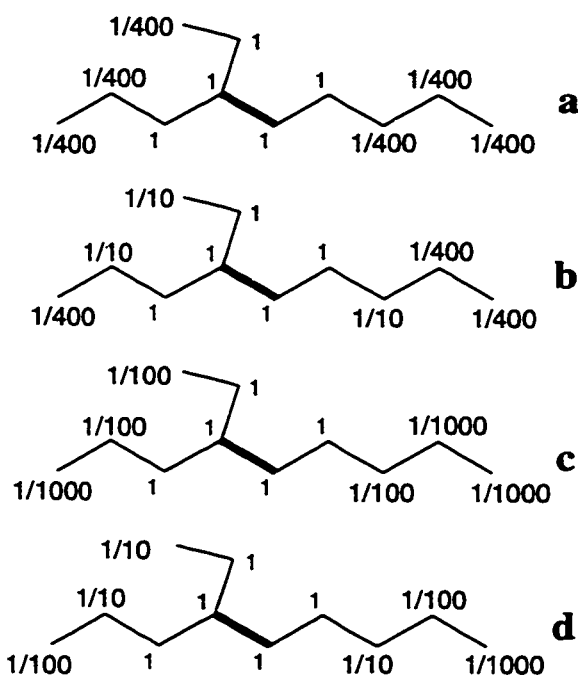


Figure 5.12 Mass rescaling schemes used for the QM/MM dynamics simulations of 4-ethylnonane shown in Figures 5-10 and 5-12. The values next to the backbone carbon atoms reflect the fraction that the standard masses were rescaled. Thus, 1/400 means that the 12.0 amu mass of carbon was rescaled to a value of 0.03 amu. Masses of the hydrogen atoms were similarly rescaled.

Next, we investigate the amount of over-sampling that can be effectively applied to our 4-ethylnonane complex. Figure 5.13 compares the energy conservation of the control to a pair of simulations where the MM masses have been rescaled by a factor of 1/1000 and a multiple time step ratio of 100:1 has been applied. The rescaling schemes of the two simulations are shown in Figures 5.12c and 5.12d. The rescaling schemes are both gradual, but the step sizes in scheme c are greater than in scheme d. With rescaling scheme c, the energy conservation is diminished from the control as evidenced by the

faster drift in the total energy. With scheme d, the more gradual rescaling, the level of energy conservation of the control is matched. Although the integration accuracy with scheme d is excellent, the amount of over-sampling at the 100:1 level is minimal since only one carbon atom (terminal C9) is rescaled by the 1/1000 factor. The results suggest that, in order to attain the level of energy conservation of the control, the masses can be graduated by no more than an order of magnitude for each level of connectivity away from the QM subsystem. Therefore, the necessity of using a gradual rescaling of the masses imposes a practical limit to the amount of over-sampling that can be achieved with this technique.

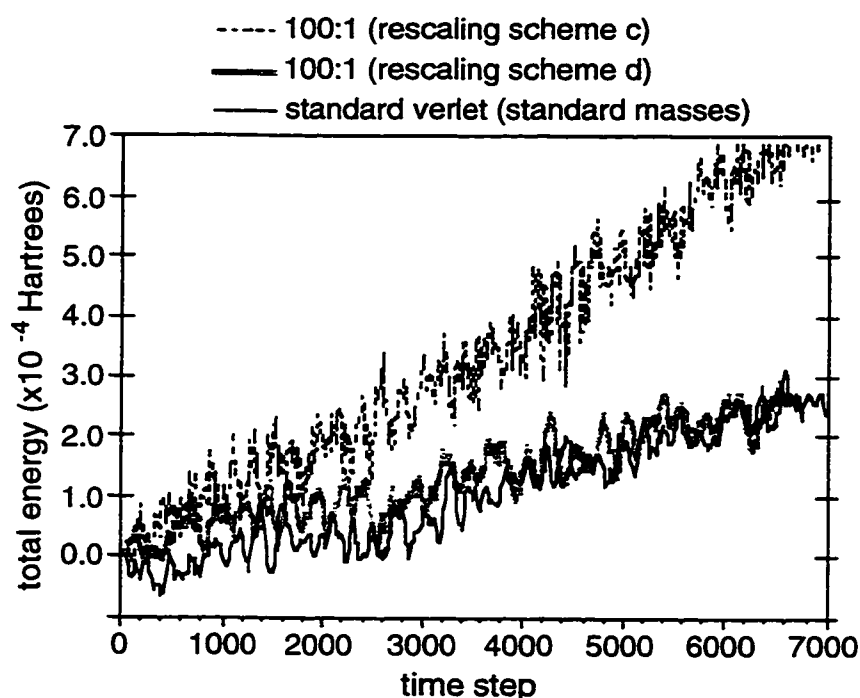


Figure 5.13 Comparison of the energy conservation of the multiple time step simulations of 4-ethylnonane. Over-sampling ratios of 100:1 were utilized with rescaling of the masses shown in Figure 5.12. Plotted are the total (conserved) energies of the simulations relative to the initial value. The energy conservation of the multiple time step simulations are compared to that of the standard Verlet simulation with no mass rescaling. The temperature in these simulations was 300 K.

Finally, we demonstrate how the multiple time step QM/MM technique can accelerate the equilibration process and ultimately configurational sampling compared to a standard simulation in which there is no mass rescaling. Two simulations of normal undecane(C11) have been performed where the terminal methyl groups make up the QM

region as illustrated in Figure 5.14.[◊] One simulation was performed with the standard Verlet propagator where "standard" masses for the whole system were utilized (12.0 amu for C and 1.5 amu for H). In the other simulation, the standard masses were rescaled in the MM region by a factor of 1/400 and the multiple time step algorithm was used with an over-sampling ratio of 20:1. The masses used in the multiple time-step simulation are detailed in Figure 5.14 for the carbon atoms of the backbone (hydrogen atoms were similarly rescaled). A high energy conformation of the hydrocarbon chain was selected as the initial structure.[§] For both simulations, the free, unthermostated dynamics was commenced from this structure with no initial velocities. Additionally, the constraint shown in Figure 5.14 was applied to the system. Here the distance between one of the terminal carbon atoms and a proton of the other terminal carbon atom was constrained to a distance of 4 Å throughout the dynamics (The reason for applying the constraint will be explained later)

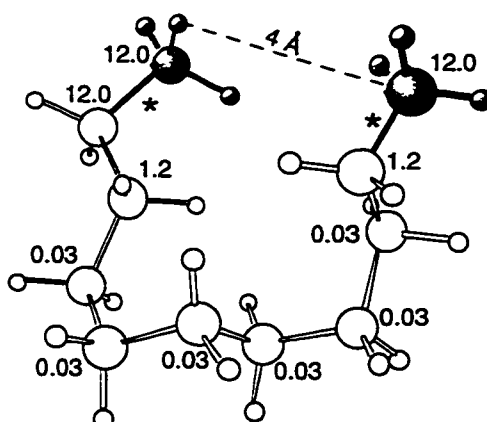


Figure 5.14 QM/MM partitioning, mass rescaling scheme and constraint definition for the molecular dynamics simulations of *n*-undecane. The shaded regions represent the QM region. The two link bonds, which are labeled with asterisks have been capped with hydrogen atoms, such that the QM model system consists of two methane molecules. The rescaling of the masses in the multiple time step simulation are shown in atomic mass units. Hydrogen atoms are similarly rescaled.

The temperature evolution of the QM and MM subsystems for both the standard and the multiple time-step simulation is shown in Figure 5.15. Since the dynamics was

[◊] The calculation of the QM model system involved two methane molecules contained within a 8.5 Å cubic cell.

[§] With the QM subsystems frozen, the global minimum energy structure of the MM backbone was determined from fully optimizing structures sampled every 1 ps from a 50 ps dynamics simulation run at 800 K. From the same simulation, a high energy structure of the MM backbone was selected that was conformationally distinct from global minimum structure.

initiated from a high energy conformation, there is a steep rise in the temperature of both the QM and MM systems in the first 100 fs of the simulation. When the whole system is properly equilibrated, both the QM and MM systems should be at the same temperature. For the multiple time-step simulation the temperature evolution plotted in Figure 5.14b reveals that the QM and MM systems both attain a steady state temperature of approximately 400 K. The temperature of the two systems is well equilibrated at about the 800 fs mark of the simulation. In contrast, for the standard Verlet simulation with no mass rescaling, equilibration does not occur in the first 1400 fs of the simulation. Even at the 1400 fs mark, the fluctuations are large and disparity between the QM and MM temperatures is still rather large. The continuation of the temperature evolution for the standard time step simulation is plotted in Figure 5.16. The plot reveals that equilibration does not begin to occur until the 5500 fs mark where an equilibrium temperature of 400 K is being established. However, even after 8000 fs temperature equilibration has not been fully established.

It is apparent from Figures 5.15 and 5.16 that temperature equilibration of the system occurs much more rapidly with multiple time-step simulation than it does with the standard simulation. The light masses in the MM region allows this subsystem to equilibrate itself rapidly to the slowly changing QM subsystem. Figure 5.15b reveals that within the first 20 fs of the simulation a steady temperature of approximately 500 K is attained in the MM region. Following the initial equilibration of the MM subsystem, there is the steady transfer of energy into the QM subsystem. This results in the slow cooling of the MM subsystem as the whole QM/MM system equilibrates to a final temperature of just under 400 K. Thus, the rescaling of the masses in the MM subsystem which allows for the rapid equilibration of the MM system, facilitates the equilibration of the whole system. In the standard simulation, both subsystems are "heavy" and slow to equilibrate which delays the process for the whole system.

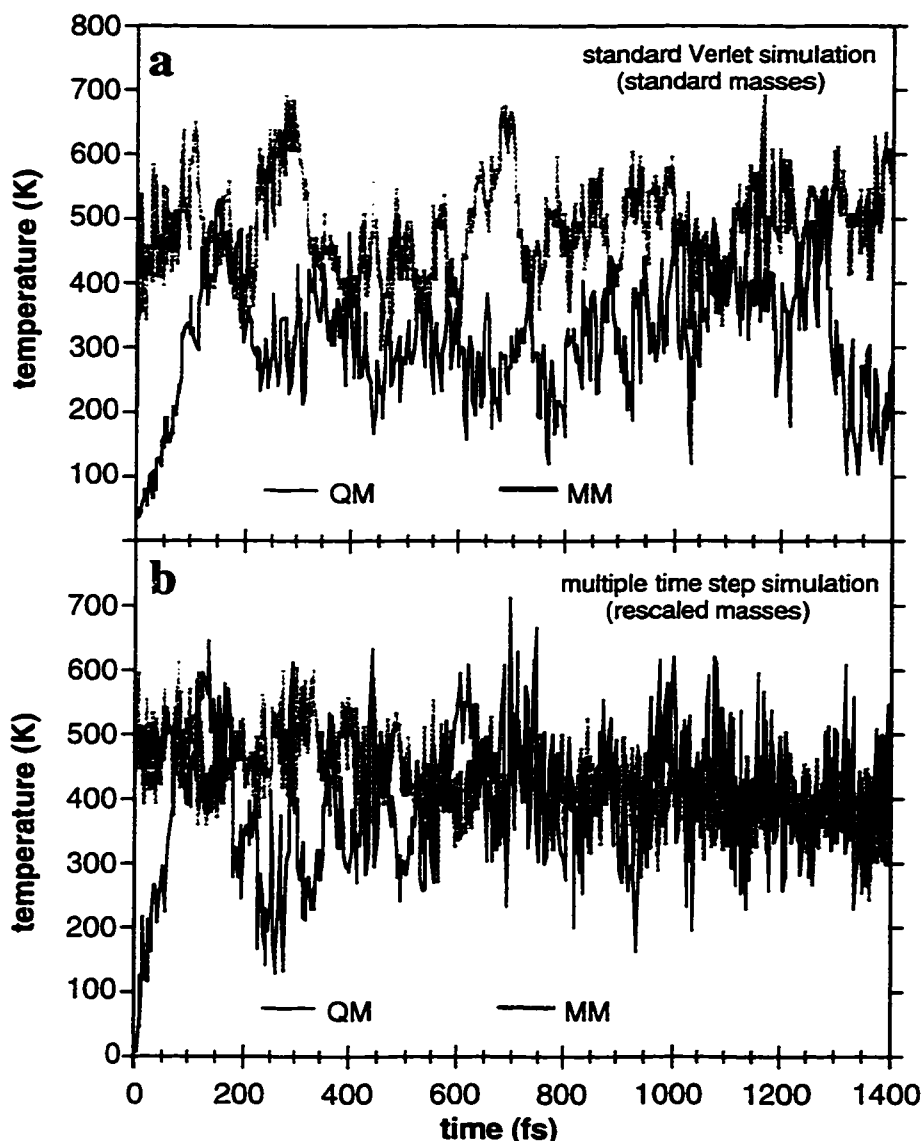


Figure 5.15 Temperatures of the QM and MM subsystems of the dynamics simulation undecane with a) standard masses and b) rescaled masses as depicted in Figure 5.14. In simulation b) where the masses have been rescaled, the multiple time step method was used with an over-sampling ratio of 20:1 (i.e. 20 small time steps for each large one).

The distance constraint was imposed during the dynamics of undecane in order to evaluate if the multiple time step method would be effective in accelerating the convergence of the constraint force. The convergence of the force is important since the slow growth simulations we perform to map out reaction free energy profiles involves the integration of the constraint force. A faster convergence of the constraint force would then correspond to an acceleration in the configurational averaging in these simulations and also smaller errors. Although the undecane system doesn't correspond to a real

reaction, the simulation does imitate the condition where the structure of the MM subsystem strongly influences the force on the reaction coordinate. In the undecane simulation, the constraint force involving the distance between the terminal methyl groups will be regulated by the structure of the hydrocarbon backbone. Thus, the faster the structure of the back bone equilibrates, the faster the constraint should converge. Since most of the backbone resides in the MM partition, we expect that the QM/MM multiple time-step procedure will accelerate the convergence of the force compared to the standard simulation.

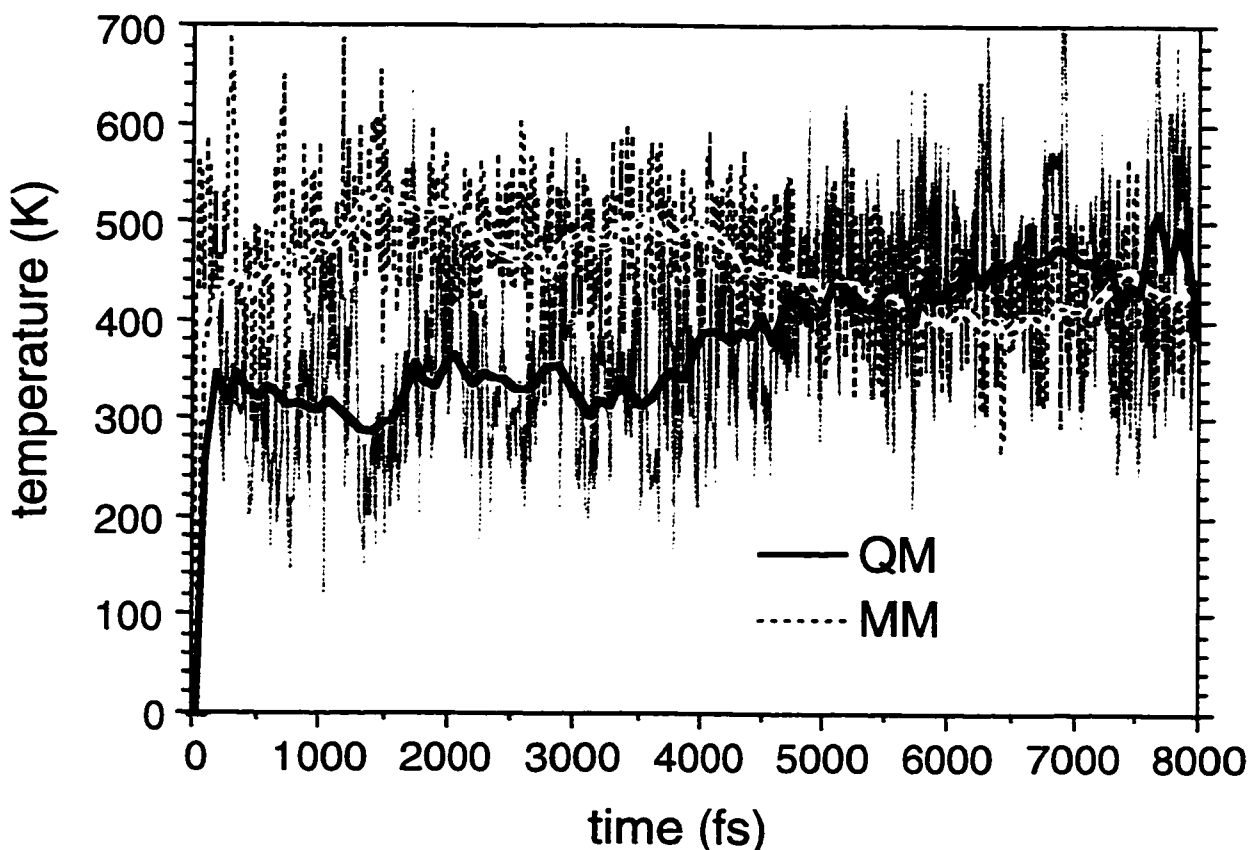


Figure 5.16 Temperature evolution of the QM and MM subsystems of the dynamics simulation of undecane with standard masses and the standard Verlet propagator. This plot is a continuation of Figure 5.15a. The solid lines are the temperature and its running average (with a window of 100 fs) for the QM subsystem and the dashed lines are the same quantities for the MM subsystem.

The evolution of the average constraint force, $\langle F \rangle$, during the two undecane simulations is plotted in Figure 5.17. Since a high energy starting structure of the backbone was selected, the force on the constraint is initially high. As the backbone structure equilibrates, the force on the constraint should relax to a steady state value. The

average constraint force decays much more rapidly in the multiple time-step simulation than in the standard simulation. This is because the heavier MM subsystem in the standard simulation is slower to settle into an equilibrium conformation. Figure 5.16 shows that the constraint force in the multiple time-step simulation achieves a steady state value within approximately 4000 fs. The constraint force in the standard simulation, which should converge to the same value, is slow to decay and convergence is not observed in the first 8000 fs of the simulation. The simulation was stopped after 50000 time steps, since it was evident that there is an accelerated relaxation of the average force with the multiple time step method. Furthermore, since temperature equilibration in the standard simulation does not begin to arise until the end of the 8 ps simulation, the convergence of the constraint force will not occur for some time later.

When using the slow growth technique to map out free energy surfaces, it is actually the ensemble averaged force on the constraint that is the ideal force used in the integration. Thus, the evolution of the averaged force plotted in Figure 5.16 emphasizes that the multiple time-step QM/MM method can provide for better sampling and smaller errors. Uncertainty estimates in a slow growth simulation are determined by the amplitude of the fluctuations in the constraint force.¹⁷⁴ The larger the fluctuations the larger the uncertainties are in the calculated relative free energies. Examination of the unaveraged forces on the constraint (not plotted) show the amplitude of the fluctuations is approximately 50% smaller in the multiple time-step simulation compared to the standard simulation. This corresponds to roughly 20% smaller error bars in the multiple time-step simulation.

The undecane simulation was designed such that the structure of the MM system strongly influenced the constraint force. Therefore, a significant acceleration in the convergence of the constraint force was observed with the multiple time-step method. However, most systems are more balanced in that the QM system has a stronger influence on the constraint force. Thus, the benefit of the multiple time-step method will be less pronounced for most simulations. On the other hand, even if the improvement is small, the additional computational effort is minimal (assuming that the computational expense of the MM system is negligible compared to the QM system). In the Car-Parrinello QM/MM simulation of the Brookhart catalyst described in the previous section, the calculation of the MM forces amounted to less than 0.01% of the total computational effort.[◊] Therefore, if the multiple time-step technique were to be applied to the system

[◊] Interestingly the time needed to calculate the MM forces at every time step amounted to half of the time needed to write the output during the simulation.

with a high oversampling ratio of 100:1, the 100 fold increase in computing the MM forces would still be negligible. Therefore, in these cases where the computational expense of the MM subsystem is negligible and where time-dependent properties are not being investigated, there is no reason not to apply the multiple time-step procedure.

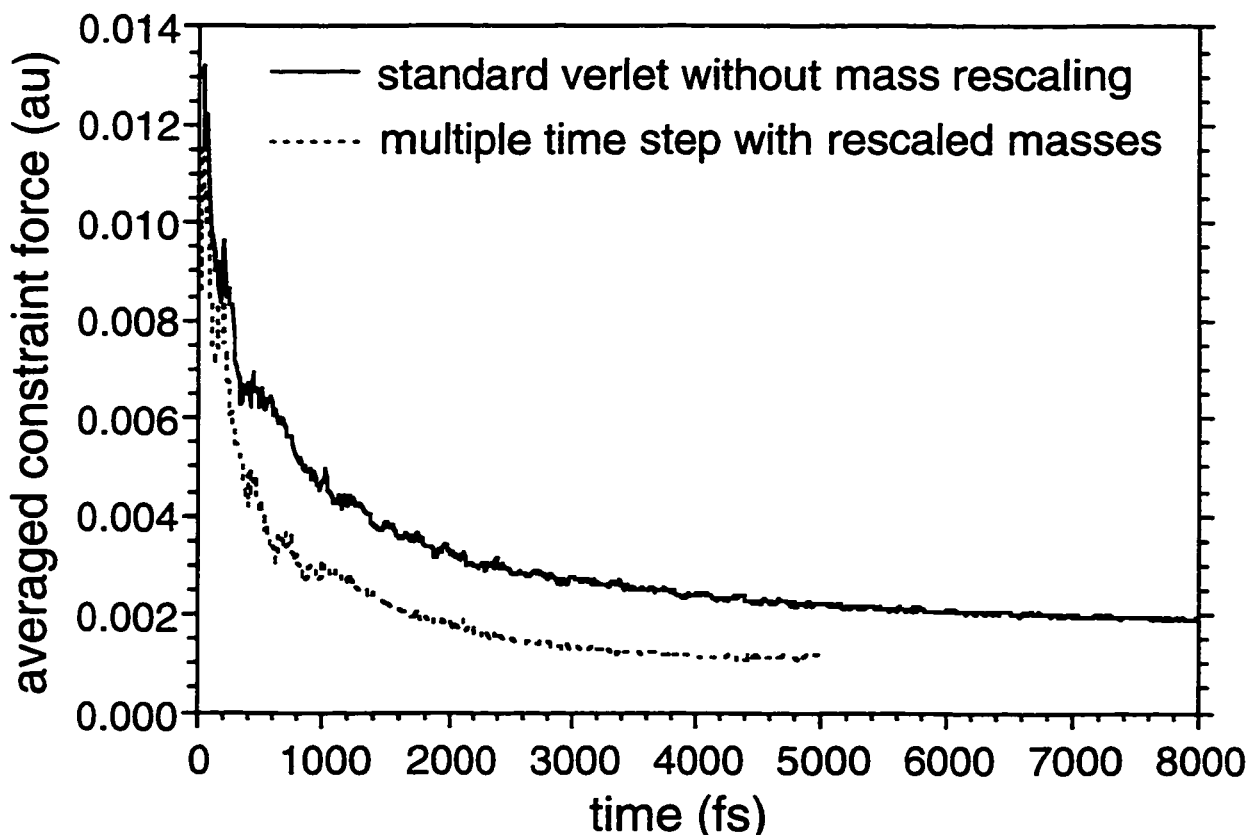


Figure 5.17 Evolution of the average constraint force during the standard(solid lines) and multiple time step(dashed lines) dynamics of undecane. The multiple time step simulation was stopped after 5000 fs upon convergence of the average force.

5.7 Conclusions

A new implementation to carry out Car-Parrinello *ab initio* molecular dynamics simulations of extended systems using a combined quantum mechanics and molecular mechanics potential is presented. Our implementation allows the QM/MM boundary to cross covalent bonds such that the potential surface of a single molecular system is described by a hybrid potential. Since the potential surface of the molecular mechanics region is usually much less computationally demanding to calculate than that in the QM region, we have implemented a multiple time step technique to over-sample the MM region relative to the QM region. The goal here is to provide better ensemble averaging in the MM region which is usually larger in size and therefore usually has a higher degree

of configurational variability. We have demonstrated the multiple time step integrator will generate the same trajectory as a standard molecular dynamics integrator. Moreover, with a gradual rescaling of masses the energy conservation of a multiple time step simulation can be brought to the same level as a standard simulation. Finally we have demonstrated that the multiple time step QM/MM method can accelerate the equilibration and configurational sampling of a molecular dynamics simulation.

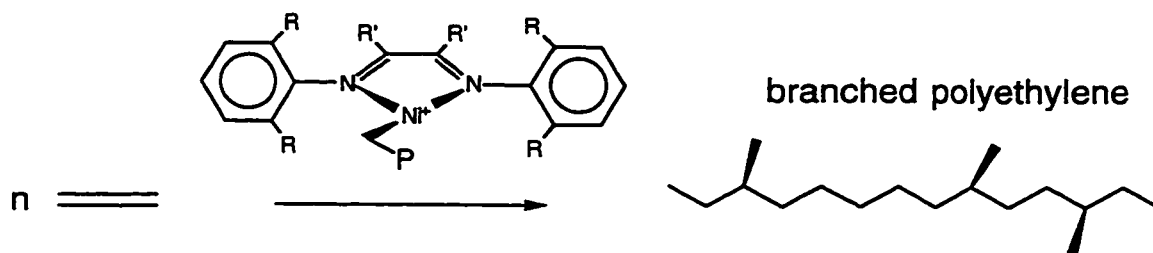
In this chapter we have also demonstrated the applicability of the combined QM/MM AIMD approach for studying transition metal based catalytic systems. In particular, we have examined the chain termination process in Brookhart's Ni(II) diimine olefin polymerization catalyst. In this simulation the QM/MM boundary crosses several covalent bonds, such that the Ni diimine core is treated by the DFT potential while the large bulky substituents are treated with the AMBER molecular mechanics force field. For the chain termination, the calculated free energy barrier of $\Delta F^\ddagger = 14.8$ kcal/mol at 25°C is in good agreement with the experimental result of $\Delta G^\ddagger = 15.5$ -16.5 kcal/mol at 0°C.¹²²

Chapter 6

Monomer Capture in Brookhart's Ni(II) Diimine Olefin Polymerization Catalyst: A Static and Dynamic QM/MM Study.

6.1 Summary

Mechanistic aspects of transition metal catalyzed olefin polymerization have been extensively studied, both experimentally and theoretically.¹²³ The focus of theoretical studies is most often the monomer insertion and chain termination processes. The capture or ejection of the monomer are either neglected or not thoroughly examined. However, the capture and expulsion are also integral parts of the catalytic cycle. Obviously, for chain growth to occur, the monomer must be captured and inserted into the growing polymer chain. For chain termination which is believed to occur via either unimolecular or bimolecular β -elimination, the ultimate result is the expulsion of the olefinic terminated polymer chain that was grown at that center. In the case of Brookhart's relatively new Ni diimine olefin polymerization catalyst which can produce polyethylene with a controlled level of short chain branching (Scheme 6.1), the capture process may play a key role controlling the extent of the chain branching. To date, no detailed theoretical studies of the capture/ejection processes in olefin polymerization catalysts have appeared. This is in part due to the scarcity of experimental data and due in part to the theoretical difficulty of treating the process. In this chapter we examine the monomer capture/ejection process with Brookhart's Ni-diimine catalyst with a combination of the ADF QM/MM and PAW QM/MM methods.



Scheme 6.1

6.2 Chain Branching Control in Brookhart's Ni-diimine Olefin Polymerization Catalyst System

6.2.1 Introduction

One of the most unique aspects of Brookhart's Ni diimine catalyst system, is that a controlled level of short chain branching is possible with the homopolymerization of ethylene (Scheme 6.1). Normally, branching is introduced in polyethylene via the introduction of short chain α -olefin comonomers, such as 1-hexene. Thus, this property is of commercial interest because it offers potential economic advantages. The degree of chain branching is observed to decrease with increasing monomer concentration whereas both the activity and molecular weights are found to be more or less independent of the monomer concentration.¹ Consistent with these observations, Johnson *et al.*¹ proposed the mechanism depicted in Figure 6.1. Both the insertion and termination proceed from the π -complex which has been identified as the catalyst resting state. The branching, however, is believed to proceed from the 'naked' metal alkyl complex via an isomerization mechanism as previously examined in Chapter 3. The monomer concentration effect on the chain branching can then be explained in terms of the equilibrium or kinetics involving the metal alkyl complex and the π -complex. The higher monomer concentrations, the faster the π -complex is formed and the less time there is to allow the isomerization process to take place from the metal alkyl complex. Therefore, the observed amount of branching diminishes with increased monomer concentration.

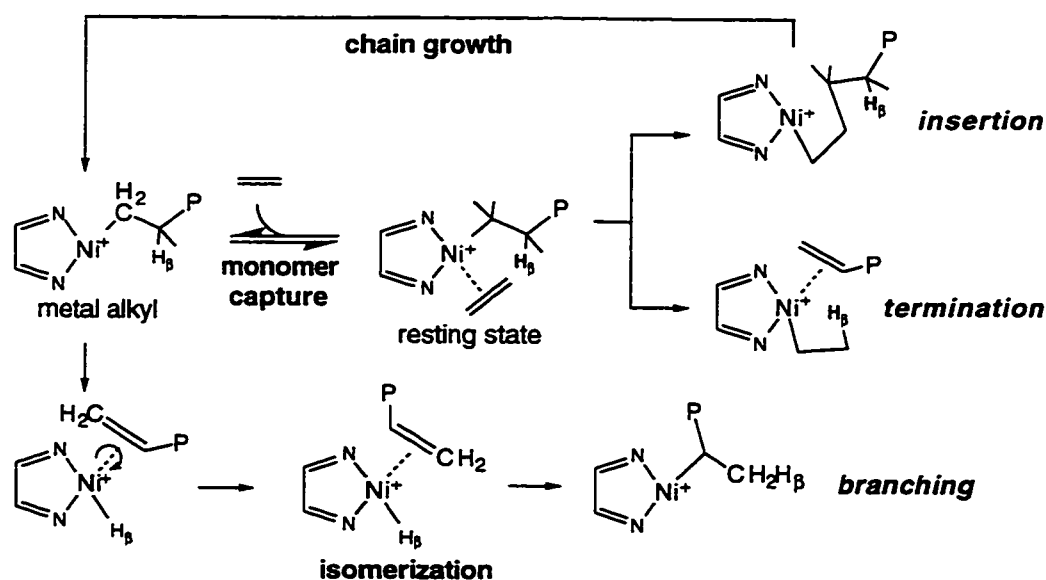
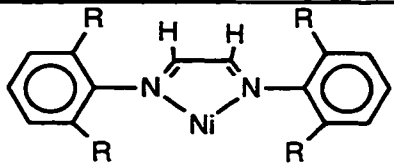
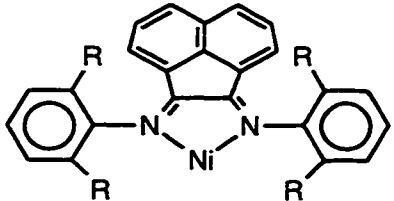
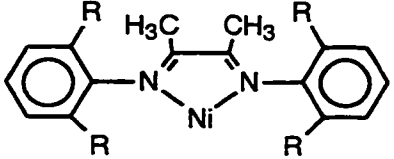


Figure 6.1 Proposed chain branching mechanism in Brookhart's Ni(II) diimine olefin polymerization catalyst system. Unlike the insertion and termination, the chain branching is proposed to proceed from the metal alkyl complex.

Increasing the steric bulk of the R substituents (Scheme 6.1) on the aryl rings dramatically increases the amount of branching that is observed. This can be explained in a straightforward manner with the proposed mechanism of Figure 6.1 in terms of the capture process. Brookhart and Johnson¹ have argued that increasing the bulk of the aryl substituents has the effect of hindering access of the olefin to the metal center. This has the effect of shifting the equilibrium towards the free alkyl, thus allowing for more branching to occur. Our previous QM/MM and pure QM calculations^{29,59} also agree with this argument since we find that the barrier of isomerization is not substantially influenced by the aryl substituents.

Another interesting chain branching substituent effect that has been observed experimentally involves the pendant R' group of the diimine ring. Table 6.1 details the observed experimental trends in terms of the amount of chain branching found in the resultant polymer versus the R' substitution. In each case the substituents on the aryl group are the same (R=*i*-Pr), and the polymerization conditions are identical (in toluene with MAO cocatalyst at 0°C with ethylene at 1 atm pressure). With R'=H, the lowest amount of chain branching is observed with only 7.0 branches per 1000 carbons of the polymer chain. Conversely, with R'=CH₃ in 3, the chain branching occurs with the highest frequency at 48.0 branches per 1000 carbons. When the pendant R groups are replaced with an acenaphthalene(ANAP) substituent as in 2, an intermediate amount of chain branching is observed with 24 branches per 1000 C. It is important to note that the amount of branching observed is dependent upon both the rate of branching and the rate of chain growth. For example, if we consider the rate of branching to be constant, then an increased rate of chain growth will result in less branching, and *vice versa*. By taking into account the rate of chain growth, which is shown in Table 6.1 in terms of the catalyst activity, the observed branches per 1000 C has been normalized to the activity observed with catalyst 3 in the last column. The normalized values provide an estimate of the rate (as opposed to the amount) of chain branching in each of the systems in relative terms. Table 6.1 reveals that the same overall trends are observed with the rates of chain branching as with the amount of chain branching. However, we notice that the disparity in branching between catalysts 2 and 3 is dramatically reduced upon considering the normalized data.

Table 6.1 Experimental Chain Branching Data.¹

Catalyst structure, R= <i>i</i> -Pr	structure no.	Activity (kg/mol cat /hr)	branches per 1000 C	
			raw	normalized to activity of catalyst 3
	1	6118	7.0	14
	2	5301	24.0	42
	3	3000	48.0	48

Since the R' substituents are physically removed from the active site they cannot directly block the access of the olefin to the metal center as do the R substituents on the aryl rings. Thus, the effect has been assumed to be electronic in nature.¹²² Based on our previous combined QM/MM study (Chapter 3) we suggest that there may be an indirect steric effect at work. The aryl rings, which prefer an orientation parallel to the central diimine ring due to an enhanced conjugation, are inhibited to do so by substitution in the R' position. The greater the hindrance, the more perpendicular the aryl rings become to the diimine ring. This has the effect of 'closing' the active site as depicted in Figure 6.2 for R'=H and CH₃. Figure 6.2 reveals that with the smaller R'=H substituent, the aryl rings can assume a more parallel orientation, thus opening up one side of the metal center for olefin capture. Thus, the substitution in the R' position may have both an indirect steric influence in addition to the electronic influence on the capture equilibrium/barrier.

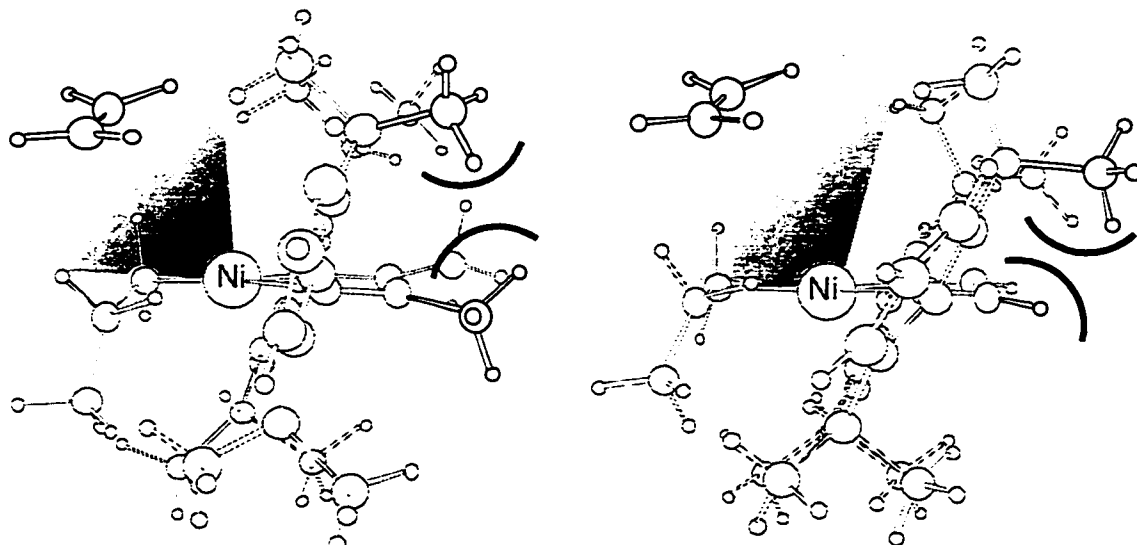


Figure 6.2 Possible indirect steric effect of the R' diimine substituents on the monomer capture process.

In Chapter 3, we explored the isomerization process with the combined QM/MM method. As previously noted, both theoretical and experimental results suggest that the equilibrium or possibly the kinetics between the metal alkyl and the π -complex control the rate of branching with the isomerization process playing a less consequential role. In all of the theoretical studies of Brookhart's catalyst that have recently appeared,^{63,175,176} none have examined the olefin capture process from naked alkyl to the π -complex. In this section we examine the interesting R' substitution effect on the chain branching rates as shown in Table 6.1. If the branching is controlled by the equilibrium between the naked alkyl and the π -complex, then the effect of the substitution can be determined by examining the thermochemistry of the naked alkyl versus the π -complex.

6.2.2 Computational Details

The methodology followed here is identical to that used in Chapter 3, with the following exceptions and modifications. The most notable methodological difference was that in this study the modified IMOMM coupling scheme⁹⁸ introduced in Chapter 2 was used instead of the original IMOMM scheme.¹⁵ Here a link bond ratio, α , of 1.385 was used for the N-C(aryl) link bond in order to reproduce the average bond distance of 1.44 Å observed in related experimental X-ray crystal structures.¹⁷⁷⁻¹⁷⁹ In calculations where the pendant R' group is treated in the MM region, a link bond ratio of 1.38 was adopted when R'=CH₃ and a ratio of α =1.34 was used when R'=ANAP. In these cases, the link bond ratios were adjusted to reproduce the bond distances from calculations where the R' group is included in the QM region.

In this study, structural optimization of the QM/MM complexes involved a global minimum search of the MM subsystem with the QM subsystem frozen (The procedure is outlined in Chapter 2). The global minimum search involved performing 100 ps of molecular dynamics on the MM subsystem at 800 K where structures were sampled every 2 ps. Each of the 50 sampled structures was then partially optimized. The best 10 of these partially optimized structures was then fully optimized. The resulting lowest energy structure was considered to be the 'global' minimum for the particular frozen QM geometry. During the full optimization of the QM/MM system, the global minimum search was performed once at the beginning to provide the 'best' initial MM structure for the given QM structure. The global search was not used in subsequent geometry optimization cycles. However, upon convergence of the geometry optimization, the global search was repeated in order to ensure that a new global MM minimum did not evolve as the QM subsystem changed. If the resulting structure was found to be more stable than the original by 0.2 kcal/mol, then the whole QM/MM optimization process was repeated starting from this new structure.

Ethene binding energies were calculated as the total energy of the olefin π -complex subtracted from the total energy of the free metal alkyl complex plus the free ethene. For all complexes, the growing chain was modeled by a propyl group. The propyl group has been previously shown¹²¹ to be an appropriate model for the growing chain since it accounts for the β - and γ -agostic interactions with the metal center.

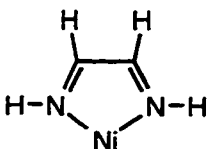
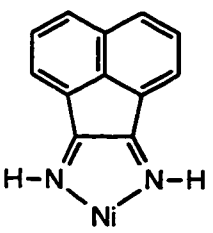
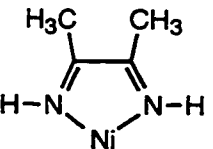
6.2.3 Results and Discussion

In this study we attempt to correlate the olefin binding energy to the rate of chain branching that is observed experimentally, in order to elicit the nature of the branching control. We are making two primary assumptions here. First, we assume that the equilibrium between the free alkyl and the π -complex dominates the control of the branching rate. Thus, we are neglecting the influence of the capture barrier and the isomerization barrier on the branching rate. Since it is really the free energy difference ΔG° that is directly related to the equilibrium constant, the second assumption we are making is that the trends in olefin binding energy will be the same as the free energy trends. Since the binding energies are generally fairly substantial for cationic single-site catalysts,¹⁸⁰ this is a reasonable approximation according to standard enthalpy-entropy compensation arguments.¹⁸¹⁻¹⁸³ The goal in this study is not to quantify the equilibrium between the free alkyl and the π -complex, but rather to determine the nature of the R'

substituent effect on the branching. Later in this chapter we will attempt to estimate ΔG° and ΔG^\ddagger for the olefin capture process.

We first try to correlate the branching rates to the capture energy as a pure electronic effect of the R' substitution. For this purpose, the catalyst systems without the aryl rings should be a good model since in their absence the indirect steric interactions can not occur. Therefore, if the R' substituents are treated at the QM level, the trends seen in the capture energy will be purely electronic in nature. We will assign these model systems for catalysts 1, 2, 3 the "a" sub-label to indicate that the aryl rings have been replaced with hydrogen atoms and that the systems are treated purely at the QM level. The olefin binding energies with model systems 1a, 2a and 3a are given in Table 6.2.

Table 6.2 Capture Energies without steric effects.

Pure QM structures	model	$\Delta E_{\text{capture}}$ (kcal/mol)
	1a	-16.9
	2a	-14.7
	3a	-15.0

Comparing the binding energies of 3a and 1a where R'=CH₃ and H, respectively, we note that the electronic effect of the CH₃ substitution is to reduce the binding energy. If we compare this result to the observed branching rates presented in Table 6.1, we note that the trend is compatible with our proposed model. In other words, since the binding energy is decreased upon replacement of R'=H with R'=CH₃, the equilibrium is shifted towards the metal alkyl complex in 3a where more branching can occur. When the binding energy of 2a with the ANAP substituent is considered, we find that it does not follow the observed trends in the branching rates. Whereas the rate of branching for

catalyst **2** lies between those of **1** and **3**, the binding energy of **2a** is the smallest of all the systems.

Although the binding energies for **1-3a** do not correlate exactly with the branching data, we can explain the trends observed in Table 6.2 in terms of the π -donating abilities of the R' substituents. We first consider the nature of the interaction between the olefin and the metal center in the π -complex. As is commonly done, we separate the π -bonding into two components. The first component involves the donation of electron density from the π -orbital of the olefin to the empty d orbitals of the metal. Conversely, the second component involves the back-donation of charge density from the Ni center to the empty π^* orbitals of the olefin.

Table 6.3 The effect of R' substitutions on the charge density on Ni and the back-bonding in the π -complex.

model	Ni charge ^a in alkyl complex (e)	olefinic C-C distance in π -complex (Å)
1a	+0.546	1.389
2a	+0.487	1.394
3a	+0.505	1.391

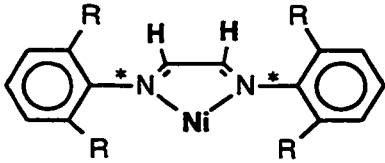
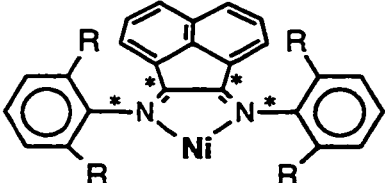
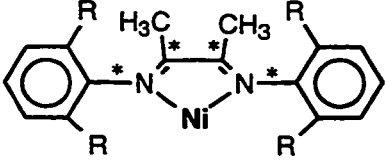
^aMulliken charge analysis.

Although the Ni has a formal d-electron count of 8, theoretical calculations show the presence of little back donation in the π -complexation.⁵⁹ Distortion of the bound ethene moiety can be used as a metric of this, since the more back-bonding there is present the longer the olefinic C-C bond becomes. Table 6.3 shows that the calculated olefin C-C bonds in all three π -complexes of **1-3a** are approximately 1.39 Å, an elongation of only 0.07 Å from the free ethene value which is calculated to be 1.32 Å. Such an elongation is typical of that observed in d⁰ metal olefin π -complexes where there is negligible back-donation because of the low d-electron count. Thus, the olefin binding in the Ni diimine systems appears to be dominated by the donation of olefin π -density into the empty d-orbitals of the metal center. Therefore, the more electron-deficient the Ni center is, the stronger the olefin binding becomes. Table 6.3 gives the net atomic charges on the Ni in the alkyl complex based on a Mulliken population analysis. The results show that the order of electron deficiency, R'=H > CH₃ > ANAP, is consistent with the binding energies in Table 6.2. In terms of the R' groups, the better the π -donor ability of the substituent, the more electron density it is capable of donating to the metal and therefore the smaller the olefin binding energy. The trends in the binding energy

expressed in Table 6.2 are consistent with this model since π -donor ability of the substituents is generally ordered as $H \ll Me \sim aryl$.¹⁸⁴

If the R' substituent effect is purely steric in nature, then a model system in which the electronic effects of the substituents are removed can be used to test the hypothesis. With the QM/MM method, we can construct just such a model where the various R' substituents are modeled by a MM potential, and the electronic effects are kept constant by using the same model QM system. In this way, catalysts **1-3** can be modeled such that the $(HN=CH-CR=NH)Ni-Pr^+$ molecule is used for the QM model system, while the aryl rings and the R' substituents are treated by the AMBER95 force field. We will assign these "purely steric" model systems the "b" sub-label. Shown in Table 6.4 are the calculated olefin binding energies using the "purely steric" models **1b**, **2b** and **3b**. First we note that the QM component of the binding energies all reside close to 18 kcal/mol. This is to be expected since the QM models systems are the same in each calculation. The small variations in QM component of the capture energies are a result of the different steric environments presented by the catalyst framework due to the variation of the R' substituents.

Table 6.4 Capture Energies without electronic influence of the R' substituents.

QM/MM structures ^{a,b}	model	$\Delta E_{\text{capture}}$ (kcal/mol)	ΔE_{QM} (kcal/mol)	ΔE_{MM} (kcal/mol)
	1b	-16.1	-17.7	+1.63
	2b	-16.0	-18.5	+2.47
	3b	-13.7	-18.8	+5.12

^aasterisks denote the QM/MM link bonds. ^bin all cases the QM model system is $(HN=CH-CH=NH)Ni-Pr^+$.

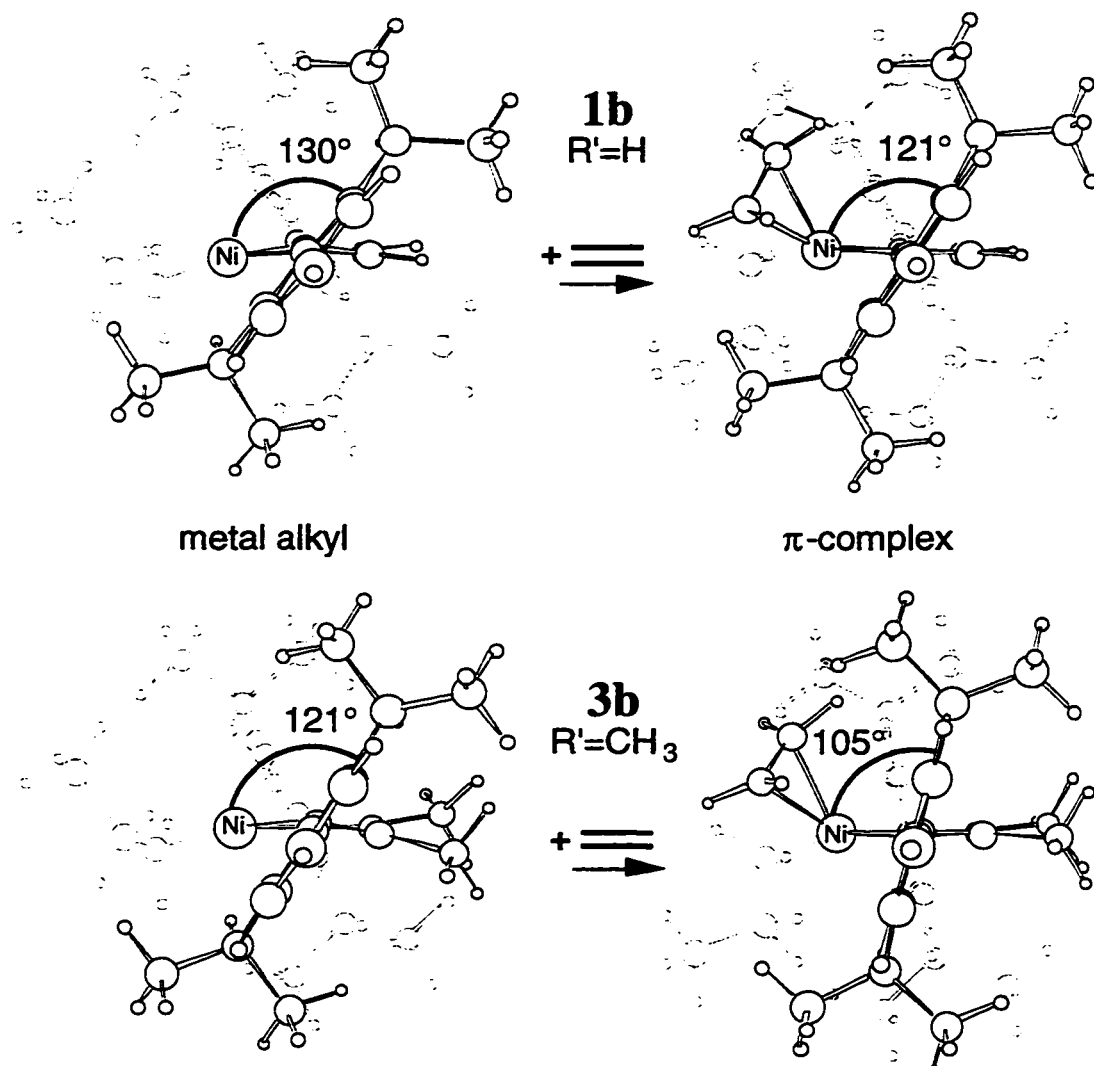


Figure 6.3 Optimized metal alkyl and π -complex structures of the model systems **1b** and **3b**. The ring plane angle, θ , of the foremost aryl ring is shown for each structure. The back-most aryl ring and the alkyl chain are ghosted for clarity.

The indirect steric effect as we have called it can be examined in more detail by comparing the olefin capture results of models **1b** and **3b**, where there is a 2.4 kcal/mol shift in the capture energy upon modifying $R'=H$ to $R'=CH_3$. First, recall that there is an electronic preference for the aryl rings to be aligned parallel to the diimine rings as to maximize π -density overlap and conjugation of the rings. Conversely, the electronically least favourable orientation of the aryl rings is perpendicular to the diimine rings where there is a minimal amount of π -overlap. In our QM/MM potential, this effect is modeled by a molecular mechanics N(diimine)-C(aryl) torsional potential. The torsional energy is related to the torsional angle between the diimine ring plane and the aryl ring planes,

which we have previously termed the "plane angle", θ (Figure 3.5). When the plane angle is 0° or 180° the diimine ring and the aryl ring are exactly parallel with one another, thus maximizing the conjugation. (Incidentally, in these systems such plane angles are physically unattainable because the *i*-Pr groups of the aryl rings would crash into both the R' group and the Ni center.) When the plane angle is 90° , the two rings are perpendicular to one another and there is no stabilization due to the ring conjugation.

Figure 6.3 shows the structures the metal-alkyl complex and the olefin π -complex for both structures **1b** (R'=H) and **3b** (R'=CH₃). The structures are oriented such that the N(diimine)-C(aryl) bonds lie perpendicular to the plane of the page as to emphasize the plane angles between the aryl rings and the central Ni-diimine ring. Also shown are the ring plane angles of the foremost ring of each of the four structures. Without the complexed olefin, the propyl chain in the metal alkyl complexes lies roughly in the plane of the Ni-diimine ring. Since the alkyl coordination sites of the Ni center are vacant, this allows the aryl rings to align themselves in a more parallel fashion to the Ni-diimine ring. In doing so, an *i*-Pr group of one aryl ring partially occupies one axial site of the metal center while an *i*-Pr group from the other aryl ring fills up the opposite axial site. In **3b** the ring plane angle is 121° whereas it is slightly larger in **1b**. Here the larger methyl group of **3b** prevents the ring from swinging back as much compared to that in **1b**.

Upon formation of the π -complex, the propyl group shifts to occupy one axial site of the Ni center since the olefin coordinates to the opposite site. The formation of the π -complex therefore forces the aryl rings to assume a more perpendicular orientation as to accommodate the olefin and alkyl chain. For model **1b**, the olefin complexation causes the plane angle in the foremost ring (Figure 6.3) to shrink by 9° from 130° to 121° . However, in model **3b** for which R'=CH₃, the effect is more severe with the plane angle shrinking by 16° from 121° to 105° upon olefin complexation. Thus, the complexation of the olefin more severely distorts the orientation of the aryl rings away from their preferred orientation in **3b** compared to **1a**. In our QM/MM potential, this has the effect of increasing the MM torsion energy. Summarized in Table 6.5 are the changes in the plane angles and MM torsion energy upon coordination of the olefin. We notice that the larger change in plane angle incurred with **3b** is reflected in a more unfavourable increase in the torsion energy. Specifically, the change in torsion energy, ΔE_{tors} , in **3b** is 7.5 kcal/mol whereas it is only 4.16 kcal/mol in **1b**. Also provided in Table 6.5 is the change in non-bonded van der Waals energy upon olefin complexation. The net values are negative because of the long range attractive component of the van der Waals potentials. (This effect has been previously observed with gas-phase combined QM/MM and pure

MM calculations of coordination complexes.)^{185,186} The change in van der Waals energy upon complexation is -2.17 kcal/mol in **1b** whereas it is only -0.21 kcal/mol in **3b**. The more repulsive van der Waals complexation energy in **3b** can be explained in terms of the increased steric repulsion that occurs between the R'=CH₃ groups and the *i*-Pr groups which parallels the unfavourable perpendicular orientation of the aryl rings relative to the central Ni-diimine ring.

Table 6.5 Change in geometry and energy components during olefin complexation.

model	change in plane angle, $\Delta\theta$		ΔE_{tors}	ΔE_{vdw}
	a ^a	b		
1b	-8.7°	-5.6°	4.16	-2.17
2b	-9.4°	-2.1° ^b	5.51	-2.92
3b	-16.0°	-16.9°	7.50	-0.21

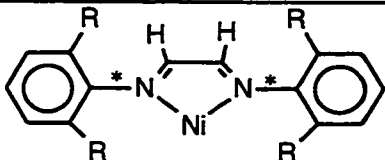
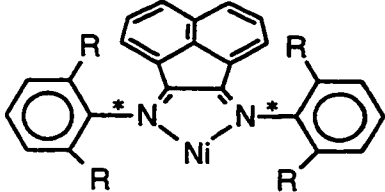
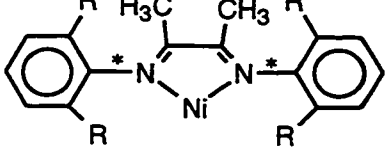
^asame as the foremost ring plane angle displayed in Figure 6.3. ^bthe ring plane angle here actually changes from 60.4° to 110.2°, but the deviation from the 90°, which has the energetic consequences, changes by -2.1° upon olefin complexation.

The steric demands of the R'=ANAP substituent of **2b** can be expected to be somewhere between that of the R'=H and R'=CH₃ substituents of **1b** and **3b**, respectively. Like the R'=H substituent in **1b**, the atoms of the R'=aryl substituent in **2b** lie in the plane of the Ni-diimine plane. However, the steric demands of the R'=ANAP group can be expected to be slightly larger due to the fact that the van der Waals radius of C is about 30% larger than H and that the aryl group extends out further than the R'=H does. Conversely the steric demands of the aryl group will be less than the methyl group, whose hydrogen atoms project out of the Ni-diimine plane, thus enhancing the interaction with the *i*-Pr groups. Table 6.4 shows that the olefin complexation energy with model **2b** is 16.0 kcal/mol, matching that of **1b**. Table 6.5 reveals that the change in plane angle is roughly equivalent with that observed in **1b**. This suggests that the steric demands of the R'=aryl substituent are similar to those of R'=H in this context. The change in torsion energy upon complexation is 5.51 kcal/mol. This is 1.4 kcal/mol higher than the 4.16 kcal/mol change observed with **1b**. The higher ΔE_{tors} in **2b** compared to that of **1b** can be accounted for in the torsional distortions in the ANAP group due to the interaction with the *i*-Pr groups of the aryl rings. Although the steric demands of **2b** can be estimated to be slightly more than **1b**, the van der Waals energy of complexation is actually enhanced. This seemingly contradicts the correspondence between the two. However, we notice that the R'=ANAP substituent has more atoms than either the R'=H

or $R'=CH_3$ groups which corresponds to more van der Waals interactions between the R' groups and the olefin that all lie in the long range attractive region of the potentials. Such a counter-intuitive size dependence with complexation energies has been previously observed with molecular mechanics studies of phosphine coordination energies with transition metals.^{185,186} Here it was found that using a standard Lennard-Jones potential the phosphine coordination energies were actually found to be enhanced with increasing size and cone angle due to this effect. Thus, in this QM/MM model the olefin binding energy of **2b** relative to that of **1b** and **3b** is slightly over estimated.

The olefin binding energies of the purely steric model, **b**, do not correlate well with the observed branching rates presented in Table 6.1. Whereas the branching rate of the $R'=ANAP$ catalyst, **2**, lies close to the extreme of the $R'=CH_3$ catalyst, **3**, the purely steric model places the olefin binding energy of **2b** much closer to **1b** than **3b**. If we admit to a slight overbinding of the olefin due to the van der Waals potential in model **2b** then the correlation is improved to a small degree.

Table 6.6 Capture Energies with both steric and electronic effects incorporated.

QM/MM structures ^a	model	$\Delta E_{\text{capture}}$ (kcal/mol)	ΔE_{QM} (kcal/mol)	ΔE_{MM} (kcal/mol)
	1c^b	-16.1	-17.7	+1.63
	2c	-14.0	-14.8	+0.76
	3c	-12.9	-16.9	+4.00

^aasterisks denote the QM/MM link bonds. ^bstructure **1c** is the same as that of **1b**. The results are repeated for comparison.

The purely electronic model, **a**, and the purely steric model, **b**, produced opposing trends in the olefin binding energy, neither of which correlated well with the branching rates. This suggests that the indirect steric effect may play a larger role than previously thought in controlling the olefin binding energy. We now incorporate both the electronic

and steric effects of the R' substituents in our model QM/MM potential. In this new model, which we sub-label **c**, the R' groups are relegated to the QM region such that their electronic effects are included in the potential. However, unlike the pure electronic model, the indirect steric effect is accounted for in the present treatment by including the aryl rings in the MM region. The electronic effects of the R' substituents are included in this treatment since they are part of the QM subsystem whereas in the previous models, **b**, they were treated in the MM region. (With this being the only difference, the optimized structures of the catalyst framework from the two models should be similar. Comparison of the ring plane angles of each of the structures with their counterparts in the other model show good agreement in the geometries of **2b** and **3b** with **2c** and **3c**.[‡] The RMS difference in the plane angles is only 3.2° with a maximum deviation of 7.2°.)

The capture energies for the mixed model, **c**, are given in Table 6.6 for the R'=H, ANAP and CH₃ substituents. The correlation between the estimated capture energies and the branching rates provided in Table 6.1 are better with the present model than either the purely steric or electronic models. Most significantly the expected trend is clearly reproduced with the order of the olefin capture energy being H > ANAP > CH₃. In the mixed model, the QM component, ΔE_{QM} , of the total olefin binding energy follows the trends of the pure electronic model (Table 6.2).

We note that the electronic characteristics of the ANAP substituent appear to dominate its influence on the olefin binding energy. This is evidenced by the fact that the difference in olefin binding energies between the ANAP catalyst and the R'=H system is the same in the present model as with the pure electronic model, **a** (Table 6.2). The results are therefore consistent with the notion that the planar ANAP substituent is only slightly more sterically demanding than the R'=H substituent. Trends in MM component of the complexation energy given in Table 6.6 show an anomalously low ΔE_{MM} for the ANAP catalyst. Again this can be attributed to the size dependent overbinding of the van der Waals potentials as previously discussed. The difference in ΔE_{MM} for the ANAP system in models **b** and **c** (+2.47 vs. +0.76 kcal/mol) is due to the fact that the torsional distortion of the ANAP substituent upon olefin complexation is accounted for in the MM energy in model **b** but in the QM energy in model **c**.

Whereas the influence of the ANAP substituent appears to be electronic in nature (relative to R'=H), the influence of the R'=CH₃ substituent can be attributed to both electronic and steric factors. The difference in olefin binding energy in the purely

[‡] Models **1b** and **1c** are the same.

electronic and purely steric models are 0.8 kcal/mol and 2.4 kcal/mol, respectively. The combined effect as modeled in **3c** is nearly additive with difference in olefin binding energy of 3.2 kcal/mol.

The energetic consequence of the indirect steric effect is largely dependent upon the molecular mechanics N(diimine)-C(aryl) torsional potential used. The stronger the barrier the more enhanced the steric effect is likely to be. The success we have attained with our earlier study of the Brookhart catalyst provided in Chapter 3, suggests that the standard AMBER95 potential used is a reasonable approximation to the true potential. However, we admit to some uncertainty in this potential. Despite this, the results show that the never before considered indirect steric influence is real. Thus, we conclude that the observed branching rates can be correlated to both the steric demands of the R' substituent in addition to the electronic nature of the substituent. Thus, increased branching can be achieved by enhancing the π -donating ability of the R' substituent or by increasing its steric bulk.

6.2.4 Conclusions

The goal of this study was to examine the nature of the R' substitution on the chain branching in the Brookhart Ni(II) diimine olefin polymerization catalysts. The branching rates were found to follow the trend $R'=H < ANAP < CH_3$. Experimental results suggest that the branching rates are controlled by the equilibrium between the π -complex and the metal alkyl.¹ Since the pendant R' groups are removed from the active site of the metal center, it has been assumed that the exhibited trends in the branching rates are an electronic effect of the R' groups. However, we have suggested there may also be an indirect steric effect at work due to an interaction of the R' groups with the aryl rings. This interaction forces the aryl rings to adopt an orientation which restricts access to the active site. Thus, the bulkier the R' groups the more sterically encumbered the active site becomes and the less favourable the olefin complexation. Therefore, the proposed net effect of the indirect steric interaction of the R' groups with the aryl rings is to shift the equilibrium towards the metal alkyl complex as to allow more branching to occur.

To test this hypothesis, three model systems were constructed - a) a pure electronic model where the indirect steric interactions were impossible, b) a purely steric model where the electron influence of the R' substituents were removed and c) a mixed model where both steric and electronic effects were included. Each of the three models were evaluated in terms of how well the olefin binding energies correlated to the

experimentally observed branching rates. The resulting olefin binding energies of neither the purely electronic model or the purely steric model reproduced the trends in the branching rates. With the purely electronic model, the binding energies were found to follow the trend $R'=H > CH_3 > ANAP$, whereas with the purely steric model the trend was $R'=H \approx ANAP > CH_3$. Both trends could easily be accounted for in terms of the electronic and steric characteristics of the R' substituents.

In the last model, where both the steric and electronic effects of the R' substituents were incorporated, the olefin binding energies were found to correlate well with the observed branching rates. Although the experimental data set is small, the results do suggest that both the steric and electronic characteristics of the R' substituents must be considered when tuning the chain branching capabilities of the catalyst. Recently, a number of promising olefin polymerization catalyst systems have appeared^{40,187-190} that strongly resemble the basic structure of the Brookhart catalyst, in that they possess two aryl rings that act to block the axial coordination sites of the metal center. In some of these related systems, the central ring involving the metal center is not fully conjugated. Therefore, the electronic effects of the equivalent R' substituents in these systems may be significantly weaker than in the present catalyst system. Thus, the indirect steric effect may be more dominant in controlling the chemistry of the system. Indeed we have utilized the idea of the indirect steric effect to enhance the molecular weight properties of the Zr-McConville¹²⁷ catalyst.

It is very common in catalytic systems that there is a strong interplay between electronic and steric effects. We have demonstrated how the QM/MM methodology can be used to isolate and decompose the effects of each. In this capacity the QM/MM method has great potential to be used as an analytical tool to provide a deeper understanding of the catalytic control.

6.3 Olefin Capture Barrier in Brookhart's Catalyst - A Static and Dynamics Study

6.3.1 Introduction

There have been an abundant number of computational studies of olefin polymerization catalysts including pure molecular mechanics studies,^{83,85,86,89,124} conventional electronic structure calculations,^{51-54,56,58,60,61,63,88,91,124,126,176,191-196} and now Car-Parrinello MD^{121,133,135,166,197,198} and QM/MM simulations.^{29,30,175} Virtually all of the theoretical studies have focused on the insertion and chain termination processes. One part of the chain propagation that has been overlooked in theoretical (and experimental) studies, is the monomer capture process. The reason for this is that the

capture of the monomer is not considered to be the rate determining step under normal polymerization conditions.¹²³ The specific case of Brookhart's Ni(II) olefin polymerization catalyst is unique in that the capture process is believed to play an integral role in controlling the chain branching. Thus, in the previous section we examined the thermodynamic aspect of the capture process.

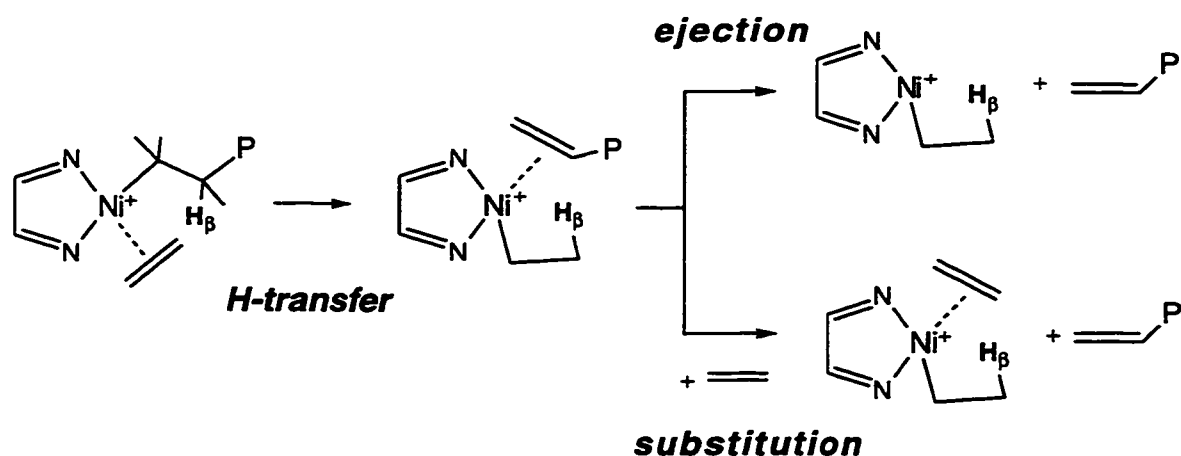


Figure 6.4 Full chain termination process including the loss of the olefin terminated polymer chain.

However, the reverse of the capture process, the monomer ejection, plays a role in the chain termination that is also often neglected. In most single-site catalytic systems, β -hydrogen elimination has been experimentally implicated to be the dominant chain termination process.¹²³ Whether the β -hydrogen elimination process is a unimolecular β -hydrogen transfer to the metal (not shown) or a bimolecular β -H transfer to the monomer (Figure 6.4), the process is not completed until the olefinic terminated polymer chain is ejected. The rate determining step has been assumed to be the hydrogen transfer process and not the ejection of the π -bound polymer chain. As depicted in Figure 6.4, the ejection of the polymer chain can occur via a purely dissociative manner or by the associative displacement by the monomer or solvent. Detailed theoretical studies of the termination process generally neglect the ejection process even though the olefin binding energies are often calculated to be in excess of 30 kcal/mol. Although there is an entropic cost to association that offsets the strong enthalpic tendency for olefin complexation, this has a limiting value of 12-15 kcal/mol ($T\Delta S^\circ$ at 298 K) for typical sized catalyst systems.¹⁹⁹ Thus, in some cases the ejection of the chain may in fact be the rate limiting process and not the hydrogen transfer.

The free energy of the olefin capture/ejection process can be mapped out by performing a series of frequency calculations on the static potential energy surface. Since these are computationally extensive calculations, even with density functional methods, these calculations are sparse. Furthermore, only the free energies of the overall capture process have been examined in this way.[◊] To date no one has examined the 'whole' free energy profile of the capture/ejection process, in order to determine if there is a barrier to the process. The mapping out of the entire free energy profile of the capture is hampered by the fact that the free energy transition is likely to lie in the weak bonding regime where there may be difficulties in applying a frequency calculation.³⁴ Furthermore, since the process has a large entropic contribution, the maximum on the zero-temperature energy surface is not likely to match the position of the free energy transition state. Thus, a number of expensive frequency calculations along the surface would be necessary to locate the maximum on the free energy surface. Finally, this is all further complicated when considering the process in solution where entropies of molecules are subject to more uncertainties.¹⁸¹ An alternative to the static approach to examining the free energy profile of the process is to use molecular dynamics or Monte Carlo methods. Here, the PAW QM/MM method provides us with a unique tool to explore the process.

In this section we map out the free energy surface of the monomer capture process for Brookhart's Ni(II) olefin polymerization catalyst, $(\text{ArN}=\text{C}(\text{R}')-\text{C}(\text{R}')=\text{NAr})\text{Ni}^{\text{II}}-\text{R}^+$ using a combination of static and dynamic methodologies. Our previous QM/MM calculations (Chapter 3) revealed that there was no enthalpic capture barrier for the $\text{Ar}=2,6\text{-C}_6\text{H}_3(i\text{-Pr})_2$, $\text{R}' = \text{CH}_3$ catalyst system. However, the existence of a free energy barrier can not be precluded. If a significant free energy barrier exists, then this may have possible implications to the chain termination and branching processes.

6.3.2 Computational Details

The computational method used in the PAW QM/MM simulations of the olefin capture process are the same as those used in Section 5.4. The most notable difference was that the multiple time step QM/MM method was applied to enhance the sampling of the large and 'floppy' aryl rings. The molecular mechanics region was over-sampled by a 20:1 ratio over the QM region, time steps of 7 au and 7/20 au were used for the QM and MM subsystems, respectively. Masses of the nuclei were set to 50.0 amu for Ni, 2.0 amu for N and C, and 1.5 amu for H in the QM region (including the MM link atoms). MM

[◊] In general, the corrections are found to be near the entropic limit of approximately 13 kcal/mol at 300 K.^{53,63}

atoms directly bonded to the MM link atoms were rescaled 10 fold such that the masses of hydrogen and carbon were 0.15 and 0.2 amu, respectively. The masses of all other MM nuclei were rescaling 400 fold, to 0.005 amu for carbon and 0.00375 amu for hydrogen. Unless otherwise specified, the electronic structure calculation of the QM model system involved a unit cell spanned by the lattice vectors $[[0.0\ 9.5\ 9.5][9.5\ 0.0\ 9.5][9.5\ 9.5\ 0.0]]$. The slow growth reaction coordinate used in all simulations was the Ni-olefin carbon midpoint distance. Scan times will be reported individually when discussed.

The details of all of the ADF QM/MM calculations reported are the same as that provided in Section 6.2.2. For the linear transit calculations reported, all degrees of freedom were optimized except for reported reaction coordinate. Both forward and backward scans were performed within the critical sections of the potential energy surface (i.e. stationary points or similar). QM/MM Frequency calculations were performed using the method described in Chapter 2. With QM/MM and pure QM frequency calculations, two point numerical differential of the energy gradient was performed in order to determine the Hessian matrix. Thermodynamic properties were evaluated according to standard textbook procedures.^{43,106} Since the vibrational entropy computed from the harmonic frequencies is extremely sensitive to variations in frequencies under 200 cm^{-1} it is recommended practice to replace the harmonic approximation for low-lying modes with a more realistic expansion of the potential surface.⁴³ However, in the present case the low lying-modes involved cannot be described within one of the well known approximations such as the hinder-rotor model. Unless otherwise specified, modes under 50 cm^{-1} have been removed from the analysis, the default setting in ADF. We estimate errors in our relative free energy calculations due to this approximation to be $\pm 4\text{ kcal/mol}$ for $T\Delta S_{\text{vib}}$, $\pm 1.2\text{ kcal/mol}$ for ΔE_{zpe} and ± 0.5 for ΔH_{vib} at 298 K. The error bars were estimated by examining the variation in these properties as a function of the cut-off used in our frequency analysis.

The PAW QM/MM simulations sample from the NVT ensemble and therefore the profiles correspond to Helmholtz free energies. We use ΔF to refer to the Helmholtz free energy determined from the PAW simulations. The frequency calculations correspond to Gibbs free energies, ΔG . In the limit of zero pressure, the Helmholtz and Gibbs free energies are equivalent.

Static profiles reported were generated from ADF. PAW was not used for this purpose because the program is not designed to conveniently perform these types of 'static' calculations. However, for both the pure QM model 4 and the QM/MM model 6,

an equivalent, but more sparse linear transit calculation has been performed with the PAW QM/MM program. Comparing the results generated from the PAW and ADF programs, the relative energies compared to the corresponding π -complex, were all within 0.8 kcal/mol.

6.3.3 Results and Discussion

We have examined the free energy surface of the capture process for three variations of the Brookhart Ni diimine catalyst, $(\text{ArN}=\text{C}(\text{R}')-\text{C}(\text{R}')=\text{NAr})\text{Ni}^{\text{II}}\text{-propyl}^+$. The first model, **4**, lacks any of the bulky substituents such that $\text{Ar}=\text{H}$ and $\text{R}'=\text{H}$. In the last two models, **5** and **6**, the bulky aryl rings $\text{Ar}=2,6\text{-C}_6\text{H}_3(i\text{-Pr})_2$ are modeled by a MM potential. With catalyst model **5** $\text{R}'=\text{H}$ while for **6** the $\text{R}'=\text{CH}_3$ group is also partitioned to the MM region. (The three complexes in this study can be related to the model systems described in Section 6.2. **4** corresponds to model **1a**, while **5** and **6** correspond to models **1b** and **3b**, respectively.) In all three cases, the electronic structure calculation is performed on the same model system where $\text{Ar}=\text{H}$ and $\text{R}'=\text{H}$.

Static Capture Profiles We first examine the 'static' potential energy surface of the olefin capture process. In our previous pure QM and QM/MM studies of the Brookhart Ni-diimine catalyst, it was mentioned that no enthalpic barrier to the capture process could be located. Here we present a more detailed examination of the potential energy surface in order to relate it to the free energy surface. Figure 6.5 shows the calculated enthalpy profiles of the ethene capture process for models **4**, **5** and **6**. The profiles were determined from a series of static ADF linear transit calculations where the reaction coordinate is defined as the distance between the midpoint of the olefin double bond and the metal center. The energies plotted are relative to that when the Ni-olefin midpoint distance is 7.0 Å.

Without the influence of the bulky aryl rings, olefin capture in **4** shows a gradual stabilization of the complex as the olefin approaches the metal center. The long range stabilization is due to the favourable electrostatic interactions of the electropositive metal center and the olefin. The short range and strong stabilization is attributed to the π -donor-acceptor interactions between the olefin and metal center as previously discussed. In models **5** and **6** the strong stabilizing interactions are offset by the repulsive steric interactions between the olefin and the aryl rings that force the rings to less favourable perpendicular orientations. Thus, the addition of the bulky rings in the hybrid QM/MM potentials in **5** and **6** produce two notable changes in the capture profiles. First, the

exothermicity of the olefin binding decreases as first presented in Section 6.2. Secondly, although there is no clear transition state, there is a plateau with a steep enthalpic cliff leading to the π -complex. The ledge of the plateau occurs at approximately 2.9 Å for 5 and slightly more inwards at 2.8 Å for 6. Again this can be rationalized in terms of an increased steric hindrance to the formation of the π -complex that delays the net stabilization due to the electronic interaction between the olefin and the metal center.

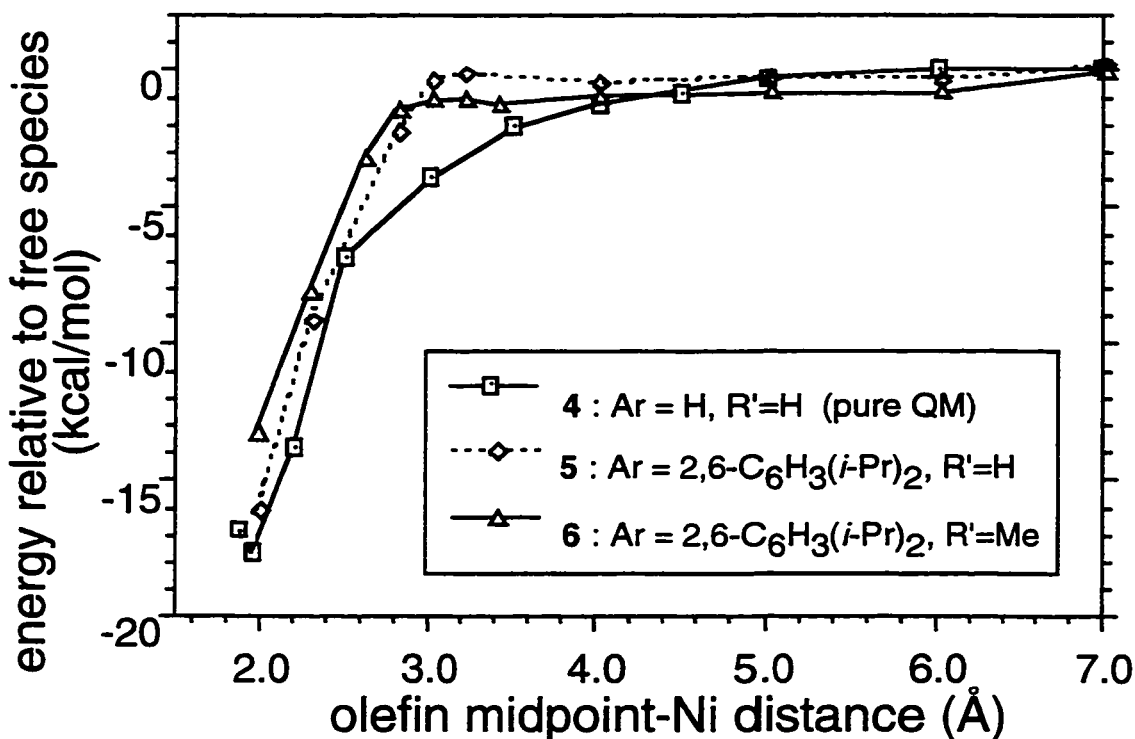


Figure 6.5 'Static' linear transit energy profiles of the capture process. The reaction coordinate of the linear transit calculations was the distance between the Ni and the midpoint of the olefin double bond. Energies are plotted relative to their the energy at RC=7.0 Å.

Slow Growth Free Energy Profiles In order to explore the free energy surface of the capture process at 300 K, we have performed a series of molecular dynamics simulations of the process for models 4, 5 and 6 using the slow growth method. The slow growth reaction coordinate utilized in all simulations was the olefin midpoint to Ni distance. For all three models, forward and reverse scans were performed where the reaction coordinate was continuously varied from 4.0 Å to ~2.3 Å over 20000 timesteps. Plotted in Figure 6.6 are the resulting free energy profiles of the forward scans (capture). The profiles for all three models are plotted relative to the state at the beginning of the simulation where the reaction coordinate is 4.0 Å. Extension of the profile beyond the RC=4.0 Å mark was only performed for model 6 which amounts to 3.5 kcal/mol. The

profiles of **4** and **5** are plotted in Figure 6.6 assuming the same long range behaviour of the free energy profile.

The baseline used in Figure 6.6 demands some explanation. Extension of the free energy profile beyond the 4.0 Å point is complicated by the fact that the demands of the electronic structure calculation grow with the cell size and at large reaction coordinate values, a relatively large simulation cell is required. For the RC=2.3-4.0 Å simulation window, the electronic structure calculation is already quite demanding and extension of the free energy profile for larger reaction coordinate values requires an even larger simulation cell, thereby putting enormous strains on the computational resources. For these reasons, only the free energy profile of **6** was extended beyond the 4.0 Å point. In this extended simulation window a unit cell spanned by the lattice vectors ([0.0 11.5 11.5] [11.5 0.0 11.5] 11.5 11.5 0.0)) in Ångstroms was utilized. Only the outward scan was performed where the reaction coordinate was varied from 4.0 Å to 6 Å over 16000 time steps. At approximately the 5.5 Å mark, the free energy begins to level out where it is 3.4 kcal/mol lower than at the 4.0 Å mark. For all three model systems, the free energy was still dropping at the RC=4.0 Å mark. However, we note that the slope of profiles begin to converge at the 3.70 Å point. Comparison of the absolute constraint forces during the simulations reveals that there is also a convergence of the absolute value of the force. This further suggests that in the long range region, the behaviour of the profiles of the three models are similar. This is a reasonable assumption for models **5** and **6**, which have nearly identical structures. However, for model **4** which does not have the large bulky aryl rings this assumption is more approximate and the extended profile for this model is likely to drop off faster, likely resulting in an overestimation of the barrier in this case.

With the approximation that the same baseline is used for all three model systems for both forward and reverse scans, the slow growth capture barriers are reported in Table 6.7, with error estimates based on the hysteresis. Also provided in Table 6.7 are the locations of the free energy maxima in terms of the reaction coordinate. The capture barriers follow the expected trend with $4 < 5 < 6$. Without the bulky aryl rings the capture barrier of **4** lies about 3 kcal/mol lower than that either **5** and **6**. The free energy barrier of **6**, with R'=CH₃ is slightly larger than **5** with R'=H. Since the R' group is treated in the MM region the enhanced barrier of **6** is only steric in nature. Our earlier study of the electronic and steric effects of the R' substituents suggests that the inclusion of electronic effects in the model **6** may further enhance the barrier.

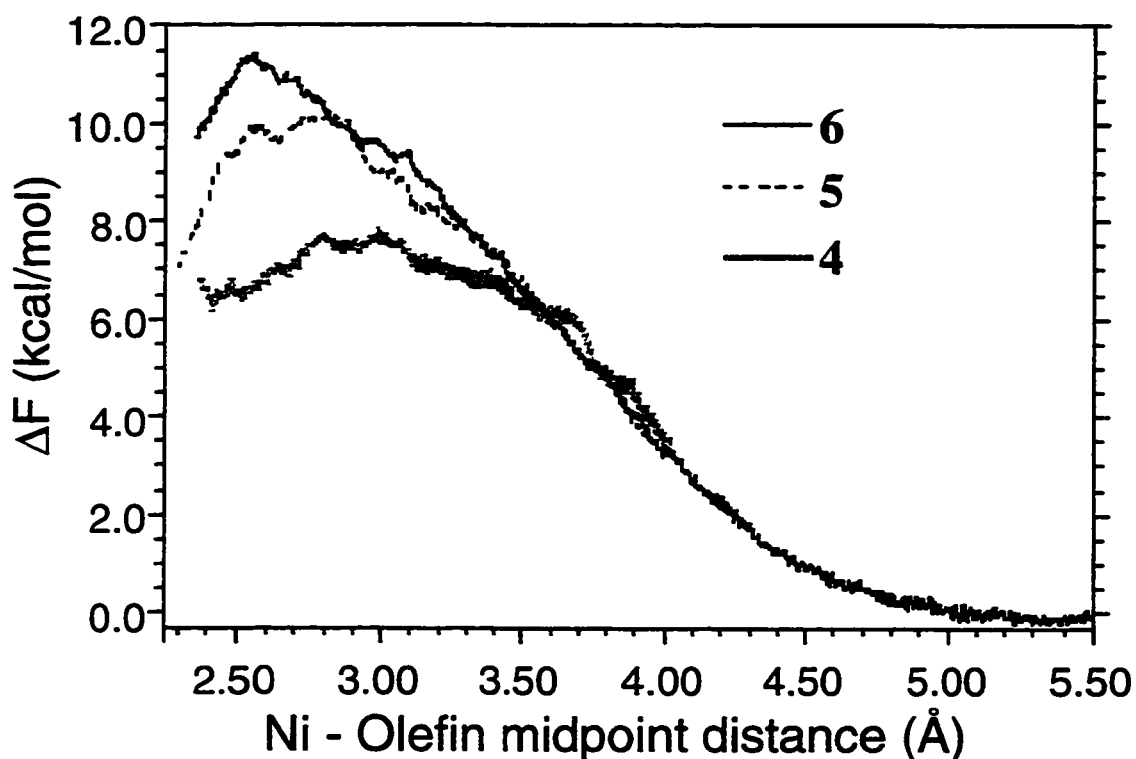


Figure 6.6 Slow growth free energy profiles of the capture process at 300 K for models 4, 5 and 6. Free energies are all plotted with the same baseline at a reaction coordinate value of 4.0 Å were only the profile of 6 is extended.

The location of the free energy maxima also follow the expected trends. As the steric congestion about the metal center increases, the location of the maximum decreases. These trends are in line with the trends observed with the potential 'ledges' in our static calculations of the potential surface given in Figure 6.5. Some other noteworthy observations can be made that relate the free energy profiles with the static potential energy profiles. For example, the gradual slope of the static potential of 4 is translated into a broad free energy barrier. This contrasts the profiles of 5 and 6 which have steep enthalpic 'ledges' and also steeper behaviour of the free energy surface near the maximum. Consistent with the notion that the enthalpic tendency to form the π -complex is offset by entropic factors, the free energy maxima of 5 and 6 lie slightly more inwards (~ 0.2 Å) than the steep ledges of their respective enthalpic profiles shown in Figure 6.5. There is one noticeable difference between the 'static' profiles and the free energy barriers of Table 6.7. The olefin capture energies of models 5 and 6 differ by 2.4 kcal/mol whereas the free energies are approximately the same. Thus, the uptake and capture barriers in this case may be controlled by different factors.

Table 6.7 Free energy barriers including hysteresis from slow growth simulations of the capture process.

structure	description	$\Delta G_{\text{capture}}^{\ddagger}$ ^{a,b} (kcal/mol)	barrier distance ^b (Å)
4	Ar=H, R'=H	7.5 ± 0.4	2.93 ± 0.05
5	Ar= 2,6-C ₆ H ₃ (<i>i</i> -Pr) ₂ , R'=H	10.3 ± 0.2	2.75 ± 0.08
6	Ar= 2,6-C ₆ H ₃ (<i>i</i> -Pr) ₂ , R'=CH ₃	10.8 ± 0.5	2.66 ± 0.10

^aassuming the baseline at a reaction coordinate value of 4.0 Å can be used for all trajectories as discussed in the text. ^berror bars determined from hysteresis

Nature of the Free Energy Barrier. Even without the bulky aryl rings the free energy barrier of capture for model complex **4** is significant, amounting to 7.5 kcal/mol at 300 K according to our slow growth simulations. The slow growth free energy profile of **4** has a maximum at approximately 2.93 Å. At this point the static capture profile of Figure 6.5 shows that the olefin-catalyst complex is only stabilized by 3.5 kcal/mol. If the entropic cost of the association at this point is large then this could account for the large barriers observed. In order to further understand the nature of the capture barrier, we have attempted to elicit a free energy barrier of **4** from static frequency calculations. Full ADF frequency calculations of the optimized π -complex and the free alkyl have been performed. Additionally, a constrained frequency calculation has been performed on the linear transit structure at RC=3.0, approximately where we estimate the free energy maximum to be from the PAW MD simulations. In this frequency calculation the degree of freedom associated with the reaction coordinate is constrained.

The resulting free energies relative to the free metal-alkyl and ethene are reported in Table 6.8. The free energy of olefin complexation is estimated to be exergonic $\Delta G_{\text{capture}}^{\circ} = -3.1$ kcal/mol at 298.15 K. Based on the constrained frequency calculation of the transition state complex where the reaction coordinated is fixed to a value of 3.0 Å, the capture barrier is estimated to be 7.7 kcal/mol at 298 K which is in reasonable agreement with the barrier predicted from the slow growth simulation. (We will discuss the comparison in more detail later) Table 6.8 reveals that the entropic cost of association at this point amounts to 10 kcal/mol whereas the enthalpic stabilization at this point is only 3.4 kcal/mol. Thus, based on this approximation the capture barrier can be considered to be an entropic barrier resulting in the loss of translational and rotational degrees of freedom upon association.

Table 6.8 Thermodynamic data at 298 K for the olefin complexation for model catalyst 4 relative to the free species.^a

quantity	contribution to ΔG° (kcal/mol)	
	π -complex	RC=3.0 Å
$-T\Delta S_{\text{trans}}$	+10.6	+10.6
$-T\Delta S_{\text{rot}}$	+5.2	+5.1
$-T\Delta S_{\text{vib}}$	-3.2	-5.7
$-T\Delta S_{\text{total}}$	+12.5	+10.0
ΔH_{trans}	-0.889	-0.889
ΔH_{rot}	-0.889	-0.889
ΔH_{vib}	+1.6	+2.3
ΔE_{ZPE}	+1.6	+0.5
$\Delta E_{\text{complexation}}$	-16.9	-3.4
ΔH_{total}	-15.6	-2.3
ΔG at 298 K	-3.1	+7.7

At this point let us examine the effect of the approximations made in this analysis. We have assumed that the 6 rotational and translational degrees of freedom are completely converted into vibrational degrees of freedom. When the olefin is weakly bound, the resulting vibrations associated with the olefin metal bond will be of low frequency. Classical statistical thermodynamics¹⁰⁶ reveals that the absolute vibrational entropy associated with a particular normal mode vibration is inversely proportional to its frequency. Thus, when the olefin is weakly bound the potentially large loss of rotational and translation entropies is offset because they are transformed into vibrational degrees of freedom with high entropies associated with them. Oppositely, when the olefin is more strongly bound, the vibrations are of higher frequency and therefore have lower absolute entropies associated with them. Thus, the more strongly bound the complex, the higher the entropic cost of association. In general terms, there is an inverse relationship between the exothermicity and the entropic cost of association.¹⁸²

In comparing relative free energy of the π -complex where the olefin is strongly bound and the transition state structure, we notice that the results exhibit this inverse relationship. At the transition state structure, the enthalpic stabilization amounts to only 3.4 kcal/mol and the $-T\Delta S_{\text{vib}}$ compensation is -5.7 kcal/mol. In comparison, at the π -complex where the enthalpic stabilization is about 17 kcal/mol the compensatory

component is diminished to -3.2 kcal/mol. Since all frequencies under 50 cm^{-1} were removed in the thermodynamic analysis, we suggest that estimated capture free energy barrier of 7.7 kcal/mol provides an upper limit. This is because, in this case, the lowest four vibrational modes were discarded in each calculation and therefore, potentially four of the six vibrational modes associated with the olefin complexation were removed. Since most of the high entropy vibrational modes that would offset the loss in rotational and translation entropy have been removed from the analysis, we are overestimating the entropic cost of association.

In our treatment we have assumed that the translational and rotational entropies of the interacting components are completely lost and replaced with the vibrational terms. In the limit of no bonding, these vibrational degrees of freedom will become indistinguishable from the lost rotational and translational ones. Thus, it has been suggested that a better approach to treating the entropic cost of weak associations (as in our transition state structure), is to assume that the translation and rotational entropies of the separate components is not completely lost upon association.²⁰⁰ In this way, the entropic cost of association is treated as some fraction of the 15.7 kcal/mol maximum ($T\Delta S_{\text{rot}} + T\Delta S_{\text{trans}}$ of Table 6.8) that is dependent upon the exothermicity of the association.^{181,182} Unfortunately, this approach is also problematic since there is no satisfactory relationship to determine what fraction to use.

In order to compare the capture barriers from the static calculations and the molecular dynamics simulations, we must correct the static barrier estimate for terms not accounted for in the MD simulation. The thermodynamic components given in the Table 6.8 that are not accounted for in the PAW slow growth simulation are ΔE_{ZPE} , ΔH_{vib} , ΔH_{trans} and ΔH_{rot} .[◇] When these components are removed from the static barrier, it drops from 7.7 kcal/mol to 6.8 kcal/mol. This compares to the 7.5 kcal/mol slow growth barrier of the capture process for complex 4. As discussed before, we suggest that the static barrier estimate represents an upper limit and thus, it seems that the slow growth method has overestimated the barrier. One explanation that we have discussed is extended tail of the free energy profile which was taken from the simulation of 6 is not appropriate for the pure QM model 4.

The calculated slow growth barrier for the pure QM model 4 was estimated to be 7.5 kcal/mol whereas for models 5 and 6, they are 10.3 and 10.8 kcal/mol, respectively.

[◇] The equipartition of energy theorem states that all degrees of freedom contribute $RT/2$ to the enthalpy. Since the energy levels in our classical molecular dynamics simulation are continuous, there is no change in the sum of ΔH_{vib} , ΔH_{trans} and ΔH_{rot} throughout the slow growth simulation.

Thus, the addition of the bulky aryl rings increases the barrier by only 3 kcal/mol. Since the barrier is entropic in nature, the difference must arise from the constriction of the active site cavity of metal center by the aryl rings which would enhance the loss of rotational and translational entropy of the complexing olefin. From Table 6.8, we note that for model 4 the entropic cost of association at the transition state is 10 kcal/mol. The same quantity for the π -complex where the olefin is strongly bound is 12.5 kcal/mol, a difference of 2.5 kcal/mol. We would expect that the entropic cost of association at the transition states of 5 and 6 would be somewhere between that of the π -complex and transition state of 4. With this argument, the difference of 3 kcal/mol observed for the barriers of 5 and 6 with that of 4 is reasonable, albeit somewhat high.[◊]

The small, but observable difference in capture barriers between models 5 and 6 can be qualitatively rationalized on similar grounds. We suggest that the $R'=CH_3$ substituent in 6 acts to close off the active site due to the interaction with the aryl rings more so than does the $R'=H$ group in 5. This has been depicted earlier in Figure 6.2. The openness of the coordination site can be directly related to the angle ϕ as defined in Figure 6.7b. The ϕ angle is related to the plane angle θ except that it measures the angular deviation from the perpendicular orientation of the aryl ring with the central Ni-diimine ring as opposed to the deviation from the parallel orientation. Thus, the larger the ϕ angle, the more open one of the axial coordination sites of the Ni center as shown in Figure 6.2. Plotted in Figure 6.7b are the ϕ angles for models 5 and 6 during the course of the slow growth simulation of the capture process. We notice that for complex 6 the ϕ angles remain under 20° throughout the simulation, whereas in model 5 one of aryl rings has a much larger ϕ angle. Thus, Figure 6.7 offers a crude rationalization of the barrier difference as arising from a more adverse entropic cost to association in 6 due to the restriction of the translational and rotational degrees of freedom of the ethene molecule in the more hindered active site compared to that of 5.

[◊] Unfortunately, constrained QM/MM frequency calculations at the capture transition states of 5 and 6 could not be performed. Therefore we have not estimated the free energy barrier of capture from frequency calculations of models 5 and 6.

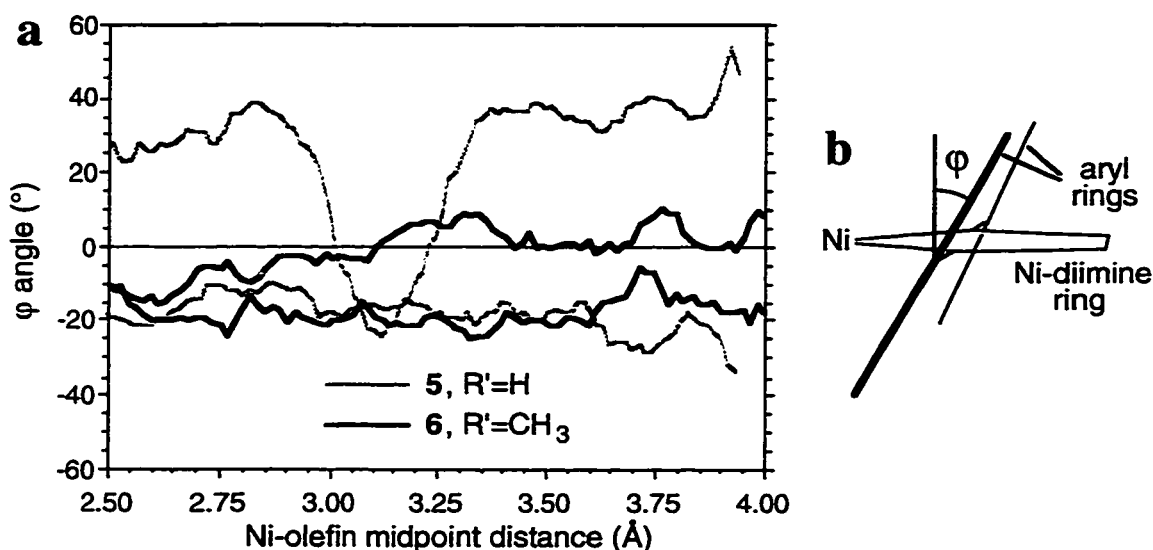


Figure 6.7 a) Deviation of the plane angle from perpendicular orientation of the aryl rings relative to the diimine ring extracted from the slow growth simulation of the capture process for models 5 and 6. b) definition of the angle ϕ .

Stability of the olefin π -complex Based on experimental NMR studies, the olefin π -complex is believed to be the catalytic resting state with Brookhart's Ni-diimine catalyst system.¹ We can estimate the free energy of capture from our molecular dynamics simulations if the trajectory is continued inward until the formation of the π -complex. For model system 6, for which the free energy surface was mapped outward until it leveled off, a slow growth simulation has been performed where the reaction coordinate has been varied from a value of 1.8 Å to 2.75 Å over 15000 time steps. Thus, the entire free energy profile has been mapped out from the olefin π -complex to the 'free' species over three simulation windows. The full - piecewise free energy profile is given in Figure 6.8. Since the outermost slow growth simulation where the reaction coordinate was varied from 4.0 Å to 6 Å corresponds to the reverse scan, it was decided to also perform the reverse scan of the innermost simulation window from the π -complex to free energy transition state. Thus, plotted in Figure 6.8 is the full unidirectional slow growth free energy profile of the olefin ejection process from the π -complex outward. The corresponding forward scan of the entire capture process has not been performed because of computational expense of the simulation particularly for the outermost simulation window.

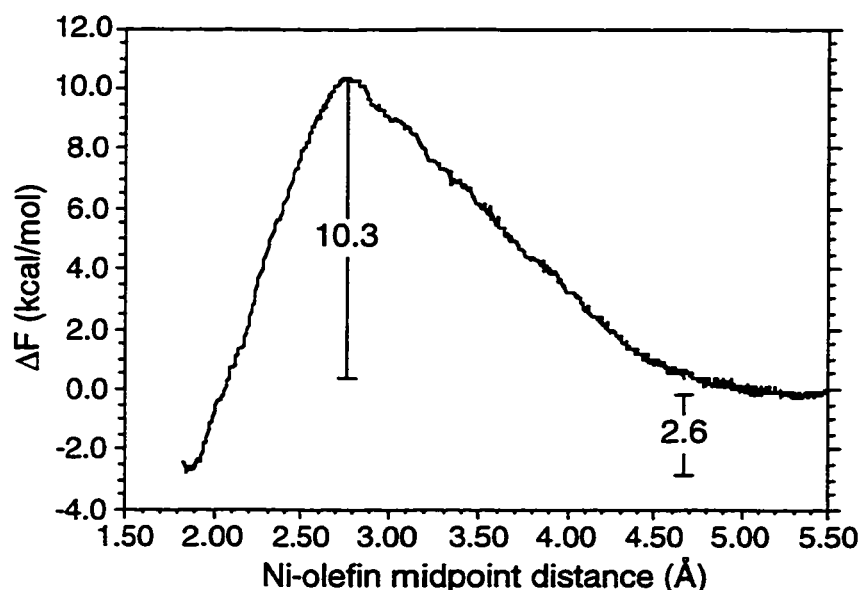


Figure 6.8 Slow growth free energy profile of the olefin ejection process for model catalyst system **6**. The total profile consists of three separate simulation windows. The innermost window spanning a reaction coordinate range of 1.8 Å to 2.75 Å, the middle window spanning 2.75 Å to 4.0 Å and the outermost window spanning the reaction coordinate values of 4.0 to 6 Å.

Figure 6.8 reveals that the olefin capture is favourable with $\Delta F^{\circ}_{\text{capture}} = -2.6$ kcal/mol. Thus, the slow growth simulation suggests that (without quantum dynamical effects accounted for) the olefin π -complex is stable in the gas-phase limit at 300 K. This agrees with the experimental observations.¹ This result also agrees with our previous molecular dynamics simulation of the olefin π -complex.²⁰¹ Using the same methodology,[§] the olefin π -complex of **6** was simulated for 1 ps[◇] where no constraint was used to tether the olefin to the metal center. Within this simulation time, the olefin π -complex was found to be stable. This contrasts previous *ab initio* molecular dynamics simulations of zirconocene olefin polymerization catalyst¹⁶⁶ where during simulations of the π -complex it was observed that the olefin would immediately detach itself from the metal center at 300 K if a constraint were not imposed. Interestingly, the catalytic resting state in these complexes is considered to be the free alkyl complex.¹²³

[§] The exception here is that the multiple-time step procedure was not applied.

[◇] With mass rescaling the fictitious time scale is equivalent to approximately 1.5 ps.

Table 6.9 Thermodynamic data at 298.12 K for the olefin complexation for model catalyst **6** based on a QM/MM frequency calculation.^a

quantity	contribution to ΔG° (kcal/mol)
$-T\Delta S_{\text{trans}}$	+10.7
$-T\Delta S_{\text{rot}}$	+5.6
$-T\Delta S_{\text{vib}}$	-3.2
$-T\Delta S_{\text{total}}$	12.9
ΔH_{trans}	-0.889
ΔH_{rot}	-0.889
ΔH_{vib}	+1.8
ΔE_{ZPE}	+2.7
$\Delta E_{\text{complexation}}$	-13.7
ΔH_{total}	11.0
ΔG° at 298 K	+1.9

We have also estimated the free energy of capture from QM/MM frequency calculations of the free alkyl and the π -complex of **6**. From this we can compare the results from the methods and correct the slow growth estimate for quantum dynamical effects. Table 6.9 details the various components of the free energy of complexation resulting from this analysis. The entropic cost of association is estimated to be $-T\Delta S = 12.9$ kcal/mol which is similar to that presented in Table 6.8 for model catalyst **4** were $-T\Delta S = 12.5$ kcal/mol. The similarity in the results suggests that the free energy of olefin uptake and therefore the equilibrium between the π -complex and metal alkyl is controlled primarily by the enthalpy of binding. The entropic cost of olefin complexation has been measured experimentally by Rix and Brookhart²⁰² for a similar Pd(II) ethylene-CO copolymerization catalyst and found to be $-T\Delta S = +10.8$ kcal/mol at 300 K. ($\Delta S_{\text{complexation}} = -36$ e.u.) The agreement between the experimental and theoretical results is fair, but they reaffirm our analysis that we are overestimating the entropic cost of association in our static calculations. At the same time, the overestimate is not too severe.

The total free energy of olefin complexation is calculated to be endergonic with $\Delta G^\circ_{\text{capture}} = +1.9$ kcal/mol. Thus, in the gas phase our static QM/MM model implies that the olefin π -complex is not stable, which contradicts our molecular dynamics simulations. However, the terms of the static free energy estimate not included in the classical MD

simulations amount to +2.7 kcal/mol. When these terms are removed from the static estimation of the free energy, it also becomes negative with $\Delta G^\circ = -0.8$ kcal/mol. Thus, when the free energies are properly compared, there is good agreement. Additionally, as previously stated we are likely overestimating the entropic cost of association in the static calculations. Thus, when this is considered, the agreement between the static and dynamic calculations improves.

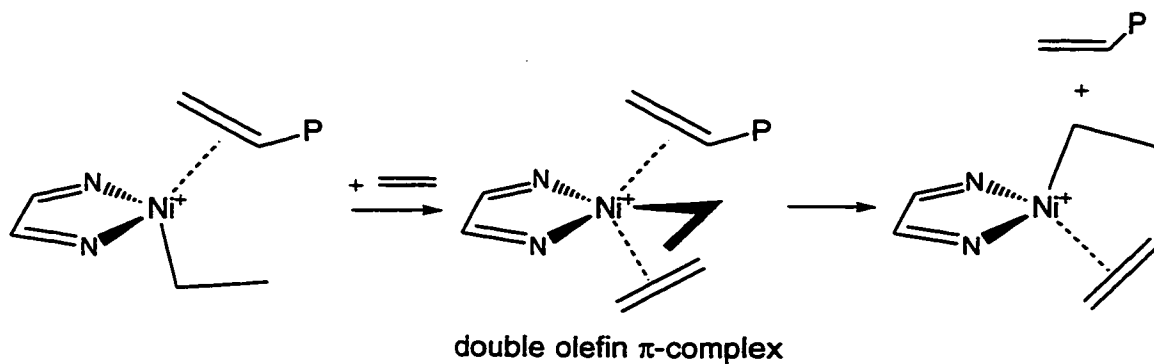
When the quantum effects are corrected for in the slow growth estimate of the free energy of capture, the capture becomes endergonic with $\Delta F^\circ_{\text{capture}} = +0.1$ kcal/mol. Thus, both the PAW and the ADF QM/MM estimates of the free energy of complexation are slightly endergonic in the gas-phase. This does not agree with the experimental results which identify the olefin π -complex to be the catalytic resting state. When the electronic effects of the R' substituents are accounted for, we can expect the estimate of the capture free energy to become even more endergonic (Section 6.2). Since these experiments are performed in dichloromethane, the discrepancy between the calculated and experimental results may be due to the solvation. For the low dielectric solvents used for polymerization, we estimate that the effect of solvent upon the free energy of olefin capture will be small. On enthalpic grounds, the solvation will slightly weaken the olefin binding energy. Based on continuum solvation calculations using the COSMO²⁰³ implementation within ADF,²⁰⁴ we predict that the olefin binding energies will diminish by less than 2.7 kcal/mol in dichloromethane.[◊] On entropic grounds, the binding will be slightly more favourable in solution, since at standard states the free species have less volume available to them in solution than in the gas-phase. The value of the entropic adjustment can be estimated from the solvent density,²⁰⁵ and in the case of dichloromethane, it amounts of 3.2 kcal/mol at 300 K. Thus, we suggest that the effect of solvation is to shift the free energy balance toward that of the complexed species.

The results of the static and dynamic results are in good agreement with one another. Although the calculated free energies of capture are estimated to be positive, values are close to zero. Aside from sampling errors in the dynamics simulations and the errors due to the low frequency modes in the normal mode analysis, there is another possible explanation to account for the calculated positive free energies of complexation. As mentioned in Section 6.2, the so-called indirect steric effect may be overestimated in

[◊] COSMO calculations have been performed on the pure QM model, 4, using the gas-phased optimized structures of the π -complex, ethene and the metal-alkyl complexes. Since, the cavitation free energy has not been considered, the value given (2.7 kcal/mol) is a high estimate.

our QM/MM model because of an overly strong torsional potential used for the N(diimine)-C(aryl) bond.

Associative versus Dissociative Displacement. Our studies of the monomer capture process can act as a model for the unimolecular ejection of the polymer chain from the catalyst center. Alternatively, the olefin terminated polymer chain can be ejected by the associative displacement by an incoming monomer molecule. Particularly in high monomer concentrations, the associative displacement of the olefin terminated chain may be more favourable than dissociative displacement. We have performed preliminary static ADF QM/MM calculations to try to establish the favourability of the associative displacement process compared to that of the dissociative process. We have examined the associative displacement for the pure QM model, **4** and the QM/MM model, **6**. As a model for the olefin terminated growing chain, a propene moiety was utilized. For both model catalysts, a stable intermediate was located that could be characterized as a double π -complex as depicted in Scheme 6.2. To investigate the associative displacement, we have performed a series of linear transit calculations where first the incoming olefin is pulled in using the Ni-olefin midpoint as a reaction coordinate. Then from the double π -complex, the propene moiety is then pulled out using the equivalent reaction coordinate. The barriers reported here, correspond to the maxima of the linear transit profile which have not been further refined using true transition state optimizations.



Scheme 6.2

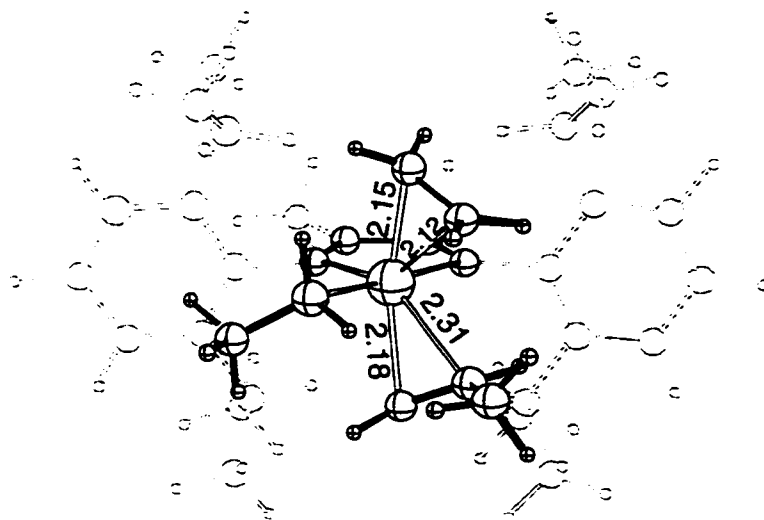


Figure 6.9 Optimized structure for the double olefin π -complex of model 6.

Without the bulky ligands in 4, the formation of double olefin π -complex is exothermic by $\Delta E_{2\text{nd capture}} = -12.2$ kcal/mol and forms without an enthalpic barrier. Subsequent removal of the propene complex also occurs without barrier. The overall substitution process without the bulky ligands is determined to be slightly endothermic with $\Delta E_{\text{substitution}} = 0.6$ kcal/mol. When the bulky ligands are considered in model 6, the substitution profile is drastically different. First the exothermicity of the second olefin uptake drops dramatically to only $\Delta E_{2\text{nd capture}} = -2.3$ kcal/mol and a linear transit profile reveals that there is a small enthalpic barrier of 1.7 kcal/mol. When the propene moiety is removed from the double π -complex, there is calculated barrier of 3.3 kcal/mol with the overall substitution process being slightly exothermic with $\Delta E_{\text{substitution}} = -1.5$ kcal/mol. The optimized double olefin π -complex is sketched in Figure 6.9 and the reaction profile is sketched in Figure 6.10.

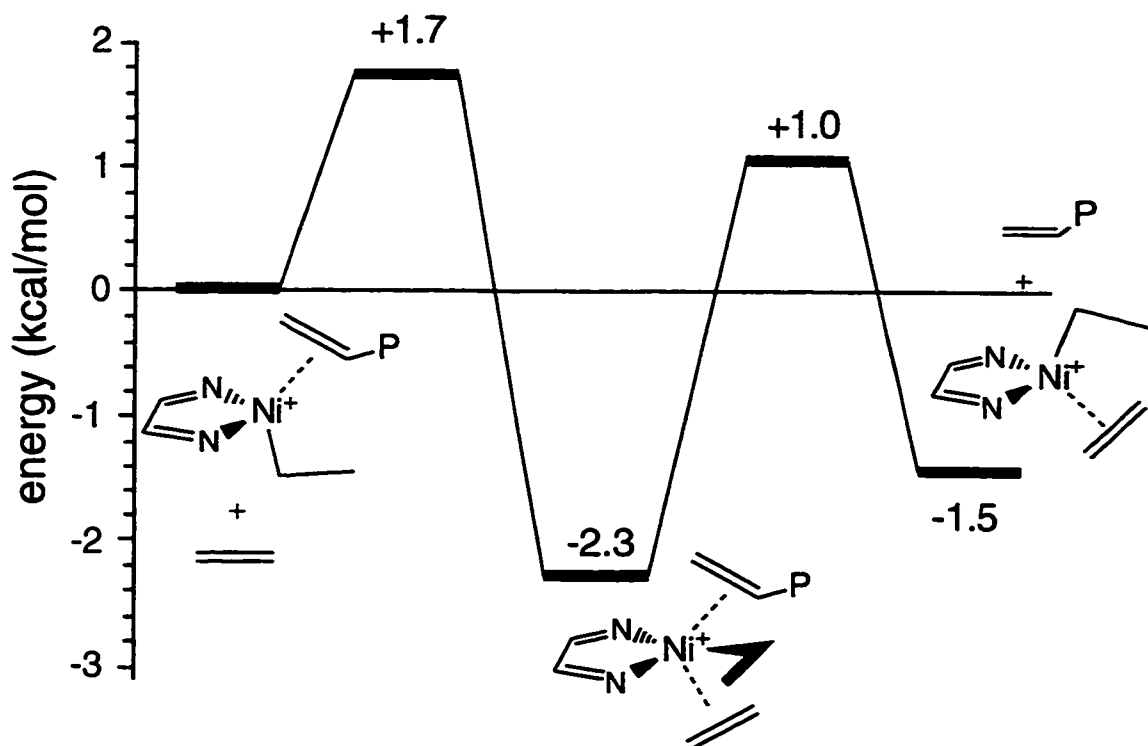


Figure 6.10 Static energy profile for the formation of the double olefin π -complex in catalyst 6.

The shallow nature of the substitution profile depicted in Figure 6.10 reveals that the associative displacement process will be dominated by entropic factors. Future studies of the process, therefore must examine on the free energy surface and not just enthalpic profile. Based on our studies of the ejection process, we can offer a very rough estimate of the gas-phase free energy barrier of substitution. Using the enthalpic barrier of the formation of the double olefin π -complex, and the entropic cost of association of $-T\Delta S_{\text{tot}} = 12.9$ kcal/mol from Table 6.9 we can roughly estimate an upper bound for the gas-phase free energy barrier of substitution to be 14.8 kcal/mol at 300 K.

Implications to Chain Termination and Chain Branching The overall chain termination process involves a hydrogen transfer process which results in the formation of a olefin terminated chain which is π -complexed to the metal as depicted in Figure 6.4. The termination process is completed when the long chain is ejected. If the ejection is dissociative, then this process is the reverse of the olefin capture process that we have simulated with a series of slow growth molecular dynamics calculations of models 4, 5 and 6. The assumption made here is that the ethene moiety is a reasonable approximation to the olefin terminated long chain.

Experimentally, the free energy barrier of termination for catalyst **6** where $\text{Ar}=2,6\text{-C}_6\text{H}_3(i\text{-Pr})_2$ and $\text{R}=\text{CH}_3$ is estimated¹²² to be $\Delta G^\ddagger = 15.5\text{-}16.5$ kcal/mol at 273 K. This agrees with our unidirectional slow growth gas-phase free energy barrier of estimate of $\Delta F^\ddagger = 14.8$ kcal/mol at 300 K (Chapter 5). The estimated capture barrier from our PAW QM/MM slow growth simulation amounts to 10.8 kcal/mol at 300 K. Since free energy of capture is estimated to be -2.6 kcal/mol (without quantum dynamical corrections), the PAW QM/MM slow growth ejection barrier is then 12.9 kcal/mol. The results imply that the hydrogen transfer step is indeed the rate limiting in the overall chain termination process, even in the gas phase. This agrees with the experimental observation that the polymer molecular weights are found to be independent of monomer concentration.¹

Our analysis of the nature of the olefin complexation suggests that the entropic gain of dissociation in the gas-phase is near the limit of 15 kcal/mol at 300 K. For the Brookhart catalysts which have olefin uptake energies in the same range, this puts the overall free energy of ejection close to zero. However, for other single-site catalysts, the olefin uptake energies have been calculated to be more than 30 kcal/mol.¹⁸⁰ Thus, for such systems ejection of the chain may be the rate limiting step in the overall termination process. If this is the case, then high molecular weights may be achievable even though the hydrogen transfer process has a low barrier. We should note in this case that the associative displacement must be considered in more detail.

In Section 6.2, we were able to correlate the olefin uptake energy to the experimentally observed branching rates. The arguments presented there suggest that the branching rates are controlled by the thermodynamics of the capture process and not the kinetics. Our investigation of the nature of the capture barrier concurs with this conclusion. Since we have determined the capture barrier to be entropic in nature, it would be difficult to explain the observed trends in the branching rates for the $\text{R}'=\text{H}$, ANAP and CH_3 series (Table 6.1) if the capture barriers controlled the branching rates. This is because according to the arguments presented here, we would expect the size of the active site in the $\text{R}'=\text{ANAP}$ catalyst to be more similar to that of the $\text{R}'=\text{H}$ system than to the $\text{R}'=\text{CH}_3$ catalyst. This then contradicts the observed branching rates. Although the investigation of the capture barrier is interesting, we conclude that it does not play a dominant role in determining the branching rates.

6.3.4 Conclusions

In this section we have attempted to map out the free energy surface of the olefin capture and ejection events in the catalytic cycle of olefin polymerization by Brookhart's Ni-diimine catalysts of the type $(\text{ArN}=\text{C}(\text{R}')-\text{C}(\text{R}')=\text{NAr})\text{Ni}^{\text{II}}\text{-propyl}^+$. We have used both conventional 'static' frequency calculations and slow growth molecular dynamics methods to examine the process for three model catalytic systems. The pure QM model 4 with $\text{R}'=\text{H}$ and $\text{Ar}=\text{H}$ does not possess the bulky aryl rings. In models 5 ($\text{R}'=\text{H}$) and 6 ($\text{R}'=\text{CH}_3$) where $\text{Ar}=\text{Ar}=2,6\text{-C}_6\text{H}_3(i\text{-Pr})_2$, the aryl rings and the R' substituents are accounted for via a molecular mechanics potential. In all three models, the electronic structure calculation involves the $(\text{HN}=\text{CH}-\text{CH}=\text{NH})\text{Ni}^{\text{II}}\text{-propyl}^+$ molecule.

Examination of the static potential energy surface of all three models, 4, 5 and 6, reveals that there is no enthalpic barrier to the capture process. However, both the static and molecular dynamics simulations suggest that there is an entropic barrier to the association that originates in the loss of rotational and translational entropies upon association that is not compensated by the enthalpy of coordination. The PAW QM/MM slow growth barriers were calculated to be 7.5, 10.3 and 10.8 kcal/mol at 300 K for catalysts 4, 5 and 6, respectively. Our analysis suggests that the trend in the barriers can be related to the size of the active site. The more constricted the active site, the greater the loss of entropy before the system can be stabilized by the coordination. From this simple picture the PAW slow growth simulations of the olefin capture exhibit the expected trends in the capture barriers. Catalyst 4 lacks the bulky aryl rings that can block the coordination sites of the metal center, resulting in a 3 kcal/mol smaller barrier than either 5 or 6. The small difference in capture barriers between 5 and 6 can be rationalized in terms of the interaction of the R' group with the aryl rings that in 6 acts to close off the active site. The free energy barrier for the pure QM model 4 has also been estimated from a series of frequency calculations. This approach provides a barrier of 7.7 kcal/mol (and 6.8 kcal/mol without quantum dynamical contributions.) which is in fair agreement with the 7.5 kcal/mol barrier (without quantum dynamical contributions) calculated from the slow growth simulations. Analysis of the estimate from the frequency calculations suggests that this barrier estimate represents an upper limit since the components of the vibrational entropy that compensate the loss of rotational and translational entropy upon association are partially neglected in the treatment.

In terms of the chain branching, we conclude that the capture barrier does not influence the branching rates. Rather it is the thermodynamics of the capture and not the kinetics of the capture that control the branching.

We have also examined the stability of the π -complex in the Brookhart catalyst system **6** which is believed to be the catalytic resting state. The PAW QM/MM slow growth profile of the capture process suggests that the π -complex is more stable than the free metal alkyl and ethene molecule in the gas phase with $\Delta G^\circ_{\text{capture}} = -2.6$ kcal/mol at 300 K. This agrees with our PAW QM/MM dynamics simulation of the π -complex which reveals that the olefin does not detach within the 1 ps simulation. On the other hand, our ADF QM/MM calculations suggest that the free energy of olefin complexation is positive with $\Delta G^\circ_{\text{capture}} = +1.9$ kcal/mol at 298 K. When quantum corrections are added to the PAW slow growth estimate of the free energy of capture, it also becomes slightly positive, thereby improving the agreement between the two methods. The calculated endergonic gas-phase free energies contrast the experimental result that the olefin π -complex is the catalytic resting state. The discrepancy may be due to solvation effects.

The associative displacement of the olefin terminated polymer chain by ethene has also been examined. In this preliminary study, the potential energy surface was mapped out using the ADF QM/MM method. For both the pure QM model **4** and the QM/MM model catalyst **6** a stable intermediate is located that can be characterized as a double olefin- π complex. The formation of the double olefin π -complex in **4** is exothermic with $\Delta E_{2\text{nd capture}} = -12.2$ kcal/mol, whereas in model **6**, the addition of the aryl rings significantly reduces this to $\Delta E_{2\text{nd capture}} = -2.3$ kcal/mol. Further studies must be conducted to elicit the free energy surface of the substitution process.

Despite the difficulty in examining the free energy surface, useful conclusions have been drawn and the work lays the foundation for further studies of the process. (In our current studies^{206,207} of related olefin polymerization systems,^{187,189} we are finding the capture process to play an even more critical role than in the current system)²⁰⁶ We find that the static and dynamic methods complement one another well. Thus, with the rapid advances in computation power, the combination of the ADF QM/MM and PAW QM/MM methods should provide a powerful tool for studying the free energy surfaces of transition metal based catalytic reactions in the future.

Chapter 7

Towards Solvation Simulations with the PAW QM/MM Method

7.1 Introduction

The presence or absence of solvent in a chemical system can lead to completely different chemical behaviour and reactivity. For this reason, the incorporation of solvent effects into quantum mechanical potential energy surfaces has been and still is an active area of theoretical chemistry. Methods for introducing solvent effects in quantum chemical calculations can be broadly divided into two categories²⁰⁸ - i) continuum models^{203,209,210} and ii) explicit solvent models. With continuum models the solvent molecules are not treated explicitly but rather they are expressed as a homogenous medium characterized by a bulk dielectric constant. This is shown pictorially in Figure 7.1a. The effect of the solvent is modeled by a buildup of charges[§] on the continuum surface such that there is a polarization of the QM wave function within the solute cavity. The amount of charge buildup and subsequently the polarization of the wave function is a function of the dielectric constant of the solvent. Continuum models have been quite successful in capturing the general aspects of solvation²¹⁰ and in many cases can be used for quantitative predictions. Since the solvent molecules are not treated explicitly, continuum models are relatively efficient. On the other hand, the lack of an explicit treatment has the disadvantage that continuum models do not provide any specific information concerning the intermolecular interactions.¹⁰

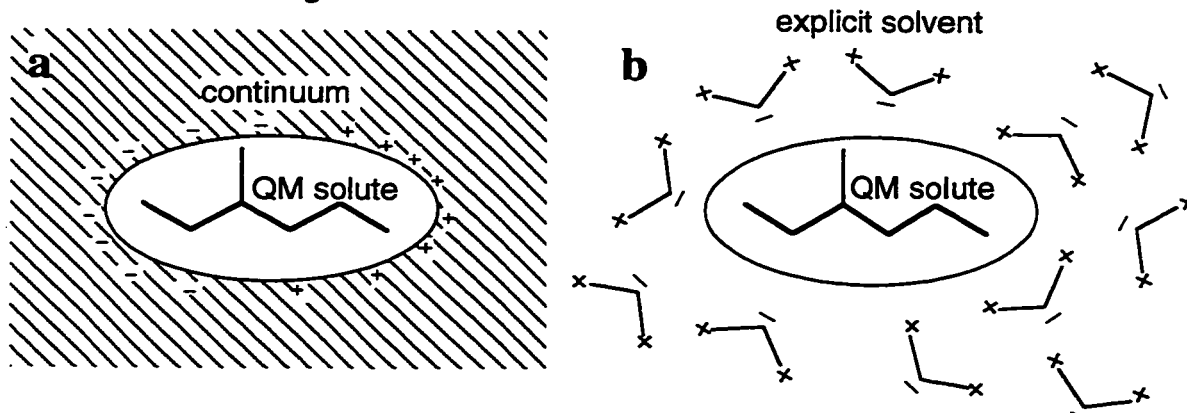


Figure 7.1. a) Continuum solvation model. b) explicit solvation model.

[§] Surface dipoles and other more complicated schemes can be envisioned.

The other broad approach to introducing solvent effects into the quantum mechanical potential surface is to treat the solvent molecules explicitly. With standard electronic structure calculations, this is achieved by surrounding the solute molecule with solvent molecules - all of which are treated quantum mechanically. For *ab initio* level calculations, generally only a few solvent molecules can be included. Although the interactions between the solvent molecules and solute molecule are treated rigorously - a few solvent molecules does not simulate the bulk solvent. Therefore, even qualitative conclusions can be dubious in nature. Recently, the Car-Parrinello¹³⁰ molecular dynamics method has allowed for simulations of bulk liquid to be carried out at the density functional level.²¹¹⁻²¹³ Although the approach is promising, it is still impractical for anything but the smallest solute and solvent molecules (e.g. water in water and methanol in water). The combined QM/MM approach seems well suited for performing explicit solvation simulations. A natural partition exists such that the solute is treated with quantum mechanics, while the explicit solvent molecules are handled by a much more efficient MM force field. Pioneering the approach, Gao and co-workers^{10,14,27,208,214,215} have demonstrated that the QM/MM method can be used to predict solvent polarization effects at the quantitative level for such properties as reaction barriers, equilibrium constants and solvation free energies.

In this chapter our efforts towards introducing explicit solvation effects into the Car-Parrinello framework with our PAW QM/MM implementation are presented. First we will briefly describe how the bulk liquid is to be simulated with periodic boundary conditions. Next we will provide a description of the QM/MM intermolecular potential that will be used to describe the interaction between the QM solute and MM solvent. Following this general discussion, details of the PAW QM/MM electrostatic coupling will then be given. Then the PAW QM/MM model will be evaluated for its ability to represent the true intermolecular interaction potential and to perform energy conserving dynamics. This work has the ultimate goal of allowing us to introduce solvent effects into our dynamical simulations of olefin polymerization catalysts. Although this has not yet been achieved, this chapter provides a foundation for future work.

7.2 Periodic Boundary Conditions

One of the most fundamental problems with applying the explicit solvation model involves the proper simulation of the bulk solvent. Consider the simulation of 1000 water molecules. At a density of 1.0 g/mL, these 1000 molecules would only fill a 30x30x30 Å container. Furthermore, the surface tension would force the system to assume a spherical

shape. In this microscopic drop of water, nearly half of the solvent molecules in our simulation would be at the surface of the drop. This will create many undesired effects, since it is known that water molecules at the liquid-vacuum surface behave quite differently than in the bulk. Thus, even a simulation of a 1000 water molecules, which is quite substantial in computational terms, is not a good model of the bulk liquid.

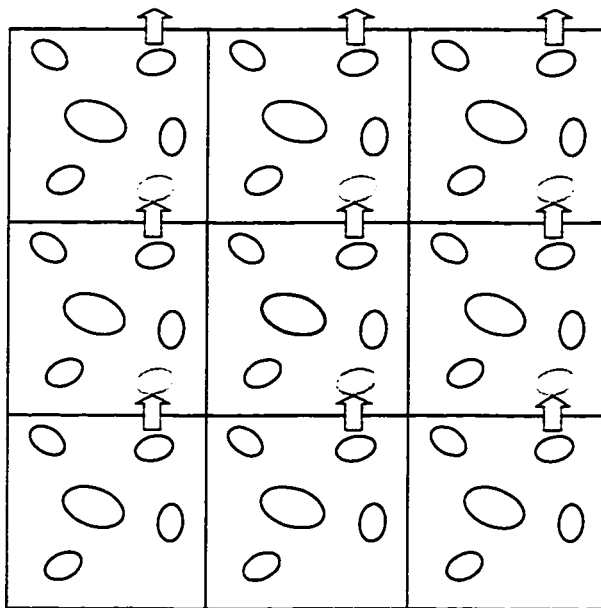


Figure 7.2. Two dimensional representation of periodic boundary conditions. The primary cell (shaded) is surrounded by periodic copies of itself in all directions. (Figure adapted from reference 31.)

The most common way to realistically simulate bulk liquid and to minimize the "surface" effects is to apply the technique of periodic boundary conditions.[◊] Conceptually, the system is placed in a simulation box that is surrounded by an infinite number of images of itself as depicted in Figure 7.2. The particles in the central cell interact with the images such that there is no liquid-vacuum surface. Furthermore, when a molecule leaves the central cell, it enters the opposite face with the same velocity as sketched in Figure 7.2. In this way, the bulk liquid is approximated. Since the central cell is exactly replicated in all directions, a periodic crystal is actually simulated. Thus care must be taken to insure that the periodic system is a good approximation to the macroscopic bulk liquid. Generally this is achieved by using a large simulation cell so as to minimize the artificial effects imposed by the symmetry and periodicity of the cell.

[◊] This was also discussed in Chapter 4 in the context of the Car-Parrinello methodology where the periodic boundary conditions were an unwanted artifact of the plane wave basis sets. Here the periodic boundary conditions are introduced in order to simulate the bulk liquid.

The size of the cell necessary for a particular simulation is primarily governed by the range of the intermolecular potentials involved and the range of the phenomenon under investigation.³¹ For determining equilibrium behaviour of liquids away from any phase transitions, periodic boundary conditions have been shown to be an excellent approximation. A detailed discussion of the periodic boundary approximation and its limitations can be found in the book of Allen and Tildesly.³¹

Minimum Image Convention. With the periodic boundary approximation, the central cell is conceptually surrounded by an infinite number of images of itself in order to simulate the bulk. The sum of interactions between the central cell and its infinite images is an undesirable quantity to calculate. For this reason, the "minimum image convention" is commonly adopted. The principle assumption here is that the largest contributions to the forces acting on a particle come from its nearest neighbours. Thus, with the minimum image convention an atom in the central cell will only interact with the closest periodic image of the other atoms. This is sketched in Figure 7.3 where the minimum image convention is illustrated for atom 1.

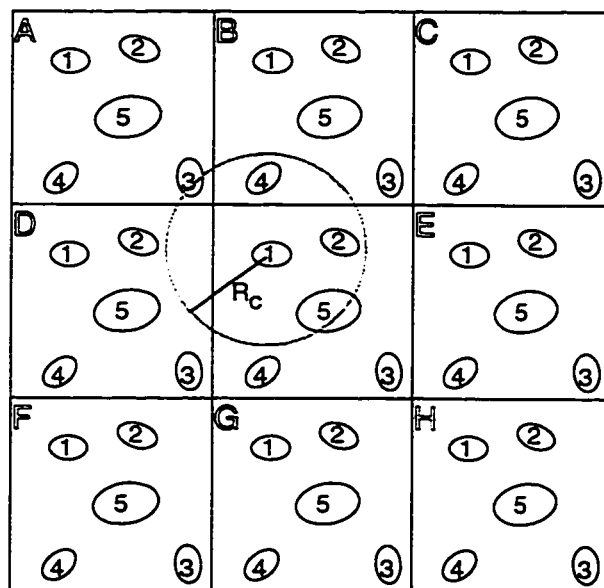


Figure 7.3. Example of the minimum image convention applied to atom 1. (Figure adapted from reference 31.)

The circle surrounding atom 1 with a "cut-off" radius R_c is used to show which pair potentials are included and which are discarded with the minimum image convention. For example, particle 2 of the central cell lies within the radius, R_c , and therefore this interaction is included in determining the force on atom 1. All other interactions with the periodic images of particle 2 are then discarded. Particle 4 of central

cell lies outside the cut-off radius and therefore this interaction is not included. However, its periodic image in the cell labeled 'B' does lie within the cut-off radius and, therefore, it is only this interaction that contributes to the total force on atom 1.

The minimum image convention can be enforced by imposing a cut-off function to all non-bonded potentials that all interactions involving distances greater than the cut-off radius, R_c , are set to zero. If the cut-off radius is too long, the minimum image convention will be violated. For the example shown in Figure 7.3, the cut-off radius must be less than $L/2$, where L is the dimension of the simulation box. In other words, with $R_c > L/2$, two images of the same particle may lie within the cut-off radius. The truncation of the infinite sums in the application of the periodic boundary conditions offers substantial computational savings. The minimum image convention is a natural truncation scheme and it is one that allows for easy vectorization³¹ of the computer code, a valuable computational asset. For these reasons, the application of periodic boundary conditions with the minimum image convention is the most widely used method for simulating liquids at the atomic level.

For the simulation of some systems, such as an ionic liquid, the neglect of the long range electrostatic interactions can effect the calculation of structural and thermodynamic properties.³¹ In this case, special methods to approximate the infinite summations have to be implemented. One such technique used to evaluate the interaction of a charge with all of its periodic images is the Ewald summation method.¹⁶⁹ At this point, however, these have not been implemented into our QM/MM code.

Cell Shapes. The cubic simulation box is the most common cell shape, however, any space filling shape can in principle be used. In the present QM/MM program, two different cell shapes have been implemented - the simple cubic cell and the truncated octahedron. The truncated octahedron is sketched in Figure 7.4 and can be described as a cubic box with all eight of its corners cropped. The truncated octahedron has the advantage over the cubic cell in that, fewer solvent molecules are required to surround a solute molecule because the corners of the simulation box need not be filled. (There is generally about a 25% savings when using a truncated octahedron compared to a cubic cell with the same cell length L). Moreover, this savings comes with little additional computational effort over the cubic cell.¹⁶⁹

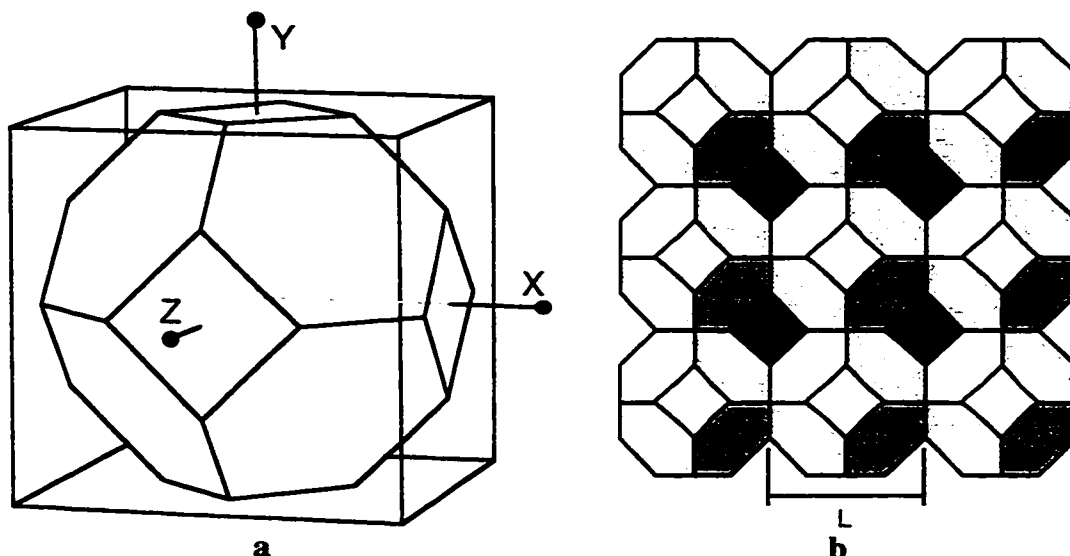


Figure 7.4 Truncated octrahedron. a) single cell contained within a cubic cell of the same cell length. b) One layer of an array of cells, showing the space filling nature of the cell shape.

7.3 The QM/MM Solute-Solvent Intermolecular Potential

In this section we begin to discuss QM/MM solute-solvent intermolecular potential. For the time being let us confine ourselves to the situation where the QM/MM boundary does not cross any covalent bonds. This would be the case if we were to treat our solute molecules entirely at the quantum mechanical level and the solvent molecules at the molecular mechanics level. With this condition, the QM and MM molecules interact only through non-bonded potentials. These non-bonded interactions can be conveniently separated into two parts, an electrostatic component and a so called van der Waals component. Here, we provide a general introduction to how these non-bonded interactions are represented within a combined QM/MM potential with an emphasis on how the hybrid potential can be calibrated to properly represent 'true' intermolecular potential.

Electrostatic Component. Electrostatic coupling involves the Coulombic interaction between the charge density of the QM wave function and a charge distribution set up in the MM region. Since no electronic structure is determined for the MM molecules, an appropriate representation of the charge distribution in the MM region is required. The most convenient one is to assign fixed partial charges to MM atoms, the magnitudes of which ideally reproduce the electrostatic moments of the MM molecules. Of course more sophisticated charge representations can be devised that use

polarizabilities and higher multipoles, but the simple point charge model is a reasonable first step that, as we will see, works surprisingly well.

In order to model the polarization of the solute by the solvent, the charges assigned to the MM atoms should act to distort the QM wave function. This type of electrostatic coupling involves optimizing the wave function in the electrostatic field created by the MM charges. In a conventional Hartree-Fock or DFT QM/MM calculation this is most often achieved by the addition a MM charge/QM-electron term to the one-electron matrix of the Fock equations.^{8,13,162,163,216} Equation 7-1 expresses the Kohn-Sham Fock matrix element, where the last term in the bracket introduces the effect of the MM partial charges.

$$F_{ij} = \int \psi_i(\mathbf{r}) \left(-\frac{1}{2} \nabla^2 + \sum_I^{N_{QM}} \frac{Z_I^{QM}}{|\mathbf{r} - \mathbf{R}_I|} + \int \frac{\rho(\mathbf{r}')}{|\mathbf{r} - \mathbf{r}'|} d\mathbf{r}' + V_{xc}(\mathbf{r}) + \sum_\gamma^{N_{MM}} \frac{q_\gamma^{MM}}{|\mathbf{r} - \mathbf{R}_\gamma|} \right) \psi_j(\mathbf{r}) d\tau \quad (7-1)$$

In the presence of the MM charge distribution, the QM wave function will be polarized as to enhance the favourable electrostatic interactions. It is important to note that there is an energy penalty for the distortion of the wave function from its gas phase state which is sometimes termed the distortion energy, ΔE_{dist} . From classical linear response theory¹⁴ the distortion energy is one-half of the gain in the interaction energy from polarizing the wavefunction.[◊]

Van der Waals Component. The second component of the non-bonded interactions between the QM and MM molecules is the so called van der Waals component. This component accounts for the repulsive steric and the attractive dispersion interactions between molecules. In computer simulations, van der Waals interactions between molecules are almost exclusively represented as a sum of two body potentials between the atoms within the molecules. The general behaviour of a typical van der Waals potential used in computer simulations is shown in Figure 7.5 where the interaction energy is plotted against the distance, r , between two atomic centers. The distinctive feature of the potential is the attractive well that exists at a distance R_0 and with a depth D_0 . The steeply repulsive region of the potential at short distances, $r < R_0$, models the steric or Pauli repulsion due to the overlap of electron clouds. The long range

◊ For molecular systems, linear response corresponds to (dipole) polarizability-the extent to which the charge density distorts to form an additional dipole moment as a result of the permanent electric field. A more detailed discussion of this is provided by Gao and Xia in reference 14.

tail in the van der Waals potential at $r > R_0$ accounts for the attractive 'London' dispersion interactions due to the instantaneous correlation of electron clouds surrounding the atoms.

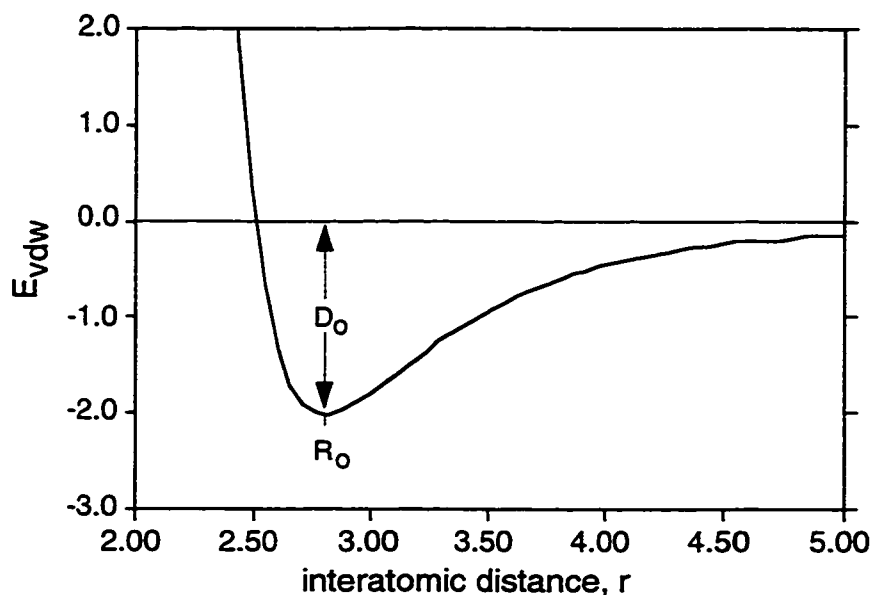


Figure 7.5 Example of a van der Waals non-bonded potential between atoms.

Two common functions used to represent the van der Waals potential in empirical force fields are the Lennard-Jones 12-6 potential (Equation 7-2) and the Buckingham exponential-6 potential (Equation 7-3). These functions reproduce the general behaviour of real interactions as described above, in an empirical way. For both functions, the long ranged attractive component which models the dispersion interactions, decays with a r^6 relationship. For the short-ranged steric component, the two potentials differ in their representation. The more common Lennard-Jones potential utilizes a R^{12} function while the Buckingham potential uses an exponential relationship. Although, the Lennard-Jones potential is often considered more computationally efficient, its representation of the repulsive wall is sometimes too steep. Oppositely, whereas the Buckingham potential is more computationally demanding, it also more correctly models the exponential behaviour of the steric wall.

$$E_{vdw}^{LJ}(r_{ij}) = D_o \left[\left(\frac{R_o}{r_{ij}} \right)^{12} - 2 \left(\frac{R_o}{r_{ij}} \right)^6 \right] \quad (7-2)$$

$$E_{vdW}^{Buck}(r_{ij}) = D_o \left\{ e^{\zeta \left(1 - \frac{R_o}{r_{ij}} \right)} - 2 \left(\frac{R_o}{r_{ij}} \right)^6 \right\} \quad \zeta = 12.0^{\S} \quad (7-3)$$

The van der Waals potential is characterized by the well position, R_o , and the well depth, D_o . In a typical molecular mechanics force field, values are assigned to each atom type and are fit to generate results consistent with the rest of the force field. The atom type is generally defined in terms of the atomic element, its hybridization and the functional group it is contained within. Table 7.1 shows some values from the AMBER95⁷⁷ molecular mechanics force field. When the van der Waals potential is required for two atoms of differing type, say between CT and O, they are generated from the two homonuclear parameters using some kind of combination rule such as that expressed in Equations 7-4 and 7-5.

$$D_o^{CT-O} = \sqrt{D_o^{CT} D_o^O} \quad (7-4)$$

$$R_o^{CT-O} = \frac{1}{2}(R_o^{CT} + R_o^O) \quad (7-5)$$

Table 7.1 Typical van der Waals parameters from the AMBER-95⁷⁷ molecular mechanics force field.

atom type ^a	description	R_o (Å)	D_o (kcal/mol)
CT	sp ³ carbon	3.816	0.1094
CA	aromatic sp ² carbon	3.816	0.0860
HC	hydrogen bound to CT	2.918	0.0150
N3	sp ³ nitrogen	3.750	0.1700
P	phosphate phosphorus	4.200	0.2000
O	sp ² oxygen	3.322	0.2100
OS	sp ³ oxygen in ethers	3.367	0.1700
F	fluoride	3.500	0.0610
Li	lithium cation	2.274	0.0183

^aatom types as defined in reference 77.

Molecular mechanics simulations using the simple van der Waals and fixed point charge intermolecular potential have a rich history for simulating liquids.³¹ With the adjustment of the van der Waals parameters and the partial atomic charges, these simple potentials have been successfully applied to simulate liquids as complex as

[§] ζ is generally set to a value of 12.0 as to reproduce the long range behaviour of the Lennard-Jones potential. In some cases this parameter is also adjusted.

water.^{32,217,218} A good example of this is the TIP3P³² force field developed by Jorgenson and co-workers to simulate liquid water. The TIP3P model employs partial charges of +0.417e on the hydrogen atoms and a charge of -0.834e on the oxygen atom of the water molecules. For the van der Waals interaction, only a single Lennard-Jones potential is employed between the oxygen atoms of the water molecules. Despite the simplicity, Monte Carlo simulations of liquid water at 25°C and 1 atm have yielded excellent results for both thermodynamic and structural properties of water. The density, heat of vaporization and the heat capacity at constant pressure were found to be within 2%, 0.5% and 6% of the experimental values, respectively.³² For other liquids, mostly organic solvents, simple intermolecular potentials of similar quality have also been developed by Jorgensen and coworkers.^{159,219}

The pioneering work by Jorgensen and others acts as a good starting point for incorporating solvent effects via the QM/MM method. Since the solvent-solvent interactions have been carefully parameterized, the application of the QM/MM method can focus on the development of realistic intermolecular interactions between the QM and MM molecules. This is achieved by the optimization of the adjustable parameters in our hybrid potential, namely the van der Waals parameters involving the QM and MM atoms. Gao and coworkers were the first to do this successfully, where van der Waals parameters were optimized for their combined semi-empirical AM1/TIP3P potential. The potential was parameterized to reproduce a comprehensive set of gas-phase solute-water interaction energies obtained from experiment and high level *ab initio* calculations. Using this parameterization, Gao and co-workers were able to estimate free energies of hydration in good agreement with experiment.²⁰⁸ Parameterization specific to each kind of QM/MM implementation is necessary, even if the same MM water model is used. This is because wave functions of different levels of theory react differently to the same perturbation, in this case the MM point charges. Furthermore, the approximations of the QM/MM model and differences in the implementation can be remedied by the empirical refinement of the potential.

In this and the previous section, we have reviewed how solvent simulations are generally performed with computational methods, particularly, in the QM/MM approach. We now turn to a specific discussion of our efforts towards incorporating solvent effects into our PAW QM/MM molecular dynamics simulations. First, we will discuss the nature of the QM-MM electrostatic interactions used in our implementation. This will be followed by our parameterizations of the PAW QM/MM hybrid potential to match the 'true' potential.

7.4 QM/MM Electrostatic Coupling in PAW

QM/MM electrostatic coupling refers to the Coulombic interaction of the MM charge distribution with that in the QM system. The most simple coupling method, aside from its absence, does not involve the QM wave function directly. Instead, the interaction of the QM system with the MM charges is calculated using atomic point charges (or equivalent) assigned to the QM atoms.^{13,164} The point charges are generally extracted from the QM wave function using some sort of charge density partitioning scheme^{220,221} such as a Mulliken population analysis. Alternatively, they are adjusted to reproduce the electrostatic potential of the wave function in what is called an electrostatic potential fit (ESP fit).²²²⁻²²⁴ Although the QM charge density can be adequately represented by the point charge model, this coupling method (sometimes called mechanical coupling)¹³ does not allow for the distortion or polarization of the wave function by the MM solvent molecules. In general, this is a necessity for properly simulating the effect of the solvent. Charge density polarization effects are introduced 'quantum mechanically' where the wave function is optimized in the electrostatic field due to the MM charge density. As outlined in the previous section, this is generally achieved by adding a one electron integral term into the Fock matrix elements.

The electrostatic coupling in the PAW QM/MM implementation can be conceptually thought of a hybrid of the two coupling schemes. Similar to the simple mechanical coupling scheme, a model charge density is extracted from true density of the QM wavefunction. The electrostatic coupling energy is expressed in terms of the interaction between this model charge density and the MM point charges. However, unlike the mechanical coupling, this approach allows the MM point charges to polarize the QM wave function and therefore is appropriate for solvent simulations. In this section the electrostatic coupling in the PAW QM/MM program is outlined. Blöchl's charge isolation scheme in the PAW program forms the basis of the PAW QM/MM charge coupling, which involves the construction of a model charge density that we now introduce.

The true density, $\rho(r)$, of the QM wave function within each periodic simulation cell is represented by a model charge density, $\hat{\rho}(r)$, composed of a sum of atom centered spherical Gaussians as shown in Equation 7-6.

$$\hat{\rho}(\mathbf{r}) = \sum_I \sum_n \frac{Q_{I,n}}{(\sqrt{\pi}\zeta_n)^3} e^{-\left(\frac{|\mathbf{r}-\mathbf{R}_I|}{\zeta_n}\right)^2} \quad (7-6)$$

Here the index I runs over the QM atoms, the index n runs over the number of Gaussians assigned to each atom, R represents the coordinates of the QM atom, ζ_n is the decay factor of each Gaussian, and Q is the total charge. In the model charge density presented in Equation 7-6 there are three sets of adjustable parameters available for the fit, namely, the Q 's, the ζ 's and the number of Gaussians on each center. To simplify matters, the number of Gaussians assigned to each atom is fixed (generally 3-4 are used) and the decay factors for all centers are assigned the same set of values. In this way, the only free variables to be adjusted during the fit are the charges, Q .

The charges are chosen such that the electrostatic multipole moments of the true density within each simulation cell are reproduced. In other words a multipolar expansion of the true density is performed such that the long-range electrostatic potential is reproduced. This seemingly complex fit can be accomplished at a relatively small expense in the plane wave formalism.¹⁴² Following a Fourier transform of the true density, the requirements can be expressed in a linear system of equations which can be solved for the Q 's. Since the Fourier transform of the density is ordinarily performed in the Car-Parrinello method, the additional cost of the multipolar expansion of the true density is negligible and essentially involves the inversion of an $N_g \times N_g$ matrix where N_g is the total number of Gaussians. Blöchl's scheme provides an accurate multipolar expansion of the true continuous charge density. The fitted charges are found to reproduce point charges[◊] obtained from experimental multipole moments to within 0.01e and dipole moments to within 0.2 D for a set of small organic and inorganic molecules.

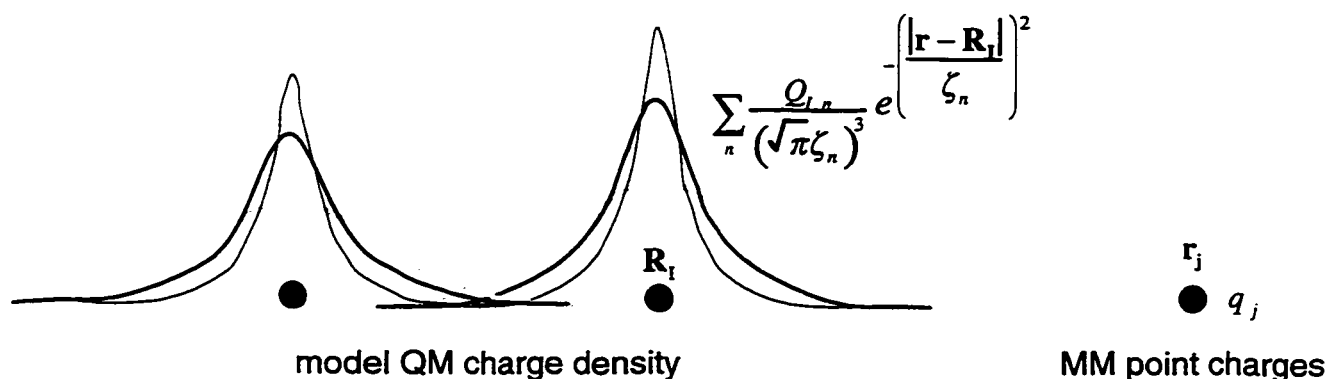


Figure 7.6 Schematic representation of the PAW QM/MM electrostatic coupling involving the fitted model charge density in the QM region and the MM point charges.

[◊] Here the Gaussian charge distribution can be collapsed into a single point charge by summing up the Q 's on each atomic center.

Using the principle that interaction energies between separated densities can be expressed entirely through their electrostatic multipoles, and making the assumption this is valid for our solvent-solute model, we use the model charge density to express the electrostatic coupling between the QM and MM regions. The total electrostatic interaction energy between the fitted Gaussian charge distribution of the QM region and a point charges of the MM system, q_j , is expressed in equation 7-6 and represented pictorially in Figure 7.6.

$$E_{QM/MM}^{elstat} = \frac{1}{4\pi\epsilon} \sum_j^{N_{MM}} \sum_l^{N_{QM}} \sum_n \frac{q_j Q_{l,QM,n}}{|\mathbf{r}_j - \mathbf{R}_l|} \text{erf}\left(\frac{|\mathbf{r}_j - \mathbf{R}_l|}{\zeta_n}\right) \quad (7-6)$$

Up to this point, the electrostatic coupling appears to be the same as the simple mechanical coupling where no polarization of the QM wave function occurs. How then is the polarization achieved in this scheme? In the Car-Parrinello molecular dynamics framework the polarization of the wave function can be expressed through the force on the expansion coefficients in the coupled equations of motion.

$$\mu \ddot{c}_{i,k} = -\frac{\partial E}{\partial c_{i,k}} - \sum_l \lambda_{i,l} c_{i,k} \langle \varphi_i | \varphi_l \rangle \quad (7-7)$$

We first calculated the potential of the Gaussian charge distribution due to the MM point charges which is given in Equation 7-8 for each Gaussian.

$$\frac{\partial E_{l,n}}{\partial Q_{l,n}} = \frac{1}{4\pi\epsilon} \sum_j^{N_{MM}} \frac{q_j}{|\mathbf{r}_j - \mathbf{R}_l|} \text{erf}\left(\frac{|\mathbf{r}_j - \mathbf{R}_l|}{\zeta_n}\right) \quad (7-8)$$

The potential acting on the wave function is then obtained using the chain rule and the partial derivatives of the fitted charges with respect to the expansion coefficients.

$$\frac{\partial E}{\partial c_{i,k}} = \frac{\partial E}{\partial Q_l} \frac{\partial Q_l}{\partial c_{i,k}} \quad (7-9)$$

Thus, the potential acting on the Gaussian charge distribution (Eqn. 7-8) is transferred to the force on the wavefunction via Equation 7-9. It is this bridging relationship that mediates the polarization of the wave function by the MM charge distribution through the model charge distribution.

The force on the atomic position of the QM atoms due to interaction between the model charge density and the MM charges is given by equations 7-10, with a similar expression for the force on the MM atoms.[§]

$$\frac{\partial E_{l,n,j}}{\partial \mathbf{R}_l} = \frac{1}{4\pi\epsilon} \frac{q_j^{MM} Q_{l,n}}{|\mathbf{r}_j - \mathbf{R}_l|} \left[\frac{2}{\sqrt{\pi}\zeta_n} e^{-\left(\frac{|\mathbf{r}_j - \mathbf{R}_l|}{\zeta_n}\right)^2} - \frac{1}{|\mathbf{r}_j - \mathbf{R}_l|} \operatorname{erf}\left(\frac{|\mathbf{r}_j - \mathbf{R}_l|}{\zeta_n}\right) \right] \frac{\partial |\mathbf{r}_j - \mathbf{R}_l|}{\partial \mathbf{R}_l} \quad (7-10)$$

For the forces on the QM atoms, there is an additional force resulting from the sensitivity of the fitted charges on the atomic positions. The so called Pulay forces²²⁵ are given by equation 7-11.

$$\mathbf{F}_{R_l}^{Pulay} = - \sum_i^{N_{QM}} \sum_n \frac{\partial E_{l,n}}{\partial Q_{l,n}} \frac{\partial Q_{l,n}}{\partial \mathbf{R}_l} \quad (7-11)$$

The Pulay term expressed in equation 7-11 ensures that the total energy is consistent with the gradients, a necessary ingredient for performing energy conserving dynamics. The exact expressions for the partial derivatives of the fitted charges with respect to the expansion coefficients used in equation 7-9 and with respect to the nuclear position used in equation 7-11 are detailed elsewhere since they were originally derived for the charge isolation scheme in PAW.¹⁴²

Although the electrostatic coupling approach used in the PAW QM/MM implementation is exact, the multipolar expansion of the true density is strictly only valid for long-range interactions. Thus, the model charge density may not properly represent the electrostatic potential acting on the MM charges for close range interactions between the solvent and QM solute molecules. Since the total QM/MM interaction potential is empirical in nature, it is possible that optimization of the adjustable parameters within the potential will be able to compensate for these defects (if any) in the PAW QM/MM electrostatic coupling scheme. In the following sections this and other aspects of the electrostatic coupling will be tested.

[§] The last term of equation 7-10 is replaced by $\frac{\partial |\mathbf{r}_j - \mathbf{R}_l|}{\partial \mathbf{r}_j}$.

7.5 Testing of the PAW QM/MM Coupling: Molecular Dynamics

In order for the QM/MM electrostatic coupling scheme to be used for molecular dynamics simulations, it must allow for energy conserving dynamics to be performed. In this section we examine this aspect of the PAW QM/MM implementation. As a preliminary test we have examined the energy conservation associated with the QM/MM dynamics of an ethane molecule in ethane at 200 K (liquid). In this simulation 17 ethane molecules have been simulated with periodic boundary conditions in a 25 Å cubic cell where one of the molecules was treated at the density functional level. Jorgensen's OPLS-AA¹⁵⁹ molecular mechanics force field parameters were used. The OPLS-AA charges assigned to the MM carbon and hydrogen atoms are -0.18 and +0.06 e, respectively. A molecular dynamics time step of 3.0 a.u. was used with the standard Verlet propagator. Masses of 12.0 amu and 1.5 amu were used for carbon and hydrogen atoms, respectively. The system was slowly heated to 200 K and equilibrated for 500 fs. No thermostats were applied to any of the three subsystems (wavefunction, MM nuclei, QM nuclei). The details of the Car-Parrinello simulation of the QM subsystem are essentially the same as those presented in Section 5.3, the only notable difference being that of the simulation temperature and the polarizable electrostatic coupling.

Figure 7.7a shows the total conserved energy relative to the initial value during the 1 ps simulation. For comparison, the energy conservation of the same system (initiated in the same way) where the polarizable electrostatic coupling is replaced with mechanical electrostatic coupling is plotted as the ghosted line in Figure 7.7a. The total conserved energy of the reference system drifts at a small rate of 2×10^{-7} Hartrees per femtosecond of simulation time. When the polarizable electrostatic coupling is evoked, the energy conservation is slightly degraded, with a linear drift of 3.5×10^{-7} Hartrees/fs. We also note that the polarizable coupling run exhibits slightly larger oscillations in the conserved energy. The energy conservation of the polarizable coupling run is still considered to be excellent.^{137,171}

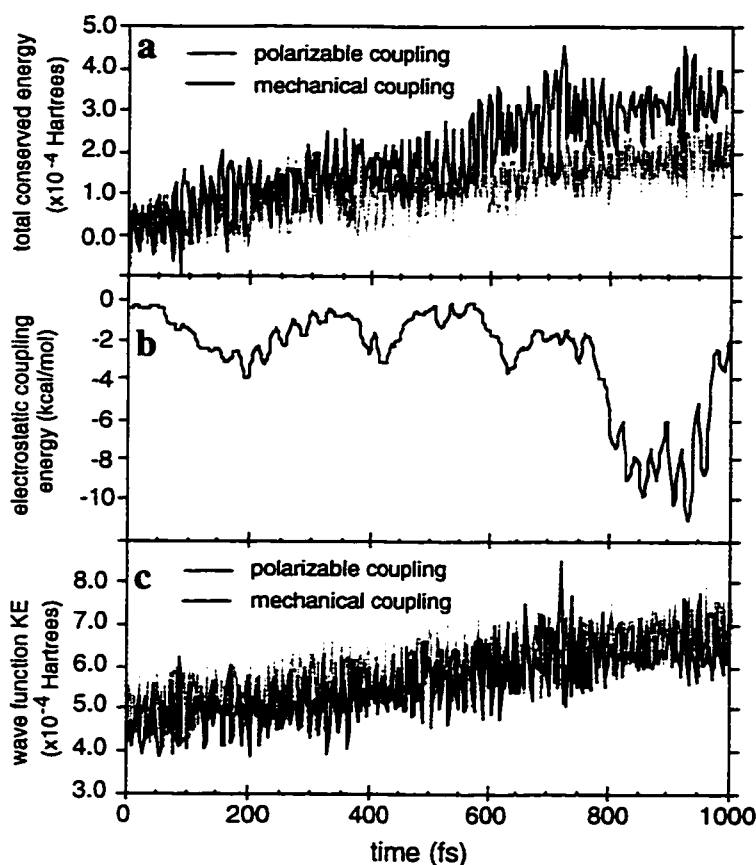


Figure 7.7 Various energetic quantities traced during the PAW QM/MM simulation of ethane in ethane. a) Total conserved energy relative to the initial value. b) QM/MM electrostatic coupling energy as defined in Equation 7-6. c) Wave function kinetic energy. Solid lines refer to the system where polarizable coupling is enabled whereas the patterned lines correspond to the control system where the polarizable electrostatic coupling is replaced with mechanical electrostatic coupling.

The electrostatic coupling energy is plotted in Figure 7.7b. More specifically, this is the interaction energy between the MM point charges and the model charge density of the QM ethane molecule as defined in Equation 7-6. For most of the simulation the electrostatic coupling energy is small, fluctuating around 2 kcal/mol. However, at a simulation time of approximately 800 fs, a close contact with a MM ethane molecule increases the interaction energy to a value of roughly 10 kcal/mol. Notably, the enhanced electrostatic interaction does not affect either the drift of the total conserved energy or the amplitude of its oscillations.

One component of the combined Car-Parrinello Lagrangian that might be sensitive to the electrostatic coupling is the dynamics of the wave function. The fluctuating electrostatic potential due to the MM charges may cause the wave function to

become 'hot' such that there is a degenerative deviation from the Born-Oppenheimer potential surface. Worse still, intermolecular collisions may cause more violent perturbations in the wave function that can potentially dislodge the wave function from the Born-Oppenheimer potential surface. Although this is likely to be exhibited in the energy conservation, the kinetic energy of the wave function is most sensitive to it. Plotted in Figure 7.7c is the kinetic energy of the wave function for both the polarizable electrostatic coupling run and the mechanically coupled QM/MM run. We notice that there is a small, but equal rate of drift in both cases. Application of a wave function thermostat as prescribed by Parrinello and Blöchl¹⁴⁹ will minimize the deviation of the wave function from the Born-Oppenheimer state and counter the drift in both cases. Importantly, at the 800 fs mark where there is an enhanced electrostatic coupling energy, there is no significant increase in the wave function kinetic energy and therefore no evidence of the wave function dislodging from the Born-Oppenheimer surface.

In this section we have only demonstrated the energy conservation of the coupling in the PAW QM/MM implantation. Future studies should include a more thorough examination of the potential consequences of the QM/MM electrostatic coupling on the Car-Parrinello coupled dynamics. In this case, such studies will have ramifications to other Car-Parrinello QM/MM implementations where the electrostatic coupling allows for polarization of the wave function.

7.6 Testing of the PAW QM/MM Coupling: Li-Water Interaction Potential

The two component QM/MM interaction potential involving a van der Waals component and an electrostatic component (including polarization of the wave function) has been shown by others to represent the true quantum mechanical interaction potential well enough to provide quantitative results for solvation effects. The electrostatic coupling scheme used in the PAW QM/MM implementation involves a multipolar expansion of the true density that is strictly valid only for long range interactions. In this section we will examine if this coupling scheme can be used to correctly model the true quantum mechanical interaction potential at critical short range distances.

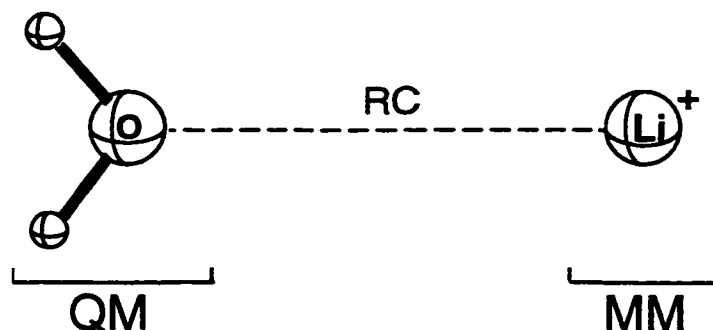


Figure 7.8. Partitioning of the Li^+ - water system. The 'reaction coordinate' (RC) is defined as the distance between the oxygen and Li ion. Geometry of the water molecular was fixed and a C_{2v} symmetry was maintained.

For this purpose we will explore the interaction between a water molecule and a Li^+ cation. The interaction potential will be determined by the PAW QM/MM method where the water molecule is treated in the QM region and the Li^+ ion is partitioned to the MM region as illustrated in Figure 7.8. The reference potential used to judge the quality of the PAW QM/MM method will be the 'pure QM' potential calculated with gradient corrected density functional theory. The details of the QM component of the PAW QM/MM calculations are as follows. The wave function of the water molecule was expanded in plane waves up to an energy cutoff of 30 Ry within a 18.4 \AA cubic cell. The Becke¹⁰³-Perdew86^{104,105} gradient corrected exchange-correlation functional was used in conjunction with the local density parameterization of Perdew and Zunger.¹¹⁸ For the pure QM calculation of the reference potential energy surface, the ADF program (version 2.3) was employed. Here the standard ADF triple- ζ STO basis with polarization functions were employed. The Becke-Perdew86¹⁰³⁻¹⁰⁵ exchange-correlation functional was also used in the ADF calculations. For both the ADF and PAW calculations, a [He] frozen core was utilized for oxygen. For all potential surfaces shown, the geometry of the water molecule was fixed ($R_{\text{OH}} = 0.974 \text{ \AA}$ and $\angle\text{HOH} = 103.58^\circ$) and a C_{2v} symmetry was maintained such that the oxygen atom is oriented towards the Li^+ ion as shown in Figure 7.8. The pure QM reference potential was calculated using ADF instead of PAW because the memory requirements for calculating the long range Li-water interactions with PAW were not available. (For long separations a large PAW simulation cell is required).

For the MM component of the PAW QM/MM calculation there are some adjustable parameters, namely the charges assigned to the MM atoms and the van der Waals parameters of all atoms involved. In this case, the Li cation has an unambiguous charge assignment of $+1e$. For all of the calculations described in this section, the TIP3P

van der Waals parameters for water will be used without adjustment. This leaves only the van der Waals parameters of the Li^+ ion and the choice of the van der Waals potential that can be adjusted.

Table 7.2 Water- Li^+ interaction energies and fitted charge of the water molecule.

Li-O distance (Å)	ΔE_{QM}^a (kcal/mol)	PAW/AMBER interaction energy ^b (kcal/mol)				PAW fitted charges (e)	
		$\Delta E_{QM/MM}^{total}$	$\Delta E_{QM/MM}^{elstat}$	$\Delta E_{QM/MM}^{vdW}$	ΔE_{dist}	oxygen	hydrogen ^c
1.00	261.48	18914.68	-130.57	19010.4	34.80	-1.42	0.71
1.50	-10.17	68.28	-102.02	141.44	28.86	-1.42	0.71
1.60	-20.16	0.71	-86.59	63.98	23.32	-1.34	0.66
1.65	-23.32	-15.22	-79.88	43.69	20.96	-1.30	0.65
1.70	-25.58	-24.84	-73.79	30.11	18.84	-1.27	0.63
1.75	-27.13	-30.41	-68.34	20.91	17.01	-1.23	0.62
1.80	-28.12	-33.40	-63.38	14.62	15.35	-1.20	0.60
1.85	-28.66	-34.73	-58.96	10.28	13.94	-1.18	0.59
1.90	-28.87	-35.01	-54.91	7.26	12.62	-1.15	0.57
1.95	-28.81	-34.63	-51.29	5.15	11.49	-1.12	0.56
2.00	-28.52	-33.83	-47.96	3.66	10.45	-1.10	0.55
2.10	-27.53	-31.61	-42.19	1.85	8.72	-1.06	0.53
2.20	-26.20	-29.13	-37.41	0.92	7.36	-1.02	0.51
2.30	-24.70	-26.69	-33.38	0.44	6.24	-0.99	0.49
2.50	-21.61	-22.40	-27.03	0.06	4.56	-0.94	0.47
2.70	-18.70	-18.96	-22.36	-0.03	3.43	-0.89	0.45
3.00	-15.09	-15.03	-17.30	-0.05	2.32	-0.84	0.42
3.50	-10.85	-10.76	-12.04	-0.02	1.30	-0.79	0.39
4.00	-8.14	-8.09	-8.85	-0.014	0.77	-0.75	0.37
5.00	-5.10	-5.07	-5.39	-0.004	0.32	-0.70	0.35
6.00	-3.50	-3.48	-3.63	-0.001	0.15	-0.68	0.34
7.00	-2.55	-2.54	-2.62	-0.001	0.07	-0.66	0.33
8.00	-1.96	-1.95	-1.98	-0.000	0.02	-0.65	0.32
10.00	-1.25	-1.24	-1.25	-0.000	0.00	-0.64	0.32
12.00	-0.89	-0.85	-0.86	0.000	0.00	-0.63	0.31

^aPure QM energetics as calculated at the non-local density functional level with ADF. ^bPAW QM/MM results using the original AMBER95 van der Waals parameters for Li^+ and the TIP3P parameters for water.

^ccharges on hydrogen atoms are equal due to symmetry constraints.

In our first approximation we will use the original Li^+ parameters of the AMBER95 force field with the Lennard-Jones 12-6 van der Waals function (i.e. Eqn 7-2). We will call this the PAW/AMBER potential. The PAW/AMBER potential for the water-lithium interaction is compared to the reference pure QM potential in Table 7.2. Also displayed Table 7.2 is a partitioning of the PAW/AMBER interaction energy into its electrostatic, $\Delta E_{QM/MM}^{elstat}$, and van der Waals, $\Delta E_{QM/MM}^{vdW}$, components. The electrostatic component refers to the interaction energy between the model charge density of the QM region and the MM charges as expressed in equation 7-6.

The long-range part of the PAW/AMBER potential compares well with the reference potential. For distances of 3.0 Å and greater, the deviation of the hybrid potential from the reference is no more than 0.15 kcal/mol. For this range, the electrostatic contribution to the total interaction energy dominates, with the van der Waals energy accounting for less than 1% of the total. The agreement in this region shows that the model charge density used in the PAW QM/MM coupling represents the true density exceptionally well for long distance interactions.

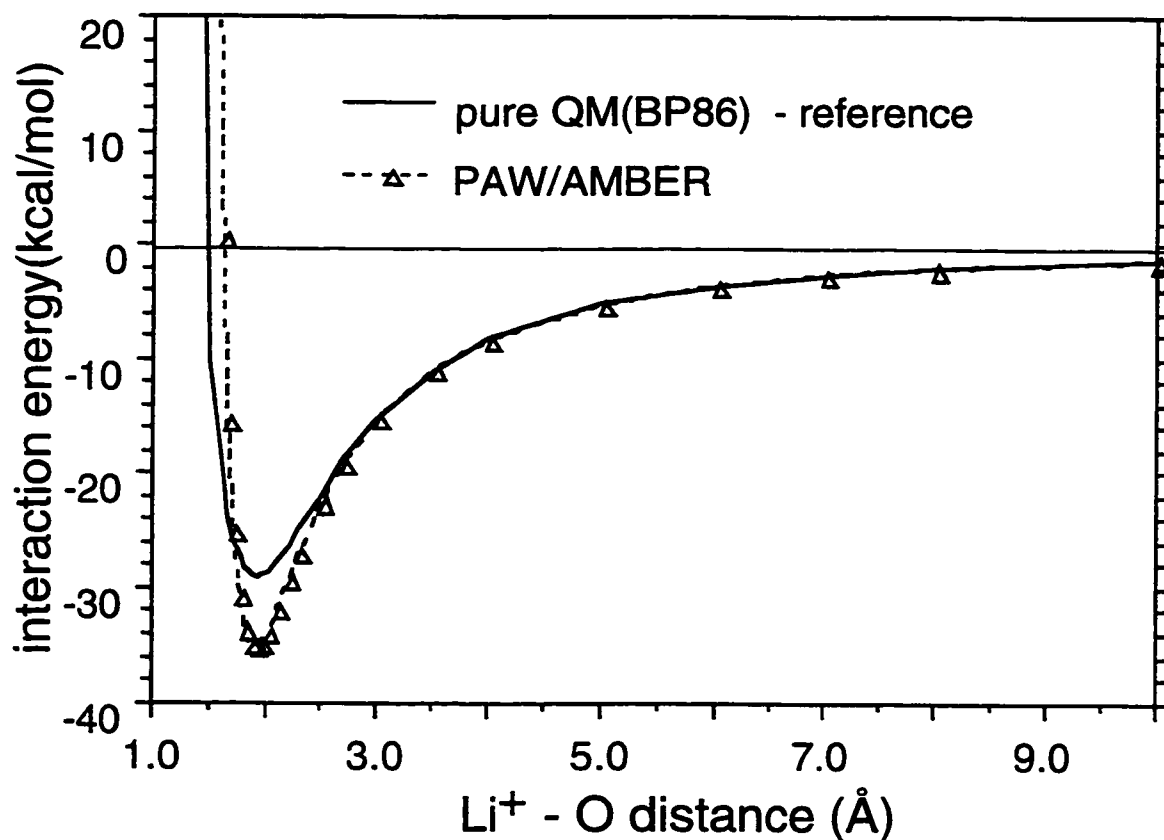


Figure 7.9 Li⁺-water interaction profile for the pure QM reference potential and the hybrid PAW/AMBER potential.

At close range, the steric component of the van der Waals potential begins to play a more dominant role. The position and depth of the potential minimum is governed by the delicate balance between the repulsive steric and the attractive electrostatic components. The PAW/AMBER potential compares surprisingly well to the reference potential, considering that the parameters used were not optimized for this purpose. Figure 7.9 shows that the position of the potential minimum at 1.9 Å is almost exactly reproduced by the hybrid potential. Unfortunately, the well depth is over estimated by 6 kcal/mol or approximately 20%. The good agreement between the PAW/AMBER

potential and the reference potential suggests that by adjusting the van der Waals potential, we should be able to improve the hybrid potential.

Table 7.3 Comparison of the fitted charges from the PAW QM/MM calculation and a pure QM PAW calculation.

Li-O distance (Å)	PAW QM/MM charges		pure QM PAW charges ^a		
	oxygen	hydrogen	oxygen	hydrogen	lithium
1.70	-1.27	0.63	-1.00	-0.51	0.98
1.90	-1.15	0.57	-0.97	0.50	0.97
2.50	-0.94	0.47	-0.90	0.46	0.98
3.00	-0.84	0.42	-0.84	0.43	0.99

^a calculated with the same PAW settings as the PAW QM/MM simulation except that a 24.0 Å cubic simulation cell is used.

As the lithium ion is brought closer to the oxygen atom, there should be a polarization of the water molecule, such that charge density is drawn towards the oxygen atom. Displayed on the right-hand side of Table 7.2 are the fitted charges of the water molecule from the PAW QM/MM calculation. (The unperturbed charges from the PAW calculation of free water are $-0.62e$ and $0.31e$ for the oxygen and hydrogen, respectively.) As the lithium ion is drawn closer to the oxygen, the charge on the oxygen atom steadily increases while the hydrogen charge diminishes, showing that there is indeed a polarization of the wave function in the PAW QM/MM model. The energetic cost of distorting the wave function from its unperturbed density can be easily calculated as the difference between $(\Delta E_{QM/MM}^{elstat} + \Delta E_{QM/MM}^{vdW})$ and the total interaction energy. The distortion energy, ΔE_{dist} , as we have defined it is also presented in Table 7.2. In the long range, the distortion energy is zero and should increase for closer interactions. For example, at 12 Å the distortion is negligible, at 3 Å it is 2.1 kcal/mol or 15% of the interaction energy, while at the potential minimum the distortion energy amounts to 12.6 kcal/mol or 36% of the total interaction energy.

The polarization of the wave function in the QM/MM model can be examined by comparing the fitted charges from the PAW QM/MM calculation to the fitted charges from a pure QM PAW calculation. For this purpose, a series of pure QM PAW calculations on the lithium ion-water system have been performed in a 24.0 Å cubic simulation cell. The fitted charges are compared in Table 7.3. Even at a distance of 3.0 Å, the polarization is not trivial as evidenced with the fitted charge on oxygen increasing by about 0.2e compared to the free state. At this point, the QM/MM charges compare very well to those of the pure QM calculation differing by less than 0.01e. At the

potential minimum where the Li-oxygen distance is 1.90 Å, the QM/MM fitted charge on oxygen has almost doubled from that in the free state to a value of -1.15 e. Compared to the pure QM PAW calculation which gives a fitted charge of -0.97e on oxygen the polarization is slightly too high. The over-polarization further increases as the distance is decreased. This discrepancy can be attributed to two factors. First, the pure QM calculation allows for a small charge transfer from the water molecule to the lithium ion which cannot occur in the QM/MM calculation. Secondly, the charge distribution of the lithium ion is more diffuse in the pure QM calculation compared to the point charge distribution in the QM/MM interaction. For these reasons, the polarization of the water molecule is slightly exaggerated in the short-range region in the combined QM/MM model.

Table 7.4 Li⁺ van der Waals parameters used in the various hybrid potentials.

hybrid potential	D ₀ (kcal/mol)	R ₀ (Å)
PAW/AMBER	0.0183	2.274
Best Fit 12-6	0.1100	2.200
Best Fit exp-6	0.1510	2.900

By adjusting only the D₀ and R₀ van der Waals parameters (equation 7-2) for Li⁺ from the original PAW/AMBER potential, the hybrid potential has been optimized such that the well depth and well position are in better agreement with the reference potential. Since we retained the Lennard-Jones 12-6 van der Waals potential used in the original PAW/AMBER calculation, we will call this new hybrid potential the 'best fit 12-6' potential. The new van der Waals parameters for lithium resulting from the fit are provided in Table 7.4 along with the original AMBER parameters.

Table 7.5 Comparison of the optimized PAW/MM potentials with the pure QM Water-lithium ion potential.

Li-O distance (Å)	ΔE_{QM}^a (kcal/mol)	$\Delta E_{QM/MM}$ (kcal/mol)	
		best fit 12-6	best fit exp-6
1.00	261.48	39890.82	159.95
1.50	-10.17	223.50	-10.86
1.60	-20.16	70.71	-20.07
1.65	-23.32	32.49	-23.10
1.70	-25.58	7.95	-25.33
1.75	-27.13	-7.70	-26.89
1.80	-28.12	-17.57	-27.92
1.85	-28.66	-23.64	-28.51
1.90	-28.87	-27.21	-28.77
1.95	-28.81	-29.13	-28.76
2.00	-28.52	-29.95	-28.52
2.10	-27.53	-29.69	-27.59
2.20	-26.20	-28.20	-26.27
2.30	-24.70	-26.28	-24.76
2.50	-21.61	-22.38	-21.63
2.70	-18.70	-19.02	-18.74
3.00	-15.09	-15.10	-15.10
3.50	-10.85	-10.80	-10.86
4.00	-8.14	-8.11	-8.15
5.00	-5.10	-5.07	-5.09
6.00	-3.50	-3.48	-3.49
7.00	-2.55	-2.55	-2.55
8.00	-1.96	-1.95	-1.95
10.00	-1.25	-1.24	-1.24
12.00	-0.89	-0.85	-0.85

^areference data repeated from Table 7.2 for comparison with new potentials.

The best fit 12-6 potential is detailed in Table 7.5 for the whole range examined from a Li-O distance of 1.00 Å to 12.00 Å. The well depth of the total interaction potential has been improved such that it lies only 1.1 kcal/mol or 4% lower than the reference. This is a significant improvement over the first PAW/AMBER potential with the 'unoptimized' parameters, where the same comparison yields a difference of 20%. Unfortunately, the position of the well depth has been shifted outwards by a tenth of an Ångstrom compared to the reference, whereas it was reproduced by the first PAW/AMBER potential. Figure 7.10 compares the close-range region of both the 'best fit' potential and the original PAW/AMBER potential to that of the reference. This comparison shows that for both the original PAW/AMBER and 'best fit 12-6' potentials the repulsive steric region is a slightly harder/steeper than the reference potential. This agrees with the sentiment that the 12-6 potentials tend to exaggerate the short-ranged repulsion.⁷⁷

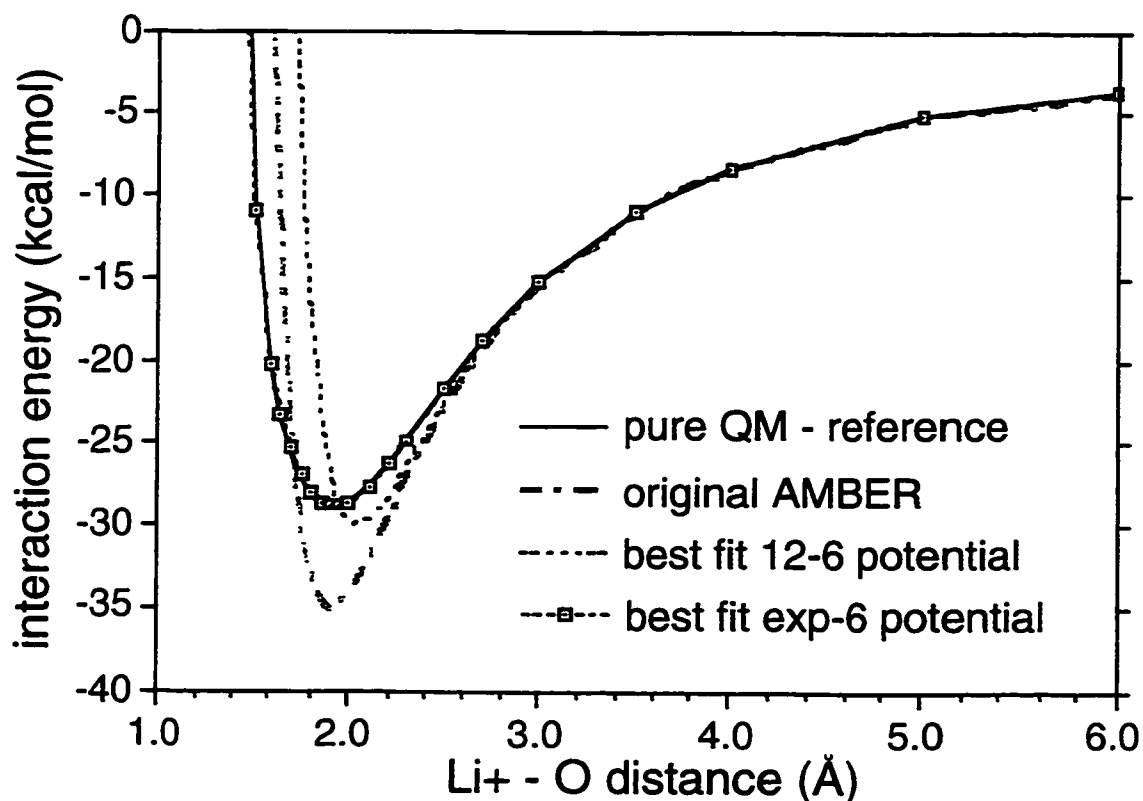


Figure 7.10 Comparison of the Li-water interaction potentials for various hybrid PAW QM/MM potentials. The reference 'pure QM' potential is also shown. The three hybrid potentials differ by only the van der Waals potentials used.

By switching from the Lennard-Jones 12-6 to the Buckingham exponential-6 representation of the van der Waals potential and optimizing the Li+ parameters, an exceptional fit is achieved[§]. This potential, which is detailed in Table 7.5 and plotted in Figure 7.10, will be labeled the 'best fit exp-6' potential. For interaction distances greater than 1.5 Å, the hybrid potential differs by no more than 0.3 kcal/mol from the reference. Table 7.5 shows that only at the severely repulsive region where $R < 1.5$ Å, does the best fit exp-6 potential begin to significantly deviate from the reference potential.[§] The improvement in the fit over the 'best fit 12-6' potential can be attributed to the softer exponential potential which more correctly represents the behaviour of the steric repulsion.

[§] The PAW and ADF QM/MM code has the option of mixing different van der Waals potentials. Thus, in a QM/MM hydrated solvent simulation, the MM water-water interactions could be treated with the 12-6 van der Waals potentials for which the TIP3P parameters were optimized with. The Water-QM solute van der Waals interactions could then be treated with the exponential-6 potential.

[§] For the ultra-short region the exponential-6 potential actually becomes attractive with a $-\infty$ value at the $r=0$ limit. Thus, for unphysical interaction distances, the best fit exp-6 potential could deviate dramatically from the reference potential.

The PAW QM/MM electrostatic coupling is strictly only valid for long range interactions. However, this example demonstrates that the critical close range region of the intermolecular interaction potential can also be exceptionally well represented by the simple two component hybrid potential. Thus, defects associated with the diminished validity of the multipolar expansion of the wave function in this short-range region can be "smoothed" over by the appropriate adjustment of the van der Waals potential. In this specific case, a near exact fit was achieved when the Lennard-Jones 12-6 potential was replaced by the exponential-6 potential. We mention that there are other alternatives to tuning the total QM/MM interaction potential to match the reference. One option, involves modifying the van der Waals potentials of the water molecule. Recall that the TIP3P model of water has only one van der Waals potential centered on the oxygen atom. Thus, improvement in the fit could be achieved by adding a van der Waals potential on the hydrogen atoms. Another alternative would be to modify the charge representation of the MM region.

7.7 Fitting of Bimolecular Hydrogen Bond Interactions

In the Section 7.5 the PAW QM/MM potential was fit to a single interaction, namely the lithium ion-water potential. In this section we further evaluate the applicability of the PAW QM/MM approach for performing explicit solvation simulations, by expanding the fit set. We have followed the procedure of Freindorf and Gao²¹⁶ who optimized van der Waals parameters for their combined Hartree-Fock 3-21G and TIP3P potential which they termed the AI-3/MM potential. Lennard-Jones parameters were adjusted to reproduce the pure QM interaction energies and geometries determined at the Hartree-Fock 6-31G* level for a fit set of 27 organic compound-water bimolecular interactions shown in Figure 7.11.[◊] The resulting agreement between the hybrid AI-3/MM potential and the pure QM potential is excellent. For example, the root mean square(rms) deviation in the interaction energies was found to be a remarkable 0.70 kcal/mol for the set of 27 complexes. Furthermore, the optimized interaction distances with the hybrid AI-3/MM potential were found to deviate from the pure QM results by only rms=0.06 Å. Freindorf and Gao's fit set was chosen for purpose of eventually simulating organic compounds and biopolymers in solution. In this case we utilize the

[◊] There is one exception here. The fit set of Freindorf and Gao involved a water-sodium complex, which is replaced by a water-chloromethane interaction in the fit set shown in this figure. The reason for this substitution is that a PAW core description for sodium was not available.

same fit set in order to evaluate the PAW QM/MM model by comparing the quality of the fit to the standard set by Freindorf and Gao.

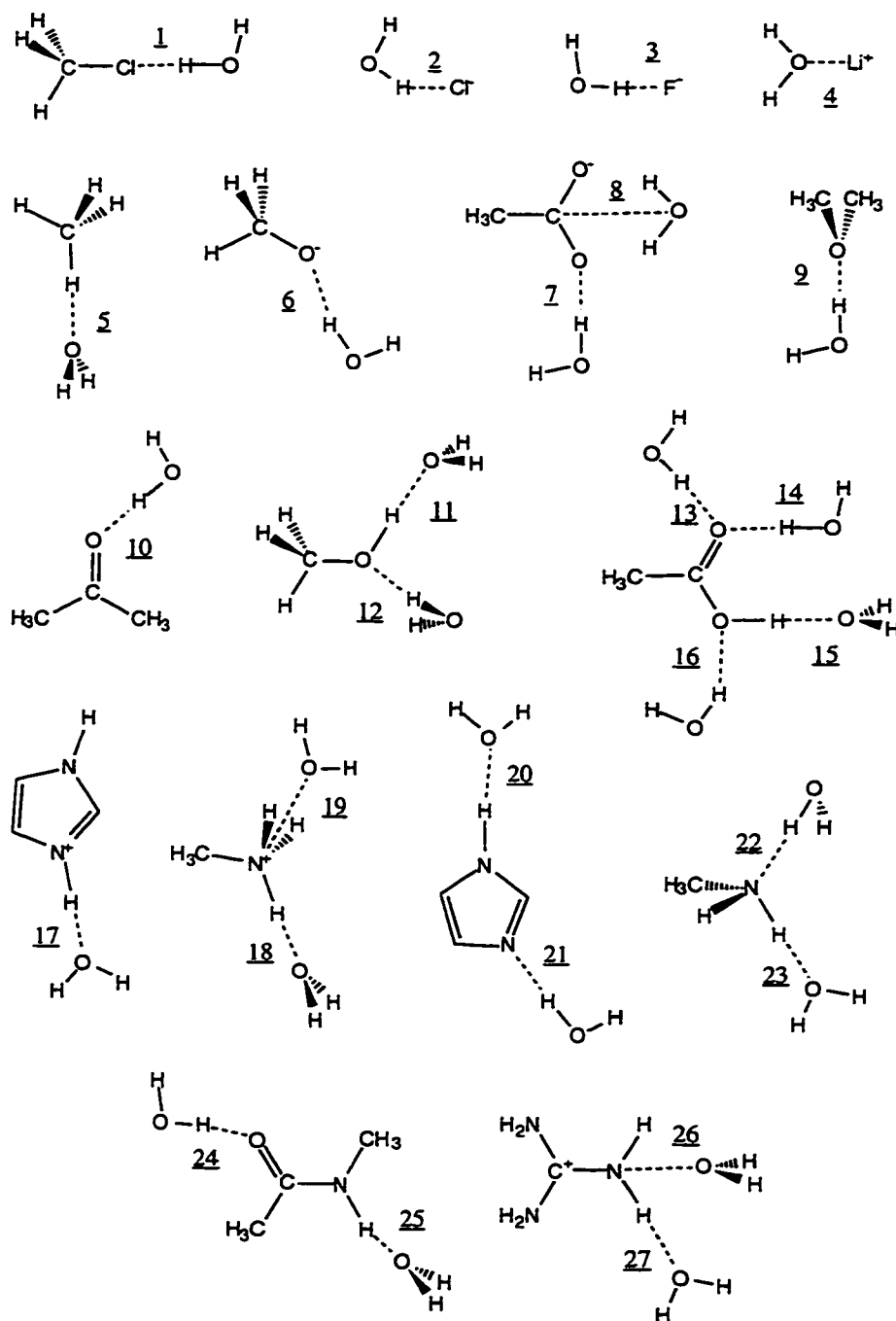


Figure 7.11 Bimolecular complexes used in the parameterization of the PAW QM/MM potential. With the exception that the water- Na^+ complex has been substituted by a water-chloromethane complex, this is the same fit set used by Freindorf and Gao.²¹⁶ Some complexes are drawn with several water molecules, but all calculations involved only a single monomer molecule and a single water molecule. For the combined QM/MM calculations, the water molecules were treated within the molecular mechanics approximation, while the solute molecules were treated at the DFT level.

Although we have adopted their fit set, our optimization of the PAW QM/MM potential is somewhat different than that of Freindorf and Gao. Most importantly, our reference geometries and energies were calculated with density functional theory with the Becke-Perdew86¹⁰³⁻¹⁰⁵ gradient corrected exchange correlation functional. For this purpose we used the ADF package. ADF's standard triple-zeta STO basis augmented with polarization functions was utilized with [He] frozen cores for the first row elements. Reference geometries were obtained by optimizing the water-monomer complex with the geometry of the water molecule fixed to the TIP3P molecular mechanics structure. No symmetry constraints were imposed during the optimizations and the monomer geometry was allowed to fully relax. Basis set superposition errors (BSSE) in the interaction energies were corrected for using the standard counterpoise method.^{226,227} In general, the BSSEs were relatively small^{228,229} with all errors amounting to no more than 14% of the total interaction energy. For the hybrid PAW QM/MM calculations, the TIP3P³² charges and van der Waals parameters for the MM water molecules were utilized. The monomer wave functions were expanded in plane waves up to a 30 Ry cutoff with the frozen core approximation used for the first row elements. As with the ADF calculations, the Becke-Perdew86 gradient corrected exchange correlation functional was applied. Simulation cells were chosen on an individual basis such that the minimum distance between periodic images was greater than 6 Å. Additionally, spurious long-range electrostatic interactions between periodic images were removed with the isolation scheme of Blöchl.¹⁴² The PAW QM/MM complexes were optimized with the monomer geometry fixed to that of the reference geometry, while the geometry of the TIP3P water molecule was allowed to relax. The fit set of complexes shown in Figure 7.11 is the same as that used by Freindorf and Gao with one exception that the water-sodium ion interaction was replaced with a water-chloromethane interaction. The reason for this substitution is that an appropriate PAW core description for sodium was not available.

Presented in Table 7.6 are the optimized Lennard-Jones parameters from Freindorf and Gao²¹⁶ that acted as the starting point for our parameterization. We note that there are two sets of hydrogen parameters, one for those bonded to carbon (HC) and the other for those bonded to heteroatoms (HX). There are also distinct parameters for nitrogen atoms within neutral and cationic complexes labeled N and N+, respectively. Similarly, there are different parameters for oxygen atoms within neutral and anionic complexes. It is also notable, that during the parameterization, Freindorf and Gao made an effort to generate a set of Lennard-Jones parameters that resembled those of the

OPLS^{159,219} molecular mechanics force fields. Presumably, this was done to maintain a level of transferability for the parameters.

Table 7.6 Optimized Lennard-Jones Parameters for the Combined Hartree-Fock 3-21G and TIP3P potential of Freindorf and Gao.²¹⁶

atom type	D ₀ (kcal/mol)	R ₀ (Å)
C	0.08	3.80
HC (hydrogen on carbon)	0.008	2.60
HX (hydrogen on heteroatoms)	0.10	1.30
O	0.15	3.60
O-	0.15	3.20
N	0.20	3.90
N+	0.15	3.35
F-	0.40	2.80
Li+	0.80	1.50
Cl-	0.11	4.20

During the course of our parameterization, a number of modifications to the PAW QM/MM interaction potential were made aside from the simple adjustment of the van der Waals parameters. First we found that it was necessary to introduce a new atom type for hydrogens bound to a nitrogen atom with a formal positive charge as in complexes 17, 18 and 19. For these interactions it was found that the hydrogen parameters that worked well with the other complexes were too repulsive. This resulted in interaction energies that were too small. Thus, by spawning a new atom type the resulting interaction energies were significantly improved. We have labeled this atom type HN+. Subsequently, when the HN+ atom type was introduced we found that the N and N+ parameters converged to the same values. Thus, the N and N+ parameters were unified into a single set that was used for all nitrogen atoms.

Table 7.7 Computed interaction energies for the monomer-water fit set with various potentials.

complex no.	complex-water interaction energy (kcal/mol)			
	pure QM HF 6-31G* ^a	pure QM BP86-DFT ^b	PAW QM/MM ^c	deviation ^d
<u>1</u>	-	-0.99	-0.88	0.11
<u>2</u>	-14.3	-13.86	-14.04	-0.18
<u>3</u>	-23.3 ^e	-25.65	-25.60	0.05
<u>4</u>	-34. ^e	-29.30	-29.46	-0.16
<u>5</u>	-0.58	-0.31	-0.39	-0.08
<u>6</u>	-21.1	-20.88	-19.69	1.19
<u>7</u>	-14.2	-14.54	-15.40	-0.86
<u>8</u>	-18.1	-17.15	-19.18	-2.03
<u>9</u>	-5.7	-3.89	-3.53	0.37
<u>10</u>	-5.9	-5.01	-5.25	-0.24
<u>11</u>	-3.5	-3.50	-4.81	-1.31
<u>12</u>	-7.3	-3.86	-4.36	-0.50
<u>13</u>	-5.4	-3.82	-4.48	-0.65
<u>14</u>	-5.5	-4.01	-4.29	-0.28
<u>15</u>	-7.4 ^e	-6.50	-4.90	1.60
<u>16</u>	-2.4	-2.58	-3.60	-1.02
<u>17</u>	-16.1	-14.75	-15.37	-0.62
<u>18</u>	-19.1	-17.95	-17.55	0.40
<u>19</u>	-16.3	-16.30	-18.71	-2.41
<u>20</u>	-6.3	-5.77	-5.34	0.43
<u>21</u>	-5.7	-4.35	-5.58	-1.23
<u>22</u>	-6.5	-6.01	-5.37	0.64
<u>23</u>	-2.5	-1.49	-2.63	-1.14
<u>24</u>	-5.4	-4.32	-5.64	-1.32
<u>25</u>	-7.3	-5.15	-5.58	-0.43
<u>26</u>	-18.2	-15.60	-16.75	-1.15
<u>27</u>	-13.8	-12.18	-12.87	-0.70
RMS deviation:				0.98 kcal/mol

^afrom Freindorf and Gao²¹⁶ and references therein. ^bcalculated with ADF at the Becke-Perdew86 level. ^ccalculated without electrostatic scaling (see text). ^ddeviation of the PAW QM/MM results from pure QM Becke-Perdew86 results for which they were fit. ^eexperimental results from references 216 and 230-232.

Using the new set of atom types, Lennard-Jones parameters for the PAW QM/MM potential have been optimized to reproduce the reference ADF DFT results. The interaction energies for the fit set of 27 complexes (Figure 7.11) are displayed in Table 7.7. For comparison, the interaction energies of Freindorf and Gao²¹⁶ determined primarily at the Hartree-Fock 6-31G* level are also provided in Table 7.7. The rms deviation between the PAW QM/MM and the reference DFT interaction energies is 0.98 kcal/mol, with a maximum deviation of 2.41 kcal/mol. This compares to a rms deviation of 0.70 kcal/mol and a maximum deviation of 1.5 kcal/mol obtained by Freindorf and

Gao while optimizing their AI-3/MM parameters to match the Hartree-Fock 6-31G* results. We note that the reference DFT results used here and the reference Hartree-Fock 6-31G* results used by Freindorf and Gao differ from one another with a rms deviation of 1.66 kcal/mol and a maximum deviation of 4.7 kcal/mol. Since the two reference potentials differ from one another more than either of the two fitted hybrid potentials do from their reference sets, we can conclude that the results of the PAW QM/MM fit are respectable. (It is not our intent to discuss which of the two reference potentials is more appropriate.) Although the quality of our fit is reasonable, we notice that the PAW QM/MM interaction energies are systematically too negative compared to the reference DFT results. This suggests that the electrostatic component of the QM/MM interaction potential is too attractive and perhaps an improvement in the fit can be achieved by modifying it.

There are several possibilities for modifying the electrostatic component of the PAW QM/MM potential. First the TIP3P charges on the MM water molecules can be altered. However, this is undesirable since it would disturb the finely tuned parameterization of the water-water interactions. More appropriately, we could retain the original TIP3P charges for the water-water interactions, while a different set could be specified for the QM-MM electrostatic interactions. Alternatively, the electrostatic coupling energy could be reduced by applying an effective scaling factor to these interactions. This would be akin to modifying the dielectric constant.

Table 7.8 Optimized Lennard-Jones Parameters for the PAW QM/MM potential using an effective electrostatic scaling factor of 0.95

atom type	D_0 (kcal/mol)	R_0 (Å)
C	0.060	4.42
HC (hydrogen on carbon)	0.022	2.49
HX (hydrogen on heteroatoms)	0.155	1.24
HN+(hydrogen on N+)	0.010	1.07
O	0.141	3.66
O-	0.019	3.32
N	0.196	3.66
F-	1.300	1.56
Li+	0.241	1.74
Cl-	0.308	2.93

Using the last option, an effective scaling factor has been introduced into the PAW QM/MM electrostatic energy expression of Equation 7-6.[◇] An optimal electrostatic scaling factor of 0.95 was estimated by simply rescaling the electrostatic component of the total interaction energy from first PAW QM/MM calculations (Table 7.7). Using this 'optimal' scaling factor, the PAW QM/MM calculations were all redone and a new set of van der Waals parameters has been optimized which are shown in Table 7.8. The computed interaction energies from the new PAW QM/MM potential are provided in Table 7.9. With the new scaling factor, the rms deviation from the reference is reduced from 0.98 kcal/mol (Table 7.7) to 0.80 kcal/mol. Similarly the maximum deviation is improved with the scaling factor, down from 2.4 kcal/mol to 1.5 kcal/mol. This is comparable to the fit quality of Freindorf and Gao for their AI-3/MM potential which was found to have rms deviation of 0.70 kcal/mol and a maximum deviation of 1.5 kcal/mol for an almost identical fit set.

The computed bond distances using the PAW QM/MM potential are also in good agreement with the reference geometries. This comparison is made in Table 7.10. For the 27 hydrogen bond distances shown in Figure 7.11, the rms deviation from the reference DFT results is computed to be 0.11 Å with a maximum deviation of 0.27 Å, which compares reasonably to the 0.06 Å rms deviation and 0.14 Å maximum deviation obtained for the AI-3/MM potential fit. Again we compare the results to the deviation between the two reference calculations, namely Gao's Hartree-Fock 6-31G* structures and our DFT Becke-Perdew86 geometries. As with the interaction energies we find that the rms deviation of 0.12 Å between the two reference calculations is larger than the deviation between the fitted QM/MM potentials from their respective references. On the other hand, the maximum deviation in bond distances between the 6-31G* and DFT geometries of 0.23 Å is slightly smaller than the maximum deviation of 0.27 Å found between the fitted PAW QM/MM geometries and its respective reference set.

[◇] The electrostatic scaling factor subsequently propagates through to equations 7-8 and 7-10.

Table 7.9 PAW QM/MM interaction energies using an electrostatic scaling factor of 0.95

complex no.	complex-water interaction energy (kcal/mol)		
	pure QM ^a	QM/MM	ΔE
<u>1</u>	-0.99	-0.92	0.07
<u>2</u>	-13.86	-13.76	0.10
<u>3</u>	-25.65	-25.26	0.39
<u>4</u>	-29.30	-29.29	0.01
<u>5</u>	-0.31	-0.47	0.11
<u>6</u>	-20.88	-19.80	1.08
<u>7</u>	-14.54	-15.24	-0.71
<u>8</u>	-17.15	-18.13	-0.98
<u>9</u>	-3.89	-3.35	0.54
<u>10</u>	-5.01	-4.63	0.38
<u>11</u>	-3.50	-4.81	-1.31
<u>12</u>	-3.86	-4.10	-0.24
<u>13</u>	-3.82	-4.13	-0.31
<u>14</u>	-4.01	-3.91	0.10
<u>15</u>	-6.50	-5.22	1.28
<u>16</u>	-2.58	-3.40	-0.82
<u>17</u>	-14.75	-15.46	-0.71
<u>18</u>	-17.95	-17.47	0.48
<u>19</u>	-16.30	-18.16	-1.86
<u>20</u>	-5.77	-5.13	0.63
<u>21</u>	-4.35	-5.80	-1.45
<u>22</u>	-6.01	-5.14	0.87
<u>23</u>	-1.49	-2.58	-1.09
<u>24</u>	-4.32	-5.30	-0.99
<u>25</u>	-5.15	-5.25	-0.10
<u>26</u>	-15.60	-15.73	-0.13
<u>27</u>	-12.18	-12.54	-0.36
RMS error: 0.80 kcal/mol			

^acalculated with ADF at the Becke-Perdew86 level

We conclude this section with a few remarks concerning further validation of the PAW QM/MM coupling model. As previously noted, the multipolar expansion of the true density used in our PAW QM/MM electrostatic coupling is strictly valid in the long range limit. The improvement achieved by introducing an electrostatic scaling factor suggests that there may be deficiencies in the coupling scheme for close range interactions. As with the Li-water potential, these defects have been smoothed out by modifying the van der Waals potential or by introducing other empirical parameters. Although there is no indication that serious complications will arise a thorough study of this issue has not been conducted and future applications of the method should include this.

Table 7.10 Computed interaction Distances for the Monomer-water Fit Set.^{a, b}

complex no.	pure QM DFT	PAW QM/MM ^c	complex no.	pure QM DFT	PAW QM/MM ^c
<u>1</u>	2.56	2.61	<u>15</u>	1.84	1.98
<u>2</u>	2.14	2.13	<u>16</u>	2.09	2.13
<u>3</u>	1.50	1.30	<u>17</u>	1.69	1.73
<u>4</u>	1.92	1.96	<u>18</u>	1.66	1.70
<u>5</u>	2.67	2.60	<u>19</u>	2.76	2.77
<u>6</u>	1.63	1.44	<u>20</u>	1.93	1.94
<u>7</u>	1.72	1.46	<u>21</u>	1.97	1.99
<u>8</u>	3.13	2.94	<u>22</u>	1.93	1.88
<u>9</u>	1.90	1.89	<u>23</u>	2.25	2.08
<u>10</u>	1.88	1.93	<u>24</u>	1.94	1.93
<u>11</u>	1.94	1.99	<u>25</u>	1.88	1.93
<u>12</u>	1.91	1.93	<u>26</u>	3.36	3.43
<u>13</u>	1.97	2.00	<u>27</u>	1.80	1.91
<u>14</u>	1.93	1.97			

^ainteraction distances measured are defined in Figure 7.11 ^bdistances reported in Ångstroms. ^coptimized using an effective electrostatic scaling factor of 0.95.

In this optimization of the PAW QM/MM potential, no attempt was made to generate a set of van der Waals parameters that resembled those of standard molecular mechanics force fields. This contrasts the fit of Gao and Friendorf who made a conscious effort not to deviate significantly from 'standard' van der Waals parameters. Selected van der Waals parameters of the established AMBER95 force field are shown in Table 7.1, the optimized parameters of Freindorf and Gao are given in Table 7.6 and our best optimized parameters with the electrostatic scaling factor are given in Table 7.8. For the most part the parameters generated for the PAW QM/MM fit agree well with those of Gao and the AMBER95 force field. However, there are significant deviations in the R_0 parameters for the C, F, Cl atom types. For example, from our fit the R_0 parameter is optimized to be 4.42 Å whereas it is found to be 3.80 and 3.816 Å for the AI-3/MM potential and the AMBER95 potential, respectively. The most severe deviation occurs for Cl where we optimized a value of $R_0=2.93$ Å, whereas it is 4.20 from the AI-3/MM parameterization. (There is no AMBER parameter for this atom type.) Since the QM/MM potential is empirical in nature, this deviation from so called standard values is not 'wrong' in any way. However, it does put the transferability of the parameters generated into question. Again this is an issue that should be explored in future validations of the model.

Of course the ultimate test of the PAW QM/MM method is to actually apply the model to simulate the condensed phase. These calculations have not been performed. However, in view of the results of Gao and co-workers,^{14,208,216} the good agreement

between the PAW QM/MM results and the reference potentials shows that the such calculations are a realistic goal in the near future.

7.7 Conclusions

In this chapter we have laid the foundations for performing condensed phase simulations with the PAW QM/MM method. The work has the goal of allowing for explicit solvent effects to be incorporated into our *ab initio* molecular dynamics simulations. The electrostatic coupling scheme used in the PAW QM/MM implementation is somewhat different from conventional QM/MM implementations. Most importantly, it involves a multipolar expansion of the true density which is strictly only valid for long range interactions. We have tested the appropriateness of the coupling scheme for the critical close range distances by comparing the PAW QM/MM potential to that of a pure QM reference DFT potential for a single lithium ion-water interaction and a set of 27 hydrogen bonded complexes. The empirical parameters in the PAW QM/MM model allow for the optimization of the hybrid potential to match that of the reference potential. For the lithium ion-water interaction a near 'perfect' fit was attainable by using an exponential-6 representation of the van der Waals potential and modifying only the Li parameters. In the case of the 27 hydrogen bonded complexes, optimization of the van der Waals parameters lead to a good agreement in the interaction energies between the PAW QM/MM potential and the reference DFT potential. A rms deviation in the 27 interaction energies was computed to be only 0.98 kcal/mol. This compares well to the work of Freindorf and Gao who fit their Hartree-Fock 3-21G/TIP3P hybrid potential to a Hartree-Fock 6-31G reference potential for the same fit set. They were able to obtain a remarkable rms deviation of only 0.70 kcal/mol. In an attempt to improve the quality of our PAW QM/MM model, we further modified the electrostatic component of the QM/MM potential. By introducing a scaling factor that reduced the electrostatic interaction energy between the QM wave function and the MM charges by 95%, the rms deviation in the interaction energies was reduced from 0.98 kcal/mol to 0.80 kcal/mol. Other metrics of the fit quality were also improved and found to be comparable to the results of Freindorf and Gao. Finally, in this chapter we have also demonstrated that the PAW QM/MM coupling scheme allows for energy conserving dynamics, a minimum prerequisite for performing molecular dynamics simulations. In view of the results presented here, combined QM/MM *ab initio* molecular dynamics simulations with explicit solvent molecules is an attainable goal for future work. Coupled with our multiple time step procedure to accelerate the sampling of the MM subsystem, we hope

that the combined PAW QM/MM method will become a practical tool for future studies of olefin polymerization catalyst and other systems.

Chapter 8

Summary and Outlook

The goal of this thesis has been to develop more realistic, yet practical, computational models of chemical processes at the density functional level using the combined QM/MM and *ab initio* molecular dynamics methods. Towards this goal, the combined QM/MM methodology has been implemented into both the ADF density functional package and the PAW *ab initio* molecular dynamics program. The implementations allow both the molecular mechanics and quantum mechanics regions to reside within the same molecule following the basic capping atom approach of Singh and Kollman.⁸ We have also adapted⁹⁸ the IMOMM method of Maseras and Morokuma¹⁵ to allow for both normal-mode frequency calculations and molecular dynamics simulations to be performed. Although the modification of the method is simple, it is significant in the sense that free energy surfaces can now be explored using the IMOMM method via frequency calculations and dynamics simulations.

The implementation of the hybrid potentials have allowed us to examine olefin polymerization systems where the influence of the extended ligand systems are included. The ADF QM/MM method has been applied to study Brookhart's Ni-diimine catalyst system^{1,2} of the type $(\text{ArN}=\text{C}(\text{R}')-\text{C}(\text{R}')=\text{NAr})\text{Ni}(\text{II})\text{-alkyl}^+$ where the bulky $\text{R}'=\text{Me}$ and $\text{Ar}=2,6\text{-C}_6\text{H}_3(i\text{-Pr})_2$ play a critical role in controlling the polymerization chemistry. The chain propagation, termination and isomerization processes were investigated with the hybrid potential where the R' and Ar ligands have been treated with a molecular mechanics potential. The calculated relative and absolute enthalpic barriers were found to be in good agreement with experimental values. Moreover, insight into the role of the bulky ligands has been revealed including aspects never before proposed. The study has also set a firm foundation for the application of the QM/MM method to more recently invented catalysts.^{40,187-190} Application of the ADF QM/MM method to McConville's group 4 diamide catalysts has lead to the suggestion of new ligand structures for which calculations show improved catalytic properties. Experimental confirmation of the predictions is forthcoming.¹²⁹ Thus, with the ADF QM/MM approach we have taken an important step toward the goal of *a priori* catalyst design on the computer.

The application of the *ab initio* molecular dynamics (AIMD) method has enabled us to include finite temperature effects into our models of transition metal based systems.

The AIMD approach has been particularly useful for initially charting flat and complicated potential energy surfaces, thereby allowing static methods to be applied in a more efficient manner. We have also used the AIMD approach to study the time scale of the fluxional rearrangement of the growing polymer chain in a single-site catalyst system. Via the slow growth method, we have explored the reaction free energy profiles for a number of chain termination processes using the AIMD method. In more than one case we have found the AIMD method useful for finding new and ultimately more favourable reaction channels. In one instance we accidentally discovered a new reaction that may provide an explanation for many side products observed in propene polymerization systems.^{154,233}

The QM/MM methodology has been implemented within the Car-Parrinello *ab initio* molecular dynamics framework for the first time. We have also demonstrated that the method can be a practical tool for studying transition metal based catalytic systems. Here, the β -hydrogen transfer to the monomer process in Brookhart's Ni-diimine catalyst was examined at 300 K. The slow growth barrier for the process was determined to be 14.8 kcal/mol which agrees well with the experimental value of 15.5-16.5 kcal/mol.¹²² We have also put forward a unique application of the multiple time step technique within the framework of combined QM/MM molecular dynamics method. In combination with mass rescaling techniques we have demonstrated that the combined QM/MM multiple time step dynamics method can be used to improve configurational averaging on the hybrid QM/MM potential surface during classical molecular dynamics simulations. Although it has yet to be determined how effective the method is in 'real life' applications, the additional cost of the technique is generally small.

Using both the ADF QM/MM and PAW QM/MM packages, we have explored the olefin capture process in Brookhart's Ni-diimine catalyst system. The unique chain branching ability of the catalyst is controlled by the olefin capture process. We have been able to correlate the olefin uptake energies with the observed branching rates. With a series of calculations where electronic and steric effects were separated in a unique manner with the ADF QM/MM method, we have been able to rationalize a puzzling substituent effect that is observed experimentally. With a combination of static and dynamics simulations we have also explored the free energy profile of the olefin capture process. The calculations suggest that the barrier is entropic in nature where the barrier height increases with increasing crowding of the active site.

Inroads have been made for allowing explicit solvent effects to be incorporated into PAW QM/MM simulations of chemical reactions. The polarizable electrostatic

coupling scheme that has been implemented into the PAW QM/MM program provides a firm foundation for this. We have demonstrated that by adjusting various parameters of the coupling model, the PAW QM/MM potential can reproduce the 'true' interaction potentials for a range of complexes. Completion of this work is the most obvious avenue for extending the research presented in this thesis. Such future work has the promise of allowing for the exploration of reactions in the condensed phase with the PAW QM/MM method.

Potential applications of the QM/MM method are tremendous. However, in relation to our studies of olefin polymerization catalysts, the next important step in increasing the 'realism' of our simulations is to include the effects of the counter-ions (sometimes called cocatalysts). The active catalytic species are generally cationic, and the nature of the corresponding counterion can have a dramatic influence on the polymerization chemistry of the system.¹²³ Since the size of the counterions generally dwarfs that of the catalyst itself, the QM/MM method is an aptly suited computational tool for studying the role of the counterion in these catalyst systems.

The application and development of the QM/MM method is currently an active field of research. It is also a relatively new field of research and for this reason there are many unexplored aspects of the QM/MM family of methods. One such area that has received significant attention within the QM/MM arena is the inclusion of polarizable molecular mechanics force fields in the hybrid potential. This not only allows the wave function to be polarized by the charge distribution of the MM system, but also allows the MM charge distribution to correspondingly distort. Particularly in biological systems, it is important to model the polarization effects realistically since there are often subtle but important interactions between the components of the active site and charged residues in the extended protein matrix. Unfortunately, with traditional approaches the incorporation of a polarizable force field significantly increases the computational expense of the QM/MM calculation. This is where the Car-Parrinello QM/MM method shows some promise. Here, the Car-Parrinello Lagrangian could be further extended such that the evolution of the charge distribution of the MM subsystem is treated as yet another dynamical subsystem. The computational expense of treating the additional subsystem would be negligible and therefore the Car-Parrinello QM/MM method offers an efficient way to include a polarizable molecular mechanics force field in the hybrid QM/MM potential.

It is hoped that future studies of transition metal based catalytic processes will include extended ligand effects, finite temperature effects and solvent effects as to build

more realistic computational models of the systems. The ultimate goal here, is to gain a deeper understanding of the fascinating and complicated chemistry of these systems.

References

- (1) Johnson, L. K.; Killian, C. M.; Brookhart, M. *J. Am. Chem. Soc.* **1995**, *117*, 6414.
- (2) Johnson, L. K.; Mecking, S.; Brookhart, M. *J. Am. Chem. Soc.* **1996**, *118*, 267.
- (3) Haggin, J. in *Chemical and Engineering News*, February 5, 1996; p. 6.
- (4) Strain, M. C.; Scuseria, G. E.; Frisch, M. J. *Science* **1996**, *271*, 51.
- (5) White, C. A.; Johnson, B. G.; Gill, P. M. W.; Head-Gordan, M. *Chem. Phys. Lett.* **1996**, *253*, 268.
- (6) Yang, W.; Lee, T.-S. *J. Chem. Phys.* **1995**, *103*, 5674.
- (7) Warshel, A.; Levitt, M. *J. Mol. Biol.* **1976**, *103*, 227.
- (8) Singh, U. C.; Kollman, P. A. *J. Comput. Chem.* **1986**, *7*, 718.
- (9) Field, M. J.; Bash, P. A.; Karplus, M. *J. Comput. Chem.* **1990**, *11*, 700.
- (10) Gao, J. in *Reviews in Computational Chemistry*; K. B. Lipkowitz and D. B. Boyd, Ed.; VCH: New York, 1996; Vol. 7, p. 119.
- (11) Bash, P. A.; Field, M. J.; Karplus, M. *J. Am. Chem. Soc.* **1987**, *109*, 8092.
- (12) Hartsough, D. S.; Merz Jr., K. M. *J. Phys. Chem.* **1995**, *99*, 11266.
- (13) Bakowies, D.; Thiel, W. *J. Phys. Chem.* **1996**, *100*, 10580.
- (14) Gao, J.; Xia, X. *Science* **1992**, *258*, 631.
- (15) Maseras, F.; Morokuma, K. *J. Comput. Chem.* **1995**, *16*, 1170.
- (16) Eichler, U.; Kölmel, C. M.; Sauer, J. *J. Comput. Chem.* **1997**, *18*, 463.
- (17) Stanton, R. V.; Hartsough, D. S.; Merz Jr., K. M. *J. Comput. Chem.* **1995**, *16*, 113.
- (18) Tuñón, I.; Martins-Costa, M. T. C.; Millot, C.; Ruis-López, M. F. *J. Chem. Phys.* **1997**, *106*, 3633.
- (19) Stanton, R. V.; Hartsough, D. S.; Merz Jr., K. M. *J. Phys. Chem.* **1993**, *97*, 11868.
- (20) Liu, H. Y.; Mullerplathe, F.; van Gunsteren, W. F. *J. Mol. Biol.* **1996**, *261*, 454.

- (21) Lyne, P. D.; Mulholland, A. J.; Richards, W. G. *J. Am. Chem. Soc.* **1995**, *117*, 11345.
- (22) Harrison, M. J.; Burton, N. A.; Hillier, I. H.; Gould, I. R. *Chem. Commun.* **1996**, 2769.
- (23) Bash, P. A.; Field, M. J.; Davenport, R.; Ringe, D.; Petsko, G.; Karplus, M. *Biochemistry* **1991**, *30*, 5826.
- (24) Elcock, A. H. E.; Lyne, P. D.; Mulholland, A. J.; Nandra, A.; Richards, W. G. *J. Am. Chem. Soc.* **1995**, *117*, 4706.
- (25) Ho, L. L.; MacKerell Jr., A. D.; Bash, P. A. *J. Phys. Chem.* **1996**, *100*, 4466.
- (26) Warshel, A. *Computer Modelling of Chemical Reactions in Enzymes and Solutions*; John Wiley & Sons: New York, 1991.
- (27) Gao, J. *J. Phys. Chem.* **1992**, *96*, 537.
- (28) Matsubara, T.; Maseras, F.; Koga, N.; Morokuma, K. *J. Phys. Chem.* **1996**, *100*, 2573.
- (29) Deng, L.; Woo, T. K.; Cavallo, L.; Margl, P. M.; Ziegler, T. *J. Am. Chem. Soc.* **1997**, *119*, 6177.
- (30) Woo, T. K.; Margl, P. M.; Blöchl, P. E.; Ziegler, T. *J. Phys. Chem. B* **1997**, *101*, 7877.
- (31) Allen, M. P.; Tildesley, D. J. *Computer Simulation of Liquids*; Oxford University Press: Oxford, 1987.
- (32) Jorgensen, W. L.; Chandrasekhar, J.; Madura, J. D.; Impey, R. W.; Klein, M. L. *J. Chem. Phys.* **1983**, *79*, 926.
- (33) McCammon, J. A.; Harvey, S. C. *Dynamics of Proteins and Nucleic Acids*; Cambridge University Press: Cambridge U.K., 1987.
- (34) Beveridge, D. L.; DiCapua, F. M. *Annu. Rev. Biophys. Chem.* **1989**, *18*, 431.
- (35) Sinclair, K. B.; Wilson, R. B. in *Chemistry and Industry*, November 1994; p. 857.
- (36) Baerends, E. J.; Ellis, D. E.; Ros, P. *Chem. Phys.* **1973**, *2*, 41.

- (37) Baerends, E. J.; Ros, P. *Chem. Phys.* **1973**, *2*, 52.
- (38) Baerends, E. J. PhD Thesis, Free University, Amsterdam, The Netherlands, 1975.
- (39) te Velde, G.; Baerends, E. J. *J. Comput. Chem.* **1992**, *99*, 84.
- (40) Scollard, J. D.; McConville, D. H. *J. Am. Chem. Soc.* **1996**, *118*, 10008.
- (41) Blöchl, P. E. *Phys. Rev. B* **1994**, *50*, 17953.
- (42) van Leeuwen, P. W. N. M.; Morokuma, K.; van Lenthe, J. H. *Theoretical Aspects of Homogenous Catalysis*; Kluwer Academic Publishers: London, 1995.
- (43) Hehre, W. J.; Radom, L.; Schleyer, P. v. R.; Pople, J. A. *Ab Initio Molecular Orbital Theory*; John Wiley & Sons, Inc.: New York, 1986.
- (44) Szabo, A.; Ostlund, N. S. *Modern Quantum Chemistry*; 1st ed.; McGraw-Hill: New York, 1982.
- (45) Kohn, W.; Sham, L. J. *Phys. Rev.* **1965**, *A140*, 1133.
- (46) Kohn, W.; Becke, A. D.; Parr, R. G. *J. Phys. Chem.* **1996**, *100*, 12974.
- (47) Hohenberg, P.; Kohn, W. *Phys. Rev.* **1964**, *B136*, 864.
- (48) Ziegler, T. *Chem. Rev.* **1991**, *91*, 651.
- (49) Ziegler, T.; Folga, E.; Berces, A. *J. Am. Chem. Soc.* **1993**, *115*, 636.
- (50) Woo, T. K. Ph.D. Thesis Proposal, Department of Chemistry, University of Calgary, 1993.
- (51) Woo, T. K.; Fan, L.; Ziegler, T. *Organometallics* **1994**, *13*, 2252.
- (52) Woo, T. K.; Fan, L.; Ziegler, T. *Organometallics* **1994**, *13*, 432.
- (53) Lohrenz, J. C. W.; Woo, T. K.; Ziegler, T. *J. Am. Chem. Soc.* **1995**, *117*, 12793.
- (54) Lohrenz, J. C. W.; Woo, T. K.; Fan, L.; Ziegler, T. *J. Organomet. Chem.* **1995**, *497*, 91.
- (55) Fan, L.; Krzywicki, A.; Somogyvari, A.; Ziegler, T. *Inorg. Chem.* **1994**, *33*, 5287.
- (56) Fan, L.; Harrison, D.; Deng, L.; Woo, T. K.; Swerhone, D.; Ziegler, T. *Can. J. Chem.* **1995**, *73*, 989.

- (57) Fan, L.; Krzywicki, A.; Somogyvari, A.; Ziegler, T. *Inorg. Chem.* **1996**, *25*, 4003.
- (58) Fan, L.; Harrison, D.; Woo, T. K.; Ziegler, T. *Organometallics* **1995**, *14*, 2018.
- (59) Deng, L.; Margl, P. M.; Ziegler, T. *J. Am. Chem. Soc.* **1997**, *119*, 1094.
- (60) Margl, P. M.; Ziegler, T. *J. Am. Chem. Soc.* **1996**, *118*, 7337.
- (61) Margl, P.; Ziegler, T. *Organometallics* **1996**, *15*, 5519.
- (62) Froese, R. D. J.; Musaev, D. G.; Morokuma, K. *J. Am. Chem. Soc.* **1997**, *119*, 7190.
- (63) Musaev, D. G.; Froese, R. D. J.; Svensson, M.; Morokuma, K. *J. Am. Chem. Soc.* **1997**, *119*, 367.
- (64) Bernardi, F.; Bottoni, A.; Calcinari, M.; Rossi, I.; Robb, M. A. *J. Phys. Chem. A* **1997**, *101*, 6310.
- (65) Stanton, R. V.; Merz Jr., K. M. *J. Chem. Phys.* **1993**, *100*, 434.
- (66) Thiel, W. *Tetrahedron* **1988**, *44*, 7393.
- (67) Stewart, J. J. P. in *Reviews in Computational Chemistry*; K. B. Lipkowitz and D. B. Boyd, Ed.; VCH: New York, 1990; Vol. 1; p. 45.
- (68) Zerner, M. C. in *Reviews in Computational Chemistry*; K. B. Lipkowitz and D. B. Boyd, Ed.; VCH: New York, 1991; Vol. 2; p. 313.
- (69) Pople, J. A.; Santry, D. P.; Segal, G. A. *J. Chem. Phys.* **1965**, *43*, S129.
- (70) Pople, J. A.; Beveridge, D. L.; Dobosh, P. A. *J. Chem. Phys.* **1967**, *47*, 2026.
- (71) Bingham, R. C.; Dewar, M. J. S.; Lo, D. H. *J. Am. Chem. Soc.* **1975**, *97*, 1285.
- (72) Dewar, M. J. S.; Thiel, W. *J. Am. Chem. Soc.* **1977**, *99*, 4899.
- (73) Dewar, M. J. S.; Zoebisch, E. G.; Healy, E. F.; Stewart, J. J. P. *J. Am. Chem. Soc.* **1985**, *107*, 3902.
- (74) Stewart, J. J. P. *J. Comput. Chem.* **1989**, *10*, 209.
- (75) Thiel, W.; Voityuk, A. A. *Theor. Chim. Acta.* **1996**, *93*, 315.
- (76) Thiel, W.; Voityuk, A. A. *J. Phys. Chem.* **1996**, *100*, 616.

- (77) Cornell, W. D.; Cieplak, P.; Bayly, C. I.; Gould, I. R.; Merz Jr., K. M.; Ferguson, D. M.; Spellmeyer, D. C.; Fox, T.; Caldwell, J. W.; Kollman, P. A. *J. Am. Chem. Soc.* **1995**, *117*, 5179.
- (78) Brooks, B. B.; Bruccoleri, R. E.; Olafson, B. D.; States, D. J.; Swaminathan, S.; Karplus, M. *J. Comput. Chem.* **1983**, *4*, 187.
- (79) Allinger, N. L. *J. Am. Chem. Soc.* **1977**, *99*, 8127.
- (80) Allured, V. S.; Kelly, C. M.; Landis, C. R. *J. Am. Chem. Soc.* **1991**, *113*, 1.
- (81) Rappé, A. K.; Casewit, C. J.; Colwell, K. S.; Goddard III, W. A.; Skiff, W. M. *J. Am. Chem. Soc.* **1992**, *114*, 10024.
- (82) Casewit, C. J.; Colwell, K. S.; Rappé, A. K. *J. Am. Chem. Soc.* **1992**, *114*, 10046.
- (83) Cavallo, L.; Guerra, G.; Oliva, L.; Vacatello, M.; Corradini, P. *Polymer Comm.* **1989**, *30*, 16.
- (84) Corradini, P.; Guerra, G.; Vacatello, M.; Villani, V. *Gazz. Chim. Ital.* **1988**, *118*, 173.
- (85) Cavallo, L.; Guerra, G.; Corradini, P.; Resconi, L.; Waymouth, R. M. *Macromolecules* **1993**, *26*, 260.
- (86) Guerra, G.; Cavallo, L.; Moscardi, G.; Vacatello, M.; Corradini, P. *J. Am. Chem. Soc.* **1994**, *116*, 2988.
- (87) Woo, T. K.; Fan, L.; Ziegler, T. in *Ziegler Catalysts: Recent Scientific Innovations and Technological Improvements*; G. Fink; R. Mülhaupt and H. H. Brintzinger, Ed.; Springer-Verlag: Berlin, 1996; p. 291.
- (88) Castonguay, L. A.; Rappé, A. K. *J. Am. Chem. Soc.* **1992**, *114*, 5832.
- (89) Hart, J. R.; Rappé, A. K. *J. Am. Chem. Soc.* **1993**, *115*, 6159.
- (90) Höweler, U.; Mohr, R.; Knickmeier, M.; Erker, G. *Organometallics* **1994**, *13*, 2380.
- (91) Kawamura-Kuribayashi, H.; Koga, N.; Morokuma, K. *J. Am. Chem. Soc.* **1992**, *114*, 8687.
- (92) Corchado, J. C.; Truhlar, D. G. *J. Phys. Chem. A* **1998**, *102*, 1895.

- (93) Théry, V.; Rinaldi, D.; Rivail, J.-L.; Maigret, B.; Ferenczy, G. G. *J. Comput. Chem.* **1994**, *15*, 269.
- (94) Bersuker, I. B.; Leong, M. K.; Boggs, J. E.; Pearlman, R. S. *J. Comput. Chem.* **1997**, *63*, 1051.
- (95) Humbel, S.; Sieber, S.; Morokuma, K. *J. Chem. Phys.* **1996**, *105*, 1959.
- (96) Ravenek, W., *Algorithms and Applications on Vector and Parallel Computers*; H. J. J. te Riele; T. J. Dekker and H. A. van de Horst Ed.; Elsevier: Amsterdam, The Netherlands, 1987.
- (97) Versluis, L.; Ziegler, T. *J. Chem. Phys.* **1988**, *88*, 322.
- (98) Woo, T. K.; Cavallo, L.; Ziegler, T. *Theor. Chem. Act.* accepted, July 14, 1998.
- (99) Patchkoviskii, S.; Woo, T. K.; Ziegler, T., unpublished work.
- (100) Woo, T. K. "ADF and PAW QM/MM User's Manual," Department of Chemistry, University of Calgary, Calgary, Alberta, Canada., 1998.
- (101) Weiner, P. K.; Kollman, P. A. *J. Comput. Chem.* **1981**, *2*, 287.
- (102) Matsubara, T.; Sieber, S.; Morokuma, K. *Int. J. Quantum Chem.* **1996**, *60*, 1101.
- (103) Becke, A. *Phys. Rev. A* **1988**, *38*, 3098.
- (104) Perdew, J. P. *Phys. Rev. B* **1986**, *34*, 7406.
- (105) Perdew, J. P. *Phys. Rev. B* **1986**, *33*, 8822.
- (106) McQuarrie, D. A. *Statistical Thermodynamics*; Harper & Row: New York, 1973.
- (107) Svensson, M.; Humbel, S.; Froese, R. D. J.; Matsubara, T.; Sieber, S.; Morokuma, K. *J. Phys. Chem.* **1996**, *100*, 19357.
- (108) Silverstein, R. M.; Bassler, G. C.; Morrill, T. C. *Spectrometric Identification of Organic Compounds*; 5th ed.; John Wiley & Sons, Inc.: New York, 1991.
- (109) Killian, C. M.; Tempel, D. J.; Johnson, L. K.; Brookhart, M. *J. Am. Chem. Soc.* **1996**, *118*, 11664.
- (110) Wilke, G. *Angew. Chem., Int. Ed. Engl.* **1988**, *27*, 185.
- (111) Keim, W. *Angew. Chem., Int. Ed. Engl.* **1990**, *29*, 235.

- (112) Abecywickrema, R.; Bennett, M. A.; Cavell, K. J.; Kony, M.; Masters, A. F.; Webb, A. G. *J. Chem. Soc., Dalton Trans.* **1993**, 59.
- (113) Brown, S. J.; Masters, A. F. *J. Organomet. Chem.* **1989**, 367, 371.
- (114) Snijders, J. G.; Baerends, E. J.; Vernoijs, P. *Atomic and Nuclear Data Tables* **1982**, 26, 483.
- (115) Vernoijs, P.; Snijders, J. G.; Baerends, E. J. "Slater Type Basis Functions for the Whole Periodic System," Department of Theoretical Chemistry, Free University: Amsterdam, The Netherlands, 1981.
- (116) Krijn, J.; Baerends, E. J. "Fit Functions in the HFS Method," Department of Theoretical Chemistry, Free University: Amsterdam, The Netherlands, 1984.
- (117) Vosko, S. H.; Wilk, L.; Nusair, M. *Can. J. Phys.* **1980**, 58, 1200.
- (118) Perdew, J. P.; Zunger, A. *Phys. Rev. B* **1981**, 23, 5048.
- (119) Snijders, J. G.; Baerends, E. J. *Molecular Physics* **1978**, 36, 1789.
- (120) Snijders, J. G.; Baerends, E. J.; Ros, P. *Molecular Physics* **1979**, 38, 1909.
- (121) Woo, T. K.; Margl, P. M.; Lohrenz, J. C. W.; Blöchl, P. E.; Ziegler, T. *J. Am. Chem. Soc.* **1996**, 118, 13021.
- (122) Brookhart, M., Department of Chemistry, University of North Carolina at Chapel Hill. A private communication.
- (123) Brintzinger, H. H.; Fischer, D.; Mülhaupt, R.; Rieger, B.; Waymouth, R. M. *Angew. Chem. Int. Ed. Engl.* **1995**, 34, 1143.
- (124) Cavallo, L.; Guerra, G. *Macromolecules* **1996**, 29, 2729.
- (125) Hart, J. R.; Rappé, A. K. *J. Am. Chem. Soc.* **1993**, 115, 6159.
- (126) Morokuma, K.; Yoshida, T.; Koga, N. *Organometallics* **1996**, 15, 2766.
- (127) Deng, L.; Ziegler, T.; Woo, T. K.; Margl, P. M.; Fan, L. *Organometallics*, **1998**, 17, 3240.
- (128) McConville, D. H., Department of Chemistry, University of British Columbia. A private communication.

- (129) Piers, W. E., Department of Chemistry, University of Calgary. A private communication.
- (130) Car, R.; Parrinello, M. *Phys. Rev. Lett.* **1985**, *55*, 2471.
- (131) Margl, P.; Blöchl, P.; Ziegler, T. *J. Am. Chem. Soc.* **1995**, *117*, 12625.
- (132) Margl, P.; Schwarz, K.; Blöchl, P. E. *J. Am. Chem. Soc.* **1994**, *116*, 11177.
- (133) Woo, T. K.; Margl, P. M.; Blöchl, P. E.; Ziegler, T. *Organometallics* **1997**, *16*, 3454.
- (134) Woo, T. K.; Margl, P. M.; Deng, L.; Ziegler, T. in *Science and Catalysis: Advances and Applications of Computational Chemical Modelling to Heterogeneous Catalysis*; M. Neurock and R. A. van Santen, Ed.; Elsevier: in press.
- (135) Margl, P. M.; Woo, T. K.; Blöchl, P. E.; Ziegler, T. *J. Am. Chem. Soc.* **1998**, *120*, 2174.
- (136) Tuckerman, M. E.; Parrinello, M. *J. Phys. Chem.* **1996**, *100*, 12878.
- (137) Remler, D. K.; Madden, P. A. *Mol. Phys.* **1990**, *70*, 921.
- (138) Verlet, L. *Phys. Rev.* **1967**, *159*, 98.
- (139) Hockney, R. W. *Methods Comp. Phys.* **1970**, *9*, 136.
- (140) Hartke, B.; Carter, E. A. *J. Chem. Phys.* **1992**, *97*, 6569.
- (141) Hartke, B.; Carter, E. A. *Chem. Phys. Lett.* **1992**, *189*, 358.
- (142) Blöchl, P. E. *J. Chem. Phys.* **1995**, *103*, 7422.
- (143) Blöchl, P. E.; Margl, P. M.; Schwarz, K., *ACS Symposium Series 629: Chemical Applications of Density-Functional Theory*; B. B. Laird; R. B. Ross and T. Ziegler Ed.; American Chemical Society: Washington, DC, 1996, p. 54.
- (144) Carter, E. A.; Ciccotti, G.; Hynes, J. T.; Kapral, R. *Chem. Phys. Lett.* **1989**, *156*, 472.
- (145) Paci, E.; Ciccotti, G.; Ferrario, M.; Kapral, R. *Chem. Phys. Lett.* **1991**, *176*, 581.

- (146) Straatsma, T. P.; Berendsen, H. J. C.; Postma, J. P. M. *J. Chem. Phys.* **1986**, *85*, 6720.
- (147) Nosé, S. *Mol. Phys.* **1984**, *52*, 255.
- (148) Hoover, W. G. *Phys. Rev. A* **1985**, *31*, 1695.
- (149) Blöchl, P. E.; Parrinello, M. *Phys. Rev. B* **1992**, *45*, 9413.
- (150) De Raedt, B.; Sprik, M.; Klein, M. L. *J. Chem. Phys.* **1984**, *80*, 5719.
- (151) Lindsay, K. F. in *Modern Plastics*, October 1993; p. 82.
- (152) Cossée, P. *J. Catal.* **1964**, *3*, 80.
- (153) Arlman, E. J.; Cossee, P. *J. Catal.* **1964**, *3*, 99.
- (154) Karol, F. J.; Kao, S.-C.; Wasserman, E. P.; Brady, R. C. *New J. Chem.* **1997**, *21*, 797.
- (155) Galli, G.; Parrinello, M. *Phys. Rev. Lett.* **1992**, *69*, 3547.
- (156) Mauri, F.; Galli, G.; Car, R. *Physical Review B* **1993**, *47*, 9973.
- (157) Tuckerman, M. E.; Parrinello, M. *J. Chem. Phys.* **1994**, *101*, 1302.
- (158) Tuckerman, M. E.; Berne, B. J.; Martyna, G. J. *J. Chem. Phys.* **1992**, *97*, 1990.
- (159) Jorgensen, W. L.; Maxwell, D. S.; Tirado-Rives, J. *J. Am. Chem. Soc.* **1996**, *118*, 11225.
- (160) Hwang, J.-K.; King, G.; Creighton, S.; Warshel, A. *J. Am. Chem. Soc.* **1988**, *110*, 5297.
- (161) Thompson, M. A. *J. Am. Chem. Soc.* **1995**, *117*, 11341.
- (162) Thompson, M. A.; Glendening, E. D.; Feller, D. *J. Phys. Chem.* **1994**, *98*, 10465.
- (163) Cummins, P. L.; Gready, J. E. *J. Comput. Chem.* **1997**, *18*, 1496.
- (164) Wang, J.; Boyd, R. J.; Laaksonen, A. *J. Chem. Phys.* **1996**, *104*, 7261.
- (165) Strnad, M.; Martins-Costa, M. T. C.; Millot, C.; Tuñón, I.; Ruis-López, M. F.; Rivail, J. L. *J. Chem. Phys.* **1997**, *106*, 3643.

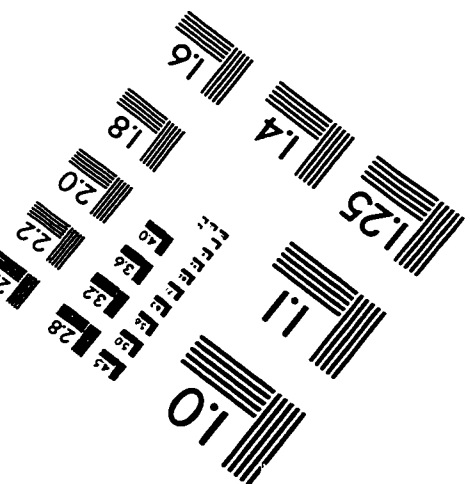
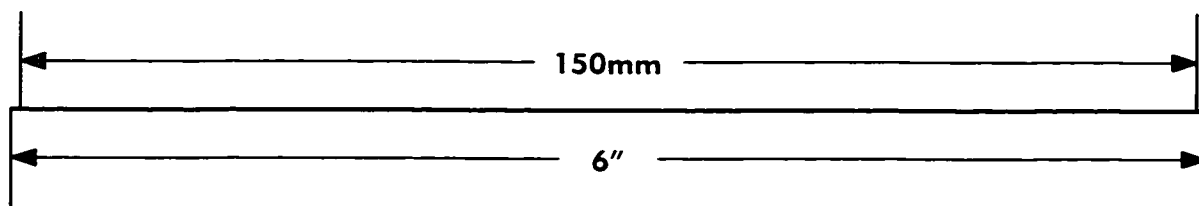
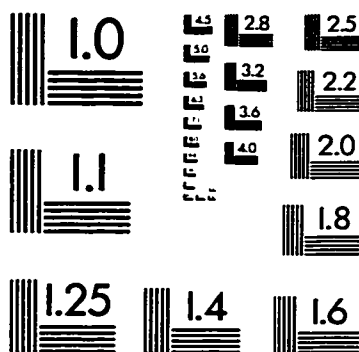
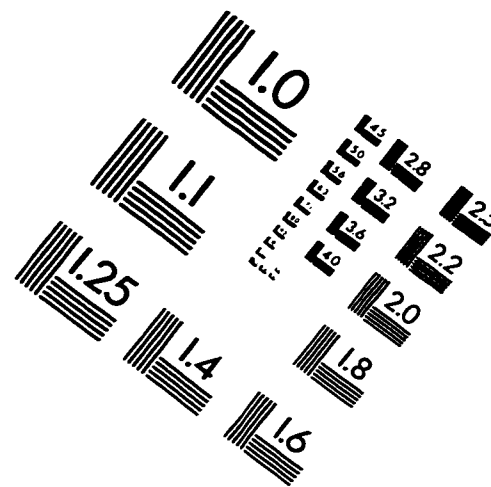
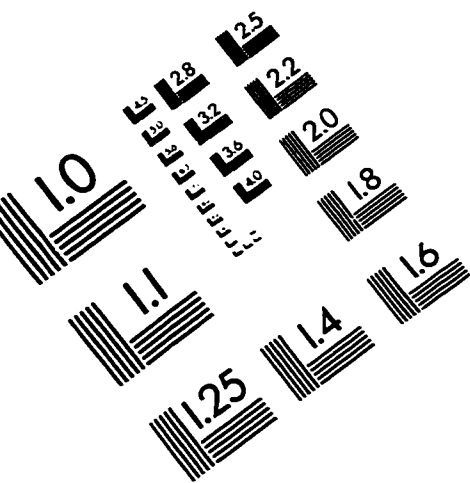
- (166) Margl, P.; Lohrenz, J. C. W.; Blöchl, P.; Ziegler, T. *J. Am. Chem. Soc.* **1996**, *118*, 4434.
- (167) Spaleck, W.; Küber, F.; Winter, A.; Rohrmann, J.; Bachmann, B.; Antberg, M.; Dolle, V.; Paulus, E. F. *Organometallics* **1994**, *13*, 954.
- (168) Li, X.-P.; Nunes, R. W.; Vanderbilt, D. *Physical Review B* **1993**, *47*, 10891.
- (169) van Gunsteren, W. F.; Berendsen, H. J. C. *Angew. Chem. Int. Ed. Engl.* **1990**, *29*, 992.
- (170) Streett, W. B.; Tildesley, D. J. *Mol. Phys.* **1978**, *35*, 639.
- (171) Gibson, D. A.; Carter, E. A. *J. Phys. Chem.* **1993**, *97*, 13429.
- (172) Martyna, G. J.; Tuckerman, M. E.; Tobias, D. J.; Klein, M. L. *Mol. Phys.* **1996**, *87*, 1117.
- (173) Tuckerman, M. E.; Parrinello, M. *J. Chem. Phys.* **1994**, *101*, 1316.
- (174) Smith, D. E.; Dang, L. X. *J. Chem. Phys.* **1994**, *100*, 3757.
- (175) Musaev, D. G.; Froese, R. D. J.; Morokuma, K. *Organometallics* **1998**, *17*, 1850.
- (176) Strömberg, s.; Zetterberg, K.; Siegbahn, P. E. M. *J. Chem. Soc., Dalton Trans.* **1997**, *1997*, 4147.
- (177) Sinnema, J. C. M.; Frendesak, G. H. B.; tom Dieck, H. J. *Organomet. Chem.* **1990**, *390*, 237.
- (178) Diercks, R.; Kopf, J.; tom Dieck, H. *Acta Crystallogr., Sect. C.* **1984**, *40*, 363.
- (179) van Asselt, R.; Elsevier, C. J.; Smeets, W. J. J.; Spek, A. L. *Inorg. Chem.* **1994**, *33*, 1521.
- (180) Margl, P. M.; Deng, L.; Ziegler, T. *Organometallics* **1998**, *17*, 933.
- (181) Searle, M. S.; Williams, D. H. *J. Am. Chem. Soc.* **1992**, *114*, 10690.
- (182) Dunitz, J. D. *Chem. Biol.* **1995**, *2*, 709.
- (183) Dunitz, J. D. *Science* **1994**, *264*, 670.
- (184) Rauk, A. *Orbital Interaction Theory of Organic Chemistry*; John Wiley & Sons, Inc.: New York, 1994.

- (185) Woo, T. K.; Ziegler, T. *Inorganic Chem.* **1994**, *33*, 1857.
- (186) Cavallo, L.; Woo, T. K.; Ziegler, T. *Can. J. Chem.* submitted.
- (187) Small, B. L.; Brookhart, M.; Benett, A. M. A. *J. Am. Chem. Soc.* **1998**, *120*, 4049.
- (188) Scollard, J. D.; McConville, D. H.; Payne, N. C.; Vittal, J. *Macromolecules* **1996**, *29*, 5241.
- (189) Britovsek, G. J. P.; Gibson, V. C.; Kimberley, B. S.; Maddox, P. J.; McTavish, S. J.; Solan, G. A.; White, A. J. P.; Williams, D. J. *Chem. Commun.* **1998**, 849.
- (190) Baumann, R.; Davis, W. M.; Schrock, R. R. *J. Am. Chem. Soc.* **1997**, *119*, 3830.
- (191) Lauher, J. W.; Hoffmann, R. *J. Am. Chem. Soc.* **1976**, *98*, 1729.
- (192) Gleiter, R.; Hyla-Kryspin, I.; Niu, S.; Erker, G. *Organometallics* **1993**, *12*, 3828.
- (193) Prosenc, M.-H.; Janiak, C.; Brintzinger, H.-H. *Organometallics* **1992**, *11*, 4036.
- (194) Kawamura-Kuribayashi, H.; Koga, N.; Morokuma, K. *J. Am. Chem. Soc.* **1992**, *114*, 2359.
- (195) Bierwagen, E. P.; Bercaw, J. E.; Goddard III, W. A. *J. Am. Chem. Soc.* **1994**, *116*, 1481.
- (196) Weiss, H.; Ehrig, M.; Ahlrichs, R. *J. Am. Chem. Soc.* **1994**, *116*, 4919.
- (197) Iarlari, S.; Buda, F.; Meier, R. J.; van DoreMaele, G. H. *J. Molecular Physics* **1996**, *87*, 801.
- (198) Meier, R. J.; van Dormaele, G. H. J.; Larlori, S.; Buda, F. *J. Am. Chem. Soc.* **1994**, *116*, 7274.
- (199) Searle, M. S.; Westwell, M. S.; Williams, D. H. *J. Chem. Soc., Perkin Trans* **1995**, *2*, 141.
- (200) Finkelstein, A. V.; Janin, J. *Protein Eng.* **1989**, *3*, 1.
- (201) Woo, T. K.; Margl, P. M.; Deng, L.; Ziegler, T., unpublished work.
- (202) Rix, F.; Brookhart, M. *J. Am. Chem. Soc.* **1995**, *117*, 1137.
- (203) Klamt, A.; Schuurmann, G. *J. Chem. Soc. Perkin Trans.* **1993**, *2*, 799.

- (204) Pye, C.; Han, Y.; Zielger, T., unpublished work.
- (205) Ben-Naim, A. *Solvation Thermodynamics*; Plenum Press: New York, 1987.
- (206) Deng, L.; Margl, P. M.; Woo, T. K.; Ziegler, T., work in progress.
- (207) Margl, P. M.; Deng, L.; Woo, T. K.; Ziegler, T., work in progress.
- (208) Gao, J. *Acc. Chem. Res.* **1996**, 29, 298.
- (209) Cramer, C. J.; Truhlar, D. G. in *Reviews in Computational Chemistry*; K. B. Lipkowitz and D. B. Boyd, Ed.; VCH Publishers: New York, 1995; Vol. 6.
- (210) Tomasi, J. *Chem. Rev.* **1994**, 94, 2027.
- (211) Curioni, A.; Sprik, M.; Andreoni, W.; Schiffer, H.; Hutter, J.; Parrinello, M. *J. Am. Chem. Soc.* **1997**, 119, 7218.
- (212) Tuckerman, M. E.; Laasonen, K.; Sprik, M.; Parrinello, M. *J. Phys. Chem.* **1995**, 99, 5749.
- (213) Tuckerman, M. E.; Laasonen, K.; Sprik, M.; Parrinello, M. *J. Chem. Phys.* **1995**, 103, 150.
- (214) Gao, J.; Xia, X. *J. Am. Chem. Soc.* **1993**, 115, 9667.
- (215) Gao, J. *Biophys. Chem.* **1994**, 51, 253.
- (216) Freindorf, M.; Gao, J. *J. Comput. Chem.* **1996**, 17, 386.
- (217) Berendsen, H. J. C.; Griera, J. R.; Straatsma, T. P. *J. Phys. Chem.* **1987**, 91, 6269.
- (218) Berendsen, H. J. C.; Postma, J. P. M.; van Gunsteren, W. F.; Hermans, J. in *Intermolecular Forces*; B. Pullman, Ed.; Reidel: Dordrecht, Holland, 1981; p. 331.
- (219) Jorgensen, W. L.; Tirado-Rives, J. *J. Am. Chem. Soc.* **1988**, 110, 1657.
- (220) Hirschfeld, F. L. *Theor. Chim. Acta.* **1977**, 44, 129.
- (221) Bader, R. F.; Bedall, P. M.; Cade, P. E. *J. Am. Chem. Soc.* **1971**, 93, 3095.
- (222) Singh, U. C.; Kollman, P. A. *J. Comput. Chem.* **1984**, 5, 129.

- (223) Bayly, C.; Cieplak, P.; Cornell, W.; Kollman, P. A. *J. Phys. Chem.* **1993**, *97*, 10269.
- (224) Bakowies, D.; Thiel, W. *J. Comput. Chem.* **1996**, *17*, 87.
- (225) Pulay, P. *Mol. Phys.* **1969**, *17*, 197.
- (226) Boys, S. F.; Bernadi, F. *Mol. Phys.* **1970**, *10*, 533.
- (227) te Velde, G. "Amsterdam Density Functional (ADF), User Guide, Release 2.3," Department of Theoretical Chemistry, Free University, Amsterdam, The Netherlands, 1997.
- (228) Simon, S.; Duran, M.; Dannenberg, J. J. *J. Chem. Phys.* **1996**, *109*, 1024.
- (229) Alagona, G.; Ghio, C. *J. Mol. Struc. (Theochem)* **1995**, *330*, 77.
- (230) Kebarle, P. *Annu. Rev. Phys. Chem.* **1977**, *28*, 445.
- (231) Meot-Ner, M. *J. Am. Chem. Soc.* **1988**, *110*, 3854.
- (232) Meot-Ner, M.; Sieck, L. W. *J. Am. Chem. Soc.* **1988**, *108*, 7525.
- (233) Resconi, L., Shell Polyolefins, Ferrara, Italy. A private communication.

IMAGE EVALUATION TEST TARGET (QA-3)



APPLIED IMAGE, Inc.
1653 East Main Street
Rochester, NY 14609 USA
Phone: 716/482-0300
Fax: 716/288-5989

© 1993, Applied Image, Inc., All Rights Reserved

